

Red for LED

New narrow band red phosphors for white light emitting diodes

Printed by: ProefschriftMaken || [Proefschriftmaken.nl](https://proefschriftmaken.nl)

ISBN: 978-94-629-5851-7

Red for LED

New narrow band red phosphors for white
light emitting diodes

Rood voor LED

Nieuwe smalbandig rode fosforen voor wit licht emitterende diodes

(met een samenvatting in het Nederlands)

Proefschrift

ter verkrijging van de graad van doctor aan de Universiteit Utrecht op
gezag van de rector magnificus, prof. dr. G.J. van der Zwaan, ingevolge
het besluit van het college voor promoties in het openbaar te verdedigen
op woensdag 31 januari 2018 des middags te 2.30 uur

door

Tim Senden

geboren op 3 september 1989 te Rotterdam

Promotoren:

Prof. dr. A. Meijerink

Prof. dr. C. R. Ronda

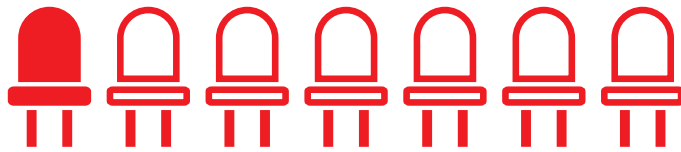
Het onderzoek beschreven in dit proefschrift werd gefinancierd door Technologiestichting STW, welke onderdeel is van de Nederlandse Organisatie voor Wetenschappelijk Onderzoek (NWO).

Table of Contents

1. Introduction	7
2. Synthesis and narrow red luminescence of $\text{Cs}_2\text{HfF}_6:\text{Mn}^{4+}$, a new phosphor for warm white LEDs	25
3. Co-precipitation synthesis and optical properties of Mn^{4+} -doped fluoroaluminate w-LED phosphors	45
4. Comparative study of the Mn^{4+} luminescence in $\text{RE}_2\text{Sn}_2\text{O}_7:\text{Mn}^{4+}$ pyrochlores ($\text{RE}^{3+} = \text{Y}^{3+}, \text{Lu}^{3+}$ or Gd^{3+})	63
5. Quenching of the red Mn^{4+} luminescence in Mn^{4+} - doped fluoride LED phosphors	79
6. The d–f luminescence of Eu^{2+} , Ce^{3+} and Yb^{2+} ions in $\text{Cs}_2\text{MP}_2\text{O}_7$ ($\text{M} = \text{Ca}^{2+}, \text{Sr}^{2+}$)	109
7. Summary and outlook	127
Samenvatting in het Nederlands	134
List of publications and conference contributions	138
Dankwoord	140
About the author	145

1

Introduction



1.1 White light emitting diodes

In the past ten years the lighting market has changed more rapidly than ever before. This has not just been triggered by the ban of incandescent lamps in large areas of the world. The rapid development of white light emitting diodes (LEDs) has started a revolution in lighting that has not ended yet. Due to their superior luminous efficacy (Figure 1.1) and long operation lifetime, white LEDs are considered to be the light sources of the future [1,2]. It is therefore anticipated that white LEDs will largely replace incandescent lamps and (compact) fluorescent tubes in the coming ten years [3]. A transition from traditional lamps to white LEDs will lead to considerable reduction of the worldwide electricity consumption, which is important in view of the climate issues and energy problems we have today [1].

The working principle of a LED is schematically depicted in Figure 1.2. A LED consists of a junction of n-type and p-type semiconductors. If a voltage is applied to this p-n junction in the forward bias direction (negative to n-type and positive to p-type), electrons and holes will flow towards the interface between the n-type and p-type region [4]. The charge carriers are collected in a confinement layer with a slightly smaller band gap. In this layer the charge carriers recombine, which results in the emission of photons (see Figure 1.2b). The energy of the emitted photon is equal to the bandgap energy of the confinement layer. The process schematically depicted in Figure 1.2b is called electroluminescence and takes place in all LEDs used in semiconductor-based solid state lighting. Electroluminescence as a phenomenon was discovered in 1907 by H.J. Round

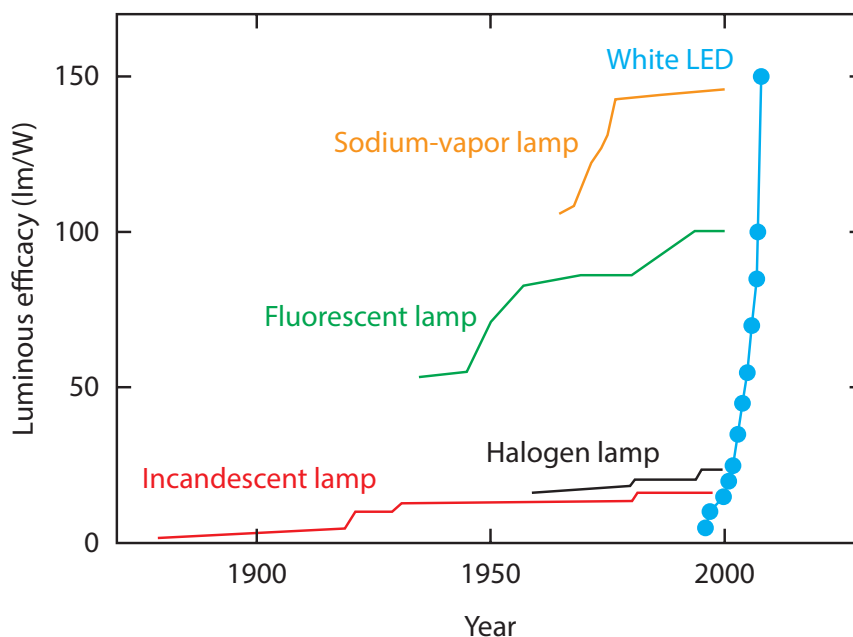


Figure 1.1 – Evolution of the luminous efficacy of incandescent, halogen, fluorescent and sodium-vapor lamps and white LEDs. Adapted from Ref. [1].

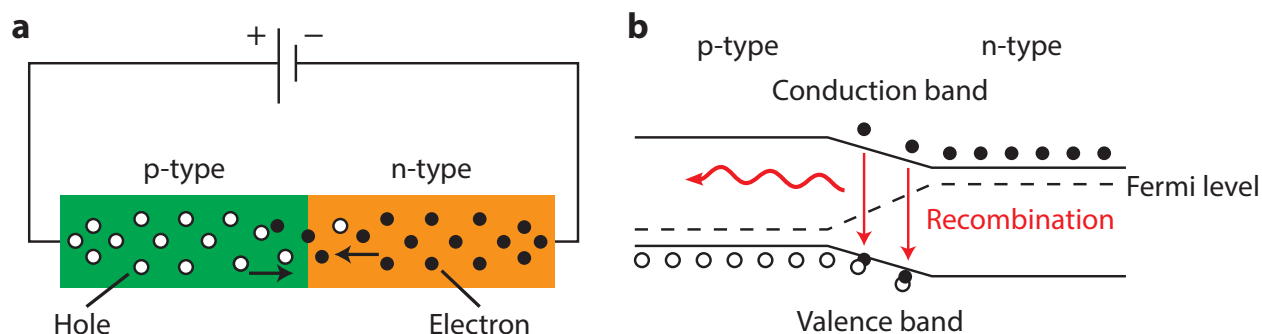


Figure 1.2 – (a) Circuit diagram of a p-n junction diode. Under forward bias the charge carriers (electrons and holes) are transferred towards the junction. (b) Energy level structure of a p-n junction under forward bias. The p-n junction diode emits photons due to radiative recombination of electrons and holes at the interface between the n-type and p-type semiconductor (red arrows).

[5]. He applied a voltage to a silicon carbide crystal and observed emission of yellow light. Later, in 1927, the Russian scientist Oleg Losev reported the creation of the first LED [6]. These discoveries remained at that time largely unnoticed and therefore it took until 1962 before the first practical visible spectrum LED was invented by Holonyak and Bevacqua [7]. They developed red-emitting Ga(As,P) LEDs, which in the decades that followed were used extensively in numeric displays and signaling applications.

The major breakthrough in LED technology however came in 1994 when Shuji Nakamura successfully fabricated the first high brightness blue LED [8,9]. This blue LED was based on (In,Ga)N and its development made it possible to use LEDs for general lighting and many other applications. In 2014 Shuji Nakamura, Isamu Akasaki and Hiroshi Amano received the Nobel Prize in Physics for the invention of efficient blue LEDs. The discovery of the blue LED was quickly followed by the production of the first commercial white LED by Nichia Corporation in 1996 [10,11]. In this device a blue-emitting LED was combined with a yellow-emitting conversion phosphor ($\text{Y}_3\text{Al}_5\text{O}_{12}:\text{Ce}^{3+}$) to generate white light (a ‘phosphor’ is a material that exhibits luminescence).

Initially the LED industry followed two approaches for obtaining a white LED. One is to use a combination of red, green and blue emitting LEDs, known as RGB LEDs. The other approach is to combine a single LED light source with one or more phosphor materials that partially or fully convert the LED emission (phosphor converted LEDs). An advantage of using RGB LEDs is that Stokes losses associated with the use of phosphors are eliminated. On the other hand, RGB LEDs need complex electronics to control the blending of the different LED emissions. The spectral shifts of red, green and blue LEDs as a function of temperature and current are in general not equal and it is therefore very difficult to maintain a constant emission color with RGB LEDs [1]. Furthermore, the efficiency of RGB LEDs is hampered by the relatively low efficiency of green-emitting LEDs [12]. Due to these disadvantages, the RGB LED approach has been abandoned

for large scale lighting and consequently most commercial white LEDs are phosphor converted LEDs (pc-LEDs).

There are different options for making white light with pc-LEDs. One option is to combine a blue LED with phosphors that emit in the green to red spectral region. The alternative is to use a (near)ultraviolet LED and fully convert the LED emission to visible light with phosphors. A downside of this approach is that the Stokes losses will be larger when compared to using blue LEDs. Currently, most commercially available white pc-LEDs consist of a blue-emitting (In,Ga)N LED chip and a yellow-emitting $\text{Y}_3\text{Al}_5\text{O}_{12}:\text{Ce}^{3+}$ (YAG:Ce) phosphor layer [1,13]. In this pc-LED the YAG:Ce phosphor is coated directly on top of the blue LED chip, as is schematically illustrated in Figure 1.3a. The YAG:Ce phosphor converts part of the blue LED emission to yellow light, which together with the transmitted blue LED emission is perceived as white light. The emission spectrum of this white LED system is shown in Figure 1.3b.

The YAG:Ce pc-LEDs find application in almost all branches of the lighting industry. They are for example used in automotive lighting, mobile phones, backlighting for LCD displays, traffic signs and home lighting. An important issue however is that this YAG:Ce pc-LED gives (bluish) cool white light. The combination of blue and yellow emission generates white light with a high correlated color temperature (CCT > 4000 K) and low color rendering index (CRI < 75) [2,14]. Many applications including home lighting however demand warm white LEDs with a high color quality, i.e. white LEDs with a CRI > 85 and CCT < 4000 K. To achieve this, a red-emitting phosphor has to be added to the white LED system presented in Figure 1.3.

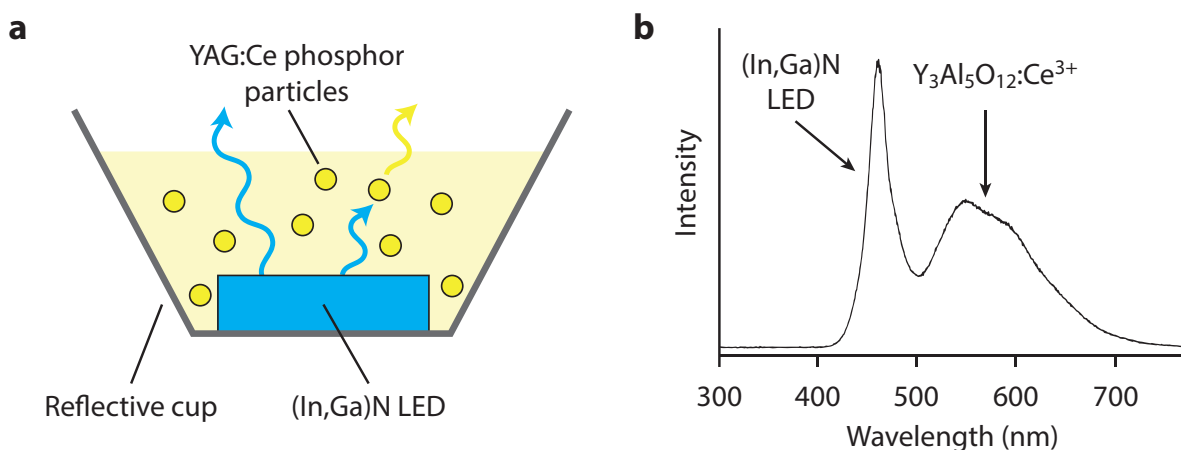


Figure 1.3 – (a) Schematic design of a phosphor converted white LED: a blue-emitting (In,Ga)N LED chip coated with a $\text{Y}_3\text{Al}_5\text{O}_{12}:\text{Ce}^{3+}$ (YAG:Ce) phosphor layer. The YAG:Ce phosphor converts part of the blue LED emission to yellow light. The blue and yellow light together are perceived as white light. (b) Emission spectrum of a white LED composed of a blue (In,Ga)N LED and a yellow $\text{Y}_3\text{Al}_5\text{O}_{12}:\text{Ce}^{3+}$ phosphor. Adapted from Ref. [15].

1.2 Red-emitting phosphors for warm white LEDs

In the last two decades extensive research has been conducted to find red phosphors that can improve the color quality of white LEDs. In the first warm white LEDs Eu^{2+} -doped sulfides like $\text{CaS}:\text{Eu}^{2+}$ were used as red-emitting phosphors. These Eu^{2+} -doped sulfide phosphors have attractive luminescence properties [16,17] but also show several drawbacks, such as strong thermal quenching [18] and poor chemical stability [19]. Alternatively, Eu^{3+} -doped hosts have been proposed as red phosphors for white LEDs [20,21]. The emission spectrum of Eu^{3+} is dominated by sharp f-f emission lines around 600 nm, which makes Eu^{3+} an ideal red emitter. The red emission of Eu^{3+} has extensively shown its usefulness in lighting, television screens and anti-counterfeiting labels [4]. The main problem for using Eu^{3+} -doped materials in white LEDs is the lack of strongly-absorbing (allowed) Eu^{3+} transitions in the blue part of the spectrum. This causes Eu^{3+} to only very weakly absorb the blue (In,Ga)N LED radiation. Furthermore, the Eu^{3+} f-f absorption lines have a much narrower bandwidth than the blue LED emission, which also limits the absorption of blue LED radiation by Eu^{3+} .

Presently, Eu^{2+} -doped nitrides like $\text{CaAlSiN}_3:\text{Eu}^{2+}$ are considered the most successful red-emitting LED phosphors and LED light sources containing these nitride phosphors have been commercialized in recent years [22–24]. The Eu^{2+} -doped nitrides exhibit high photoluminescence quantum efficiencies ($\text{QE} > 90\%$), good thermal quenching behavior and sufficient chemical stability [1,2]. They however also have some serious drawbacks. First, the Eu^{2+} -doped nitrides have a high production cost as they are synthesized at high pressures and temperatures [23,25]. Secondly, the Eu^{2+} emission band of these nitride phosphors is broad and therefore extends into the deep red and near-infrared spectral regions where the sensitivity of the human eye is low. This causes the luminous efficacy of the white LED to decrease significantly, making it a less attractive alternative for (compact) fluorescent lamps [26]. The LED industry is therefore searching for new cheap and efficient narrow band red-emitting phosphors that can be excited in the blue spectral region. It is crucial that the red phosphor has a narrow emission band as the eye sensitivity strongly drops above 640 nm.

1.3 Scope and outline of this thesis

Finding narrow band red-emitting phosphors to realize superior white LEDs combining a high color rendering with improved efficacy (lumen/W output) is an important challenge in the field of lighting. In this thesis we investigate two new types of narrow band red phosphors. The first are Mn^{4+} -doped phosphors. Fluoride hosts activated with Mn^{4+} ions show narrow red emission in a favorable spectral region (emission maximum is at 630 nm) [27,28]. The Mn^{4+} luminescence can be efficiently excited in the blue spectral region and the Mn^{4+} -doped fluorides are prepared through low-cost wet-chemical synthesis at room temperature [29,30]. These properties make Mn^{4+} -doped materials promising red phosphors for white LEDs. The second type of phosphors we investigate

are Eu^{2+} -doped $\text{Cs}_2\text{MP}_2\text{O}_7$ ($\text{M} = \text{Ca}^{2+}, \text{Sr}^{2+}$) phosphates. These Eu^{2+} -doped compounds can be interesting for white LED applications as they show unusual narrow yellow/red Eu^{2+} luminescence with a very large Stokes shift and high quenching temperature [31]. The thesis is divided into two different parts. Part one comprises Chapters 2 to 5 and involves phosphors doped with Mn^{4+} ions. The second part consists of Chapter 6 which discusses the luminescence of Eu^{2+} -doped $\text{Cs}_2\text{MP}_2\text{O}_7$ ($\text{M} = \text{Ca}^{2+}, \text{Sr}^{2+}$) phosphors. The remaining sections of this introductory chapter, Section 1.4 and 1.5, will provide some background information on the luminescent centers studied in this thesis, i.e. transition metal ions (Mn^{4+}) and lanthanide ions (Eu^{2+}).

Chapter 2 presents the synthesis and luminescence properties of a new Mn^{4+} -activated host: a Mn^{4+} -doped fluorohafnate. We prepare a novel red-emitting $\text{Cs}_2\text{HfF}_6:\text{Mn}^{4+}$ phosphor via a simple two-step co-precipitation method. The Mn^{4+} luminescence has a quantum efficiency higher than 80%, which makes $\text{Cs}_2\text{HfF}_6:\text{Mn}^{4+}$ an interesting material for applications. Detailed insight in the optical properties is obtained by studying the Mn^{4+} emission and luminescence decay down to cryogenic temperatures. Furthermore, we perform temperature-dependent luminescence measurements to investigate the thermal quenching of the Mn^{4+} emission.

Chapter 3 shows results obtained on Mn^{4+} -doped hexafluoroaluminates. We show that we can prepare different $\text{M}_3\text{AlF}_6:\text{Mn}^{4+}$ ($\text{M} = \text{Na}, \text{K}$) phosphors by co-precipitation synthesis. Our synthesis method yields $\text{K}_2\text{NaAlF}_6:\text{Mn}^{4+}$ crystallites with a narrow size and shape distribution, which is favorable for reproducible phosphor packaging. We compare the optical properties of $\text{Na}_3\text{AlF}_6:\text{Mn}^{4+}$, $\text{K}_3\text{AlF}_6:\text{Mn}^{4+}$ and $\text{K}_2\text{NaAlF}_6:\text{Mn}^{4+}$ at room temperature and 4 K. The luminescence measurements reveal that multiple Mn^{4+} sites exist in $\text{M}_3\text{AlF}_6:\text{Mn}^{4+}$, which is explained by the charge compensation that is required for Mn^{4+} on Al^{3+} sites. Thermal cycling experiments show that the site distribution changes after annealing.

In **Chapter 4** we study how the optical properties of Mn^{4+} are influenced by the host lattice the Mn^{4+} ions are situated in. We compare the luminescence of Mn^{4+} ions doped into three isostructural $\text{RE}_2\text{Sn}_2\text{O}_7$ pyrochlores ($\text{RE}^{3+} = \text{Y}^{3+}, \text{Lu}^{3+}$ or Gd^{3+}) and find that the energies of the Mn^{4+} ${}^4\text{T}_1$ and ${}^4\text{T}_2$ states significantly increase with decreasing $\text{Mn}^{4+}-\text{O}^{2-}$ distance, whereas the energy of the ${}^2\text{E}$ level shows a small shift to higher energies from $\text{RE}^{3+} = \text{Gd}^{3+}$ to Lu^{3+} to Y^{3+} . In addition to investigating the positions of the Mn^{4+} energy levels, the vibronic structure and temperature quenching of the luminescence is reported for Mn^{4+} in the three hosts.

In **Chapter 5** we investigate thermal quenching and concentration quenching of the Mn^{4+} luminescence in Mn^{4+} -doped fluorides. The quenching is studied by measuring luminescence spectra and decay curves of $\text{K}_2\text{TiF}_6:\text{Mn}^{4+}$ phosphors between 4 and 600 K and for Mn^{4+} concentrations from 0.01 to 15.7%. Temperature-dependent measurements

on $\text{K}_2\text{TiF}_6:\text{Mn}^{4+}$ and other Mn^{4+} -doped phosphors show that thermal quenching occurs through thermally activated crossover between the ${}^4\text{T}_2$ excited state and the ${}^4\text{A}_2$ ground state. Concentration-dependent studies reveal that concentration quenching effects are limited in $\text{K}_2\text{TiF}_6:\text{Mn}^{4+}$ up to 5% Mn^{4+} . This is important as high Mn^{4+} concentrations are required for sufficient absorption of the blue LED light in the parity-forbidden Mn^{4+} d–d transitions.

In **Chapter 6** we report on the luminescence of Eu^{2+} in $\text{Cs}_2\text{MP}_2\text{O}_7$ ($\text{M} = \text{Ca}^{2+}, \text{Sr}^{2+}$) phosphates. The $\text{Cs}_2\text{MP}_2\text{O}_7:\text{Eu}^{2+}$ phosphors exhibit narrow band yellow/red Eu^{2+} emission due to an unusually large Stokes shift. We investigate the origin of this large Stokes shift through measurements at cryogenic temperatures (down to 4 K) and by comparison with the d–f luminescence of Ce^{3+} and Yb^{2+} in the same host lattice. The results indicate that the unusually large Stokes shift can be explained by a Jahn–Teller like deformation in the $4\text{f}^65\text{d}^1$ excited state of Eu^{2+} .

The results presented in this thesis are summarized in **Chapter 7**. Furthermore, this chapter discusses possible further research directions and future perspectives.

1.4 Transition metal ions

The transition metals are the elements in groups 3 to 11 of the periodic table [32,33]. In this block of elements the 3d, 4d and 5d shells are filled with electrons. Most transition metals display a wide range of oxidation states. They primarily occur as cations with an electron configuration $[X]d^n$, where $X = \text{Ar, Kr or Xe}$ and n is the number of electrons in the d-shell ($n < 10$). The partially filled d-shell configurations d^n give rise to interesting optical properties. Many transition metal compounds have striking colors due to absorption of visible light by transitions within the d^n configuration (see Figure 1.4). These transitions within the d-shell are referred to as d–d transitions. Several transition metal ions such as Cr^{3+} and Mn^{4+} also show visible luminescence due to d–d transitions. They are therefore frequently used as luminescent centers in e.g. lamp phosphors and solid-state lasers [4,34]. In the rest of this section we provide some background information on the energy levels and electronic transitions of transition metal ions.

1.4.1 Energy levels of a free transition metal ion

The d^n configuration gives rise to a number of free ion energy levels as a result of repulsion interactions between the electrons in the d-shell. Under the influence of these interactions, the d^3 configuration for example splits into 8 different free ion energy levels, as is shown in Figure 1.5a. The energy levels of a free transition metal ion are labeled *LS*-terms and are denoted with a term symbol ^{2S+1}L , where L is the total orbital angular momentum of the state and S is the total spin angular momentum of the state [33]. The quantity $2S + 1$ is the spin multiplicity of the term. Instead of using the numerical value for L , a letter label is used (in analogy with the notation s, p, d, f, ... for orbitals with $l = 0, 1, 2, 3, \dots$). For $L = 0$ the letter S is used, for $L = 1$ the letter P is used, for $L = 2$ the letter D is used, etc. If we thus consider a state which has $L = 3$ and $S = 3/2$, the term symbol of that state is 4F (ground state term in Figure 1.5a).

The energy of each free ion level (*LS*-term) can be expressed in terms of the so-called Racah parameters A , B and C . These parameters describe the strength of the repulsion interactions between the d-electrons. The parameter A accounts for the average total



Figure 1.4 – Photographs of (a) nickel(II) nitrate hexahydrate, (b) cobalt(II) aluminate and (c) a ruby gemstone which consists of chromium-doped α -aluminum oxide. Photographic images taken from Refs. [35–37].

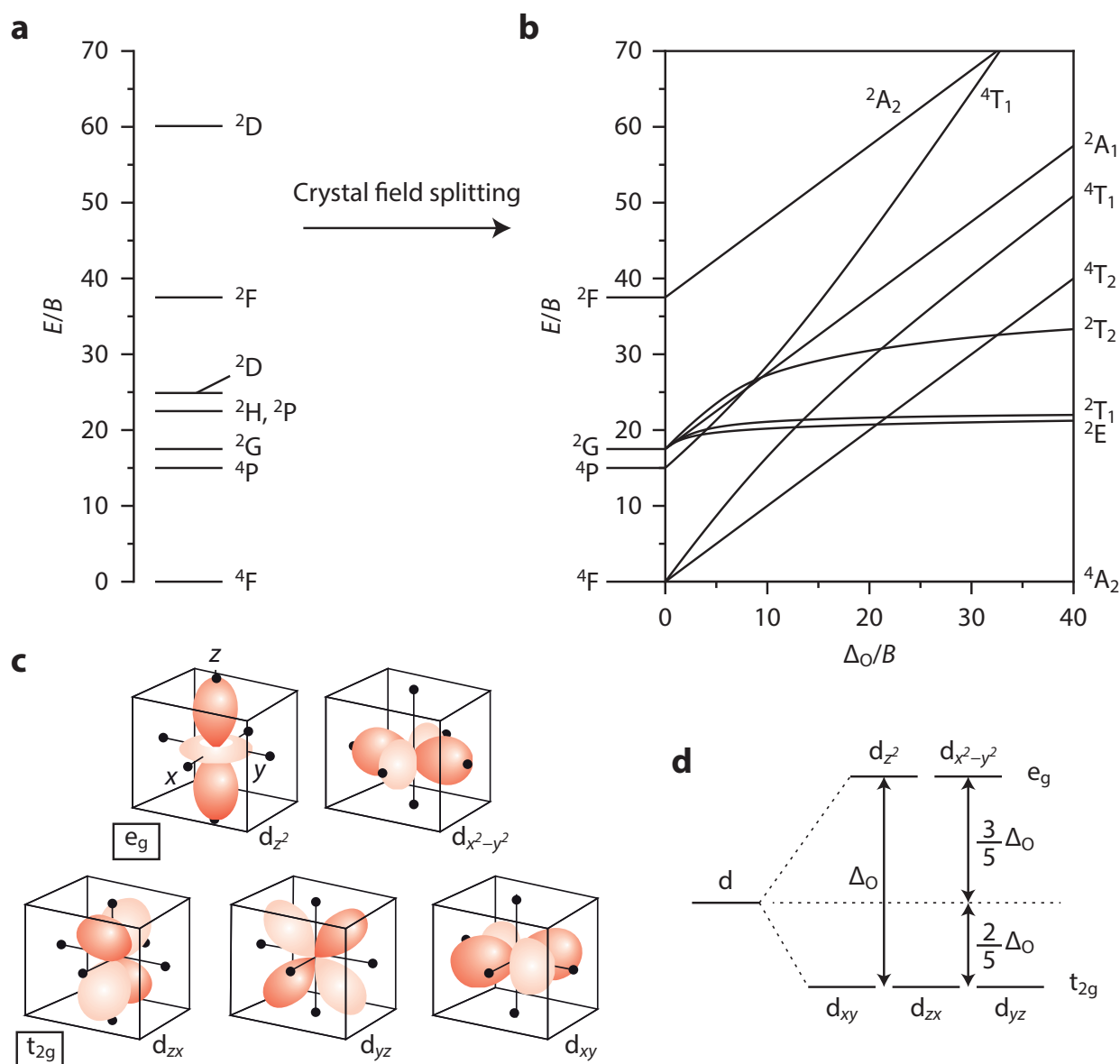


Figure 1.5 – (a) Energy levels arising from a d^3 configuration for a free transition metal ion ($C = 4.5B$). (b) Tanabe-Sugano energy level diagram for the d^3 electron configuration in an octahedral crystal field ($C = 4.5B$). (c) The orientation of the five d-orbitals with respect to the ligands of an octahedral complex. The black dots depict the ligands around the transition metal ion. Adapted from Ref. [33]. (d) Crystal field splitting for the d-orbitals in an octahedral crystal field.

interelectron repulsion and B and C relate to the repulsion energies between individual d-electrons. As an example, Table 1.1 lists the d^3 LS -term energies given as a combination of the three Racah parameters. For a d^3 ion the term $3A$ is common to all levels (the average total interelectron repulsion is the same for all LS -terms). It can therefore be ignored when one is interested in the energy separations between different energy levels. The energy level diagram displayed in Figure 1.5a was constructed by using the expressions of Table 1.1 and assuming that $C/B = 4.5$, a ratio commonly observed for these parameters [33]. Note that in this diagram the energy E is scaled to B . The values

<i>LS</i> -term	Energy
⁴ F	$3A - 15B$
⁴ P	$3A$
² H	$3A - 6B + 3C$
² P	$3A - 6B + 3C$
² G	$3A - 11B + 3C$
² F	$3A + 9B + 3C$
² D (1)	$3A + 5B + 5C + (193B^2 + 8BC + 4C^2)^{1/2}$
² D (2)	$3A + 5B + 5C - (193B^2 + 8BC + 4C^2)^{1/2}$

Table 1.1 – Energies of the free ion *LS*-terms of the d^3 configuration [34]. The energies are given as a linear combination of the Racah parameters *A*, *B* and *C*.

for *B* and *C* of a free ion can be determined by fitting the expressions of Table 1.1 to the energies observed for the *LS*-terms in spectroscopic measurements.

1.4.2 Crystal field splitting

For a free transition metal ion the five *d*-orbitals all have the same energy. When a transition metal ion is however incorporated into a crystalline lattice, the *d*-orbitals are split into groups of different energy by the ligands surrounding the transition metal ion. This splitting of the *d*-orbitals in a crystal field strongly affects the energy levels of the d^n configuration and thus the optical properties of the transition metal ion.

The splitting of the *d*-orbitals can be explained by considering a transition metal ion which is octahedrally coordinated by six ligands, a common type of coordination for a transition metal ion in a crystal. Figure 1.5c shows the orientation of the five *d*-orbitals with respect to the ligands of an octahedral complex. The negatively charged ligands are depicted by black dots on the axes of the orbitals. In the octahedral complex the electrons in the d_{z^2} and $d_{x^2-y^2}$ orbitals are concentrated close to the ligands, whereas the electrons in the d_{xy} , d_{yz} and d_{zx} orbitals are concentrated in regions that lie between the ligands. As a result, the electrons in the d_{z^2} and $d_{x^2-y^2}$ orbitals are repelled stronger by the negatively charged ligands than the electrons in the d_{xy} , d_{yz} and d_{zx} orbitals. Due to the difference in electron repulsion, the *d*-orbitals are split into two groups of different energy, as is illustrated in Figure 1.5d. The two higher energy d_{z^2} and $d_{x^2-y^2}$ orbitals are referred to as the e_g orbitals and the three lower energy d_{xy} , d_{yz} and d_{zx} orbitals are referred to as the t_{2g} orbitals (the e_g and t_{2g} labels denote the symmetry of the orbitals). If the crystal field symmetry is lower than octahedral, the *d*-orbitals can be split into more than two levels (maximum five levels).

The energy separation between the two sets of orbitals is given by Δ_O , which is the crystal-

field splitting parameter for an octahedral crystal field (the octahedral symmetry is indicated by the subscript O). In Figure 1.5d the barycenter (d) gives the average energy of the five d-orbitals. The energy of the three t_{2g} orbitals lies $\frac{2}{5}\Delta_O$ below this barycenter energy and the energy of the two e_g orbitals lies $\frac{3}{5}\Delta_O$ above this barycenter energy. The strength of the crystal field splitting Δ_O depends on several factors: the oxidation state of the central metal ion, the charge of the ligands and the distance between the central metal ion and the ligands. The crystal field splitting is typically larger for metal ions with a higher oxidation state. Mn^{4+} , the transition metal ion of interest in this thesis, has a high oxidation state and therefore in most cases experiences a strong crystal field. Furthermore, the magnitude of Δ_O will increase if 1) the distance between the metal ion and the ligands becomes shorter and 2) if the charge on the ligands increases. In the *spectrochemical series* the ligands are ranked according to the crystal field splitting they produce [38,39]:



Due to the crystal field splitting of the d-orbitals, the free ion levels of the d^n configuration (described in Section 1.4.1) split up in a number of energy levels. The splittings of the free ion states in an octahedral crystal field have been calculated by Tanabe and Sugano, and are presented in so-called Tanabe-Sugano diagrams [40,41]. Figure 1.5b shows the Tanabe-Sugano diagram of the d^3 electron configuration (electron configuration of Mn^{4+}). Tanabe-Sugano diagrams of other d^n configurations can be found in various textbooks on optical spectroscopy [33,34]. In a Tanabe-Sugano diagram the energy levels are plotted as a function of the octahedral crystal field splitting Δ_O . On the left-hand side of the diagram ($\Delta_O = 0$) we find the energy levels of the free ion (*LS*-terms). Many of the free ion levels split into two or more levels when $\Delta_O > 0$. The d^3 ground state 4F for example splits into three energy levels in an octahedral crystal field: the 4A_2 ground level and the 4T_2 and 4T_1 excited levels. The splitting of each free ion level can be determined by using group theory. Note that in the Tanabe-Sugano diagram of the d^3 configuration only the crystal field levels originating from the 4F , 4P , 2G and 2F terms are shown. The diagram in Figure 1.5b shows that some d^3 energy levels depend strongly on the crystal field splitting Δ_O (e.g. the 4T_2 level), while others are nearly independent of the crystal field strength (e.g. the 2E level).

Each crystal field level is labeled by a symbol which gives the symmetry of the state (A_1 , A_2 , E, T_1 or T_2). The left superscript of the symbol denotes the spin multiplicity $2S+1$ of the state, which is the same as for the free ion level as the spin multiplicity is not affected by the crystal field. The energy of the crystal field levels is influenced both by the crystal field splitting and the interactions between the d-electrons. A Tanabe-Sugano diagram is therefore scaled to the Racah parameter B , which accounts for the interelectronic repulsion interaction (for construction of the diagrams it is assumed that the Racah parameter $C \approx 4.5B$). The Racah parameter B is typically in the range of 500–1000 cm^{-1}

[33,38]. Its value is strongly dependent on the ligands (host lattice) around the transition metal ion, as will be explained in Section 1.4.3.

1.4.3 Nephelauxetic effect

In a crystalline host the Racah parameters B and C are reduced with respect to their free ion values. This reduction is caused by delocalization of the d-electrons over the ligand orbitals, which is known as the *nephelauxetic effect* (nephelauxetic is the Greek word for ‘cloud expanding’). The delocalization increases the average distance between the d-electrons and therefore reduces the electron–electron repulsion. With less electron–electron repulsion, the Racah parameters decrease and the d-level energy goes down.

The strength of the nephelauxetic effect (degree by which B and C are reduced) depends on the type of ligands surrounding the metal ion. The delocalization of the d-electrons is stronger for ligands which form a more covalent bond with the metal ion, i.e. ligands that have a lower electronegativity. As a result, the nephelauxetic effect is larger for ligands with a stronger covalent character. To illustrate this, we compare the energy of the $\text{Mn}^{4+} {}^2\text{E}$ state in fluoride and oxide hosts. The energy of this state is practically independent of the crystal field strength (see Figure 1.5b). Its energy is therefore solely determined by the values of the Racah parameters B and C . Given that fluorine is more electronegative than oxygen, the values of B and C will be higher when Mn^{4+} is surrounded by fluorine ions. As a result, the $\text{Mn}^{4+} {}^2\text{E}$ state is at 16000 cm^{-1} in fluorides, while it is around 14500 cm^{-1} in oxides [27].

1.4.4 The d–d transitions

Transitions between the energy levels of the d^n configuration are called d–d transitions. The d–d transitions are parity-forbidden since they occur between states of the same d^n electron configuration (parity does not change). The parity selection rule can be partly relaxed by coupling of the electronic transition with vibrations [28]. In addition, for a transition metal complex that lacks an inversion center, the parity selection rule is relaxed by odd-parity crystal field components that admix odd-parity wavefunctions into the d wavefunctions [4]. Some d–d transitions are also spin-forbidden, which is the case when the transition is between states of different spin multiplicity (e.g. the ${}^4\text{A}_2 \rightarrow {}^2\text{E}$ transition in Figure 1.5b). As the d–d transitions are parity-forbidden, they have a relatively low absorption strength ($\epsilon_{\text{max}} = 10\text{--}100 \text{ M}^{-1}\text{cm}^{-1}$). If the d–d transition is also spin-forbidden, its absorption will be even weaker ($\epsilon_{\text{max}} \leq 1 \text{ M}^{-1}\text{cm}^{-1}$).

The energies of d–d transitions depend strongly on the host material as the d-level energies are greatly influenced by the crystal field splitting and nephelauxetic effect (see Sections 1.4.2. and 1.4.3.). The d–d transitions can have narrow or broad absorption/emission bands, depending on the states that are involved in the transition. To illustrate this, Figure 1.6 shows the excitation and emission spectra of Mn^{4+} -activated K_2TiF_6 .

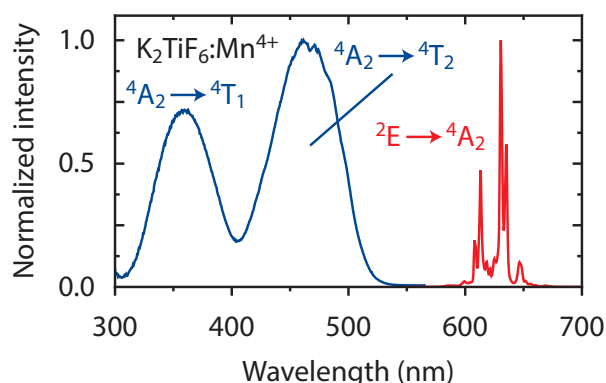


Figure 1.6 – Emission (red) and excitation spectra (blue) of K_2TiF_6 doped with 0.8% of Mn^{4+} ions. The excitation and emission bands/lines are labeled with the corresponding transitions of the d^3 Tanabe-Sugano diagram.

The $\text{Mn}^{4+} \ ^2\text{E} \rightarrow \ ^4\text{A}_2$ emission is characterized by very narrow emission lines. This is due to the fact that the emitting $\ ^2\text{E}$ state is almost independent of the crystal field splitting (nearly flat line in Tanabe-Sugano diagram). In contrast, broad bands are observed for the $\ ^4\text{A}_2 \rightarrow \ ^4\text{T}_1$ and $\ ^4\text{A}_2 \rightarrow \ ^4\text{T}_2$ transitions (see Figure 1.6). The energies of the $\ ^4\text{T}_1$ and $\ ^4\text{T}_2$ states are strongly influenced by the crystal field splitting (steep slope in Tanabe-Sugano diagram) and transitions to these states are therefore characterized by broad bands.

1.4.5 Charge-transfer transitions

Besides the *intraconfigurational* d–d transitions, also *interconfigurational* charge-transfer transitions can be observed for transition metal ions. These charge-transfer (CT) transitions are ligand-to-metal charge-transfer (LMCT) transitions. In such a transition an electron (charge) is transferred from a ligand ion to the transition metal ion. This kind of transition is fully allowed (large change in dipole moment) and therefore gives rise to intense and broad absorption bands. The CT absorption bands are broad because the chemical bonding between the metal ion and ligands strongly changes upon CT excitation. Due to the change in bonding, the potential energy curves of the CT state and ground state are largely displaced from each other, which causes the absorption bands to be broad. The CT absorption band can be in the UV or visible spectral region, depending on the type of metal ion and ligand involved. More details on the spectral positions of transition metal ion CT bands can be found in Refs. [4,33,42,43].

1.5 Lanthanide ions

The lanthanides are the elements with atomic numbers 57 (La) through 71 (Lu), which are located in the f-block at the bottom of the periodic table. In the lanthanide series of elements the 4f inner shell is filled with electrons. The most common valence state of the lanthanides is 3+ (Ln^{3+}). As a trivalent ion the lanthanides have the electron configuration $[\text{Xe}]4f^n$, where n increases from 0 for La^{3+} to 14 for Lu^{3+} . The $4f^0$ (empty

4f-shell), $4f^7$ (half-filled 4f-shell) and $4f^{14}$ (filled 4f-shell) configurations are most stable. Some lanthanides therefore also occur as divalent or tetravalent ions, with examples being Ce^{4+} ($4f^0$), Eu^{2+} ($4f^7$), Tb^{4+} ($4f^7$) and Yb^{2+} ($4f^{14}$).

Lanthanide ions have very interesting optical properties, with many of them showing characteristic narrow emission and absorption lines in the UV, visible and/or IR part of the spectrum. These narrow lines are due to transitions within the partially filled 4f-shell (intraconfigurational f–f transitions). In addition, several lanthanide ions exhibit f–d transitions in the UV or visible region of the spectrum. These are transitions between the $4f^n$ ground state and $4f^{n-1}5d^1$ excited state of the lanthanide ion. Because lanthanide ions have absorptions and emissions in the UV, visible and IR, they are extensively used as optically active centers in applications. They are for example used in fluorescent tubes, white LEDs, lasers, displays, medical imaging, biolabeling and banknotes (anti-counterfeiting labels) [1,4,44,45].

1.5.1 Intraconfigurational f–f transitions

For a lanthanide ion, the n electrons in the 4f-shell have a large number of arrangements over the 4f-orbitals, i.e. $\binom{14}{n}$ arrangements. Due to interactions between the 4f electrons, these different distributions give rise to a large number of energy levels within the $4f^n$ configuration. The $4f^n$ energy levels of the trivalent lanthanides are collected in the Dieke diagram [46]. Transitions between the $4f^n$ energy levels are parity-forbidden because they are intraconfigurational transitions. Because the f–f transitions are parity-forbidden (and in many cases also spin-forbidden), they are characterized by low molar absorption coefficients and long radiative lifetimes. Furthermore, the f–f transitions give rise to very sharp absorption and emission lines. The f–f absorption and emission lines are sharp because the 4f-orbitals do not participate in the chemical bonding and are shielded from the environment by the filled 5p and 5s orbitals.

1.5.2 Interconfigurational f–d transitions

Lanthanide ions are well known for their luminescence due to intraconfigurational f–f transitions. The Eu^{2+} ions studied in Chapter 6 of this thesis exhibit luminescence related to a different type of transitions: the interconfigurational $4f^n \rightarrow 4f^{n-1}5d^1$ transitions. These transitions are parity-allowed and give rise to intense absorption bands. The f–d transitions are observed at low energies for lanthanide ions with a low electron affinity, such as the divalent lanthanide ions (e.g. Eu^{2+} , Yb^{2+} and Sm^{2+}) and some trivalent ions (e.g. Ce^{3+} and Tb^{3+}) [47,48]. For other trivalent lanthanide ions, the $4f^n \rightarrow 4f^{n-1}5d^1$ transitions are usually located in the VUV spectral region [49,50]. As the f–d transitions are parity-allowed, they are characterized by high oscillator strengths and short excited state lifetimes (ns to μ s for spin-allowed d–f emissions).

In contrast to the f–f transitions, the f–d transitions give rise to very broad excitation and emission bands. As an example, Figure 1.7a shows an excitation spectrum (blue)

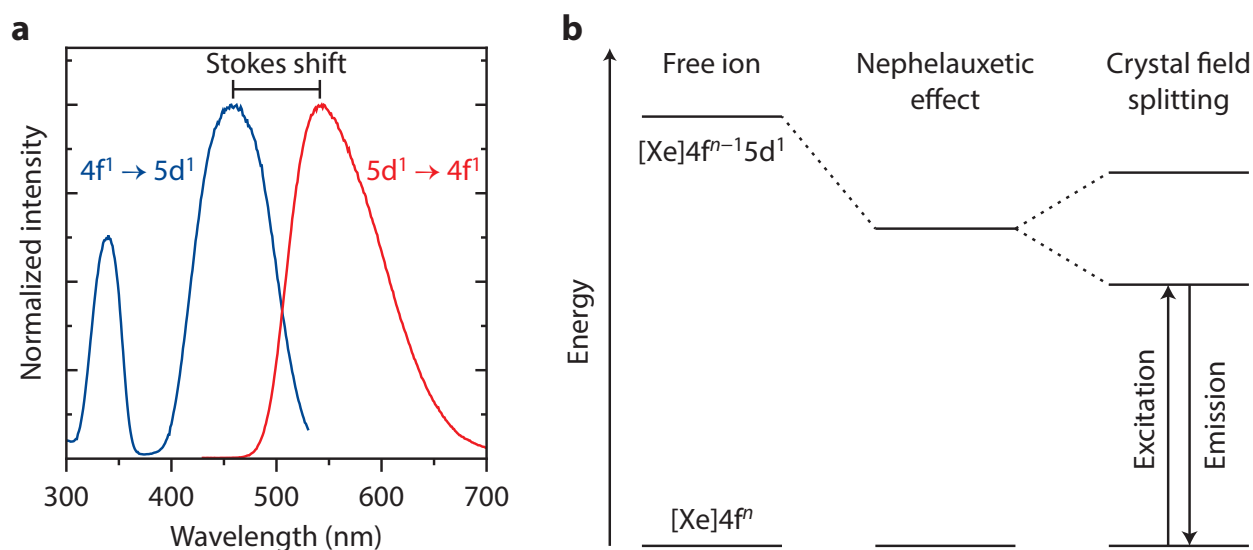


Figure 1.7 – (a) Excitation (blue) and emission (red) spectra of Ce^{3+} in $\text{Y}_3\text{Al}_5\text{O}_{12}$ (YAG:Ce). The Ce^{3+} doping concentration is 3%. The emission and excitation bands correspond to transitions between the $4f^1$ ground and $5d^1$ excited state of Ce^{3+} . The energy difference between the d–f emission band and lowest-energy f–d absorption band is the Stokes shift. (b) The influence of the nephelauxetic effect and crystal field splitting on the 5d energy levels.

and emission spectrum (red) of the $4f^1 \rightarrow 5d^1$ transition of Ce^{3+} in $\text{Y}_3\text{Al}_5\text{O}_{12}$. The f–d emission and excitation bands are broad because the chemical bonding between the lanthanide ion and ligands changes upon a f–d transition. Furthermore, the spectra in Figure 1.7a show that the maximum of the lowest-energy f–d excitation band is located at higher energies than the maximum of the d–f emission band. The energy difference between the absorption and emission maxima of the same electronic transition is called the Stokes shift. This shift originates from the vibrational relaxation that takes place in the ground and excited states. More generally, emission at energies lower than the absorbed energy is referred to as Stokes emission, and emission at energies higher than the absorbed energy is referred to as anti-Stokes emission.

The 5d-orbitals are extended and participate in the chemical bonding with the ligands. As a result, the f–d transition energy is strongly influenced by the surroundings of the lanthanide ions (host lattice). The energy of the $4f^{n-1}5d^1$ excited state is mainly influenced by the nephelauxetic effect and the crystal field splitting, as is illustrated in Figure 1.7b. First the $4f^{n-1}5d^1$ energy is lowered with respect to the free ion by expansion of the d-orbitals onto the ligand ions, the nephelauxetic effect (see also Section 1.4.3). Next, the ligand field around the lanthanide ion splits the 5d level into two to maximum five energy levels (see Section 1.4.2 on crystal field splitting). The resulting energy of the lowest-energy $4f^n \rightarrow 4f^{n-1}5d^1$ transition can, depending on the host material, be up to 34000 cm^{-1} lower than in the free ion [47]. The positions of the lowest energy f–d transition of lanthanide ions within a certain host are related. Once the lowest f–d transition energy

of a lanthanide ion in a compound is known, then the f–d transition energies of all other lanthanide ions in that same compound can be predicted [47,48,51]. In Chapter 6 we make use of this principle to compare the f–d transition energies of Eu^{2+} and Ce^{3+} in $\text{Cs}_2\text{MP}_2\text{O}_7$ ($M = \text{Ca}^{2+}, \text{Sr}^{2+}$).

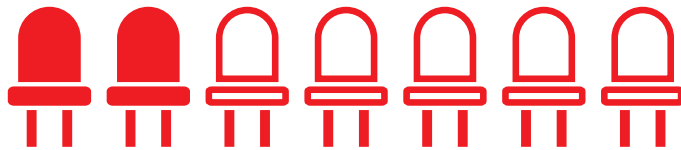
References

- [1] P. F. Smet, A. B. Parmentier and D. Poelman, *J. Electrochem. Soc.* **158** (2011) R37–R54.
- [2] M. R. Krames, O. B. Shchekin, R. Mueller-Mach, G. O. Mueller, L. Zhou, G. Harbers and M. G. Craford, *IEEE/OSA J. Disp. Technol.* **3** (2007) 160–175.
- [3] Charge of the LED brigade: A global switch to LEDs will change the lighting business, *The Economist* (2011).
- [4] G. Blasse and B. C. Grabmaier, *Luminescent Materials*, Springer-Verlag, Berlin, 1994.
- [5] H. J. Round, *Electr. World.* (1907) 309.
- [6] N. Zheludev, *Nat. Photonics.* **1** (2007) 189–192.
- [7] N. Holonyak and S. F. Bevacqua, *Appl. Phys. Lett.* **1** (1962) 82–83.
- [8] S. Nakamura, M. Senoh and T. Mukai, *Appl. Phys. Lett.* **62** (1993) 2390–2392.
- [9] S. Nakamura, T. Mukai and M. Senoh, *Appl. Phys. Lett.* **64** (1994) 1687–1689.
- [10] Y. Shimizu, K. Sakano, Y. Noguchi and T. Moriguchi, United States Patent No. US5998925A (1999).
- [11] L. Chen, C. C. Lin, C.-W. Yeh and R.-S. Liu, *Materials* **3** (2010) 2172–2195.
- [12] A. A. Setlur, *Electrochem. Soc. Interface.* **18** (2009) 32–36.
- [13] G. Blasse and A. Bril, *Appl. Phys. Lett.* **11** (1967) 53–55.
- [14] P. Pust, V. Weiler, C. Hecht, A. Tücks, A. S. Wochnik, A.-K. Henß, D. Wiechert, C. Scheu, P. J. Schmidt, and W. Schnick, *Nat. Mater.* **13** (2014) 891–896.
- [15] Spectrum of a white LED: Wikimedia Commons.
- [16] N. Yamashita, O. Harada and K. Nakamura, *Jpn. J. Appl. Phys.* **34** (1995) 5539–5545.
- [17] Y. Hu, W. Zhuang, H. Ye, S. Zhang, Y. Fang and X. Huang, *J. Lumin.* **111** (2005) 139–145.
- [18] Q. Xia, M. Batentschuk, A. Osvet, A. Winnacker and J. Schneider, *Radiat. Meas.* **45** (2010) 350–352.
- [19] N. Avci, J. Musschoot, P. F. Smet, K. Korthout, A. Avci, C. Detavernier and D. Poelman, *J. Electrochem. Soc.* **156** (2009) J333–J337.
- [20] Z. Sun, Q. Zhang, Y. Li and H. Wang, *J. Alloys Compd.* **506** (2010) 338–342.
- [21] P. Li, Z. Yang, L. Pang, Z. Wang and Q. Guo, *J. Rare Earths.* **26** (2008) 44–47.
- [22] K. Uheda, N. Hirosaki, Y. Yamamoto and A. Naito, *Electrochem. Solid-State Lett.* **9** (2006) H22–H25.
- [23] R. J. Xie and N. Hirosaki, *Sci. Technol. Adv. Mater.* **8** (2007) 588–600.
- [24] P. Pust, A. S. Wochnik, E. Baumann, P. J. Schmidt, D. Wiechert, C. Scheu and W. Schnick, *Chem. Mater.* **26** (2014) 3544–3549.
- [25] H. Zhu, C. C. Lin, W. Luo, S. Shu, Z. Liu, Y. Liu, J. Kong, E. Ma, Y. Cao, R.-S. Liu and X. Chen, *Nat. Commun.* **5** (2014) 4312.
- [26] A. A. Setlur, E. V. Radkov, C. S. Henderson, J.-H. Her, A. M. Srivastava, N. Karkada, M. S. Kishore, N. P. Kumar, D. Aesram, A. Deshpande, B. Kolodin, L. S. Grigorov and U. Happek, *Chem. Mater.* **22** (2010) 4076–4082.
- [27] M. G. Brik and A. M. Srivastava, *J. Lumin.* **133** (2013) 69–72.
- [28] A. G. Paulusz, *J. Electrochem. Soc.* **120** (1973) 942–947.
- [29] H.-D. Nguyen and R.-S. Liu, *J. Mater. Chem. C.* **4** (2016) 10759–10775.
- [30] H. F. Sijbom, R. Verstraete, J. J. Joos, D. Poelman and P. F. Smet, *Opt. Mater. Express.* **7** (2017) 3332–3365.
- [31] A. M. Srivastava, H. A. Comanzo, S. Camardello, S. B. Chaney, M. Aycibin and U. Happek, *J. Lumin.* **129** (2009) 919–925.
- [32] IUPAC Compendium of Chemical Terminology, 2nd ed., Blackwell Scientific Publications, Oxford, 1997.

- [33] D. F. Shriver and P. W. Atkins, *Inorganic Chemistry*, 4th ed., Oxford University Press, Oxford, 2006.
- [34] B. Henderson and G.F. Imbusch, *Optical Spectroscopy of Inorganic Solids*, Oxford University Press, Oxford, 1989.
- [35] <http://www.sajan-overseas.com/nickel-salts.html#nickel-nitrate-hexahydrate>.
- [36] http://commons.wikimedia.org/wiki/File:Cobalt_Blue.JPG.
- [37] <http://www.proforbes.com/ruby-gemstone>.
- [38] W. M. Yen, S. Shionoya and H. Yamamoto, *Phosphor Handbook*, CRC Press, 2007.
- [39] C. K. Jørgensen, *Struct. Bond.* **1** (1966) 3–31.
- [40] Y. Tanabe and S. Sugano, *J. Phys. Soc. Japan.* **9** (1954) 753–766.
- [41] Y. Tanabe and S. Sugano, *J. Phys. Soc. Japan.* **9** (1954) 766–779.
- [42] H. H. Tippins, *Phys. Rev. B.* **1** (1970) 126–135.
- [43] P. Dorenbos, *Opt. Mater.* **69** (2017) 8–22.
- [44] C. Feldmann, T. Jüstel, C. R. Ronda and P. J. Schmidt, *Adv. Funct. Mater.* **13** (2003) 511–516.
- [45] F. Suyver and A. Meijerink, *Chemisch2Weekblad.* **98** (2002) 12–13.
- [46] G. H. Dieke and H. M. Crosswhite, *Appl. Opt.* **2** (1963) 675–686.
- [47] P. Dorenbos, *J. Lumin.* **91** (2000) 155–176.
- [48] P. Dorenbos, *J. Phys. Condens. Matter.* **15** (2003) 575–594.
- [49] L. van Pieterse, M. F. Reid, R. T. Wegh, S. Sovarna and A. Meijerink, *Phys. Rev. B.* **65** (2002) 045113.
- [50] L. van Pieterse, M. F. Reid, G. W. Burdick and A. Meijerink, *Phys. Rev. B.* **65** (2002) 045114.
- [51] P. Dorenbos, *J. Phys. Condens. Matter.* **15** (2003) 4797–4807.

2

Synthesis and narrow red luminescence of $\text{Cs}_2\text{HfF}_6:\text{Mn}^{4+}$, a new phosphor for warm white LEDs



Abstract

Mn^{4+} -doped fluorides show narrow red line emission under blue light excitation and are therefore promising materials to improve the color rendering and luminous efficacy of white light emitting diodes (wLEDs). The synthesis of Mn^{4+} -doped fluorides is however challenging and so far only a few efficient Mn^{4+} -doped fluoride phosphors have been reported. In this chapter we present the synthesis and optical properties of a novel $\text{Cs}_2\text{HfF}_6:\text{Mn}^{4+}$ phosphor. The $\text{Cs}_2\text{HfF}_6:\text{Mn}^{4+}$ phosphor is prepared via a two-step co-precipitation method and shows bright red Mn^{4+} luminescence around 620 nm under blue light excitation. Detailed insight in the luminescence properties is obtained by studying the Mn^{4+} emission and luminescence decay down to cryogenic temperatures. The $\text{Cs}_2\text{HfF}_6:\text{Mn}^{4+}$ phosphor has a photoluminescence quantum efficiency higher than 80% which makes it an interesting red-emitting material for wLEDs and other lighting applications. As the Mn^{4+} emission from $\text{Cs}_2\text{HfF}_6:\text{Mn}^{4+}$ shows quenching above 100 °C ($T_{1/2} = 403$ K), the use of this phosphor will be limited to low-power LED lighting.

2.1 Introduction

White light emitting diodes (wLEDs) are revolutionizing the display and lighting industry due to their high energy efficiency, small size, robustness and long operation lifetime [1–5]. Most commercial high efficiency wLEDs are based on a combination of blue-emitting InGaN LED chips and yellow-emitting $\text{Y}_3\text{Al}_5\text{O}_{12}:\text{Ce}^{3+}$ (YAG:Ce) phosphors [5–8]. This combination however lacks a red-emitting component and thus gives “cool” white light with a high correlated color temperature (CCT > 4500 K) and low color rendering index (CRI < 75). This is an issue for most applications including home lighting where warm white light with a high color rendering index (CRI > 85) is required. To solve this problem, the last two decades extensive research has been conducted to find novel red phosphors that can improve the color rendering of wLEDs. Presently Eu^{2+} -doped nitrides like $\text{CaAlSiN}_3:\text{Eu}^{2+}$ are the most successful red-emitting LED phosphors [9–14] and warm wLEDs containing these nitrides have been commercialized in the last years.

Eu^{2+} -doped nitride phosphors exhibit high photoluminescence quantum efficiencies (QE > 90%), good thermal quenching behavior and sufficient chemical stability [2,5] but also have several serious drawbacks. The Eu^{2+} emission band of these phosphors is broad (full width at half maximum fwhm = 50–90 nm) and therefore extends into the deep-red spectral region ($\lambda > 640$ nm) where the eye sensitivity is low. This causes the lumen/W efficacy of the wLED to reduce significantly [7]. Furthermore, Eu^{2+} -doped nitride phosphors have a high production cost as they are synthesized under demanding conditions such as high pressure and high temperature [14,15]. Hence, the wLED industry is searching for new cheap and efficient narrow linewidth (fwhm < 40 nm) red phosphors that can be excited by blue LEDs. Red-emitting phosphors with these spectral characteristics could enable lighting systems with an increased lumen/W efficacy at a CRI of 90 or higher.

Fluoride compounds doped with Mn^{4+} ($3d^3$ electron configuration) ions show narrow red emission (fwhm < 30 nm) in a favorable spectral region ($\lambda_{\text{max}} \sim 630$ nm). Moreover, their red emission can be excited by blue light and they are therefore promising narrow linewidth red phosphors for wLEDs [16–19]. Mn^{4+} -doped fluoride phosphors can have quantum efficiencies higher than 90% [15,20] and, in contrast to the Eu^{2+} -doped nitrides, are prepared through low-cost wet-chemical synthesis at room temperature [15,21,22]. These properties give Mn^{4+} -doped fluoride phosphors large potential for application and consequently the synthesis of these phosphors has received considerable attention in recent years. The synthesis of Mn^{4+} -doped compounds is however not trivial and up to now only a few Mn^{4+} -doped fluoride hosts have been reported [19]. The many oxidation states of manganese (2+, 3+, 4+ and 7+ are most common) make it difficult to control the valence state of manganese and thereby to synthesize Mn^{4+} -doped compounds. Another issue is that manganese oxide impurities are often formed when synthesizing Mn^{4+} -doped fluorides [22,23]. Furthermore, Mn^{4+} ions substitute preferably for octahedrally

coordinated tetravalent cations, which makes it challenging to activate most fluoride lattices with Mn^{4+} ions. As a result, only a small number of Mn^{4+} -doped fluorides has been synthesized so far. All fluoride hosts activated with Mn^{4+} ions contain either Si^{4+} , Ti^{4+} , Ge^{4+} , Sn^{4+} , Zr^{4+} or Al^{3+} as their central cation [24,25]. Substitution of Mn^{4+} for other metal ions has so far not been achieved in fluorides.

In this chapter we report the synthesis and luminescence properties of a new Mn^{4+} -activated fluoride host: a Mn^{4+} -doped fluorohafnate. We synthesize a novel $\text{Cs}_2\text{HfF}_6:\text{Mn}^{4+}$ phosphor via a two-step method by initially preparing the Mn^{4+} -precursor K_2MnF_6 and then in a second step precipitating $\text{Cs}_2\text{HfF}_6:\text{Mn}^{4+}$ from an aqueous HF solution containing Cs^+ , Hf^{4+} and Mn^{4+} ions. The $\text{Cs}_2\text{HfF}_6:\text{Mn}^{4+}$ phosphor shows narrow red Mn^{4+} emission with a quantum efficiency higher than 80%, making $\text{Cs}_2\text{HfF}_6:\text{Mn}^{4+}$ an interesting red-emitting phosphor for applications. We record emission and excitation spectra at cryogenic temperatures to accurately determine the energies of the Mn^{4+} levels and MnF_6^{2-} vibrational modes in $\text{Cs}_2\text{HfF}_6:\text{Mn}^{4+}$. Furthermore, we use the low-temperature spectra to obtain the crystal field and Racah parameters. We study the thermal quenching behavior for $\text{Cs}_2\text{HfF}_6:\text{Mn}^{4+}$ by measuring the luminescence intensity and luminescence decay times as function of temperature. Because of luminescence quenching above 100 °C, application of this Mn^{4+} -doped fluorohafnate will be limited to low-power LED systems.

2.2 Methods

2.2.1 Synthesis of K_2MnF_6

K_2MnF_6 was prepared according to the procedure described in Refs. [26,27]. Briefly, 60 g of KF (Sigma-Aldrich, $\geq 99.0\%$) and 4 g of KMnO_4 (Sigma-Aldrich, $\geq 99.0\%$) were dissolved in 250 mL of a 40 wt% HF solution. The solution was cooled with an ice bath and stirred for 30 min. Next, 4.5 mL of a 30 wt% H_2O_2 solution (Sigma-Aldrich, ACS reagent) was added dropwise while stirring which resulted in the gradual precipitation of yellow K_2MnF_6 powder. The dropwise addition of H_2O_2 was stopped when the color of the solution turned from purple to red-brown indicating the formation of Mn^{4+} . K_2MnF_6 was isolated by decanting the red-brown solution, washing the precipitate twice with 100 mL of acetone and subsequently drying at 50 °C for 2 h.

2.2.2 Synthesis of $\text{Cs}_2\text{HfF}_6:\text{Mn}^{4+}$ phosphor

The $\text{Cs}_2\text{HfF}_6:\text{Mn}^{4+}$ phosphor was synthesized by a simple co-precipitation method which is schematically illustrated in Figure 2.1a. First, 10 mmol of HfO_2 (Highways International, 99.9%) was dissolved in 100 mL of a 40 wt% HF solution by stirring at 60 °C for 24 h. Subsequently, 0.2 mmol of K_2MnF_6 and a solution of 20 mmol CsF (Aldrich, 99.9%) in 3 mL 40 wt% HF were added. The solution became yellow due to the addition of K_2MnF_6 . The solution was stirred for several minutes and then poured into 200 mL of ethanol which resulted in the precipitation of $\text{Cs}_2\text{HfF}_6:\text{Mn}^{4+}$ phosphor particles.

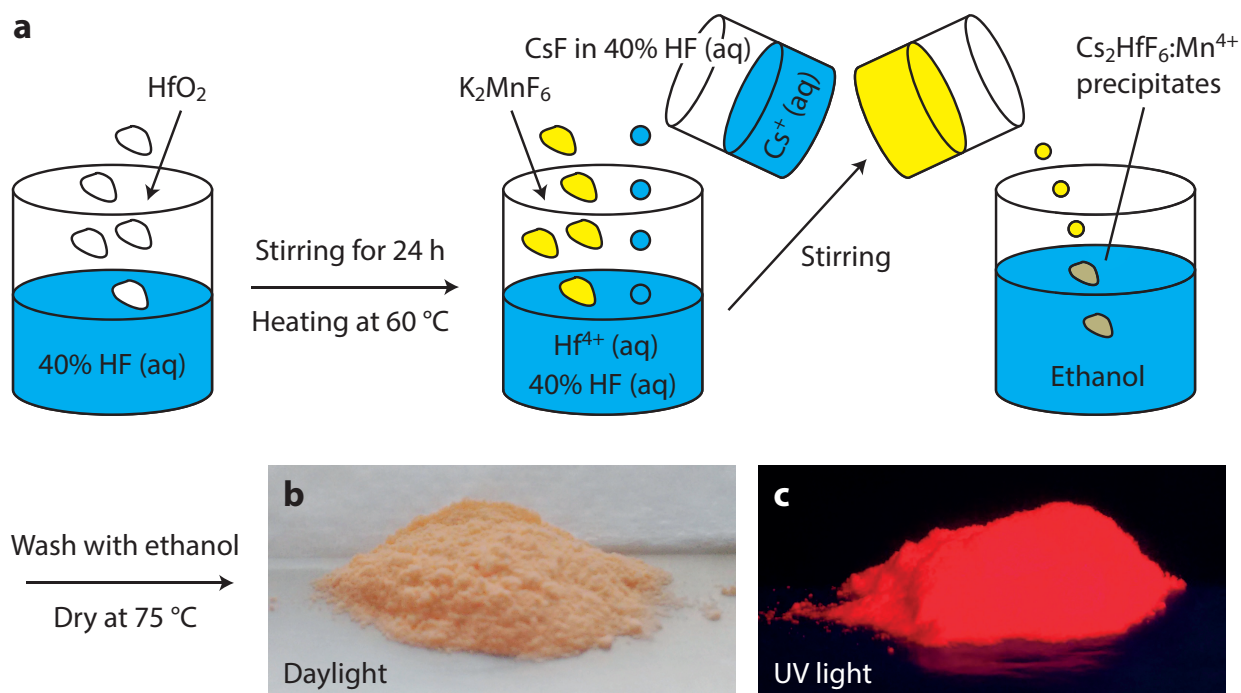


Figure 2.1 – (a) Schematic illustration of the synthesis of Cs₂HfF₆:Mn⁴⁺ and photographic images of Cs₂HfF₆:Mn⁴⁺ phosphor under (b) daylight and (c) 365 nm UV illumination.

The precipitate was washed with ethanol and dried at 75 °C for 2 h. The Cs₂HfF₆:Mn⁴⁺ phosphor has a yellow-orange body color under daylight (Figure 2.1b) and shows bright red luminescence under UV light illumination (Figure 2.1c).

2.2.3 Characterization

Powder X-ray diffraction (XRD) patterns were measured on a Philips PW1729 X-ray diffractometer using Cu K_α radiation ($\lambda = 1.5418 \text{ \AA}$). Scanning electron microscopy (SEM) images and energy-dispersive X-ray (EDX) spectra of the phosphors were obtained using a Philips XL30S FEG microscope operating at 20 keV. The manganese concentration in the synthesized Cs₂HfF₆:Mn⁴⁺ phosphor was determined with inductively coupled plasma optical emission spectroscopy (ICP-OES) performed on a Perkin-Elmer Optima 8300DV spectrometer. For the ICP-OES measurements the Cs₂HfF₆:Mn⁴⁺ phosphor was dissolved in aqua regia.

Photoluminescence (PL) measurements were performed on an Edinburgh Instruments FLS920 fluorescence spectrometer. Excitation and emission spectra were recorded with a 450 W Xe lamp as excitation source and a Hamamatsu R928 photomultiplier tube (PMT) with a grating blazed at 500 nm for detection of emission. For PL decay measurements excitation was done with a tunable optical parametric oscillator (OPO) Opotek Opolette HE 355II laser (pulse width 10 ns, repetition rate 10 Hz) and emission was detected with a Hamamatsu H74220-60 PMT. Samples were cooled down to 4 K with an Oxford Instruments liquid helium flow cryostat. For PL measurements between

300 and 600 K samples were heated in a Linkam THMS600 temperature controlled stage. The PL quantum efficiency of the phosphor was determined with a calibrated home-built setup which consisted of a 65 W Xe lamp, excitation monochromator, integrating sphere (Labsphere) and CCD camera (Avantes AvaSpec-2048).

2.3 Results and discussion

2.3.1 Structural characterization of phosphor particles

To investigate the phase purity, size, shape and composition of the $\text{Cs}_2\text{HfF}_6:\text{Mn}^{4+}$ phosphor particles, we employed different characterization methods such as powder X-ray diffraction (XRD), scanning electron microscopy (SEM), energy-dispersive X-ray spectroscopy and inductively coupled plasma optical emission spectroscopy (ICP-OES). Figure 2.2a shows the XRD pattern of the $\text{Cs}_2\text{HfF}_6:\text{Mn}^{4+}$ phosphor. The XRD pattern is in excellent agreement with the reference pattern of trigonal Cs_2HfF_6 (PDF 04-008-3370). No impurity crystal phases are observed. The trigonal crystal structure of Cs_2HfF_6 ($P\bar{3}m1$ space group) [28] is displayed in Figure 2.2b. Each Hf^{4+} ion is surrounded by six F^- ions to form a trigonally distorted HfF_6^{2-} octahedron (accentuated in Figure 2.2b). The distorted HfF_6^{2-} octahedron has a D_{3d} symmetry with Hf–F distances of 2.03 Å.

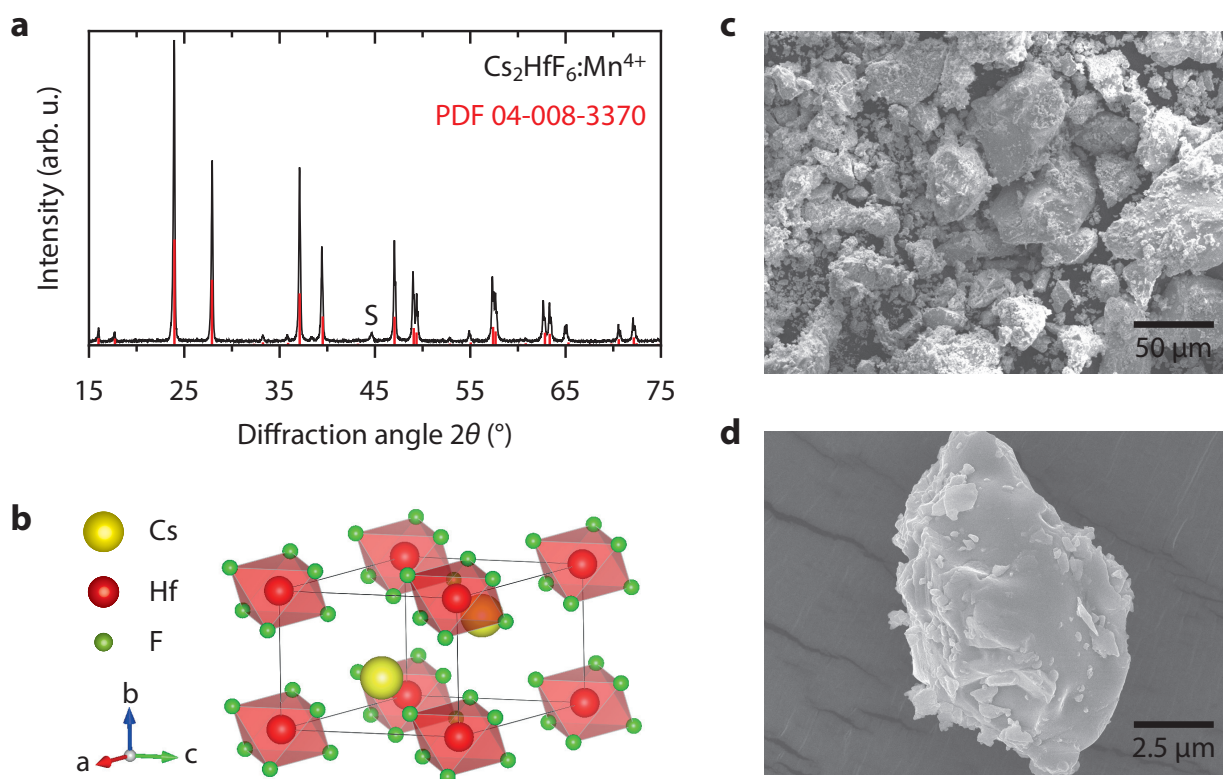


Figure 2.2 – (a) Powder X-ray diffraction (XRD) pattern of $\text{Cs}_2\text{HfF}_6:\text{Mn}^{4+}$ (black) and reference pattern of Cs_2HfF_6 (red lines, PDF 04-008-3370). The S marks a diffraction peak originating from the aluminum sample holder. (b) Crystal structure of Cs_2HfF_6 ($P\bar{3}m1$ space group). The distorted HfF_6^{2-} octahedra have been accentuated. (c,d) SEM images of $\text{Cs}_2\text{HfF}_6:\text{Mn}^{4+}$ phosphor particles.

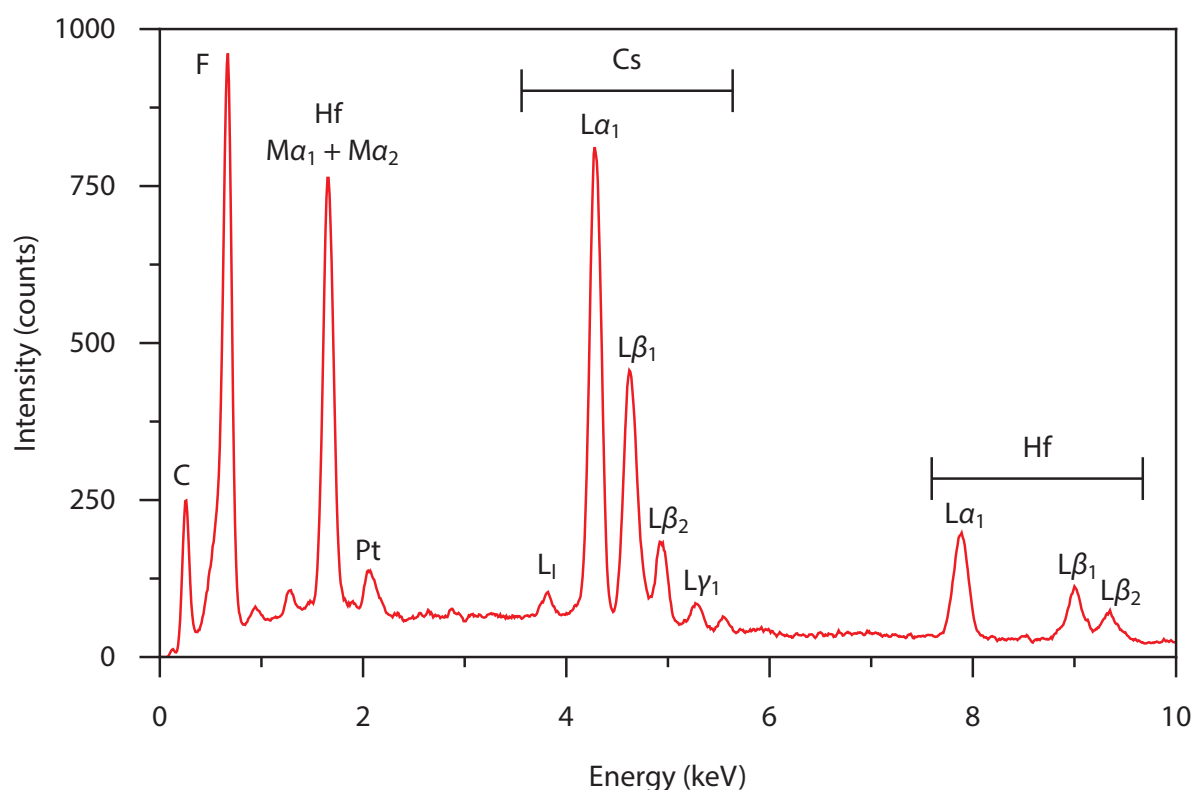


Figure 2.3 – Energy dispersive X-ray (EDX) spectrum of $\text{Cs}_2\text{HfF}_6:\text{Mn}^{4+}$. The carbon (C) and platinum (Pt) peaks originate from the carbon tape beneath the sample and the platinum layer sputtered onto the phosphor particles for the SEM-EDX measurements.

Figure 2.2c,d shows SEM images of $\text{Cs}_2\text{HfF}_6:\text{Mn}^{4+}$ phosphor particles. The particles have irregular shapes and are very polydisperse, with sizes ranging from 100 nm to 100 μm . We attribute this to fast and forced crystallization in the anti-solvent ethanol. If the $\text{Cs}_2\text{HfF}_6:\text{Mn}^{4+}$ phosphor would be formed by slowly evaporating the HF solution, monodisperse particles with a hexagonal shape may be obtained based on the trigonal crystal structure of Cs_2HfF_6 . EDX spectroscopy measurements (Figure 2.3) confirm that the $\text{Cs}_2\text{HfF}_6:\text{Mn}^{4+}$ phosphor particles shown in Figure 2.2c,d consist of cesium, hafnium and fluorine ions. All intense peaks in the EDX spectrum can be assigned to K, L or M X-ray emission lines of these elements. The manganese concentration in the particles is too low to be detected by EDX spectroscopy. Hence, we used ICP-OES as technique to determine the manganese concentration in the $\text{Cs}_2\text{HfF}_6:\text{Mn}^{4+}$ phosphor. It was found that the $\text{Cs}_2\text{HfF}_6:\text{Mn}^{4+}$ phosphor contains 1.9 mol% of manganese ions, which is close to the 2.0 mol% of K_2MnF_6 added during the synthesis.

2.3.2 Red Mn^{4+} luminescence of $\text{Cs}_2\text{HfF}_6:\text{Mn}^{4+}$

Upon illumination with UV radiation $\text{Cs}_2\text{HfF}_6:\text{Mn}^{4+}$ shows bright red luminescence, as can be seen in Figure 2.1c. To investigate this luminescence, we measured photoluminescence (PL) excitation and emission spectra of $\text{Cs}_2\text{HfF}_6:\text{Mn}^{4+}$ at room temperature. These spectra are presented in Figure 2.4a. $\text{Cs}_2\text{HfF}_6:\text{Mn}^{4+}$ shows narrow

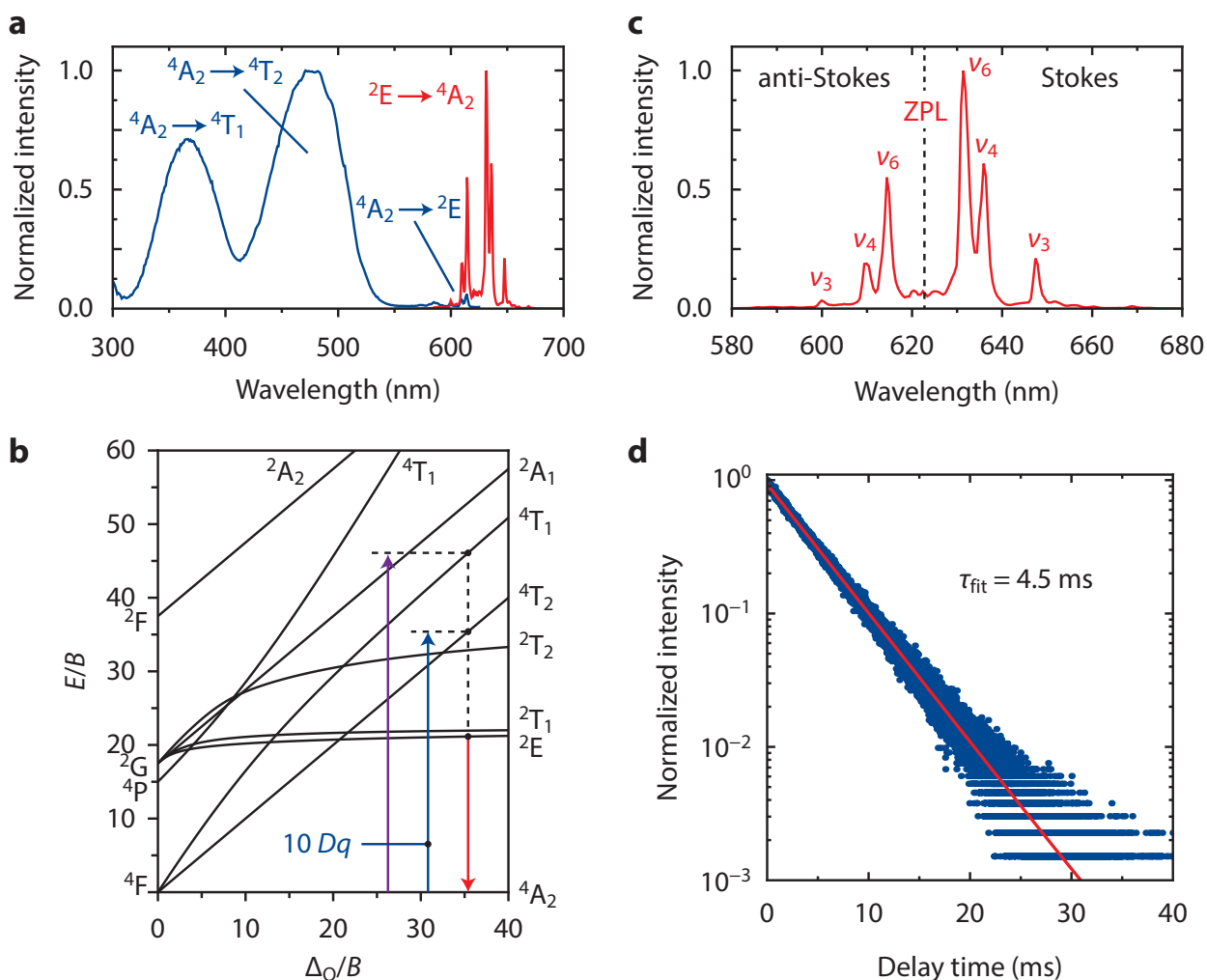


Figure 2.4 – (a) Room-temperature PL excitation (blue, $\lambda_{\text{em}} = 632$ nm) and emission (red, $\lambda_{\text{exc}} = 470$ nm) spectra of $\text{Cs}_2\text{HfF}_6:\text{Mn}^{4+}$ (1.9%). The emission and excitation bands/lines are assigned to corresponding transitions in the d^3 Tanabe-Sugano diagram. (b) Tanabe-Sugano energy level diagram of the d^3 electron configuration in an octahedral crystal field ($C = 4.5B$). The ${}^4A_2 \rightarrow {}^4T_1$, ${}^4A_2 \rightarrow {}^4T_2$ and ${}^2E \rightarrow {}^4A_2$ transitions of Mn^{4+} are indicated by the purple, blue and red arrows, respectively. Note that the excitation transitions are displaced for clarity. For a specific coordination all transitions take place around the same crystal field. The energy of the ${}^4A_2 \rightarrow {}^4T_2$ transition equals the crystal field splitting Δ_0 (or $10 Dq$). (c) Enlarged emission spectrum showing the zero-phonon line (ZPL) and (anti-)Stokes vibronic ${}^2E \rightarrow {}^4A_2$ emissions of $\text{Cs}_2\text{HfF}_6:\text{Mn}^{4+}$. (d) PL decay curve of the Mn^{4+} emission in $\text{Cs}_2\text{HfF}_6:\text{Mn}^{4+}$ (1.9%) ($\lambda_{\text{exc}} = 470$ nm, $\lambda_{\text{em}} = 632$ nm and $T = 298$ K). The decay time corresponding to the mono-exponential fit (red line) is 4.5 ms.

emission lines around 620 nm under blue light excitation ($\lambda_{\text{exc}} = 470$ nm). The main emission peaks are in the wavelength range of 610–640 nm where eye sensitivity is still relatively high, which is beneficial for applications. The red luminescence is assigned to the $\text{Mn}^{4+} {}^2E \rightarrow {}^4A_2$ transition, which is indicated by the red arrow in the Tanabe-Sugano energy level diagram of Mn^{4+} ($3d^3$) in Figure 2.4b. The Tanabe-Sugano diagram [29,30] depicts the energy levels of the d^3 electron configuration in an octahedral crystal field as a function of the crystal field splitting Δ_0 . Due to its high effective charge, the Mn^{4+} ion experiences a strong crystal field and therefore the 2E state is generally the

lowest energy excited state. The 2E excited state and 4A_2 ground state have the same t_2^3 configuration and as a result the energy of the ${}^2E \rightarrow {}^4A_2$ transition hardly depends on Δ_O . Consequently, there is little to no lateral displacement between the parabolas of the 2E and 4A_2 state (small Huang–Rhys parameter [31]) causing the ${}^2E \rightarrow {}^4A_2$ emission to be characterized by narrow zero-phonon and vibronic emission lines.

The emission spectrum of $\text{Cs}_2\text{HfF}_6:\text{Mn}^{4+}$ is displayed in more detail in Figure 2.4c. The spectrum shows a weak line at 622 nm symmetrically surrounded by lines at shorter and longer wavelengths. This resembles emission spectra observed for other Mn^{4+} -doped fluorides such as $\text{K}_2\text{SiF}_6:\text{Mn}^{4+}$ and $\text{K}_2\text{TiF}_6:\text{Mn}^{4+}$ [17,32]. In analogy, the ${}^2E \rightarrow {}^4A_2$ spectrum of $\text{Cs}_2\text{HfF}_6:\text{Mn}^{4+}$ consists of a weak zero-phonon line (ZPL) at ~ 622 nm and more intense anti-Stokes and Stokes vibronic emissions (labeled ν_3 , ν_4 and ν_6) on the high and low energy side of the ZPL, respectively. In $\text{Cs}_2\text{HfF}_6:\text{Mn}^{4+}$ the ${}^2E \rightarrow {}^4A_2$ electric dipole transition is forbidden because Mn^{4+} is located on a site with inversion symmetry (Hf^{4+} site with D_{3d} symmetry). As a consequence, the zero-phonon emission (ZPL) is very weak (see Figure 2.4c). The transition however gains intensity by coupling to asymmetric (ungerade) vibrational modes in the MnF_6^{2-} center [33,34]. Asymmetric vibrational modes induce odd-parity crystal field terms that mix some odd-parity states into the even-parity (gerade) $\text{Mn}^{4+} 3d^3$ states (in $\text{Cs}_2\text{HfF}_6:\text{Mn}^{4+}$ all $3d^3$ states have gerade symmetry as Mn^{4+} is located on a site with inversion symmetry). Due to this mixing the ${}^2E \rightarrow {}^4A_2$ transition becomes partly electric dipole allowed. The vibrational modes of the MnF_6^{2-} ion that have ungerade symmetry are the $\nu_3(T_{1u})$, $\nu_4(T_{1u})$ and $\nu_6(T_{2u})$ modes [35,36]. Hence, the most intense emission lines in Figure 2.4c are assigned to ${}^2E \rightarrow {}^4A_2$ transitions coupling with these vibrations. Thermal population of these phonon modes at room temperature allows the transition to couple with phonons in the excited state (giving rise to the anti-Stokes lines) while transitions to these phonon modes in the ground state can occur at all temperatures (Stokes lines). As a result, both anti-Stokes and Stokes vibronic emissions are observed in the room-temperature PL spectrum.

To further understand the luminescence properties of Mn^{4+} in Cs_2HfF_6 we analyze the positions of the Mn^{4+} excitation bands. The red Mn^{4+} luminescence of $\text{Cs}_2\text{HfF}_6:\text{Mn}^{4+}$ has two broad excitation bands with maxima at 367 and 477 nm, respectively (Figure 2.4a). These bands are assigned to the $\text{Mn}^{4+} {}^4A_2 \rightarrow {}^4T_1$ (4F) and ${}^4A_2 \rightarrow {}^4T_2$ transitions (violet and blue arrows in Tanabe-Sugano diagram in Figure 2.4b). The ${}^4A_2 \rightarrow {}^4T_2$ excitation band shows good overlap with the blue emission of (In,Ga)N LED chips. Besides the ${}^4A_2 \rightarrow {}^4T_1$ and ${}^4A_2 \rightarrow {}^4T_2$ excitation bands, the PL excitation spectrum exhibits some weak excitation lines around 600 nm which are assigned to $\text{Mn}^{4+} {}^4A_2 \rightarrow {}^2E$ and ${}^4A_2 \rightarrow {}^2T_1$ transitions. These transitions are spin-forbidden and therefore low in intensity relative to the spin-allowed ${}^4A_2 \rightarrow {}^4T_1$ and ${}^4A_2 \rightarrow {}^4T_2$ transitions. Since the 4T_1 and 4T_2 states have a different electron configuration than the 4A_2 ground state (t_2^2e versus t_2^3), there is an offset between the potential curve equilibrium positions of the 4A_2 ground state and the ${}^4T_{1,2}$ excited states. As a consequence, the ${}^4A_2 \rightarrow {}^4T_1$ and ${}^4A_2 \rightarrow {}^4T_2$ excitation bands are

broad (large Huang–Rhys parameter [31]) and their transition energies are sensitive to the strength of the crystal field (see Figure 2.4b). If we compare the energy of the ${}^4\text{A}_2 \rightarrow {}^4\text{T}_2$ excitation band in $\text{Cs}_2\text{HfF}_6:\text{Mn}^{4+}$ to the energy of this band in other Mn^{4+} -doped fluoride phosphors, we see the influence of the crystal field splitting on the ${}^4\text{T}_2$ and ${}^4\text{T}_1$ levels. In $\text{Cs}_2\text{HfF}_6:\text{Mn}^{4+}$ the maximum of the ${}^4\text{A}_2 \rightarrow {}^4\text{T}_2$ band is at 477 nm, where e.g. for $\text{K}_2\text{SiF}_6:\text{Mn}^{4+}$ it is centered around 450 nm [17,33]. The ionic radius of Hf^{4+} ($r = 0.71 \text{ \AA}$) is significantly larger than the ionic radius of Si^{4+} ($r = 0.40 \text{ \AA}$) [37] and therefore the Mn–F distance is longer in $\text{Cs}_2\text{HfF}_6:\text{Mn}^{4+}$. This results in a weaker crystal field splitting, causing the ${}^4\text{T}_2$ state to be at lower energy in $\text{Cs}_2\text{HfF}_6:\text{Mn}^{4+}$ when compared to $\text{K}_2\text{SiF}_6:\text{Mn}^{4+}$.

For applications in lighting it is important that the luminescence of $\text{Cs}_2\text{HfF}_6:\text{Mn}^{4+}$ has a high quantum efficiency. The PL quantum efficiency is defined as the ratio between the number of emitted and absorbed photons. We measured the PL quantum efficiency of several $\text{Cs}_2\text{HfF}_6:\text{Mn}^{4+}$ phosphor samples by using a calibrated setup with an integrating sphere (see Section 2.2.3). The $\text{Cs}_2\text{HfF}_6:\text{Mn}^{4+}$ phosphors exhibit very high PL quantum efficiencies of 80–90% which gives them large potential for application, especially since these are the first samples made and no optimization of the synthesis method has been done. The high quantum efficiency is consistent with the luminescence decay of the Mn^{4+} emission from $\text{Cs}_2\text{HfF}_6:\text{Mn}^{4+}$. The PL decay curve in Figure 2.4d shows a mono-exponential decay, confirming the decay of the ${}^2\text{E}$ excited state is mainly radiative. The fitted decay time is 4.5 ms, which is a typical radiative lifetime for the parity- and spin-forbidden ${}^2\text{E} \rightarrow {}^4\text{A}_2$ transition of Mn^{4+} .

2.3.3 Energies of the Mn^{4+} levels and vibrational modes

To accurately determine the energies of the Mn^{4+} levels in $\text{Cs}_2\text{HfF}_6:\text{Mn}^{4+}$, we recorded and analyzed high-resolution PL spectra for $\text{Cs}_2\text{HfF}_6:\text{Mn}^{4+}$ at $T = 4 \text{ K}$. At cryogenic temperatures there is less thermal broadening of emission and excitation bands and therefore zero-phonon lines (ZPLs) may be observed. These lines give the energies of the purely electronic transitions to the Mn^{4+} excited states. Furthermore, with reduced thermal broadening we can study the vibronic fine structure of the Mn^{4+} emission and excitation bands and thereby obtain the vibrational energies of the MnF_6^{2-} group.

Figure 2.5 shows low-temperature ($T = 4 \text{ K}$) spectra of the ${}^2\text{E} \rightarrow {}^4\text{A}_2$ emission and ${}^4\text{A}_2 \rightarrow {}^2\text{T}_1, {}^2\text{E}$ excitations of $\text{Cs}_2\text{HfF}_6:\text{Mn}^{4+}$. In the emission spectrum we observe the ZPL of the ${}^2\text{E} \rightarrow {}^4\text{A}_2$ transition at 621.4 nm, which means the energy of the ${}^2\text{E}$ level is 16093 cm^{-1} . As expected the ZPL of the opposite ${}^4\text{A}_2 \rightarrow {}^2\text{E}$ transition is found at the same energy in the excitation spectrum. The ${}^2\text{E}$ energy of $\text{Cs}_2\text{HfF}_6:\text{Mn}^{4+}$ is similar to the ${}^2\text{E}$ energies observed for other Mn^{4+} -doped fluorides [18,38].

In line with the luminescence properties at room temperature, the 4 K emission spectrum of $\text{Cs}_2\text{HfF}_6:\text{Mn}^{4+}$ is dominated by ν_3 , ν_4 and ν_6 vibronic ${}^2\text{E} \rightarrow {}^4\text{A}_2$ transitions of Mn^{4+} . However, at 4 K there are no anti-Stokes vibronic emissions as no phonon

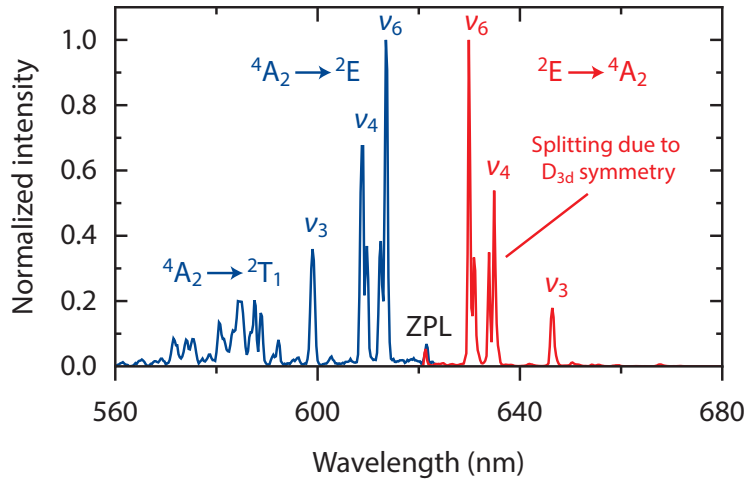


Figure 2.5 – PL excitation (blue, $\lambda_{em} = 630$ nm) and emission (red, $\lambda_{exc} = 472$ nm) spectra of $\text{Cs}_2\text{HfF}_6:\text{Mn}^{4+}$ at $T = 4$ K. For the excitation spectrum only the spectral region of the ${}^4\text{A}_2 \rightarrow {}^2\text{T}_1$ and ${}^4\text{A}_2 \rightarrow {}^2\text{E}$ transitions is shown. The ν_4 and ν_6 excitation and emission lines show a splitting due to the D_{3d} site symmetry for Mn^{4+} in $\text{Cs}_2\text{HfF}_6:\text{Mn}^{4+}$.

states are occupied in the ${}^2\text{E}$ excited state. Because of the D_{3d} site symmetry for Mn^{4+} in $\text{Cs}_2\text{HfF}_6:\text{Mn}^{4+}$, the triply degenerate $\nu_3(\text{T}_{1u})$, $\nu_4(\text{T}_{1u})$ and $\nu_6(\text{T}_{2u})$ modes (in O_h symmetry) split into a singly and a doubly degenerate mode [35,36]. The modes with T_{1u} symmetry split into an A_{2u} and E_u mode and the T_{2u} mode splits into an A_{1u} and E_u mode. At 4 K this splitting is visible in the ν_4 and ν_6 emissions but not observed in the ν_3 peak, where it can be obscured due to broadening of the individual A_{2u} and E_u emission lines.

From the emission spectrum we determine the energies of the asymmetric vibrational modes. The results are summarized in Table 2.1. The vibrational frequencies found for $\text{Cs}_2\text{HfF}_6:\text{Mn}^{4+}$ are very similar to those reported for Cs_2MnF_6 by Chodos et al. [39], which for comparison have also been listed in Table 2.1. Besides the intense ν_3 , ν_4 and ν_6 peaks, several other weak vibronic emissions are present in the emission spectrum of $\text{Cs}_2\text{HfF}_6:\text{Mn}^{4+}$ (see Figure 2.6). The weak emission lines between 620 and 630 nm are assigned to coupling with rotatory or translatory lattice modes [36]. The emission line at 642 nm (514 cm^{-1} relative to the ZPL) is attributed to the symmetric $\nu_2(\text{E}_g)$ mode of the MnF_6^{2-} group, as this mode has an energy of $\sim 500\text{ cm}^{-1}$ in Cs_2MnF_6 and other Mn^{4+} -doped fluorides [16,39]. Furthermore, all peaks at wavelengths longer than 650 nm are

Table 2.1 – Vibrational mode energies (cm^{-1}) of the MnF_6^{2-} group in $\text{Cs}_2\text{HfF}_6:\text{Mn}^{4+}$ (determined from the vibronic lines in Figure 2.5) and Cs_2MnF_6 at $T = 4$ K. The data of Cs_2MnF_6 is from Ref. [39].

Compound	ν_3	$\nu_4(\text{A}_{2u})$	$\nu_4(\text{E}_u)$	$\nu_6(\text{A}_{1u})$	$\nu_6(\text{E}_u)$
$\text{Cs}_2\text{HfF}_6:\text{Mn}^{4+}$	623	318	342	217	243
Cs_2MnF_6	633	332	338	228	

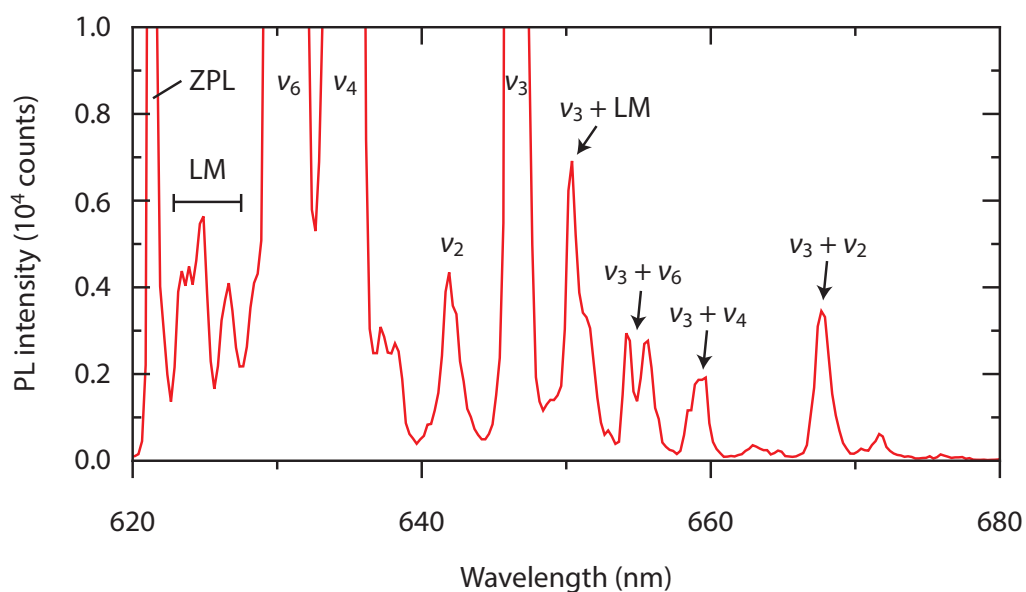


Figure 2.6 – Enlargement of the weak ${}^2E \rightarrow {}^4A_2$ vibronic emissions of Cs₂HfF₆:Mn⁴⁺ (LM = lattice modes).

ascribed to combinations of the ν_3 mode with other vibrational modes [17]. Emissions due to coupling of the electronic transition with the symmetric (gerade) ν_1 and ν_5 modes of the MnF₆²⁻ ion are not observed in the spectrum. The ν_1 and ν_5 modes have energies of ~ 600 and ~ 300 cm⁻¹, respectively [16,39]. As coupling with symmetric modes does not break the parity selection rule, these vibronic lines are expected to be very weak and are therefore probably obscured by the stronger ν_3 and ν_4 peaks.

Like the ${}^2E \rightarrow {}^4A_2$ emission, the ${}^4A_2 \rightarrow {}^2E$ excitation gains intensity by coupling with asymmetric vibrational modes. The vibrational mode frequencies of the 2E excited state will be approximately the same as those of the 4A_2 ground state. As a consequence, the ${}^4A_2 \rightarrow {}^2E$ spectrum should be a mirror image of the ${}^2E \rightarrow {}^4A_2$ emission. The excitation spectrum in Figure 2.5 confirms that this is indeed true for Cs₂HfF₆:Mn⁴⁺. At shorter wavelengths peaks due to ${}^4A_2 \rightarrow {}^2T_1$ transitions are visible in the excitation spectrum. It is difficult to locate the ZPL of the ${}^4A_2 \rightarrow {}^2T_1$ transition because of overlap with the stronger vibronic ${}^4A_2 \rightarrow {}^2E$ excitation lines. We estimate the ZPL to be at 589 nm which gives a 2T_1 level energy of 16978 cm⁻¹.

At higher energies we find the transitions to the Mn⁴⁺ 4T_1 and 4T_2 states. A low-temperature spectrum ($T = 4$ K) of the ${}^4A_2 \rightarrow {}^4T_1$ and ${}^4A_2 \rightarrow {}^4T_2$ excitation bands of Cs₂HfF₆:Mn⁴⁺ is shown in Figure 2.7a. At room temperature these transitions give rise to broad featureless bands (see Figure 2.4a), but now at 4 K a well-resolved fine structure is observed in the ${}^4A_2 \rightarrow {}^4T_2$ excitation band. The ${}^4A_2 \rightarrow {}^4T_2$ band shows a vibronic progression with an energy spacing of ~ 500 cm⁻¹. Similar progressions were observed in the ${}^4A_2 \rightarrow {}^4T_2$ band of K₂SiF₆:Mn⁴⁺, K₂TiF₆:Mn⁴⁺ and K₂GeF₆:Mn⁴⁺ [15,16,33]. There is debate about which vibration is responsible for the vibronic progression in the ${}^4A_2 \rightarrow$

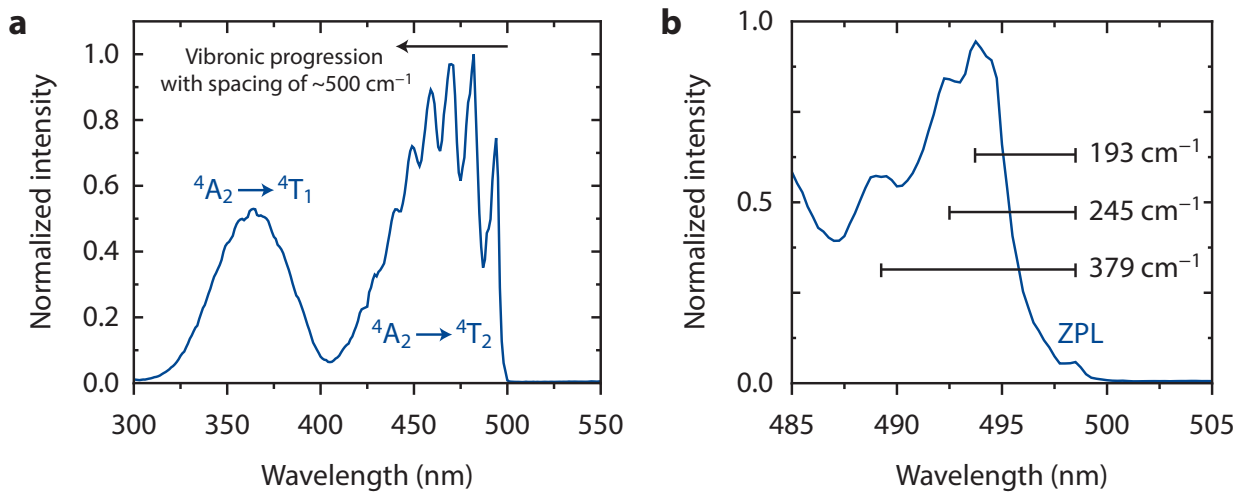


Figure 2.7 – (a) PL excitation spectrum ($\lambda_{em} = 630$ nm) of $\text{Cs}_2\text{HfF}_6:\text{Mn}^{4+}$ at $T = 4$ K. The ${}^4\text{A}_2 \rightarrow {}^4\text{T}_2$ excitation band exhibits a vibronic progression with an energy spacing of ~ 500 cm^{-1} . (b) High-resolution spectrum of the onset of the ${}^4\text{A}_2 \rightarrow {}^4\text{T}_2$ excitation band for $\text{Cs}_2\text{HfF}_6:\text{Mn}^{4+}$. The horizontal bars indicate the energy differences between the zero-phonon ${}^4\text{A}_2 \rightarrow {}^4\text{T}_2$ transition (labeled ZPL) and one-phonon vibronic ${}^4\text{A}_2 \rightarrow {}^4\text{T}_2$ excitation peaks.

${}^4\text{T}_2$ band. Adachi et al. ascribe the vibronic progression to the symmetric $\nu_2(\text{E}_g)$ mode of the MnF_6^{2-} ion [17,40]. This mode has an energy of 514 cm^{-1} for $\text{Cs}_2\text{HfF}_6:\text{Mn}^{4+}$, which is in good agreement with the progression spacing of ~ 500 cm^{-1} . Other works however assign the vibronic progression to the symmetric $\nu_1(\text{A}_{1g})$ stretching mode [15,16,33]. The energy of the ν_1 mode in the ${}^4\text{A}_2$ ground state is ~ 600 cm^{-1} , which is somewhat larger than the progression spacing of ~ 500 cm^{-1} . Paulusz [33] attributes this energy difference to a weakening of the Mn–F bond in the ${}^4\text{T}_2$ excited state due to the presence of an electron in the antibonding e_g orbitals [33]. However, the energy difference between the vibrational modes of the ground and excited states is typically much smaller than 100 cm^{-1} . For example, in $\text{MgF}_2:\text{Eu}^{2+}$ the vibrational frequencies of the Eu^{2+} $4f^65d^1$ excited state and $4f^7$ ground state differ only 0 – 30 cm^{-1} [41]. We therefore assign the vibronic progression in the ${}^4\text{A}_2 \rightarrow {}^4\text{T}_2$ band to the ν_2 mode of the MnF_6^{2-} group.

To obtain the energies of the ${}^4\text{T}_1$ and ${}^4\text{T}_2$ states, we have to locate the ZPLs of the ${}^4\text{A}_2 \rightarrow {}^4\text{T}_1$ and ${}^4\text{A}_2 \rightarrow {}^4\text{T}_2$ transitions. In many works these ZPLs are located by fitting Poisson distributions to the room-temperature excitation spectra of Mn^{4+} [17,32,42–46]. This method however gives too low ZPL energies because of thermal broadening of the excitation bands at room temperature [42]. We will therefore instead try to directly observe the ZPLs in a spectral measurement. Since the ${}^4\text{A}_2 \rightarrow {}^4\text{T}_{1,2}$ transitions are electric dipole forbidden, the ZPLs have a very low intensity compared to the vibronic ${}^4\text{A}_2 \rightarrow {}^4\text{T}_{1,2}$ excitations [16]. The ZPL of the ${}^4\text{A}_2 \rightarrow {}^4\text{T}_1$ transition will therefore never be observed as it is always obscured by stronger vibronic ${}^4\text{A}_2 \rightarrow {}^4\text{T}_2$ excitations (see Figure 2.7a). The ZPL of the lower-energy ${}^4\text{A}_2 \rightarrow {}^4\text{T}_2$ transition has however been measured for some compounds by low-temperature high-resolution absorption and two-photon excitation

spectroscopy [16,47]. Hence, we recorded a high-resolution spectrum of the low-energy side of the ${}^4A_2 \rightarrow {}^4T_2$ excitation band, which is shown in Figure 2.7b. In the spectrum a small peak is visible at 498.5 nm (20060 cm⁻¹). Based on previous observations, we assign this peak to the ZPL of the ${}^4A_2 \rightarrow {}^4T_2$ transition [47].

At wavelengths shorter than the ZPL arise the intense vibronic ${}^4A_2 \rightarrow {}^4T_2$ excitations. The horizontal bars in Figure 2.7b give the energy differences between the ZPL and the vibronic excitation peaks. Similar to the ${}^2E \rightarrow {}^4A_2$ transition, the ${}^4A_2 \rightarrow {}^4T_2$ transition can become partly allowed by coupling with asymmetric (ungerade) vibrational modes. Hence, we assign the first vibronic peak at 193 cm⁻¹ to the $\nu_6(A_{1u})$ mode of the MnF₆²⁻ ion (see also Table 2.1) [16,48]. By similar reasoning the peaks at 245 and 379 cm⁻¹ can be attributed to the $\nu_6(E_u)$ and $\nu_4(E_u)$ asymmetric vibrational modes. Alternatively, splitting of the 4T_2 state by the trigonal crystal field may give rise to a second zero-phonon line and therefore the peaks at 245 and 379 cm⁻¹ may also correspond to vibronic replicas of a second electronic origin. The present spectral data do not allow a definite assignment of the peaks around the onset of the ${}^4A_2 \rightarrow {}^4T_2$ excitation band. Based on these observations we conclude that the ${}^4A_2 \rightarrow {}^4T_2$ band structure consists of a ν_2 mode progression of ${}^4A_2 \rightarrow {}^4T_2 + \nu_u$ transitions, where ν_u is an asymmetric (ungerade) vibrational mode in the 4T_2 excited state.

The energies we have found for the various Mn⁴⁺ levels can now be used to determine the crystal field splitting $10 Dq$ (or Δ_O) and Racah parameters B and C . The Racah parameters (together with Dq) provide the energies of all Mn⁴⁺ states and furthermore give a measure of the nephelauxetic effect [29,38]. The crystal field splitting $10 Dq$ equals the energy of the ${}^4A_2 \rightarrow {}^4T_2$ transition (see Figure 2.4b). In many works on Mn⁴⁺ and Cr³⁺ the maximum of the ${}^4A_2 \rightarrow {}^4T_2$ band is therefore taken as the $10 Dq$ energy [15,49–51]. This energy is determined by both the electronic transition energy and the Stokes shift, related to the relaxation in the excited state. An alternative is to use the pure electronic transition energy and to determine the $10 Dq$ value from the energy of the zero-phonon ${}^4A_2 \rightarrow {}^4T_2$ transition. For Cs₂HfF₆:Mn⁴⁺ we observed the zero-phonon ${}^4A_2 \rightarrow {}^4T_2$ transition at 20060 cm⁻¹ and the crystal field splitting $10 Dq$ thus equals this energy. The Racah parameters B and C can then be obtained with the following relations [35]:

$$\frac{B}{Dq} = \frac{\left(\frac{\Delta E}{Dq}\right)^2 - 10 \left(\frac{\Delta E}{Dq}\right)}{15 \left(\frac{\Delta E}{Dq} - 8\right)} \quad (2.1)$$

$$\frac{E({}^2E)}{B} \cong 3.05 \left(\frac{C}{B}\right) + 7.90 - 1.80 \left(\frac{B}{Dq}\right) \quad (2.2)$$

Here ΔE is the energy difference between the 4T_1 and 4T_2 states and $E({}^2E)$ is the ZPL energy of the ${}^2E \rightarrow {}^4A_2$ transition. As we did not observe the ZPL of the ${}^4A_2 \rightarrow {}^4T_1$ transition, we estimate ΔE by taking the energy difference between the centers of the ${}^4A_2 \rightarrow {}^4T_1$ and ${}^4A_2 \rightarrow {}^4T_2$ excitation bands (centers at 364 and 474 nm, $\Delta E = 6375 \text{ cm}^{-1}$). It is a good assumption that this difference equals the energy gap between the ZPLs because the Stokes shift will be approximately similar for these transitions. With equations 2.1 and 2.2 we then find that $B = 601 \text{ cm}^{-1}$ and $C = 3825 \text{ cm}^{-1}$ for $\text{Cs}_2\text{HfF}_6:\text{Mn}^{4+}$. For comparison, we also calculate the Racah parameters with the maximum of the ${}^4A_2 \rightarrow {}^4T_2$ band as the $10 Dq$ energy. With this other $10 Dq$ energy we obtain almost similar B and C values of 596 cm^{-1} and 3832 cm^{-1} , respectively. The B and C parameters we find for $\text{Cs}_2\text{HfF}_6:\text{Mn}^{4+}$ are in good agreement with those reported for other Mn^{4+} -doped fluorides [38]. Finally, with the B and C values we can determine the β_1 parameter for $\text{Cs}_2\text{HfF}_6:\text{Mn}^{4+}$. This parameter was recently introduced by Brik and Srivastava [52] and quantitatively describes the nephelauxetic effect for Mn^{4+} . The β_1 parameter is defined as follows,

$$\beta_1 = \sqrt{\left(\frac{B}{B_0}\right)^2 + \left(\frac{C}{C_0}\right)^2} \quad (2.3)$$

where B_0 and C_0 are the free ion Racah parameters. For Mn^{4+} , $B_0 = 1160 \text{ cm}^{-1}$ and $C_0 = 4303 \text{ cm}^{-1}$ [52]. By using equation 2.3 we determine that $\beta_1 = 1.03$ for $\text{Cs}_2\text{HfF}_6:\text{Mn}^{4+}$. This is a β_1 value typically found for Mn^{4+} in fluorides [38].

2.3.4 Temperature-dependent luminescence properties

In most phosphor-converted LED systems the phosphor operating temperature is far above room temperature. For example, in high-power 5 W LEDs the temperature near the LED chip can rise to 450 K [5]. It is therefore important to study the thermal quenching behavior of potential LED phosphors. The thermal quenching of the Mn^{4+} emission in $\text{Cs}_2\text{HfF}_6:\text{Mn}^{4+}$ was investigated by measuring the Mn^{4+} emission lifetime (Figure 2.8a) and integrated PL intensity (Figure 2.8b) as a function of temperature between 4 and 550 K. The Mn^{4+} emission lifetime shows a steady decrease, starting above 50 K. The decrease in lifetime starts to level off between 200 and 300 K but then shows a rapid decrease above 350 K. To understand the peculiar temperature dependence of the Mn^{4+} emission lifetime, we first look at how the radiative decay rate of the 2E state changes with temperature. The ${}^2E \rightarrow {}^4A_2$ emission consists mainly of anti-Stokes and Stokes vibronic emissions. The transition probabilities of these vibronic emissions scale with the phonon occupation number n for anti-Stokes vibronics and $(1 + n)$ for Stokes vibronics. As a consequence, the temperature dependence of the 2E radiative lifetime τ_R is given by [35],

$$\tau_R(T) = \frac{\tau_R(0)}{2n + 1} \quad (2.4)$$

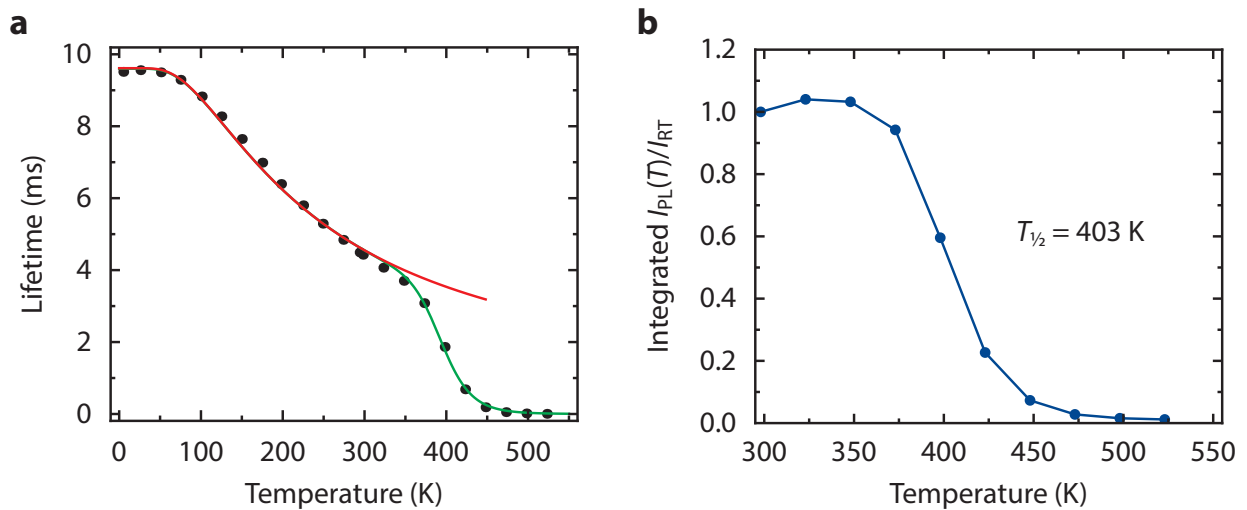


Figure 2.8 – (a) Temperature dependence of the Mn^{4+} emission lifetime in $\text{Cs}_2\text{HfF}_6:\text{Mn}^{4+}$. The solid red and green lines represent plots of equations 2.6 and 2.7 respectively. (b) Integrated PL intensity of $\text{Cs}_2\text{HfF}_6:\text{Mn}^{4+}$ ($\lambda_{\text{exc}} = 470$ nm) as a function of temperature. The luminescence quenching temperature $T_{1/2}$ is 403 K.

with the phonon occupation number n increasing with temperature according to,

$$n = \frac{1}{\exp(h\nu/k_{\text{B}}T) - 1} \quad (2.5)$$

In equations 2.4 and 2.5 $\tau_{\text{R}}(0)$ is the radiative lifetime at $T = 0$ K, k_{B} is the Boltzmann constant and $h\nu$ is the energy of the phonon coupling to the ${}^2\text{E} \rightarrow {}^4\text{A}_2$ transition. If equation 2.4 and 2.5 are combined it follows that τ_{R} can be expressed as,

$$\tau_{\text{R}}(T) = \frac{\tau_{\text{R}}(0)}{\coth(h\nu/2k_{\text{B}}T)} \quad (2.6)$$

In Figure 2.8a we plot equation 2.6 (solid red line) for $\tau_{\text{R}}(0) = 9.4$ ms and $h\nu = 215$ cm^{-1} (phonon energy of the intense ν_6 mode emission). It can be seen that equation 2.6 describes the temperature dependence of the Mn^{4+} emission lifetime up to 300 K, confirming that the decay of the ${}^2\text{E}$ state is mainly radiative up to this temperature. The present (simple) model assuming coupling with one dominant vibrational mode gives a good description of the experimentally observed decrease in decay time between 4 and 300 K. The model could be refined by including all three asymmetric modes, weighed for the relative intensities of the vibronic lines to account for the difference in coupling strength. In addition, the energy difference between the ${}^2\text{E}$ and ${}^4\text{T}_2$ state shows a small variation with temperature. This can also affect the lifetime due to partial lifting of the spin selection rule by enhanced admixture of the ${}^4\text{T}_2$ state through spin-orbit coupling when the ${}^2\text{E}-{}^4\text{T}_2$ gap becomes smaller. These effects can be neglected in first

approximation and it is clear that the decrease in lifetime up to 300 K is caused by an increase in the radiative decay rate for the Stokes and anti-Stokes vibronic lines. There is no thermal quenching of the emission up to 300 K.

Above 350 K the Mn^{4+} emission lifetime is shorter than predicted by equation 2.6 (see Figure 2.8a). This difference is explained by the onset of non-radiative transitions. The non-radiative transition probability quickly increases with temperature above 350 K and as a consequence the luminescence of $\text{Cs}_2\text{HfF}_6:\text{Mn}^{4+}$ is quenched. This is confirmed by measurements of the integrated PL intensity, shown in Figure 2.8b. The integrated PL intensity of $\text{Cs}_2\text{HfF}_6:\text{Mn}^{4+}$ is relatively constant up to 350 K but rapidly decreases above this temperature with no luminescence remaining at 550 K. The luminescence quenching temperature $T_{1/2}$, the temperature at which the PL intensity is half of its room temperature value, is determined to be 403 K (130 °C). Due to the luminescence quenching above 100 °C, application of $\text{Cs}_2\text{HfF}_6:\text{Mn}^{4+}$ will be limited to low-power LED systems. To determine the activation energy of the thermal quenching process, we fitted the data in Figure 2.8a with the following expression [53],

$$\tau(T) = \frac{\tau_R(T)}{1 + \left(\frac{\tau_R(T)}{\tau_{\text{NR}}}\right) \exp(-\Delta E/k_B T)} \quad (2.7)$$

where ΔE is the activation energy of the thermal quenching process and τ_{NR} is the non-radiative decay time. From the fit with equation 2.7 (green line in Figure 2.8a) we obtain an activation energy ΔE of 6322 cm^{-1} . The mechanism for temperature quenching of Mn^{4+} emission in fluoride hosts will be discussed in Chapter 5.

2.4 Conclusion

A new class of Mn^{4+} -doped narrow band red-emitting phosphors is introduced: Mn^{4+} -doped fluorohafnates. Single phase $\text{Cs}_2\text{HfF}_6:\text{Mn}^{4+}$ phosphor was prepared via a simple two-step co-precipitation method. ICP-OES measurements confirmed that the Mn^{4+} ions are effectively incorporated into the Cs_2HfF_6 host. Under blue photoexcitation $\text{Cs}_2\text{HfF}_6:\text{Mn}^{4+}$ shows bright narrow red Mn^{4+} luminescence that is centered around 620 nm. We have accurately determined the energies of the Mn^{4+} states and vibrational modes in $\text{Cs}_2\text{HfF}_6:\text{Mn}^{4+}$ from emission and excitation spectra recorded at 4 K. The phosphor exhibits high photoluminescence quantum efficiencies of 80–90% and this combined with the narrow red luminescence under blue light excitation makes $\text{Cs}_2\text{HfF}_6:\text{Mn}^{4+}$ an interesting material for LED applications. $\text{Cs}_2\text{HfF}_6:\text{Mn}^{4+}$ can however only be used in low-power LED systems as its luminescence is quenched above 100 °C ($T_{1/2} = 403$ K).

References

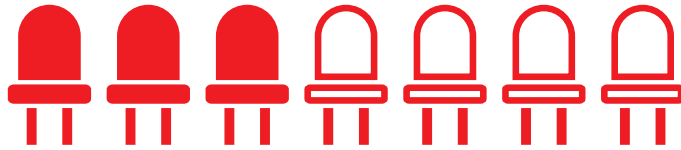
- [1] Charge of the LED brigade: A global switch to LEDs will change the lighting business, *The Economist* (2011).

- [2] M. R. Krames, O. B. Shchekin, R. Mueller-Mach, G. O. Mueller, L. Zhou, G. Harbers and M. G. Craford, *IEEE/OSA J. Disp. Technol.* **3** (2007) 160–175.
- [3] G. Harbers, S. J. Bierhuizen and M. R. Krames, *IEEE/OSA J. Disp. Technol.* **3** (2007) 98–109.
- [4] A. A. Setlur, *Electrochem. Soc. Interface.* **18** (2009) 32–36.
- [5] P. F. Smet, A. B. Parmentier and D. Poelman, *J. Electrochem. Soc.* **158** (2011) R37–R54.
- [6] V. Bachmann, C. Ronda and A. Meijerink, *Chem. Mater.* **21** (2009) 2077–2084.
- [7] A. A. Setlur, E. V. Radkov, C. S. Henderson, J.-H. Her, A. M. Srivastava, N. Karkada, M. S. Kishore, N. P. Kumar, D. Aesram, A. Deshpande, B. Kolodin, L. S. Grigorov and U. Happek, *Chem. Mater.* **22** (2010) 4076–4082.
- [8] S. Ye, F. Xiao, Y. X. Pan, Y. Y. Ma and Q. Y. Zhang, *Mater. Sci. Eng. R Reports.* **71** (2010) 1–34.
- [9] K. Uheda, N. Hirotsuki, Y. Yamamoto and A. Naito, *Electrochem. Solid-State Lett.* **9** (2006) H22–H25.
- [10] P. Pust, A. S. Wochnik, E. Baumann, P. J. Schmidt, D. Wiechert, C. Scheu and W. Schnick, *Chem. Mater.* **26** (2014) 3544–3549.
- [11] P. Pust, V. Weiler, C. Hecht, A. Tücks, A. S. Wochnik, A.-K. Henß, D. Wiechert, C. Scheu, P. J. Schmidt, and W. Schnick, *Nat. Mater.* **13** (2014) 891–896.
- [12] C. Hecht, F. Stadler, P. J. Schmidt, V. Baumann and W. Schnick, *Chem. Mater.* **21** (2009) 1595–1601.
- [13] S. Schmichen, H. Schneider, P. Wagatha, C. Hecht, P. J. Schmidt and W. Schnick, *Chem. Mater.* **26** (2014) 2712–2719.
- [14] R. J. Xie and N. Hirotsuki, *Sci. Technol. Adv. Mater.* **8** (2007) 588–600.
- [15] H. Zhu, C. C. Lin, W. Luo, S. Shu, Z. Liu, Y. Liu, J. Kong, E. Ma, Y. Cao, R.-S. Liu and X. Chen, *Nat. Commun.* **5** (2014) 4312.
- [16] L. Helmholz and M. E. Russo, *J. Chem. Phys.* **59** (1973) 5455–5470.
- [17] T. Takahashi and S. Adachi, *J. Electrochem. Soc.* **155** (2008) E183–E188.
- [18] M. G. Brik and A. M. Srivastava, *J. Lumin.* **133** (2013) 69–72.
- [19] C. C. Lin, A. Meijerink and R.-S. Liu, *J. Phys. Chem. Lett.* **7** (2016) 495–503.
- [20] J. E. Murphy, F. Garcia-Santamaria, A. A. Setlur and S. Sista, *SID Symp. Dig. Tech. Pap.* **46** (2015) 927–930.
- [21] L.-L. Wei, C. C. Lin, M.-H. Fang, M. G. Brik, S.-F. Hu, H. Jiao and R.-S. Liu, *J. Mater. Chem. C* **3** (2015) 1655–1660.
- [22] S. Adachi and T. Takahashi, *J. Appl. Phys.* **104** (2008) 23512.
- [23] Y. Arai and S. Adachi, *J. Lumin.* **131** (2011) 2652–2660.
- [24] H.-D. Nguyen and R.-S. Liu, *J. Mater. Chem. C* **4** (2016) 10759–10775.
- [25] Y. Zhu, L. Huang, R. Zou, J. Zhang, J. Yu, M. Wu, J. Wang and Q. Su, *J. Mater. Chem. C* **4** (2016) 5690–5695.
- [26] H. Bode, H. Jenssen and F. Bandte, *Angew. Chemie* **65** (1953) 304.
- [27] H.W. Roesky, Efficient Preparations of Fluorine Compounds, John Wiley & Sons Inc., Hoboken, 2012.
- [28] H. Bode and G. Teufer, *Zeitschrift Für Anorg. Und Allg. Chemie* **283** (1956) 18–25.
- [29] Y. Tanabe and S. Sugano, *J. Phys. Soc. Japan.* **9** (1954) 753–766.
- [30] Y. Tanabe and S. Sugano, *J. Phys. Soc. Japan.* **9** (1954) 766–779.
- [31] M. de Jong, L. Seijo, A. Meijerink and F. T. Rabouw, *Phys. Chem. Chem. Phys.* **17** (2015) 16959–16969.
- [32] Y. K. Xu and S. Adachi, *J. Electrochem. Soc.* **158** (2011) J58–J65.
- [33] A. G. Paulusz, *J. Electrochem. Soc.* **120** (1973) 942–947.
- [34] T. Senden, F. T. H. Broers and A. Meijerink, *Opt. Mater.* **60** (2016) 431–437.
- [35] B. Henderson and G. F. Imbusch, Optical Spectroscopy of Inorganic Solids, Oxford University Press, Oxford, 1989.
- [36] I. W. Forrest and A. P. Lane, *Inorg. Chem.* **15** (1976) 265–269.
- [37] R. D. Shannon, *Acta Crystallogr. Sect. A.* **32** (1976) 751–767.
- [38] M. G. Brik, S. J. Camardello and A. M. Srivastava, *ECS J. Solid State Sci. Technol.* **4** (2014) R39–R43.
- [39] S. L. Chodos, A. M. Black and C. D. Flint, *J. Chem. Phys.* **65** (1976) 4816–4824.
- [40] D. Sekiguchi, J. Nara and S. Adachi, *J. Appl. Phys.* **113** (2013) 183516.
- [41] S. Lizzo, A. H. Velders, A. Meijerink, G. J. Dirksen and G. Blasse, *J. Lumin.* **65** (1995) 303–311.

- [42] Y. Arai and S. Adachi, *J. Electrochem. Soc.* **158** (2011) J179–J183.
- [43] Y. K. Xu and S. Adachi, *J. Appl. Phys.* **105** (2009) 013525.
- [44] S. Adachi and T. Takahashi, *J. Appl. Phys.* **106** (2009) 013516.
- [45] D. Sekiguchi and S. Adachi, *ECS J. Solid State Sci. Technol.* **3** (2014) R60–R64.
- [46] S. Sakurai, T. Nakamura and S. Adachi, *ECS J. Solid State Sci. Technol.* **5** (2016) R206–R210.
- [47] C. Campochiaro, D. S. McClure, P. Rabinowitz and S. Dougal, *Chem. Phys. Lett.* **157** (1989) 78–82.
- [48] M. J. Reisfeld, N. A. Matwiyoff and L. B. Asprey, *J. Mol. Spectrosc.* **39** (1971) 8–20.
- [49] B. Wang, H. Lin, J. Xu, H. Chen and Y. Wang, *ACS Appl. Mater. Interfaces.* **6** (2014) 22905–22913.
- [50] V. Singh, R. P. S. Chakradhar, J. L. Rao and H. Y. Kwak, *J. Mater. Sci.* **46** (2011) 2331–2337.
- [51] L. Zhang, L. Li, Y. Huang, S. Sun, Z. Lin and G. Wang, *Opt. Mater.* **49** (2015) 75–78.
- [52] A. M. Srivastava and M.G. Brik, *Opt. Mater.* **35** (2013) 1544–1548.
- [53] A. M. Srivastava, H. A. Comanzo, S. Camardello, S. B. Chaney, M. Aycibin and U. Happek, *J. Lumin.* **129** (2009) 919–925.

3

Co-precipitation synthesis and optical properties of Mn^{4+} -doped fluoroaluminate w-LED phosphors



Abstract

Mn^{4+} -doped hexafluoroaluminates are promising red-emitting phosphors for white light emitting diodes (w-LEDs). Here we report the synthesis of $\text{Na}_3\text{AlF}_6:\text{Mn}^{4+}$, $\text{K}_3\text{AlF}_6:\text{Mn}^{4+}$ and $\text{K}_2\text{NaAlF}_6:\text{Mn}^{4+}$ phosphors through a simple two-step co-precipitation method. Highly monodisperse large ($\sim 20 \mu\text{m}$) smoothed-octahedron shaped crystallites are obtained for $\text{K}_2\text{NaAlF}_6:\text{Mn}^{4+}$. The large size, regular shape and small size distribution are favorable for application in w-LEDs. All Mn^{4+} -doped hexafluoroaluminates show bright red Mn^{4+} luminescence under blue light excitation. We compare the optical properties of $\text{Na}_3\text{AlF}_6:\text{Mn}^{4+}$, $\text{K}_3\text{AlF}_6:\text{Mn}^{4+}$ and $\text{K}_2\text{NaAlF}_6:\text{Mn}^{4+}$ at room temperature and 4 K. The luminescence measurements reveal that multiple Mn^{4+} sites exist in $\text{M}_3\text{AlF}_6:\text{Mn}^{4+}$ ($\text{M} = \text{Na}, \text{K}$) which is explained by the charge compensation that is required for Mn^{4+} on Al^{3+} sites. Thermal cycling experiments show that the site distribution changes after annealing. Finally, we investigate thermal quenching and show that the luminescence quenching temperature is high, around 460–490 K, which makes these Mn^{4+} -doped hexafluoroaluminates interesting red phosphors for w-LEDs. The new insights reported on the synthesis and optical properties of Mn^{4+} in the chemically and thermally stable hexafluoroaluminates can contribute to the optimization of red-emitting Mn^{4+} phosphors for w-LEDs.

3.1 Introduction

White light emitting diodes (w-LEDs) are nowadays widely applied in general lighting and consumer electronics because of their high energy efficiency and long operation lifetime [1–5]. Commercial w-LEDs generate white light by combining blue-emitting (In,Ga)N LED chips with inorganic phosphors that convert part of the blue LED emission to green, yellow and/or red light [5,6]. The typical red phosphors in w-LEDs are Eu^{2+} -doped nitrides. These phosphors can have quantum efficiencies (QEs) exceeding 90%, but a drawback is that the Eu^{2+} emission band extends into the deep red and near-IR regions where the sensitivity of the human eye is low [6–8]. As a result, there are significant efficacy losses (reduced lumen/W output) at high color rendering indices (CRIs) when using Eu^{2+} -doped nitrides as red phosphors in w-LEDs [9]. To overcome this issue, efficient narrow band red phosphors with $\lambda_{\text{max}} \sim 620$ nm have to be developed.

Mn^{4+} -doped fluorides are a promising class of materials to improve the color rendering of w-LEDs while maintaining a high luminous efficacy [8–11]. Upon blue photoexcitation Mn^{4+} -doped fluorides show narrow red line emission in the 600–640 nm spectral region. Furthermore, they can have a QE > 90% and are prepared through simple wet-chemical synthesis at room temperature [8,12]. These characteristics make Mn^{4+} -doped fluorides interesting narrow band red phosphors for w-LEDs. In the last years, a large number of Mn^{4+} -activated fluorides with the general chemical formula $\text{A}_2\text{MF}_6:\text{Mn}^{4+}$ (A = Na, K, Rb, Cs and NH_4 ; M = Si, Ge, Ti, Zr and Sn) and $\text{BaMF}_6:\text{Mn}^{4+}$ (M = Si, Ge, Ti and Sn) have been reported [11–13]. In these compounds Mn^{4+} substitutes for the M^{4+} cation that is octahedrally coordinated by six F^- ions. Most work has been done on the phosphor $\text{K}_2\text{SiF}_6:\text{Mn}^{4+}$ (KSF) [14,15]. The Mn^{4+} -doped fluorides have excellent luminescence properties. The deep red color of the 600–640 nm Mn^{4+} emission is particularly favorable for extending the color gamut of displays, and already KSF is widely applied in displays. In lighting large scale application is still limited, partly hampered by issues related to thermal and chemical stability and saturation at high pump powers [14,16].

Recently, the synthesis and luminescence properties of Mn^{4+} -doped hexafluoroaluminates with the compositions $\text{M}_3\text{AlF}_6:\text{Mn}^{4+}$ (M = Li, Na, K) were reported [17–20]. The ionic radius of Mn^{4+} is similar to the ionic radius of Al^{3+} (0.53 versus 0.535 Å) and as a result Mn^{4+} can easily substitute for Al^{3+} in fluoride hosts [17,21]. The $\text{M}_3\text{AlF}_6:\text{Mn}^{4+}$ phosphors have potential advantages over $\text{K}_2\text{SiF}_6:\text{Mn}^{4+}$ and other Mn^{4+} -doped fluorides. First, Na_3AlF_6 and K_3AlF_6 have a melting point of ~ 1000 °C and therefore have a much better thermal stability than K_2SiF_6 , which already decomposes at 350–400 °C [10,22–24]. Secondly, the M_3AlF_6 compounds have a lower water solubility than K_2SiF_6 , making them more chemically stable under high humidity conditions [14,25]. Thirdly, hexafluoroaluminates are already produced worldwide on a large scale as they are used as solvents for bauxite in the industrial extraction of aluminum [26]. This may facilitate cheap large scale production of Mn^{4+} -activated hexafluoroaluminates.

Until now, different methods have been used to synthesize M₃AlF₆:Mn⁴⁺ phosphors. Song et al. prepared Na₃AlF₆:Mn⁴⁺ phosphors via a co-precipitation method [17], while others synthesized K₃AlF₆:Mn⁴⁺ and K₂NaAlF₆:Mn⁴⁺ by cation exchange [18,19]. Furthermore, K₂LiAlF₆:Mn⁴⁺ was synthesized via a hydrothermal method [20]. A single convenient synthesis method to prepare M₃AlF₆:Mn⁴⁺ phosphors is thus so far lacking. The previous works on M₃AlF₆:Mn⁴⁺ have reported luminescence spectra and decay curves for different Mn⁴⁺ doping concentrations in the temperature range of 300 to 500 K [17–20]. They however provided no insight in the influence of (charge compensating) defects on the luminescence spectra and quantum efficiency of M₃AlF₆:Mn⁴⁺. Furthermore, no explanations for the thermal quenching of the Mn⁴⁺ luminescence were given.

In this chapter we report a new synthesis route for Na₃AlF₆:Mn⁴⁺, K₃AlF₆:Mn⁴⁺ and K₂NaAlF₆:Mn⁴⁺ based on a simple two-step co-precipitation method. We synthesize Mn⁴⁺-doped hexafluoroaluminates by initially preparing the Mn⁴⁺-precursor K₂MnF₆ and then in a second step precipitating M₃AlF₆:Mn⁴⁺ (M = Na, K) from an aqueous HF solution containing Al³⁺, Mn⁴⁺ and Na⁺/K⁺ ions. The presented method gives good control over the composition and homogeneity of the M₃AlF₆:Mn⁴⁺ phosphors. All synthesized M₃AlF₆:Mn⁴⁺ phosphors exhibit bright red Mn⁴⁺ luminescence around 620 nm. For K₂NaAlF₆:Mn⁴⁺ we obtain highly monodisperse and large (~20 μm) phosphor particles that exhibit narrow size and shape distributions that are superior to the size and shape distributions of other reported Mn⁴⁺-doped phosphors. This makes K₂NaAlF₆:Mn⁴⁺ interesting for use in w-LEDs as monodisperse, uniform and large particles are favorable for reproducible and high packing density of phosphors in w-LEDs.

We perform both room-temperature and low-temperature ($T = 4$ K) spectral measurements of M₃AlF₆:Mn⁴⁺. The measurements at 4 K reveal that multiple Mn⁴⁺ sites exist in M₃AlF₆:Mn⁴⁺, which was not observed in previous works on Mn⁴⁺-doped hexafluoroaluminates. The formation of multiple Mn⁴⁺ sites can be understood from the need for charge compensation for Mn⁴⁺ ions on an Al³⁺ site. Further evidence for the presence of multiple sites is obtained from thermal cycling experiments which show a change in site distribution after high temperature annealing. The charge compensation and associated defects have a large influence on the luminescence properties (e.g. quantum efficiency) of M₃AlF₆:Mn⁴⁺.

Finally, we study the thermal quenching behavior for M₃AlF₆:Mn⁴⁺ by measuring the luminescence intensity as a function of temperature between 300 and 600 K. The luminescence quenching temperature we find for M₃AlF₆:Mn⁴⁺ is 460–490 K, which is above the operating temperature of phosphors in high power w-LEDs. The thermal quenching is explained by thermally activated crossover from the ⁴T₂ excited state to the ⁴A₂ ground state. Furthermore, there is luminescence quenching due to non-radiative energy transfer from Mn⁴⁺ ions to quenching sites (defects and impurities).

3.2 Methods

The $M_3AlF_6:Mn^{4+}$ ($M = Na, K$) phosphors were synthesized through a two-step chemical co-precipitation method. In the first step the Mn^{4+} -precursor K_2MnF_6 was synthesized and in the second step the $M_3AlF_6:Mn^{4+}$ phosphor was prepared. Since K_2MnF_6 and $M_3AlF_6:Mn^{4+}$ are synthesized in corrosive HF solutions, all reactions described were carried out in plastic or Teflon beakers.

3.2.1 Chemicals

The following chemicals were purchased from Sigma-Aldrich: $KMnO_4$ ($\geq 99.0\%$), KF ($\geq 99.0\%$), H_2O_2 (30 wt% solution, ACS reagent), $Al(OH)_3$ (reagent grade), Na_2CO_3 ($\geq 99.95\%$) and K_2CO_3 ($\geq 99.0\%$). Hydrofluoric acid (HF, 40% aqueous solution) was purchased from Riedel de Haën. All chemicals were used without any further purification.

3.2.2 Synthesis of K_2MnF_6

K_2MnF_6 was prepared according to the method of Bode [27,28]. $KMnO_4$ (4 g) and KF (59.5 g) were dissolved in 250 mL of a 40% HF solution. The black-purple solution obtained was stirred for 30 min and then cooled with an ice bath. Under constant cooling and stirring, a 30 wt% H_2O_2 solution was added dropwise which resulted in the gradual precipitation of yellow K_2MnF_6 powder. The dropwise addition of H_2O_2 was stopped when the reaction solution turned from purple to red-brown, indicating the formation of Mn^{4+} . The K_2MnF_6 product was isolated by decanting the red-brown solution, washing the precipitate twice with 100 mL of acetone and finally drying the precipitate at 60 °C for 5 h.

3.2.3 Synthesis of $M_3AlF_6:Mn^{4+}$

$Al(OH)_3$ (10 mmol, 0.78 g) was dissolved in 15 mL 40% HF by stirring and heating at 60 °C. After cooling down to room temperature, 0.1 mmol K_2MnF_6 (1 mol% doping concentration) was added. Simultaneously, a solution of M^+ ions ($M = Na, K$) in 40% HF was prepared by gradually adding M_2CO_3 or MF to 40% HF (aq) while stirring. Table 3.1 lists the amounts of Na_2CO_3 , K_2CO_3 , KF and 40% HF used for preparing the M^+/HF solutions. The M^+/HF solution was added to the $Al^{3+}/Mn^{4+}/HF$ solution, which resulted in the precipitation of $Na_3AlF_6:Mn^{4+}$ and $K_2NaAlF_6:Mn^{4+}$ but not $K_3AlF_6:Mn^{4+}$

Table 3.1 – Amounts of Na_2CO_3 , K_2CO_3 , KF and 40% HF (aq) used in the synthesis of $M_3AlF_6:Mn^{4+}$ ($M = Na, K$). *A 4:1 ratio of K:Al was used as this gave K_3AlF_6 without impurity phases. With a 3:1 ratio the obtained phosphor contained impurities of other crystal phases.

Phosphor	Na_2CO_3	K_2CO_3	KF	40% HF
$Na_3AlF_6:Mn^{4+}$	15 mmol	-	-	15 mL
$K_2NaAlF_6:Mn^{4+}$	5 mmol	10 mmol	-	15 mL
$K_3AlF_6:Mn^{4+}$	-	-	40 mmol*	3 mL

phosphor. K₃AlF₆:Mn⁴⁺ was precipitated by adding 50 mL of ethanol to the mixed M⁺/Al³⁺/Mn⁴⁺/HF solution (ethanol acts as anti-solvent). The synthesized phosphors were isolated by decanting the solution, washing the precipitate twice with ethanol and subsequently drying at 75 °C for 3 h. Different Mn⁴⁺ doping concentrations could be obtained by changing the amount of K₂MnF₆ that was used in the synthesis.

3.2.4 Characterization

Powder X-ray diffraction (XRD) patterns were measured on a Philips PW1729 X-ray diffractometer using Cu K_α radiation ($\lambda = 1.5418 \text{ \AA}$). Scanning electron microscopy (SEM) images of the phosphors were obtained using a Philips XL30S FEG microscope operating at 20 keV. The manganese concentrations in the phosphors were determined with inductively coupled plasma optical emission spectroscopy (ICP-OES) performed on a Perkin-Elmer Optima 8300DV spectrometer. For the ICP-OES measurements the M₃AlF₆:Mn⁴⁺ phosphors were dissolved in aqua regia.

Photoluminescence (PL) measurements were performed on an Edinburgh Instruments FLS900 fluorescence spectrometer equipped with a double 0.22 m excitation monochromator. For recording emission and excitation spectra, we used a 450 W Xe lamp as excitation source and a Hamamatsu R928 photomultiplier tube (PMT) to detect the emission. For PL measurements down to 4 K, the phosphors were cooled in an Oxford Instruments liquid helium flow cryostat. PL measurements between 300 and 600 K were performed by heating the phosphors with a Linkam THMS600 temperature controlled stage. PL quantum efficiencies were determined with a calibrated home-built setup which consisted of a 65 W Xe lamp, excitation monochromator, integrating sphere (Labsphere) and CCD camera (Avantes AvaSpec-2048).

3.3 Results and discussion

3.3.1 Structural properties

To investigate the composition, size and shape of the M₃AlF₆:Mn⁴⁺ (M = Na, K) phosphor particles, we used different characterization techniques such as powder X-ray diffraction (XRD), scanning electron microscopy (SEM) and inductively-coupled plasma optical emission spectroscopy (ICP-OES). Figure 3.1 shows XRD patterns of the M₃AlF₆:Mn⁴⁺ phosphors. The XRD patterns are in perfect agreement with the reference patterns for Na₃AlF₆ (PDF 00-025-0772, red), K₂NaAlF₆ (PDF 01-072-2434, blue) and K₃AlF₆ (PDF 00-057-0227, green). No other crystal phases are observed, which confirms that the phosphor samples are single phase.

The XRD measurements show that incorporation of Mn⁴⁺ on the Al³⁺ sites does not significantly change the crystal structure of M₃AlF₆, which is expected as the ionic radii of Mn⁴⁺ and Al³⁺ are similar (0.53 versus 0.535 Å) [21]. The space groups of Na₃AlF₆, K₂NaAlF₆ and K₃AlF₆ are listed in Table 3.2. K₂NaAlF₆ has a highly symmetric cubic

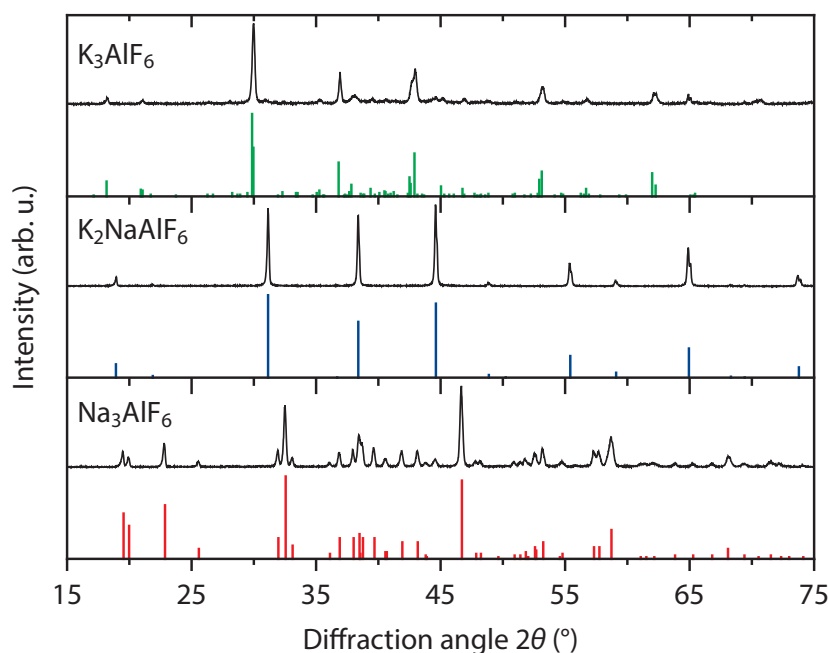


Figure 3.1 – Powder X-ray diffraction (XRD) patterns of $M_3AlF_6:Mn^{4+}$ ($M = Na, K$). The XRD patterns of the synthesized phosphors are in excellent agreement with the reference patterns for Na_3AlF_6 (PDF 00-025-0772, red), K_2NaAlF_6 (PDF 01-072-2434, blue) and K_3AlF_6 (PDF 00-057-0227, green).

crystal structure (space group is $Fm\bar{3}m$), while Na_3AlF_6 and K_3AlF_6 have a crystal structure with lower symmetry (space groups are $P2_1/n$ and $I4_1/a$, respectively) [29–31]. In the M_3AlF_6 crystal structure, the Al^{3+} ions are octahedrally coordinated by six F^- ions. Depending on the M_3AlF_6 lattice, the AlF_6 octahedron can be highly symmetric (O_h in K_2NaAlF_6) or distorted (C_i in Na_3AlF_6 and C_1 in K_3AlF_6). The average Al–F distances in the AlF_6 octahedra are around 1.8 Å.

By using ICP-OES, we measured the manganese concentrations in the synthesized $M_3AlF_6:Mn^{4+}$ phosphors (see Section 3.2.4). The XRD patterns displayed in Figure 3.1 were measured for $M_3AlF_6:Mn^{4+}$ phosphors containing 0.4 mol% ($Na_3AlF_6:Mn^{4+}$), 1.2 mol% ($K_3AlF_6:Mn^{4+}$) and 0.9 mol% Mn ($K_2NaAlF_6:Mn^{4+}$). The results presented in the rest of this chapter were obtained for $M_3AlF_6:Mn^{4+}$ phosphors having these doping

Table 3.2 – Space group, Al^{3+} site symmetry and average Al–F distance for M_3AlF_6 ($M = Na, K$); zero-phonon line (ZPL) energy of the $Mn^{4+} {}^2E \rightarrow {}^4A_2$ emission in $M_3AlF_6:Mn^{4+}$. Structural data obtained from Refs. [29–31].

Lattice	Space group	Al^{3+} symmetry	Al–F distance (Å)	ZPL energy (cm^{-1})
Na_3AlF_6	$P2_1/n$	C_i	1.808	16167
K_2NaAlF_6	$Fm\bar{3}m$	O_h	1.778	16082
K_3AlF_6	$I4_1/a$	C_1	1.810	16200

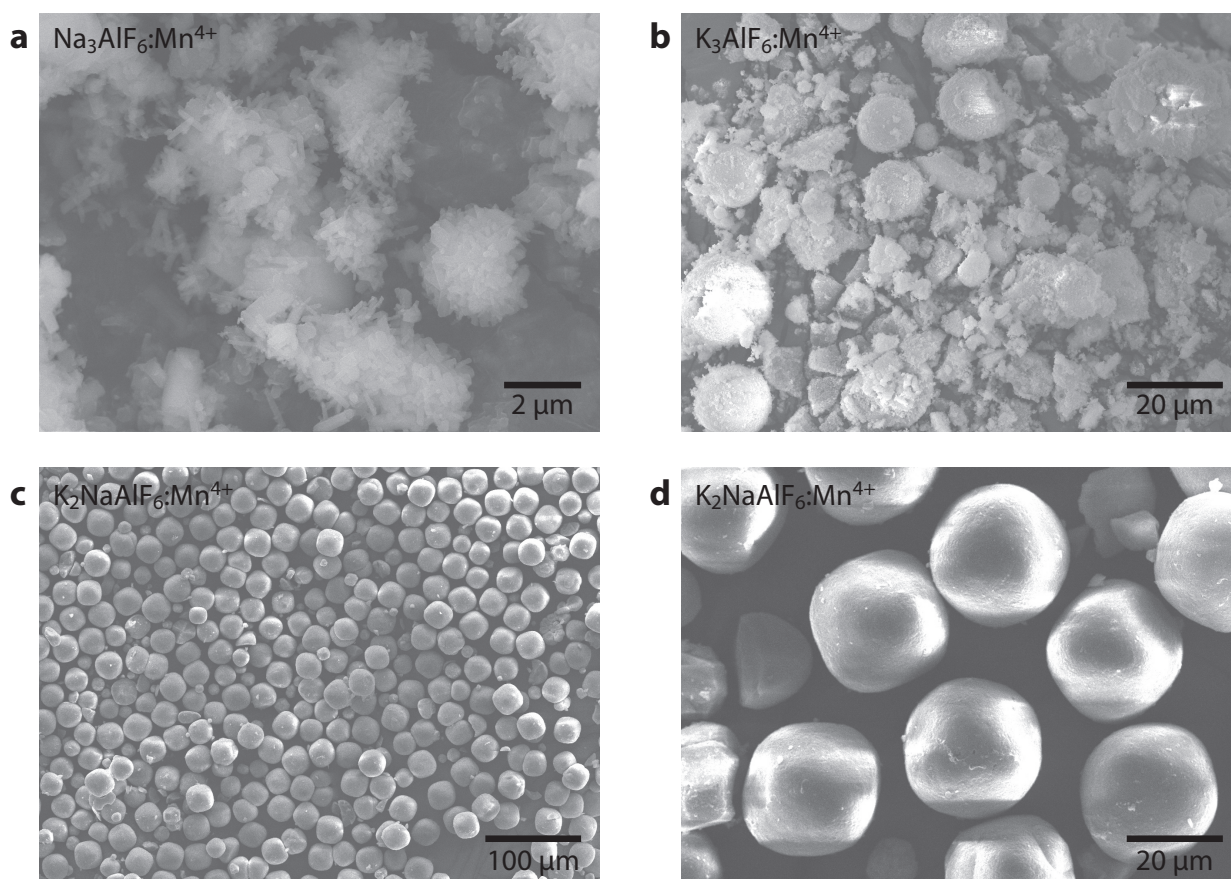


Figure 3.2 – Representative scanning electron microscopy (SEM) images of (a) Na₃AlF₆:Mn⁴⁺ (0.4%) phosphor particles, (b) K₃AlF₆:Mn⁴⁺ (1.2%) phosphor particles and (c,d) K₂NaAlF₆:Mn⁴⁺ (0.9%) phosphor particles.

concentrations. For K₃AlF₆:Mn⁴⁺ and K₂NaAlF₆:Mn⁴⁺ the measured Mn concentration is very close to the 1 mol% Mn added during the synthesis, which demonstrates that our synthesis method provides good control over the Mn⁴⁺ doping concentration. Also a substantially higher fraction of Mn⁴⁺ is incorporated into K₃AlF₆ compared to previously reported cation exchange methods for preparing K₃AlF₆:Mn⁴⁺ [18].

Figure 3.2 displays SEM images of Na₃AlF₆:Mn⁴⁺ (0.4%), K₃AlF₆:Mn⁴⁺ (1.2%) and K₂NaAlF₆:Mn⁴⁺ (0.9%) phosphor particles. The Na₃AlF₆:Mn⁴⁺ (Figure 3.2a) and K₃AlF₆:Mn⁴⁺ (Figure 3.2b) phosphors consist of irregularly shaped particles and clusters of particles with sizes ranging from ~100 nm to >10 μm. For K₃AlF₆:Mn⁴⁺ we attribute the large variety in shape and size to the rapid and forced crystallization following addition of the anti-solvent ethanol. In contrast, the synthesis of K₂NaAlF₆:Mn⁴⁺ (Figure 3.2c,d) yields highly monodisperse phosphor particles with a large average diameter of 22.5±6.1 μm. The K₂NaAlF₆:Mn⁴⁺ particles have a smoothed octahedral shape, as expected from the cubic elpasolite structure of K₂NaAlF₆ [10,19,29]. The K₂NaAlF₆:Mn⁴⁺ particles prepared with our co-precipitation method have a more uniform shape and size than

the $\text{K}_2\text{NaAlF}_6:\text{Mn}^{4+}$ particles prepared by Zhu et al. via cation exchange [19]. Moreover, the $\text{K}_2\text{NaAlF}_6:\text{Mn}^{4+}$ (0.9%) phosphor shown in Figure 3.2c,d exhibits particle size and shape distributions that are superior to the size and shape distributions of other reported Mn^{4+} -doped fluoride phosphors [10,24,32–37].

The high monodispersity of the $\text{K}_2\text{NaAlF}_6:\text{Mn}^{4+}$ crystallites reported here may originate from the synthesis method used. In order to achieve a narrow size distribution it is necessary to temporally separate the particle nucleation and growth stages [38]. As described in Section 3.2.3, we dissolve all the starting materials in HF solutions prior the formation of the phosphor particles. Mixing of the precursor solutions results in oversaturation and a rapid formation of crystal nuclei. Once the nuclei have been formed, the precursor concentrations drop and no new nuclei are formed. The particles can grow to monodisperse and large crystallites during the growth stage. This differs from syntheses where Mn^{4+} -doped particles are prepared via cation exchange or chemical etching [14]. With these methods, new precursor ions are constantly supplied to the reaction solution preventing temporal separation of nucleation and growth.

The superior size distribution gives $\text{K}_2\text{NaAlF}_6:\text{Mn}^{4+}$ potential advantages in LED applications. Monodisperse crystallites are favorable for uniform and reproducible packing of phosphors which is very important in the production of w-LEDs. In addition, phosphors with large and highly crystalline particles often display higher quantum efficiencies because of reduced concentrations of defects which act as quenching sites. Finally, a large particle size aids the long-term stability of a phosphor.

3.3.2 Mn^{4+} luminescence

Figure 3.3 shows the room-temperature emission and excitation spectra of $\text{M}_3\text{AlF}_6:\text{Mn}^{4+}$ ($\text{M} = \text{Na}, \text{K}$). Upon blue photoexcitation the Mn^{4+} -doped hexafluoroaluminates show narrow red emission lines around 620 nm (see Figure 3.3a). The emission lines are in a spectral range where the eye sensitivity is still relatively high, which is beneficial for applications. The red emission lines are assigned to spin- and parity-forbidden Mn^{4+} ${}^2\text{E} \rightarrow {}^4\text{A}_2$ transitions. Figure 3.3b shows that the red luminescence of $\text{M}_3\text{AlF}_6:\text{Mn}^{4+}$ has two broad excitation bands in the UV to blue spectral region. These bands correspond to the ${}^4\text{A}_2 \rightarrow {}^4\text{T}_1$ and ${}^4\text{A}_2 \rightarrow {}^4\text{T}_2$ transitions of Mn^{4+} . In all three lattices the ${}^4\text{A}_2 \rightarrow {}^4\text{T}_2$ excitation band is positioned at 460 nm, which indicates that the crystal field splitting is approximately equal for the investigated M_3AlF_6 hosts.

The emission spectra of $\text{M}_3\text{AlF}_6:\text{Mn}^{4+}$ in Figure 3.3a resemble the emission spectra observed for other Mn^{4+} -doped fluoride phosphors [33,39,40]. In analogy, the ${}^2\text{E} \rightarrow {}^4\text{A}_2$ emission spectra of $\text{M}_3\text{AlF}_6:\text{Mn}^{4+}$ consist of a zero-phonon line (ZPL) at ~620 nm and anti-Stokes and Stokes vibronic (ν_3 , ν_4 and ν_6) lines on the high and low energy side of the ZPL, respectively [39]. The Mn^{4+} emission spectra are dominated by vibronic lines because the parity selection rule is relaxed by coupling of the ${}^2\text{E} \rightarrow {}^4\text{A}_2$ electronic

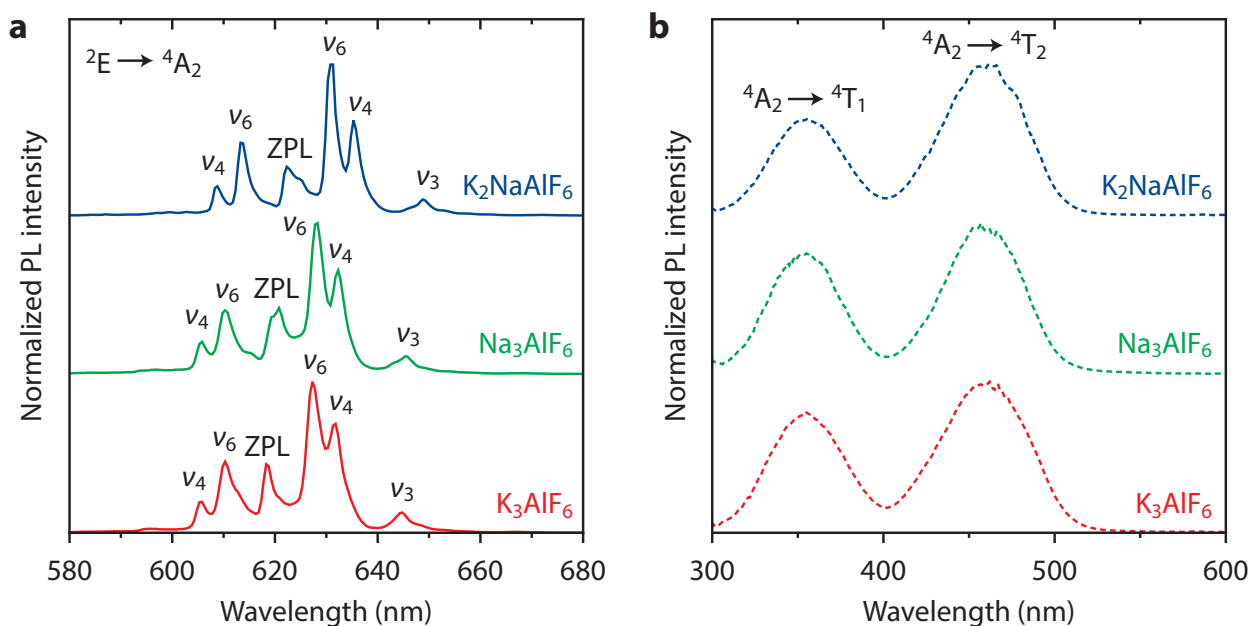


Figure 3.3 – Room-temperature luminescence spectra of $M_3AlF_6:Mn^{4+}$ ($M = Na, K$) phosphors. (a) Emission spectra ($\lambda_{exc} = 460$ nm) of $K_3AlF_6:Mn^{4+}$ (1.2%) (red), $Na_3AlF_6:Mn^{4+}$ (0.4%) (green) and $K_2NaAlF_6:Mn^{4+}$ (0.9%) (blue). The Mn^{4+} emission spectra consist of zero-phonon (ZPL) and (anti-)Stokes vibronic (ν_i) ${}^2E \rightarrow {}^4A_2$ emission lines. (b) Excitation spectra of $K_3AlF_6:Mn^{4+}$ (1.2%) (red, $\lambda_{em} = 628$ nm), $Na_3AlF_6:Mn^{4+}$ (0.4%) (green, $\lambda_{em} = 628$ nm) and $K_2NaAlF_6:Mn^{4+}$ (0.9%) (blue, $\lambda_{em} = 631$ nm). The broad excitation bands correspond to the Mn^{4+} ${}^4A_2 \rightarrow {}^4T_1$ and ${}^4A_2 \rightarrow {}^4T_2$ transitions.

transition with odd-parity vibrations (ν_3 , ν_4 and ν_6 vibrational modes) [39,41]. It is noted that the ${}^2E \rightarrow {}^4A_2$ ZPL intensity of $M_3AlF_6:Mn^{4+}$ is relatively strong when compared to other Mn^{4+} -doped fluorides. For example, in $K_2SiF_6:Mn^{4+}$ the ZPL intensity is less than 5% of the Stokes ν_6 intensity, while in $K_3AlF_6:Mn^{4+}$ the ZPL intensity is almost half of the Stokes ν_6 intensity [40]. The intense ZPL is an interesting property for (w-LED) applications, as it improves the color quality of the red Mn^{4+} phosphor. Furthermore, the observation of relatively strong zero-phonon lines is a sign that the MnF_6 centers lack inversion symmetry. The presence of odd-parity crystal field components relaxes the parity selection rule by inducing mixing with opposite parity states. As a result, the radiative lifetime of the ${}^2E \rightarrow {}^4A_2$ emission is shorter (which is beneficial to reduce saturation effects) and the ${}^4A_2 \rightarrow {}^4T_2$ absorption is stronger (and thus less material or a lower Mn^{4+} concentration is needed to absorb the desired fraction of blue LED light).

The strong ZPL intensity in $K_3AlF_6:Mn^{4+}$ can be attributed to the low symmetry for Mn^{4+} on the Al^{3+} sites, i.e. the AlF_6 octahedron lacks an inversion center (C_1 symmetry, see Table 3.2). As discussed, without inversion symmetry, the ${}^2E \rightarrow {}^4A_2$ ZPL intensity increases due to relaxation of the parity selection rule by odd-parity crystal field components that mix odd-parity states into the 3d wavefunctions [42]. In Na_3AlF_6 and K_2NaAlF_6 the AlF_6 octahedra have inversion centers (C_i and O_h symmetry, respectively) and the ${}^2E \rightarrow {}^4A_2$ ZPL is expected to be weak, since there are no odd-parity crystal

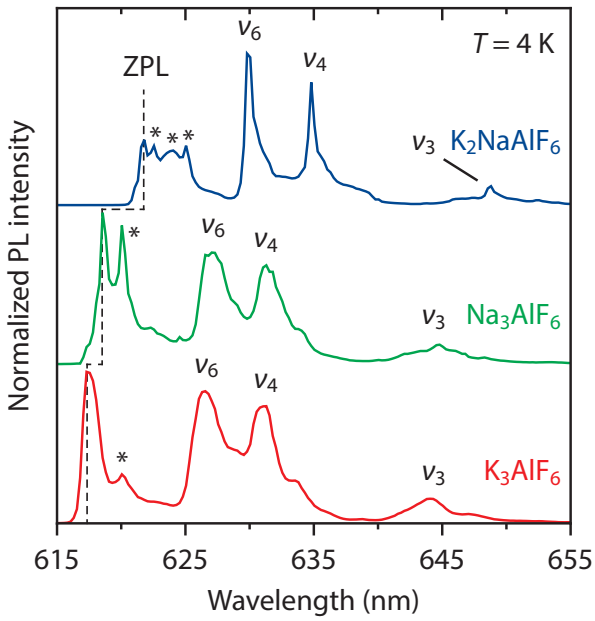


Figure 3.4 – Emission spectra of $\text{K}_3\text{AlF}_6:\text{Mn}^{4+}$ (1.2%) (red), $\text{Na}_3\text{AlF}_6:\text{Mn}^{4+}$ (0.4%) (green) and $\text{K}_2\text{NaAlF}_6:\text{Mn}^{4+}$ (0.9%) (blue) at $T = 4$ K. The excitation wavelength is 460 nm. Labels are assigned to the highest energy zero-phonon line (ZPL) and vibronic ${}^2\text{E} \rightarrow {}^4\text{A}_2$ emissions (v_3 , v_4 and v_6). The stars mark lines assigned to ZPLs of other Mn^{4+} sites (see text).

field components to relax the parity selection rule. The emission spectra in Figure 3.3a however show that the ZPLs of $\text{Na}_3\text{AlF}_6:\text{Mn}^{4+}$ and $\text{K}_2\text{NaAlF}_6:\text{Mn}^{4+}$ are significant, which indicates that at least for a part of the Mn^{4+} ions the site symmetry is lower than C_i (no inversion symmetry). This we explain by the charge compensation required for the $\text{Mn}_{\text{Al}}^\bullet$ sites (the Kröger–Vink notation is used to identify defects). The proximity of charge compensating defects (probably $\text{V}_{\text{K,Na}}'$ vacancies or F_i' interstitials) gives rise to local deformation of the MnF_6 octahedra and lifts the inversion symmetry, causing the ${}^2\text{E} \rightarrow {}^4\text{A}_2$ ZPL intensity of $\text{Na}_3\text{AlF}_6:\text{Mn}^{4+}$ and $\text{K}_2\text{NaAlF}_6:\text{Mn}^{4+}$ to increase.

Besides influencing the ${}^2\text{E} \rightarrow {}^4\text{A}_2$ ZPL intensity, the charge compensating defects have a large influence on the integrated luminescence intensity and emission lifetime of $\text{M}_3\text{AlF}_6:\text{Mn}^{4+}$. The synthesized $\text{M}_3\text{AlF}_6:\text{Mn}^{4+}$ phosphors exhibit a luminescence quantum efficiency (QE) of 20 to 55%. These QE values are below unity, which is attributed to non-radiative transfer of excitation energy from Mn^{4+} to crystal defects. At the defects the excitation energy is lost non-radiatively as heat, i.e. the defects act as quenching sites. The defect concentration will increase with the Mn^{4+} concentration, and it is therefore expected that the luminescence quenching becomes stronger at higher Mn^{4+} concentrations. Previously it was measured that the luminescence intensity and emission lifetime of $\text{M}_3\text{AlF}_6:\text{Mn}^{4+}$ significantly decrease with increasing Mn^{4+} concentration already at doping levels of 4% Mn^{4+} [17–19]. In these works, the decrease in intensity and lifetime with the Mn^{4+} concentration was explained by concentration quenching, i.e. energy migration between Mn^{4+} ions to quenchers (defects, impurities). Energy migration is however not expected at doping concentrations of 4%, as most Mn^{4+} ions will not have Mn^{4+} neighbors in this concentration range. The results presented here indicate that quenching becomes stronger due to an increase in the defect concentration

connected to the need for charge compensation and not because of enhanced energy migration among the Mn⁴⁺ ions.

We have performed low-temperature ($T = 4$ K) spectral measurements to get more insight in the Mn⁴⁺ sites in M₃AlF₆:Mn⁴⁺. In addition, the measurements at 4 K allow us to accurately compare the energy of the emitting ²E level in the different M₃AlF₆ hosts. Figure 3.4 displays emission spectra ($\lambda_{\text{exc}} = 460$ nm) at $T = 4$ K of M₃AlF₆:Mn⁴⁺. In line with the luminescence spectra at room temperature, the 4 K emission spectra of M₃AlF₆:Mn⁴⁺ consist of zero-phonon and vibronic ²E → ⁴A₂ emission lines (labeled ZPL, ν_3 , ν_4 and ν_6). Multiple lines are observed in the ZPL region. The peaks marked with a star can be due to ²E → ⁴A₂ electronic transitions that couple with low energy rotatory or translatory lattice vibrational modes [40,43]. Vibronic lines due to these modes are usually found at 50–150 cm⁻¹ relative to the ZPL in emission spectra of Mn⁴⁺. Alternatively, the peaks marked with a star can be ZPLs of Mn⁴⁺ ions located on different sites than the Mn⁴⁺ ions yielding the most intense zero-phonon emission line (labeled ZPL in Figure 3.4). Mn⁴⁺ emission lines caused by lattice modes are typically very weak and therefore it is more probable that the peaks marked with stars are ZPLs of Mn⁴⁺ ions with other geometric environments [33,43]. In addition, multiple Mn⁴⁺ sites can be expected based on the need for charge compensation. Below further evidence is given which indicates that the various sharp emission lines around 620 nm arise from differently charge compensated Mn⁴⁺ sites.

In Figure 3.5 we investigate the presence of multiple Mn⁴⁺ sites by measuring 4 K luminescence spectra of K₂NaAlF₆:Mn⁴⁺ for various excitation and emission wavelengths. The excitation spectra in Figure 3.5a show that the structure in the ⁴A₂ → ⁴T₂ excitation band of K₂NaAlF₆:Mn⁴⁺ changes significantly with emission wavelength. If only one Mn⁴⁺ site would be present in K₂NaAlF₆:Mn⁴⁺, the excitation spectrum will have the same shape and structure for all emission wavelengths. However, here the excitation spectrum changes significantly with emission wavelength, which indicates that more than one Mn⁴⁺ site is present in K₂NaAlF₆:Mn⁴⁺. Furthermore, the spectra in Figure 3.5b show that the shape of the ²E → ⁴A₂ spectrum is different for various excitation wavelengths within the ⁴A₂ → ⁴T₂ band. This confirms that multiple Mn⁴⁺ sites exist in K₂NaAlF₆:Mn⁴⁺, and likely also in K₃AlF₆:Mn⁴⁺ and Na₃AlF₆:Mn⁴⁺.

The presence of more than one Mn⁴⁺ site in M₃AlF₆:Mn⁴⁺ was not observed in previous reports on Mn⁴⁺-doped hexafluoroaluminates [17,18]. Instead, from time-resolved measurements it was concluded that only one Mn⁴⁺ emission site was present in M₃AlF₆:Mn⁴⁺. The formation of geometrically different Mn⁴⁺ sites in M₃AlF₆:Mn⁴⁺ is expected as charge compensation is required for the Mn_{Al}[•] center. The charge compensating defect can be local or distant, i.e. in the first shell of cations around the Mn⁴⁺ ion or further away in the lattice. A distant defect will not influence the local geometry around the Mn⁴⁺ ion, whereas a local defect can cause a deformation of the

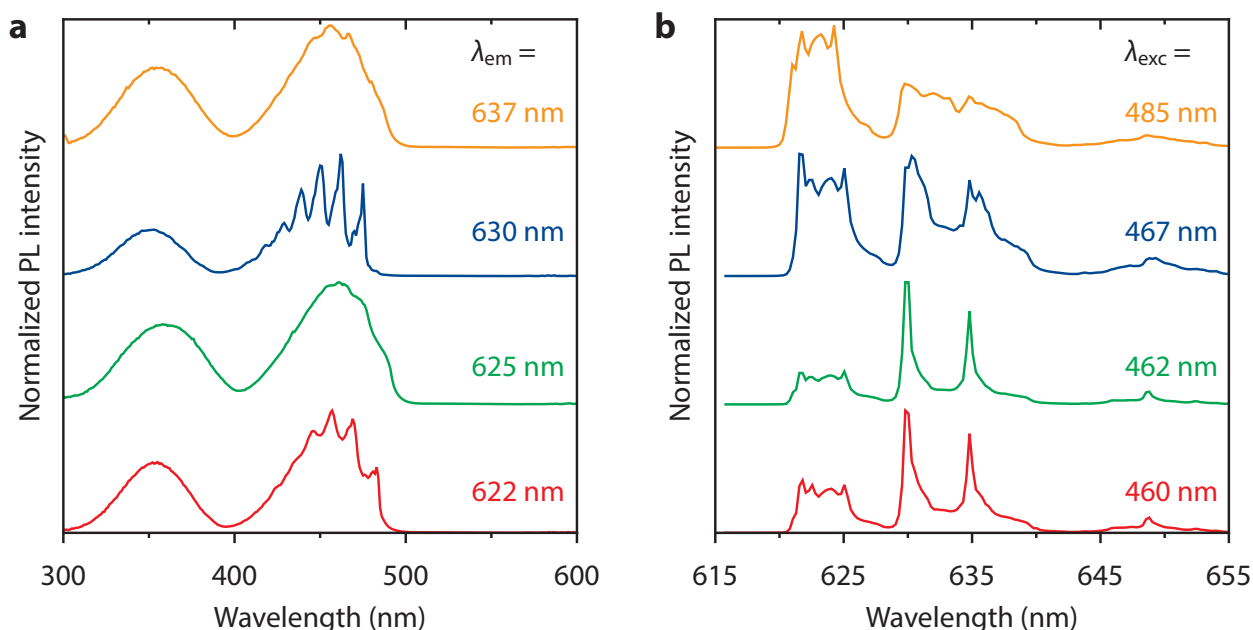


Figure 3.5 – Emission and excitation spectra of $\text{K}_2\text{NaAlF}_6:\text{Mn}^{4+}$ (0.9%) at $T = 4$ K. (a) Excitation spectra for $\lambda_{\text{em}} = 622$ nm (red), 625 nm (green), 630 nm (blue) and 637 nm (orange). (b) Emission spectra for $\lambda_{\text{exc}} = 460$ nm (red), 462 nm (green), 467 nm (blue) and 485 nm (orange).

fluorine octahedron around the Mn^{4+} ion and give rise to multiple differently charge compensated Mn^{4+} sites within the lattice depending on the type and local geometry of charge compensation.

To study the influence of the M_3AlF_6 ($M = \text{Na}, \text{K}$) host on the energy of the $\text{Mn}^{4+} {}^2\text{E}$ level, we compare the positions of the highest-energy ${}^2\text{E} \rightarrow {}^4\text{A}_2$ ZPLs in $\text{M}_3\text{AlF}_6:\text{Mn}^{4+}$. The energies of these ZPLs (labeled ZPL in Figure 3.4) are 16200 cm^{-1} ($\text{K}_3\text{AlF}_6:\text{Mn}^{4+}$), 16167 cm^{-1} ($\text{Na}_3\text{AlF}_6:\text{Mn}^{4+}$) and 16082 cm^{-1} ($\text{K}_2\text{NaAlF}_6:\text{Mn}^{4+}$). The ${}^2\text{E}$ level energies are also listed in Table 3.2. The energy of the ${}^2\text{E}$ level for Mn^{4+} in M_3AlF_6 is in good agreement with the ${}^2\text{E}$ level energy observed for Mn^{4+} in other fluoride hosts [44,45]. Furthermore, it is observed that the energy of the $\text{Mn}^{4+} {}^2\text{E}$ level increases from K_2NaAlF_6 to Na_3AlF_6 to K_3AlF_6 (see dashed line in Figure 3.4). This indicates that the local structure and type of M^+ cation in the second coordination sphere around the Mn^{4+} ion has an influence on the ${}^2\text{E}$ level energy. Previous studies on $\text{M}_2\text{SiF}_6:\text{Mn}^{4+}$ ($M = \text{Na}, \text{K}, \text{Rb}$ or Cs) also show an influence of the M^+ cation on the ${}^2\text{E}$ level energy [33,40,43]. In these compounds the energy E of the ${}^2\text{E}$ level follows the trend $E(\text{Na}^+) > E(\text{K}^+) > E(\text{Rb}^+) > E(\text{Cs}^+)$, which suggests that the ${}^2\text{E}$ level energy decreases with e.g. the radius or electron affinity of the M^+ ion [21]. This is however not confirmed by our results for the $\text{M}_3\text{AlF}_6:\text{Mn}^{4+}$ phosphors, where the highest ${}^2\text{E}$ energy is found for $\text{K}_3\text{AlF}_6:\text{Mn}^{4+}$. Instead, the results in Table 3.2 indicate that the energy of the ${}^2\text{E}$ level increases when the Mn–F (Al–F) distance becomes longer or when the symmetry of the Mn^{4+} site (Al^{3+} site) reduces. It is however not possible to draw definite conclusions from the data in Table 3.2 as the symmetry and

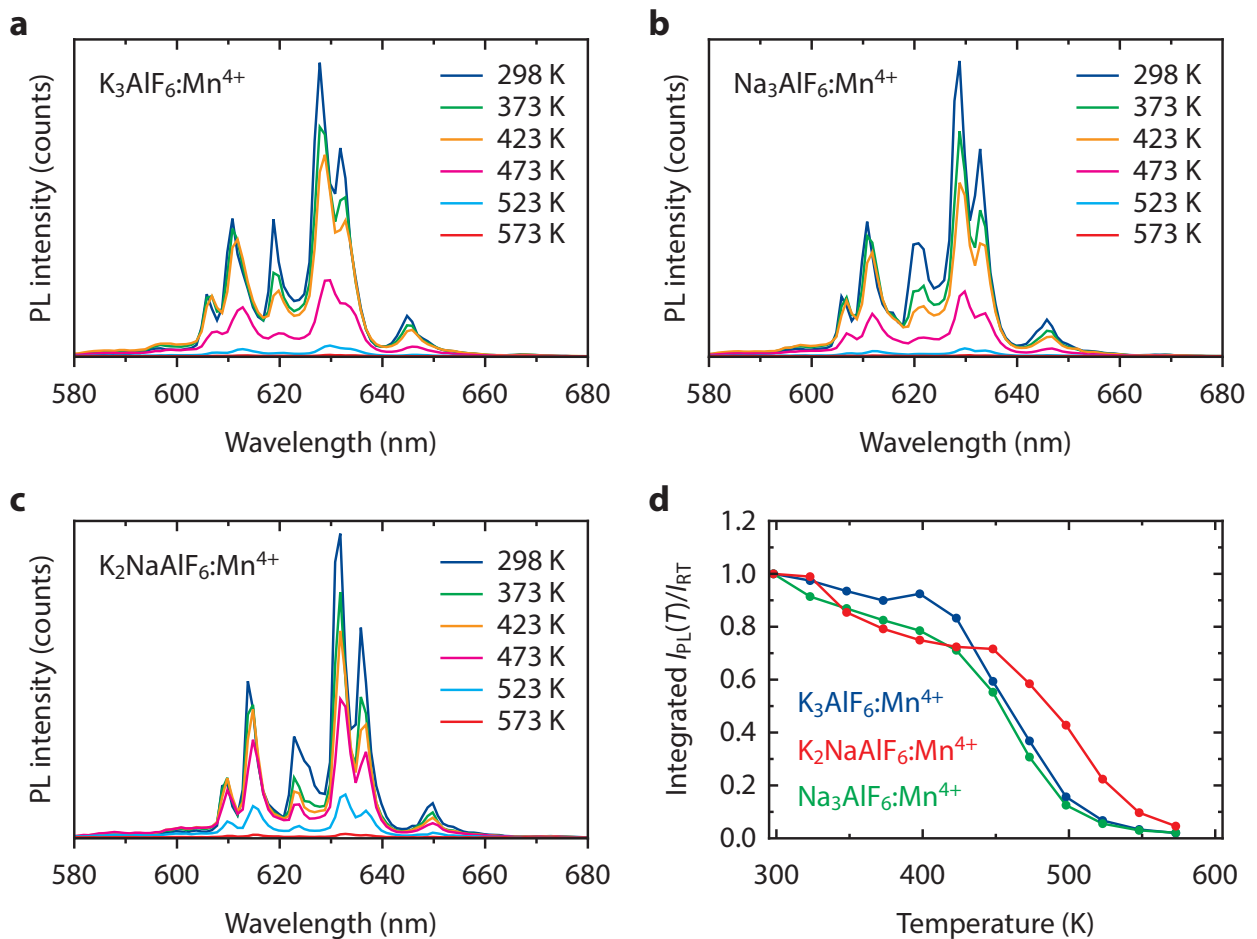


Figure 3.6 – (a–c) Emission spectra of (a) $K_3AlF_6:Mn^{4+}$ (1.2%), (b) $Na_3AlF_6:Mn^{4+}$ (0.4%) and (c) $K_2NaAlF_6:Mn^{4+}$ (0.9%) at various temperatures between 298 and 573 K ($\lambda_{exc} = 450$ nm). (d) Integrated PL intensity of $K_3AlF_6:Mn^{4+}$ (1.2%) (blue), $Na_3AlF_6:Mn^{4+}$ (0.4%) (green) and $K_2NaAlF_6:Mn^{4+}$ (0.9%) (red) as a function of temperature between 300 and 600 K. The integrated PL intensity I_{PL} is scaled to the integrated PL intensity at room temperature I_{RT} .

distances in (part of) the MnF_6 octahedra will change due to deformations caused by nearby charge compensating defects.

3.3.3 Thermal quenching in $M_3AlF_6:Mn^{4+}$

For high power w-LED applications the thermal quenching behavior of a phosphor is very important, as the temperature of the on-chip phosphor layer in a high power w-LED reaches temperatures as high as 450 K. The thermal quenching behavior of $K_3AlF_6:Mn^{4+}$ and $Na_3AlF_6:Mn^{4+}$ has been investigated by Song et al. [17,18]. They reported that thermal quenching sets in around 423 K (150 °C) for $K_3AlF_6:Mn^{4+}$ and $Na_3AlF_6:Mn^{4+}$. More interestingly, they found that the integrated photoluminescence (PL) intensity of these phosphors doubles between room temperature and 423 K. This is a very useful property for high temperature applications, but also very unexpected. For most Mn^{4+} -doped fluorides the PL intensity is relatively constant between room temperature and

the temperature at which thermal quenching sets in [8–10].

To investigate the thermal quenching of the Mn^{4+} emission in $\text{M}_3\text{AlF}_6:\text{Mn}^{4+}$ ($\text{M} = \text{Na}, \text{K}$), we measure the integrated PL intensity of $\text{M}_3\text{AlF}_6:\text{Mn}^{4+}$ as a function of temperature between 298 and 600 K. Figure 3.6a shows emission spectra of $\text{K}_3\text{AlF}_6:\text{Mn}^{4+}$ recorded in this temperature range. Emission spectra of $\text{Na}_3\text{AlF}_6:\text{Mn}^{4+}$ and $\text{K}_2\text{NaAlF}_6:\text{Mn}^{4+}$ between 298 and 600 K can be found in Figure 3.6b and 3.6c, respectively. The results show that the PL intensity of $\text{M}_3\text{AlF}_6:\text{Mn}^{4+}$ slowly decreases up to 423 K (150 °C). Above this temperature there is rapid quenching, with no emission intensity remaining at 573 K. From the emission spectra recorded between 298 and 600 K we obtain the temperature dependence of the integrated PL intensity (I_{PL}), which is displayed in Figure 3.6d. The intensity is given relative to the integrated PL intensity at room temperature (I_{RT}). The PL intensity gradually decreases between 300 and 450 K, but then at higher temperatures rapidly drops due to an increased probability for non-radiative transitions from the ${}^2\text{E}$ excited state (luminescence quenching). The luminescence quenching temperature $T_{1/2}$, the temperature at which the PL intensity is half of its initial value, is around 460 K for $\text{K}_3\text{AlF}_6:\text{Mn}^{4+}$ and $\text{Na}_3\text{AlF}_6:\text{Mn}^{4+}$ and 485 K for $\text{K}_2\text{NaAlF}_6:\text{Mn}^{4+}$. The $T_{1/2}$ values fall in the range of quenching temperatures reported for Mn^{4+} -doped fluoride phosphors [39,46]. The quenching temperatures of $\text{M}_3\text{AlF}_6:\text{Mn}^{4+}$ are above the phosphor operating temperatures of high power w-LEDs.

The temperature dependences we obtain for $\text{K}_3\text{AlF}_6:\text{Mn}^{4+}$ and $\text{Na}_3\text{AlF}_6:\text{Mn}^{4+}$ (Figure 3.6d) are significantly different from the work by Song et al. [17,18]. We observe a small decrease in the PL intensity between 298 and 423 K, while they reported a doubling of the PL intensity between these temperatures. The decrease in PL intensity between 298 and 423 K for $\text{M}_3\text{AlF}_6:\text{Mn}^{4+}$ we ascribe to an increase of the energy transfer from Mn^{4+} ions to quenching sites (defects and impurities) with temperature [47]. The rapid quenching of the Mn^{4+} luminescence above 430 K is attributed to thermally activated crossing of the Mn^{4+} ${}^4\text{T}_2$ excited state and ${}^4\text{A}_2$ ground state, as will be explained in Chapter 5.

Finally, we observe some interesting changes in the emission spectrum of $\text{K}_2\text{NaAlF}_6:\text{Mn}^{4+}$ upon heating to 573 K. This is illustrated in Figure 3.7, which displays emission spectra recorded at $T = 4$ and 298 K of $\text{K}_2\text{NaAlF}_6:\text{Mn}^{4+}$ (0.9%) for as-synthesized $\text{K}_2\text{NaAlF}_6:\text{Mn}^{4+}$ (blue spectra) and $\text{K}_2\text{NaAlF}_6:\text{Mn}^{4+}$ phosphor that was heated to 573 K (red spectra). The room-temperature spectra in Figure 3.7a show that the structure of the ${}^2\text{E} \rightarrow {}^4\text{A}_2$ ZPL emission in $\text{K}_2\text{NaAlF}_6:\text{Mn}^{4+}$ changes upon heating to 573 K. This effect is even more pronounced in the spectra measured at 4 K (Figure 3.7b). Four ZPLs of similar intensity are observed for the as-synthesized phosphor, while two ZPLs dominate the spectrum after heating at 573 K. In addition, the results in Figure 3.7b show that heating to 573 K changes the structure and intensity of the vibronic ${}^2\text{E} \rightarrow {}^4\text{A}_2$ emission lines. The changes in the emission spectra upon high temperature annealing are explained by a rearrangement of the Mn^{4+} sites in $\text{K}_2\text{NaAlF}_6:\text{Mn}^{4+}$ upon heating to 573 K. Furthermore,

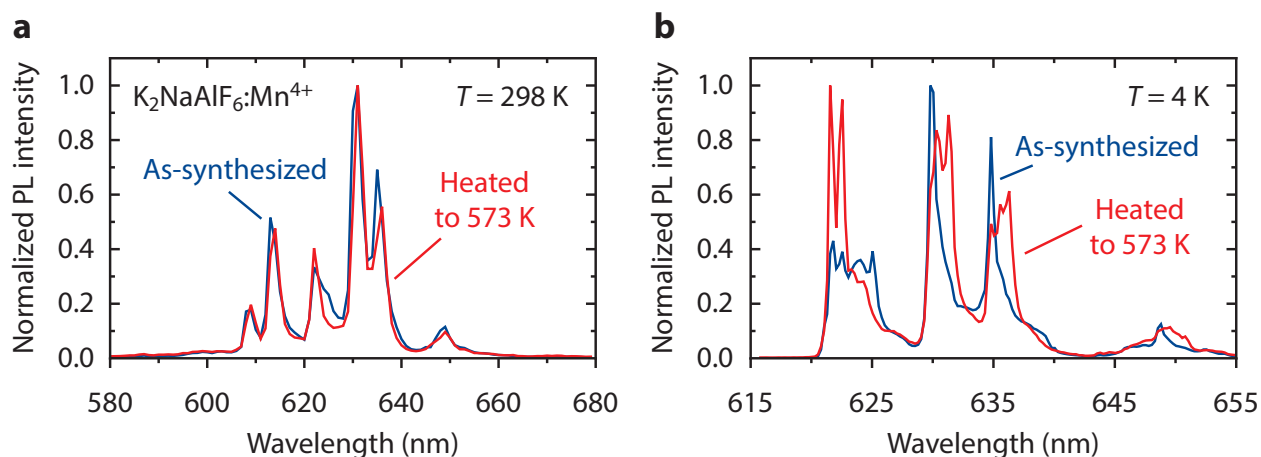


Figure 3.7 – (a) Room-temperature emission spectra ($\lambda_{\text{exc}} = 450$ nm) of $\text{K}_2\text{NaAlF}_6:\text{Mn}^{4+}$ (0.9%) for as-synthesized $\text{K}_2\text{NaAlF}_6:\text{Mn}^{4+}$ phosphor (blue) and $\text{K}_2\text{NaAlF}_6:\text{Mn}^{4+}$ phosphor that has been heated to 573 K (red). (b) Emission spectra of $\text{K}_2\text{NaAlF}_6:\text{Mn}^{4+}$ (0.9%) at $T = 4$ K ($\lambda_{\text{exc}} = 460$ nm) for as-synthesized $\text{K}_2\text{NaAlF}_6:\text{Mn}^{4+}$ phosphor (blue) and $\text{K}_2\text{NaAlF}_6:\text{Mn}^{4+}$ phosphor that has been heated to 573 K (red).

the fact that two ZPLs dominate the emission spectrum of $\text{K}_2\text{NaAlF}_6:\text{Mn}^{4+}$ after heating indicates that there is a redistribution in the abundance of different charge compensated Mn^{4+} sites. The results presented in Figure 3.7 show that post-synthesis heating can have a large effect on the luminescence properties of $\text{M}_3\text{AlF}_6:\text{Mn}^{4+}$ and other Mn^{4+} -doped fluoride phosphors.

3.4 Conclusions

Mn^{4+} -doped fluorides have recently attracted considerable attention due to their potential for application in w-LEDs. For application in w-LEDs it is important to understand and control the synthesis and luminescence properties of Mn^{4+} -doped fluoride phosphors. In this chapter we reported the synthesis of different $\text{M}_3\text{AlF}_6:\text{Mn}^{4+}$ ($M = \text{Na}, \text{K}$) phosphors via a simple two-step co-precipitation method. Our synthesis method provides good control over Mn^{4+} doping and yields highly monodisperse ~ 20 μm smoothed octahedron shaped crystallites for $\text{K}_2\text{NaAlF}_6:\text{Mn}^{4+}$, while irregularly shaped particles with a broad size distribution are obtained for $\text{K}_3\text{AlF}_6:\text{Mn}^{4+}$ and $\text{Na}_3\text{AlF}_6:\text{Mn}^{4+}$. All synthesized $\text{M}_3\text{AlF}_6:\text{Mn}^{4+}$ phosphors show narrow red $\text{Mn}^{4+} {}^2\text{E} \rightarrow {}^4\text{A}_2$ luminescence that can be excited in the UV and blue spectral region. Luminescence spectra recorded at $T = 4$ K reveal that multiple Mn^{4+} sites are present in $\text{M}_3\text{AlF}_6:\text{Mn}^{4+}$, which was not observed in previous reports. The presence of multiple Mn^{4+} sites is attributed to charge compensation that is required for Mn^{4+} on Al^{3+} sites. The results show that charge compensating defects have a large influence on the luminescence properties (e.g. spectra, quantum efficiency, luminescence lifetime) of Mn^{4+} -doped fluorides. Lowering of the QE by defect quenching is a problem for application of this class of Mn^{4+} phosphors. Finally, we investigated the thermal quenching behavior for $\text{M}_3\text{AlF}_6:\text{Mn}^{4+}$. The luminescence quenching temperature of $\text{M}_3\text{AlF}_6:\text{Mn}^{4+}$ is between 460 and 490 K, which is above the

phosphor operating temperature in high power w-LEDs. If the QE can be improved by suppressing defect quenching, Mn⁴⁺ doped hexafluoroaluminates are a promising class of materials as their chemical and thermal stability is superior to the presently used commercial Mn⁴⁺ phosphors.

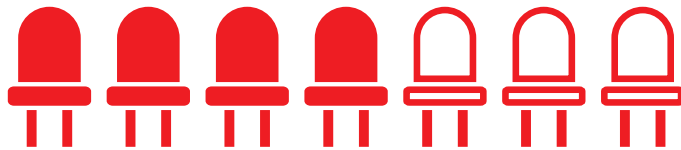
References

- [1] Charge of the LED brigade: A global switch to LEDs will change the lighting business, *The Economist* (2011).
- [2] M. R. Krames, O. B. Shchekin, R. Mueller-Mach, G. O. Mueller, L. Zhou, G. Harbers and M. G. Craford, *IEEE/OSA J. Disp. Technol.* **3** (2007) 160–175.
- [3] G. Harbers, S. J. Bierhuizen and M. R. Krames, *IEEE/OSA J. Disp. Technol.* **3** (2007) 98–109.
- [4] S. Nakamura, *MRS Bull.* **34** (2009) 101–107.
- [5] P. F. Smet, A. B. Parmentier and D. Poelman, *J. Electrochem. Soc.* **158** (2011) R37–R54.
- [6] A. A. Setlur, *Electrochem. Soc. Interface.* **18** (2009) 32–36.
- [7] R. J. Xie and N. Hirosaki, *Sci. Technol. Adv. Mater.* **8** (2007) 588–600.
- [8] H. Zhu, C. C. Lin, W. Luo, S. Shu, Z. Liu, Y. Liu, J. Kong, E. Ma, Y. Cao, R.-S. Liu and X. Chen, *Nat. Commun.* **5** (2014) 4312.
- [9] A. A. Setlur, E. V. Radkov, C. S. Henderson, J.-H. Her, A. M. Srivastava, N. Karkada, M. S. Kishore, N. P. Kumar, D. Aesram, A. Deshpande, B. Kolodin, L. S. Grigorov and U. Happek, *Chem. Mater.* **22** (2010) 4076–4082.
- [10] H. F. Sijbom, J. J. Joos, L. I. D. J. Martin, K. Van den Eeckhout, D. Poelman and P. F. Smet, *ECS J. Solid State Sci. Technol.* **5** (2016) R3040–R3048.
- [11] C. C. Lin, A. Meijerink and R.-S. Liu, *J. Phys. Chem. Lett.* **7** (2016) 495–503.
- [12] H.-D. Nguyen and R.-S. Liu, *J. Mater. Chem. C* **4** (2016) 10759–10775.
- [13] R. Hoshino and S. Adachi, *Opt. Mater.* **48** (2015) 36–43.
- [14] H. F. Sijbom, R. Verstraete, J. J. Joos, D. Poelman and P. F. Smet, *Opt. Mater. Express.* **7** (2017) 3332–3365.
- [15] J. E. Murphy, F. Garcia-Santamaria, A. A. Setlur and S. Sista, *SID Symp. Dig. Tech. Pap.* **46** (2015) 927–930.
- [16] H.-D. Nguyen, C. C. Lin and R.-S. Liu, *Angew. Chemie Int. Ed.* **54** (2015) 10862–10866.
- [17] E. H. Song, J. Q. Wang, S. Ye, X. F. Jiang, M. Y. Peng and Q. Y. Zhang, *J. Mater. Chem. C* **4** (2016) 2480–2487.
- [18] E. Song, J. Wang, J. Shi, T. Deng, S. Ye, M. Peng, J. Wang, L. Wondraczek and Q. Zhang, *ACS Appl. Mater. Interfaces* **9** (2017) 8805–8812.
- [19] Y. Zhu, L. Cao, M. G. Brik, X. Zhang, L. Huang, T. Xuan and J. Wang, *J. Mater. Chem. C* **5** (2017) 6420–6426.
- [20] Y. Zhu, L. Huang, R. Zou, J. Zhang, J. Yu, M. Wu, J. Wang and Q. Su, *J. Mater. Chem. C* **4** (2016) 5690–5695.
- [21] R. D. Shannon, *Acta Crystallogr. Sect. A.* **32** (1976) 751–767.
- [22] W. T. Thompson and D. G. W. Goad, *Can. J. Chem.* **54** (1976) 3342–3349.
- [23] *Handbook of Chemistry and Physics*, 98th ed., CRC Press/Taylor & Francis, Boca Raton, 2017.
- [24] L. Lv, X. Jiang, S. Huang, X. Chen and Y. Pan, *J. Mater. Chem. C* **2** (2014) 3879–3884.
- [25] A. A. Setlur, R. J. Lyons, P. K. Nammalwar, R. Hanumantha, J. E. Murphy and F. Garcia, World Patent WO 2015102876 A1, 2015.
- [26] D. F. Shriver and P. W. Atkins, *Inorganic Chemistry*, 4th ed., Oxford University Press, Oxford, 2006.
- [27] H. Bode, H. Jenssen and F. Bandte, *Angew. Chemie* **65** (1953) 304.
- [28] H.W. Roesky, *Efficient Preparations of Fluorine Compounds*, John Wiley & Sons Inc., Hoboken, 2012.
- [29] L. R. Morss, *J. Inorg. Nucl. Chem.* **36** (1974) 3876–3878.
- [30] F. C. Hawthorne and R. B. Ferguson, *Can. Mineral.* **13** (1975) 377–382.

- [31] A. M. Abakumov, G. King, V. K. Laurinavichute, M. G. Rozova, P. M. Woodward and E. V. Antipov, *Inorg. Chem.* **48** (2009) 9336–9344.
- [32] S. Adachi and T. Takahashi, *J. Appl. Phys.* **106** (2009) 013516.
- [33] Y. K. Xu and S. Adachi, *J. Appl. Phys.* **105** (2009) 013525.
- [34] X. Jiang, Y. Pan, S. Huang, X. Chen, J. Wang and G. Liu, *J. Mater. Chem. C* **2** (2014) 2301–2306.
- [35] M.-H. Fang, H.-D. Nguyen, C. C. Lin and R.-S. Liu, *J. Mater. Chem. C* **3** (2015) 7277–7280.
- [36] Q. Zhou, H. Tan, Y. Zhou, Q. Zhang, Z. Wang, J. Yan and M. Wu, *J. Mater. Chem. C* **4** (2016) 7443–7448.
- [37] Z. Wang, Y. Zhou, Z. Yang, Y. Liu, H. Yang, H. Tan, Q. Zhang and Q. Zhou, *Opt. Mater.* **49** (2015) 235–240.
- [38] C. de Mello Donegá, *Chem. Soc. Rev.* **40** (2011) 1512–1546.
- [39] A. G. Paulusz, *J. Electrochem. Soc.* **120** (1973) 942–947.
- [40] T. Takahashi and S. Adachi, *J. Electrochem. Soc.* **155** (2008) E183–E188.
- [41] T. Senden, F. T. H. Broers and A. Meijerink, *Opt. Mater.* **60** (2016) 431–437.
- [42] G. Blasse and B. C. Grabmaier, *Luminescent Materials*, Springer-Verlag, Berlin, 1994.
- [43] S. L. Chodos, A. M. Black and C. D. Flint, *J. Chem. Phys.* **65** (1976) 4816–4824.
- [44] M. G. Brik and A. M. Srivastava, *J. Lumin.* **133** (2013) 69–72.
- [45] M. G. Brik, S. J. Camardello and A. M. Srivastava, *ECS J. Solid State Sci. Technol.* **4** (2014) R39–R43.
- [46] S. Sakurai, T. Nakamura and S. Adachi, *ECS J. Solid State Sci. Technol.* **5** (2016) R206–R210.
- [47] V. Bachmann, C. Ronda and A. Meijerink, *Chem. Mater.* **21** (2009) 2077–2084.

4

Comparative study of the Mn^{4+} luminescence in $\text{RE}_2\text{Sn}_2\text{O}_7:\text{Mn}^{4+}$ pyrochlores ($\text{RE}^{3+} = \text{Y}^{3+}, \text{Lu}^{3+}$ or Gd^{3+})



Abstract

Red-emitting Mn^{4+} -doped crystalline materials have potential for application in light emitting devices and therefore it is important to understand how the optical properties of Mn^{4+} are influenced by the host lattice the Mn^{4+} ions are situated in. In this chapter we investigate the effect of the host cations in the second coordination sphere on the Mn^{4+} emission by studying the luminescence of Mn^{4+} ions doped into three isostructural rare earth (RE) stannate $\text{RE}_2\text{Sn}_2\text{O}_7$ pyrochlores ($\text{RE}^{3+} = \text{Y}^{3+}, \text{Lu}^{3+}$ or Gd^{3+}). It is found that the energies of the Mn^{4+} ${}^4\text{T}_1$ and ${}^4\text{T}_2$ states significantly increase with decreasing $\text{Mn}^{4+}-\text{O}^{2-}$ distance, whereas the energy of the ${}^2\text{E}$ level shows a small shift to higher energies from $\text{RE}^{3+} = \text{Gd}^{3+}$ to Lu^{3+} to Y^{3+} . The observed trend for the ${}^2\text{E}$ level energy is not related to the size of the RE^{3+} ion and is not in line with theoretical calculations reported previously. Low-temperature emission spectra of the $\text{RE}_2\text{Sn}_2\text{O}_7:\text{Mn}^{4+}$ phosphors reveal that only asymmetrical vibronic modes couple to the ${}^2\text{E} \rightarrow {}^4\text{A}_2$ transition and furthermore show there is significant and unexpected local disorder for Mn^{4+} in $\text{Gd}_2\text{Sn}_2\text{O}_7$ that is not observed for Mn^{4+} in the other hosts. Photoluminescence decay measurements demonstrate that the luminescence of $\text{RE}_2\text{Sn}_2\text{O}_7:\text{Mn}^{4+}$ is strongly quenched below room temperature which is assigned to non-radiative relaxation via a low-lying $\text{O}^{2-} \rightarrow \text{Mn}^{4+}$ charge-transfer state.

4.1 Introduction

Crystalline materials doped with Mn^{4+} ions ($3d^3$ electronic configuration) show narrow red line luminescence and are therefore interesting for applications in e.g. the lighting industry. The efficient luminescent Mn^{4+} -activated magnesium fluorogermanate is commercially used in high color rendering fluorescent lamps and high pressure mercury vapor lamps [1,2]. Furthermore, Mn^{4+} -doped fluorides and oxides can find application as red-emitting phosphors in warm-white LED devices [3–5]. Additionally, Mn^{4+} -doped materials have potential for use in holographic recording, optical data storage [6,7], thermoluminescence dosimetry [8] and as afterglow materials [9].

Because of the many potential applications, the optical properties of Mn^{4+} have been investigated for a wide variety of host lattices [3,10–12]. The practical use of Mn^{4+} -doped materials benefits from a better understanding of general relations between host lattice properties and the optical properties of the Mn^{4+} ions. For example, for lighting applications it is important to understand how the energies of the different Mn^{4+} excited states (see Figure 4.1) are influenced by the host lattice composition and Mn^{4+} -ligand distance. General studies on the spectroscopic behavior of Mn^{4+} ions in solids are however limited [10,12]. A relation has been observed between the Mn^{4+} -ligand distance and the crystal field splitting $10 Dq$ [13,14]. A higher crystal field splitting for shorter Mn^{4+} -ligand distances causes that the 4T_2 and 4T_1 excited states shift to higher energies when Mn^{4+} substitutes on a smaller lattice site. Furthermore, it has been found that substitution of cations in the second coordination sphere also affects the crystal field splitting [13,15].

Important for applications is the energy of the emitting 2E level. This energy is not strongly influenced by the crystal field and is largely determined by the local covalency. In their recent work Srivastava and Brik defined a new parameter for covalency based on both the B and C Racah parameters [10]. More electronegative ligands (such as F^-) shift the 2E emission to higher energy. The cations in the second coordination sphere also affect the energy of the 2E level. For example, in the M_2SiF_6 ($M = \text{Na}, \text{K}, \text{Rb}$ and Cs) compounds the zero-phonon line of the ${}^2E \rightarrow {}^4A_2$ emission shifts to higher energies from 16033 cm^{-1} for $M = \text{Cs}$ to 16082 cm^{-1} for $M = \text{Rb}$ and then from 16117 cm^{-1} for $M = \text{K}$ to 16230 cm^{-1} for $M = \text{Na}$ [16–19]. To get more insight in the role of cations in the second coordination sphere on the position of the $\text{Mn}^{4+} {}^2E \rightarrow {}^4A_2$ emission, here we present a comparative study of the luminescence of Mn^{4+} ions doped into three different rare earth (RE) stannate $\text{RE}_2\text{Sn}_2\text{O}_7$ pyrochlores ($\text{RE}^{3+} = \text{Y}^{3+}, \text{Lu}^{3+}$ or Gd^{3+}). In addition to investigating the positions of the energy levels, the vibronic structure and temperature quenching of the luminescence is reported for Mn^{4+} in the three hosts.

Photoluminescence (PL) excitation spectra of the $\text{Mn}^{4+} {}^4A_2 \rightarrow {}^4T_1$ and ${}^4A_2 \rightarrow {}^4T_2$ transitions for $\text{RE}_2\text{Sn}_2\text{O}_7:\text{Mn}^{4+}$ ($\text{RE}^{3+} = \text{Y}^{3+}, \text{Lu}^{3+}$ or Gd^{3+}) were recently reported by

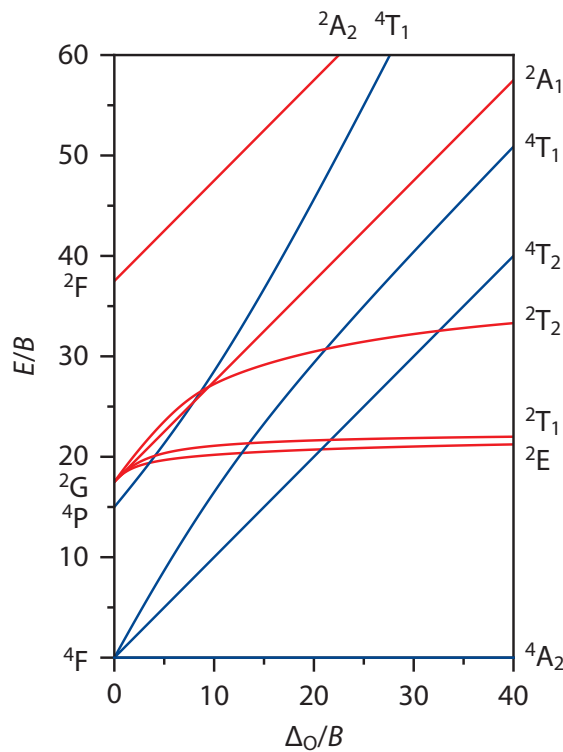


Figure 4.1 – Energy level diagram for Mn⁴⁺. Tanabe–Sugano diagram of the d³ electron configuration in an octahedral crystal field. The doublet and quartet states are shown in red and blue, respectively.

Srivastava et al. [13] to map the variation in the crystal field strength. However, in Ref. [13] the properties of the Mn⁴⁺ ²E → ⁴A₂ luminescence, e.g. the vibronic structure, energy shift and temperature quenching, were not investigated. The thermal quenching behavior is very important for application in white LEDs, as these normally operate at temperatures between 100 and 200 °C. Furthermore, the vibronic structure of the ²E → ⁴A₂ luminescence reveals the local symmetry of the Mn⁴⁺ ion and shows which vibronic modes couple to the parity- and spin-forbidden ²E → ⁴A₂ transition. Therefore, in this chapter we study and compare the electronic and vibronic structure in luminescence spectra of Mn⁴⁺ in RE₂Sn₂O₇ (RE³⁺ = Y³⁺, Lu³⁺ or Gd³⁺) by measuring PL emission and excitation spectra at cryogenic temperatures. Additionally, we measure the PL decay of the Mn⁴⁺ ²E state as a function of temperature and thereby investigate the thermal quenching behavior for Mn⁴⁺ in RE₂Sn₂O₇. It is observed that the energies of the Mn⁴⁺ ⁴T₁ and ⁴T₂ states significantly increase with decreasing Mn⁴⁺–O²⁻ distance, whereas the low-temperature measurements reveal a small energy shift for the ²E state that is not consistent with recent calculations for the ²E level of Mn⁴⁺ in these hosts. The vibronic structure of the Mn⁴⁺ luminescence reveals which vibrational modes couple to the ²E → ⁴A₂ transition. Large inhomogeneous broadening shows there is significant and unexpected local disorder for Mn⁴⁺ in Gd₂Sn₂O₇ that is not observed for Mn⁴⁺ in the other hosts. Finally, the PL decay measurements demonstrate that the luminescence of RE₂Sn₂O₇:Mn⁴⁺ is strongly quenched below room temperature with a lower quenching

temperature for Mn^{4+} in the Gd-host. The quenching is assigned to relaxation via a low-lying $\text{O}^{2-} \rightarrow \text{Mn}^{4+}$ charge-transfer state.

4.2 Methods

Microcrystalline powders of $\text{RE}_2\text{Sn}_2\text{O}_7$ ($\text{RE}^{3+} = \text{Y}^{3+}$, Lu^{3+} or Gd^{3+}) doped with 1% of Mn^{4+} ions were synthesized according to the method of Srivastava et al. [13]. The starting materials used for the syntheses were Y_2O_3 (Sigma-Aldrich, 99.99%), Lu_2O_3 (ChemPUR, 99.9%), Gd_2O_3 (Highways International, 99.999%), SnO_2 (Fisher Scientific, 99.9%) and MnCO_3 (Sigma-Aldrich, $\geq 99.9\%$). The powders were synthesized by mixing and grinding stoichiometric amounts of the starting materials with a pestle in a mortar and heating for 5 hours in a covered alumina crucible at 1000 °C in air. Next, the samples were ground a second time and heated for 10 hours in a covered alumina crucible at 1400 °C in air. The phase purity and crystal structure of the obtained light yellow-brown powders were investigated by powder X-ray diffraction (XRD). XRD patterns were recorded with a Philips PW1729 X-ray diffractometer using $\text{Cu K}\alpha$ radiation.

Photoluminescence (PL) spectra and decay curves of the samples were measured using an Edinburgh Instruments FLS920 fluorescence spectrometer equipped with a single 0.22 m excitation and emission monochromator. For recording excitation and

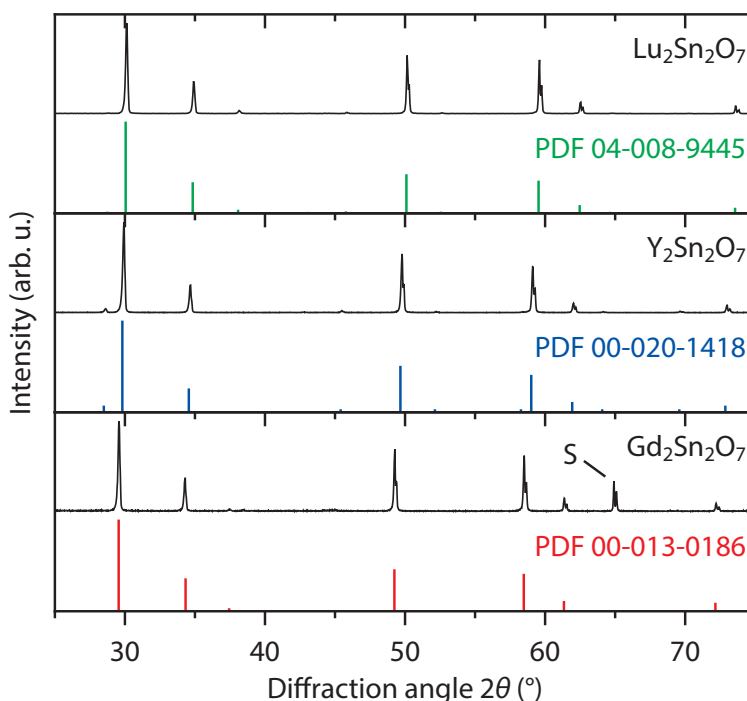


Figure 4.2 – X-ray diffraction (XRD) patterns to test the phase purity of the $\text{RE}_2\text{Sn}_2\text{O}_7:\text{Mn}^{4+}$ phosphors. The X-ray diffraction patterns of $\text{RE}_2\text{Sn}_2\text{O}_7:\text{Mn}^{4+}$ (1%) ($\text{RE}^{3+} = \text{Y}^{3+}$, Lu^{3+} or Gd^{3+}) are in excellent agreement with the reference patterns of $\text{Gd}_2\text{Sn}_2\text{O}_7$ (PDF-00-013-0186, red), $\text{Y}_2\text{Sn}_2\text{O}_7$ (PDF-00-020-1418, blue) and $\text{Lu}_2\text{Sn}_2\text{O}_7$ (PDF-04-008-9445, green). The S marks a diffraction line originating from the aluminum sample holder.

Table 4.1 – Structural properties of RE₂Sn₂O₇:Mn⁴⁺. The ionic radius of the eight-coordinated RE³⁺ ion (in Å) and the Mn⁴⁺–O²⁻ distance (in Å) of the RE₂Sn₂O₇:Mn⁴⁺ phosphors [20,21].

Pyrochlore	RE ³⁺ ionic radius (Å)	Mn ⁴⁺ –O ²⁻ distance (Å)
Lu ₂ Sn ₂ O ₇	0.977	2.040
Y ₂ Sn ₂ O ₇	1.019	2.043
Gd ₂ Sn ₂ O ₇	1.053	2.048

emission spectra, we used a 450 W Xe lamp as excitation source and a Hamamatsu R928 photomultiplier tube (PMT) for detection of emission. For PL decay measurements we used an optical parametric oscillator (OPO) system (Opotek HE 355 II) pumped by the third harmonic of a Nd:YAG laser as excitation source. This OPO system offers a continuously tunable optical range from 410 to 2400 nm, with a pulse width of 10 ns. For the PL decay measurements, the OPO system was set at $\lambda_{\text{exc}} = 470$ nm (Y₂Sn₂O₇:Mn⁴⁺) or 485 nm (Gd₂Sn₂O₇:Mn⁴⁺), with a repetition rate of 10 Hz. The PL decay was recorded with a Hamamatsu R928 PMT in combination with the multi-channel scaling (MCS) option available on the Edinburgh Instruments FLS920 fluorescence spectrometer. For PL measurements down to 4 K, the samples were cooled in an Oxford Instruments liquid helium flow cryostat. Diffuse reflection spectra were measured with a PerkinElmer 950 UV/VIS/NIR absorption spectrometer.

4.3 Results and discussion

4.3.1 Structural characterization

The crystal structure and phase purity of the RE₂Sn₂O₇:Mn⁴⁺ (1%) phosphors were investigated by powder X-ray diffraction (XRD), as is shown in Figure 4.2. The XRD patterns are in excellent agreement with reference patterns of the RE₂Sn₂O₇ pyrochlores. No traces of impurity crystal phases are observed. The diffraction lines of the RE₂Sn₂O₇:Mn⁴⁺ (1%) phosphors shift to higher angles with decreasing ionic radius of the RE³⁺ ion, as the unit cell volume of the RE₂Sn₂O₇ pyrochlore reduces when the size of the RE³⁺ ion decreases. Consequently, the Mn⁴⁺–O²⁻ (Sn⁴⁺–O²⁻) distance in the MnO₆ octahedron is shorter when the ionic radius of the RE³⁺ ion is smaller, as is shown in Table 4.1 [20,21].

4.3.2 Electronic structure for Mn⁴⁺

In a crystal field the free ion Mn⁴⁺ (3d³) *LS* terms split into a number of sublevels, depending on the crystal field strength and symmetry. The splitting of the Mn⁴⁺ energy levels in a perfect octahedral crystal field is given by the Tanabe–Sugano diagram of the d³ electron configuration [22], which is displayed in Figure 4.1. The Tanabe–Sugano diagram shows that the energies of the levels are strongly dependent on the crystal field strength (Δ_O), except for the ²E and ²T₁ state. Due to its high effective charge, the Mn⁴⁺ ion

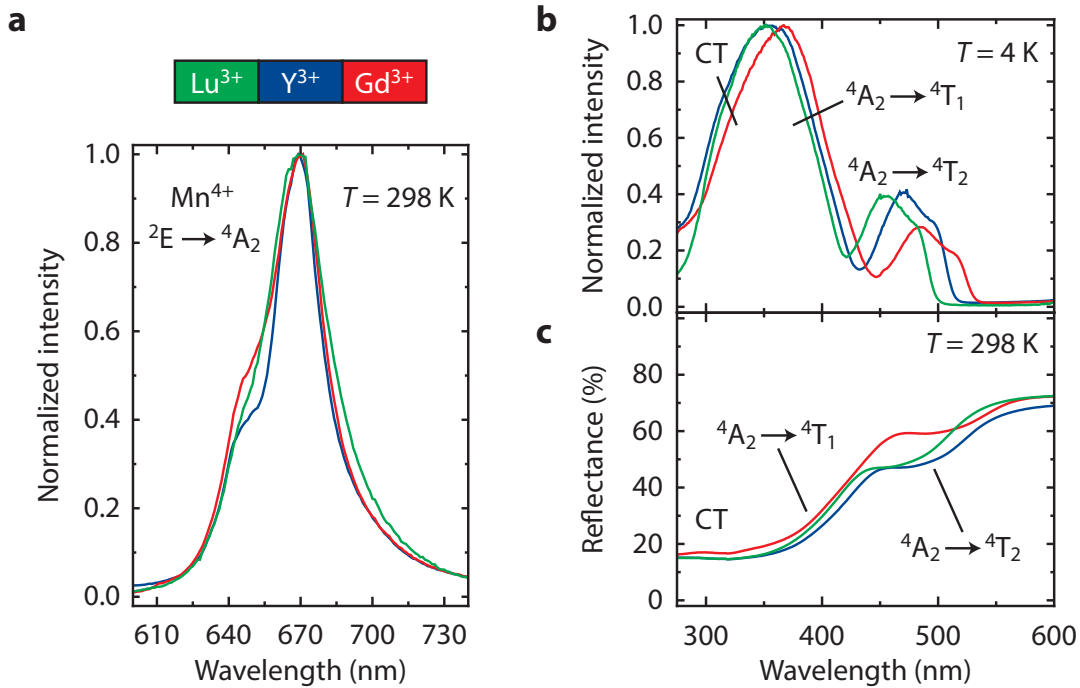


Figure 4.3 – Optical spectroscopy of Mn^{4+} in $\text{RE}_2\text{Sn}_2\text{O}_7$. (a) Room-temperature PL spectra of $\text{RE}_2\text{Sn}_2\text{O}_7:\text{Mn}^{4+}$ (1%) for $\text{RE}^{3+} = \text{Gd}^{3+}$ (red, $\lambda_{\text{exc}} = 350$ nm), Y^{3+} (blue, $\lambda_{\text{exc}} = 360$ nm) and Lu^{3+} (green, $\lambda_{\text{exc}} = 335$ nm). (b) Low-temperature ($T = 4$ K) PL excitation spectra of $\text{RE}_2\text{Sn}_2\text{O}_7:\text{Mn}^{4+}$ (1%) for $\text{RE}^{3+} = \text{Gd}^{3+}$ (red, $\lambda_{\text{em}} = 668$ nm), Y^{3+} (blue, $\lambda_{\text{em}} = 665$ nm) and Lu^{3+} (green, $\lambda_{\text{em}} = 665$ nm). (c) Room-temperature diffuse reflectance spectra of $\text{RE}_2\text{Sn}_2\text{O}_7:\text{Mn}^{4+}$ (1%) for $\text{RE}^{3+} = \text{Gd}^{3+}$ (red), Y^{3+} (blue) and Lu^{3+} (green).

experiences a strong crystal field and therefore the ${}^2\text{E}$ state is generally the lowest energy excited state. Hence, the photoluminescence (PL) spectrum of $\text{RE}_2\text{Sn}_2\text{O}_7:\text{Mn}^{4+}$ (1%) is dominated by a narrow emission band around 670 nm corresponding to the parity- and spin-forbidden ${}^2\text{E} \rightarrow {}^4\text{A}_2$ transition, as can be seen in Figure 4.3a. The emission band is narrow as the energy of the ${}^2\text{E}$ state hardly depends on the crystal field strength and because the ${}^2\text{E}$ and ${}^4\text{A}_2$ state are both derived from the same t_2^3 electronic configuration.

The low-temperature ($T = 4$ K) PL excitation spectra of $\text{RE}_2\text{Sn}_2\text{O}_7:\text{Mn}^{4+}$ (1%) in Figure 4.3b show that the narrow band ${}^2\text{E} \rightarrow {}^4\text{A}_2$ emission can be efficiently excited through the ${}^4\text{A}_2 \rightarrow {}^4\text{T}_1$ and ${}^4\text{A}_2 \rightarrow {}^4\text{T}_2$ transitions. In the spectra we observe two broad intense excitation bands around 350 and 475 nm which are assigned to the spin-allowed ${}^4\text{A}_2 \rightarrow {}^4\text{T}_1$ and ${}^4\text{A}_2 \rightarrow {}^4\text{T}_2$ transitions, respectively (see also Tanabe–Sugano diagram in Figure 4.1). The trigonal site symmetry (D_{3d}) for Mn^{4+} in $\text{RE}_2\text{Sn}_2\text{O}_7$ causes a splitting of the triplet states (${}^4\text{T}_1$ and ${}^4\text{T}_2$) into a singlet and doublet state [21,23]. This splitting is clearly visible in the excitation band corresponding to the ${}^4\text{A}_2 \rightarrow {}^4\text{T}_2$ transition but not observed for the ${}^4\text{A}_2 \rightarrow {}^4\text{T}_1$ transition, probably because this band has a strong overlap with the broad charge-transfer absorption band.

The intense Mn^{4+} ${}^4\text{A}_2 \rightarrow {}^4\text{T}_1$ and ${}^4\text{A}_2 \rightarrow {}^4\text{T}_2$ absorption bands are also observed in the

room-temperature diffuse reflection spectra of the RE₂Sn₂O₇:Mn⁴⁺ (1%) phosphors shown in Figure 4.3c. However, the most intense absorption in the diffuse reflection spectra is between 275 and 350 nm, which is assigned to the O²⁻ → Mn⁴⁺ charge-transfer (CT) transition [24]. The relative intensity of the O²⁻ → Mn⁴⁺ CT transition is weaker in the excitation spectra in Figure 4.3b, appearing only as a shoulder on the high energy side of the ⁴A₂ → ⁴T₁ excitation band. The lower intensity of the O²⁻ → Mn⁴⁺ CT transition in the excitation spectra indicates that excitation into the CT state results in less efficient luminescence than excitation into the Mn⁴⁺ crystal field states. A large offset of the CT state parabola in the configurational coordinate diagram can explain that excitation in the CT state is followed by direct relaxation to the ground state, competing with relaxation to the emitting ²E state.

The spectra in Figure 4.3b,c show that the energies of the ⁴T₁ and ⁴T₂ state depend on the type of RE³⁺ ion in the RE₂Sn₂O₇ pyrochlore. Using the data from Table 4.1 it is found that the energy of the ⁴T₁ and ⁴T₂ state, and therefore the crystal field strength for Mn⁴⁺, increases with decreasing Mn⁴⁺-O²⁻ distance and RE³⁺ ionic radius, as expected from the electrostatic point charge model. By determining the barycenter energy of the ⁴A₂ → ⁴T₂ excitation bands in Figure 4.3b, it is estimated that the crystal field strength 10 *Dq* of Mn⁴⁺ in RE₂Sn₂O₇ varies from 20234 cm⁻¹ for RE³⁺ = Gd³⁺ to 21521 cm⁻¹ for RE³⁺ = Lu³⁺. A more detailed investigation of the crystal field strength for Mn⁴⁺ and other impurity ions in stannate pyrochlores can be found in Refs. [13,25].

4.3.3 Vibronic structure of the Mn⁴⁺ ²E → ⁴A₂ luminescence

In RE₂Sn₂O₇ the Mn⁴⁺ ions are situated on a D_{3d} site with inversion symmetry. Due to the inversion symmetry, the transition between the Mn⁴⁺ ²E and ⁴A₂ state responsible for the red luminescence of RE₂Sn₂O₇:Mn⁴⁺ (see Figure 4.3a) is both parity- and spin-forbidden. The electronic transition however gains intensity by coupling to vibronic modes that induce odd-parity crystal field terms that allow admixture of opposite parity states into the ²E and ⁴A₂ states, and thereby make the transition partly allowed for electric dipole radiation. To investigate which vibronic modes couple to the ²E → ⁴A₂ transition for Mn⁴⁺ in RE₂Sn₂O₇, we studied the luminescence of RE₂Sn₂O₇:Mn⁴⁺ at temperatures down to 4 K. Figure 4.4a shows the PL spectrum of Y₂Sn₂O₇:Mn⁴⁺ (1%) at various temperatures between room temperature and 4 K. Upon cooling to cryogenic temperatures, sharp peaks emerge which correspond to the various Stokes and anti-Stokes vibronic electric dipole ²E → ⁴A₂ transitions. At 4 K all anti-Stokes emission lines have disappeared and the emission spectrum consists of the purely electronic transition (zero-phonon line; ZPL) and several vibronic ²E → ⁴A₂ emission lines on the low-energy side of the ZPL transition.

Figure 4.4b–d shows low-temperature (*T* = 4 K) high-resolution PL spectra of the ²E → ⁴A₂ luminescence of Mn⁴⁺ in Gd₂Sn₂O₇ (Figure 4.4b), Lu₂Sn₂O₇ (Figure 4.4c) and Y₂Sn₂O₇ (Figure 4.4d). For all three RE₂Sn₂O₇:Mn⁴⁺ phosphors the emission spectrum

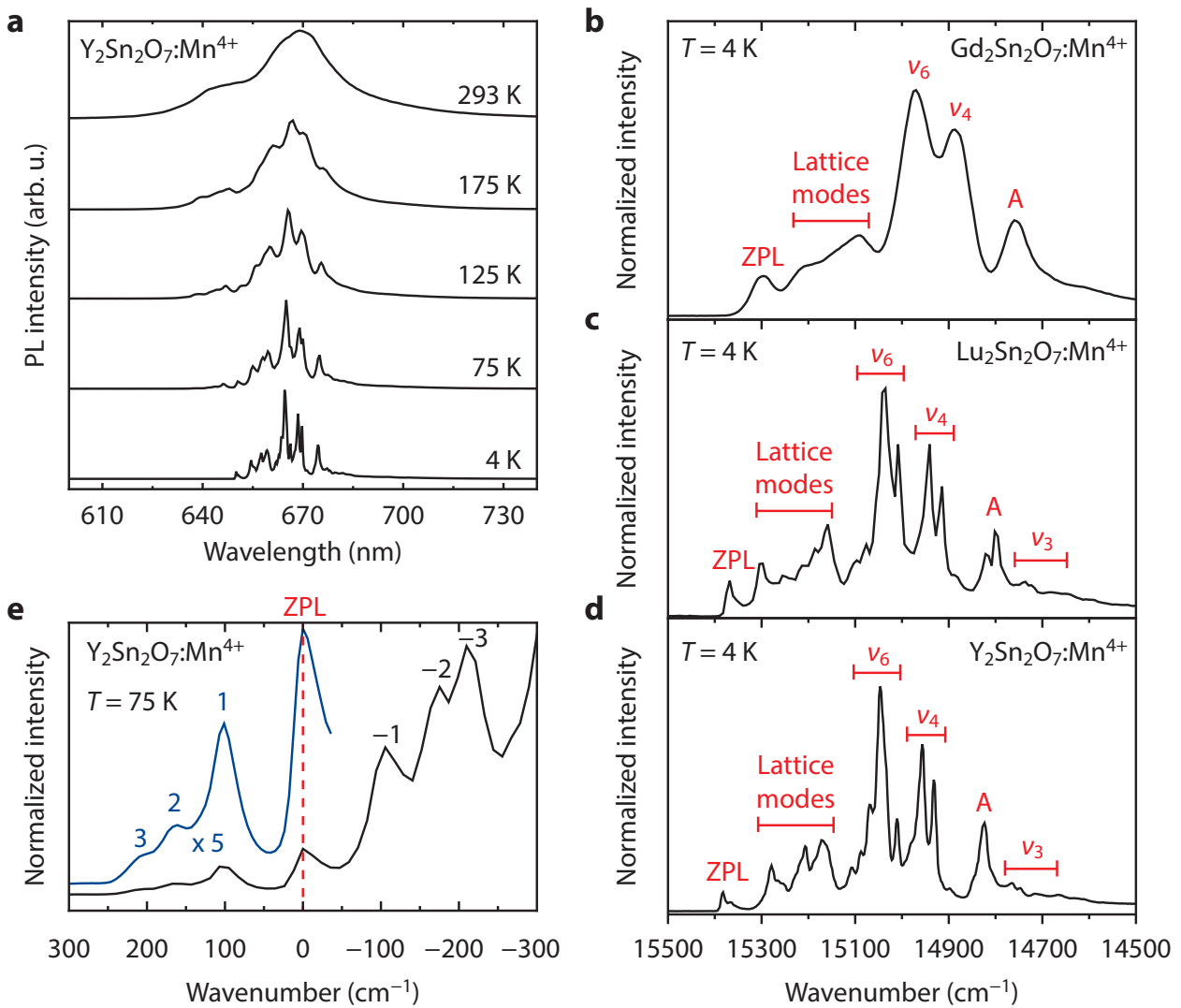


Figure 4.4 – Vibronic structure of the Mn^{4+} luminescence in $\text{RE}_2\text{Sn}_2\text{O}_7:\text{Mn}^{4+}$. (a) PL spectra of $\text{Y}_2\text{Sn}_2\text{O}_7:\text{Mn}^{4+}$ (1%) measured in the range of $T = 4$ to 293 K for $\lambda_{\text{exc}} = 360$ nm. (b)–(d) High-resolution PL spectra of $\text{RE}_2\text{Sn}_2\text{O}_7:\text{Mn}^{4+}$ (1%) at $T = 4$ K, with (b) $\text{RE}^{3+} = \text{Gd}^{3+}$; $\lambda_{\text{exc}} = 485$ nm, (c) $\text{RE}^{3+} = \text{Lu}^{3+}$; $\lambda_{\text{exc}} = 351$ nm and (d) $\text{RE}^{3+} = \text{Y}^{3+}$; $\lambda_{\text{exc}} = 470$ nm. The peaks corresponding to the zero-phonon line (ZPL) and vibronic sidebands of the ${}^2\text{E} \rightarrow {}^4\text{A}_2$ transition are indicated by the red labels. (e) PL spectra of the zero-phonon line (ZPL), anti-Stokes and Stokes emission lines of $\text{Y}_2\text{Sn}_2\text{O}_7:\text{Mn}^{4+}$ (1%) at $T = 75$ K ($\lambda_{\text{exc}} = 360$ nm). The energies of the anti-Stokes and Stokes emission lines are shown relative to the energy of the zero-phonon transition.

at 4 K consists of a group of narrow emission lines which correspond to the ZPL and vibronic sidebands of the ${}^2\text{E} \rightarrow {}^4\text{A}_2$ transition. However, a striking difference is that the emission lines in the spectrum of $\text{Gd}_2\text{Sn}_2\text{O}_7:\text{Mn}^{4+}$ are much broader and show less resolved vibronic structure than the emission lines in the spectra of the other $\text{RE}_2\text{Sn}_2\text{O}_7:\text{Mn}^{4+}$ phosphors.

The vibronic structure of the ${}^2\text{E} \rightarrow {}^4\text{A}_2$ luminescence at 4 K is expected to be similar for the three $\text{RE}_2\text{Sn}_2\text{O}_7:\text{Mn}^{4+}$ phosphors as the crystal structure of the stannate pyrochlores

and the site symmetry of the Mn⁴⁺ (Sn⁴⁺) ions are identical [21]. Hence, it is surprising that the emission lines are broader for Gd₂Sn₂O₇:Mn⁴⁺. The significant inhomogeneous broadening indicates that more disorder is present in the MnO₆ octahedrons for Mn⁴⁺ in Gd₂Sn₂O₇ compared to the other (Y and Lu) stannate pyrochlores. The disorder can be related to the larger Sn⁴⁺-O²⁻ distance in Gd₂Sn₂O₇ (see Table 4.1). There is a significant difference between the ionic radii of Sn⁴⁺ (0.69 Å) and Mn⁴⁺ (0.53 Å) ions in six-fold coordination. This difference in size can result in small geometric distortions in the MO₆ octahedron when Mn⁴⁺ substitutes for the larger Sn⁴⁺ in RE₂Sn₂O₇. This geometric distortion may be more pronounced in Gd₂Sn₂O₇ as this lattice has the largest site for Sn⁴⁺. Alternatively, it can be that the peak broadening for Mn⁴⁺ in Gd₂Sn₂O₇ is caused by coupling between the magnetic moments of the Gd³⁺ and Mn⁴⁺ ions. In contrast to Gd³⁺, Y³⁺ and Lu³⁺ have no unpaired electrons and consequently no magnetic moment which can couple to the magnetic moment of Mn⁴⁺.

The highest energy emission line in the spectra at 4 K is assigned to the zero-phonon transition between the ²E and ⁴A₂ states, labeled ZPL in Figure 4.4b–d. The energies of the ZPL, and thus the energies of the ²E level, are 15296 cm⁻¹ (Gd³⁺), 15368 cm⁻¹ (Lu³⁺) and 15382 cm⁻¹ (Y³⁺), respectively. The energy of the ²E level for Mn⁴⁺ in RE₂Sn₂O₇ is in good agreement with the ²E level energy typically observed for Mn⁴⁺ in oxides [10]. The ²E level energies of the RE₂Sn₂O₇:Mn⁴⁺ phosphors are however relatively high when compared to most other oxides, which increases their potential as red-emitting phosphor for (lighting) applications. The ZPLs have a low intensity relative to the vibronic emission lines as the zero-phonon transition is forbidden for electric dipole radiation due to the inversion symmetry of the D_{3d} site. Hence, only the magnetic dipole ²E → ⁴A₂ zero-phonon transition is allowed, which has an order of magnitude weaker oscillator strength than the electric dipole zero-phonon transition [23,26].

The results show that the type of RE³⁺ cation in the second coordination sphere has an influence on the energy of the ²E level, in agreement with the results observed for Mn⁴⁺ in the M₂SiF₆ (M = Na, K, Rb and Cs) compounds [16–19]. The energy differences between the ²E levels of the RE₂Sn₂O₇:Mn⁴⁺ phosphors are however small as the energy of the ²E state, in contrast to the ⁴T₁ and ⁴T₂ states, does not depend on the crystal field strength and is mainly determined by the local covalency (see also Figure 4.1). Consequently, it is observed that the energy of the ²E level does not increase with decreasing RE³⁺ ion size like the energy of the ⁴T₁ and ⁴T₂ excited states (see Section 4.3.2 and Table 4.1). It is interesting to compare the observed trend in the ²E energy with density functional theory (DFT) calculations for the ²E level energy of Mn⁴⁺ in RE₂Sn₂O₇ [27]. According to these DFT calculations, the Mn⁴⁺ ²E state will have the highest energy when RE³⁺ = Lu³⁺, followed by Gd³⁺ and Y³⁺. The experimental results in this chapter however show the energy *E* of the ²E level follows the trend *E*(Y³⁺) > *E*(Lu³⁺) > *E*(Gd³⁺), and the highest energy is observed in Y₂Sn₂O₇:Mn⁴⁺ for which the lowest ZPL energy was predicted. This indicates that a theoretical prediction of transition energies remains challenging.

We now proceed to discuss the more intense vibronic induced ${}^2E \rightarrow {}^4A_2$ emission lines on the low-energy side of the ZPLs. According to group theory there are six fundamental vibrational modes for an octahedron with O_h symmetry: ν_1 (A_{1g}), ν_2 (E_g), ν_3 (T_{1u}), ν_4 (T_{1u}), ν_5 (T_{2g}), ν_6 (T_{2u}) [23,28]. The Mn^{4+} 2E and 4A_2 state both have even (gerade) symmetry and therefore the parity selection rule for electric dipole radiation is only relaxed if the ${}^2E \rightarrow {}^4A_2$ transition couples with lattice vibrations that are antisymmetric (ungerade), i.e. the ν_3 , ν_4 and ν_6 mode. Hence, using the energies determined for the ungerade modes of the SnO_6 octahedron in $RE_2Sn_2O_7$ [29–31], we assign the most intense vibronic ${}^2E \rightarrow {}^4A_2$ emission lines in Figure 4.4b–d to the ν_6 ($\sim 340\text{ cm}^{-1}$ relative to the ZPL) and ν_4 mode ($\sim 430\text{ cm}^{-1}$ relative to the ZPL) of the MnO_6 octahedron. The ν_3 mode of the SnO_6 octahedron has an energy of $\sim 650\text{ cm}^{-1}$ and therefore the weak emission peaks around 14700 cm^{-1} are assigned to this vibronic mode. As the site symmetry of Mn^{4+} $RE_2Sn_2O_7$ is D_{3d} instead of O_h , the triply degenerate ν_3 , ν_4 and ν_6 modes split into a double degenerate and single degenerate mode. This splitting is observed in the spectra of $Lu_2Sn_2O_7:Mn^{4+}$ (Figure 4.4c) and $Y_2Sn_2O_7:Mn^{4+}$ (Figure 4.4d) but not in the spectrum of $Gd_2Sn_2O_7:Mn^{4+}$ (Figure 4.4b) where it is probably obscured by the broadening of the emission lines.

Besides the ${}^2E \rightarrow {}^4A_2$ emission lines induced by coupling to the antisymmetric ν_3 , ν_4 and ν_6 modes, several other vibronic ${}^2E \rightarrow {}^4A_2$ emission lines are observed in Figure 4.4b–d. The emission between 15100 and 15300 cm^{-1} is assigned to coupling of the ${}^2E \rightarrow {}^4A_2$ transition with translational or rotational lattice modes involving primarily the metal cations that have been observed between 100 and 250 cm^{-1} [28,31]. Interestingly, an $\sim 180\text{ cm}^{-1}$ mode is found only for Mn^{4+} in the Y-host consistent with the assignment in Ref. [31] to an Y-ion lattice mode at 180 cm^{-1} which is shifted to lower energies in the Gd- and Lu-host because of their higher mass. The emission line located at $\sim 550\text{ cm}^{-1}$ lower energy relative to ZPLs (labeled A) cannot be explained by coupling to antisymmetric vibrations. We do not have an explanation for what causes this emission line.

To study the vibronic structure of the anti-Stokes ${}^2E \rightarrow {}^4A_2$ emission, we measured the ZPL and anti-Stokes emission of the ${}^2E \rightarrow {}^4A_2$ transition of $Y_2Sn_2O_7:Mn^{4+}$ (1%) at $T = 75\text{ K}$, which is presented in Figure 4.4e (blue line). For comparison, in Figure 4.4e we additionally show the Stokes emission with similar energy relative to the ZPL. Three anti-Stokes vibronic sidebands of the ${}^2E \rightarrow {}^4A_2$ transition (labeled 1 to 3) are observed which are assigned to translational or rotational lattice modes coupling to ${}^2E \rightarrow {}^4A_2$ transition [28,31]. The anti-Stokes (labeled 1 to 3) and Stokes (labeled -1 to -3) vibronic emission lines are observed at similar energy relative to the ZPL, indicating that similar types of vibrational motions in the 2E and 4A_2 state are responsible for these emission lines. A detailed investigation however reveals that the energy relative to the ZPL is around 15 cm^{-1} smaller for the anti-Stokes emission lines than for the Stokes emission lines. This indicates that the energy of the vibrational modes in the 2E excited state is slightly lower than in the 4A_2 ground state.

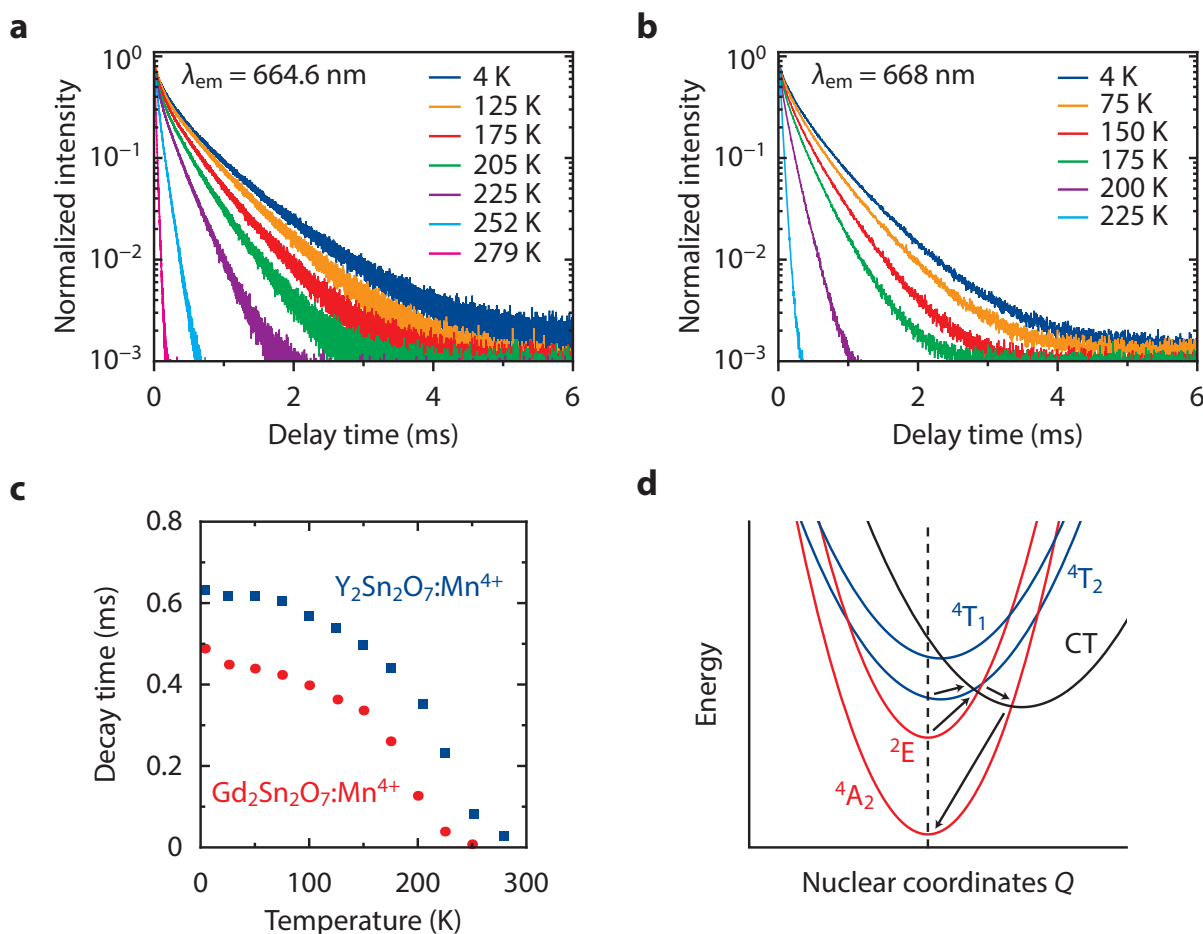


Figure 4.5 – Quenching of the Mn⁴⁺ luminescence in RE₂Sn₂O₇:Mn⁴⁺. (a,b) PL decay curves of the Mn⁴⁺ ²E excited state at various temperatures of (a) Y₂Sn₂O₇:Mn⁴⁺ (1%); λ_{exc} = 470 nm and λ_{em} = 664.6 nm, and (b) Gd₂Sn₂O₇:Mn⁴⁺ (1%); λ_{exc} = 485 nm and λ_{em} = 668 nm. (c) Average PL decay time of the Mn⁴⁺ ²E excited state of Y₂Sn₂O₇:Mn⁴⁺ and Gd₂Sn₂O₇:Mn⁴⁺ as a function of temperature. (d) Configuration coordinate diagram showing the luminescence quenching mechanism proposed for Mn⁴⁺ in RE₂Sn₂O₇.

4.3.4 Quenching of the Mn⁴⁺ ²E → ⁴A₂ luminescence

For application of Mn⁴⁺-doped materials as deep red luminescent materials, the quenching temperature of the emission is an important parameter. Both the emission intensity and luminescence decay time can be measured as a function of temperature to provide insight in the quenching temperature [1,23]. To study the thermal quenching of the ²E → ⁴A₂ luminescence for RE₂Sn₂O₇:Mn⁴⁺, here we measured the PL decay of the Mn⁴⁺ ²E state as a function of temperature. Figure 4.5a,b shows PL decay curves of the Mn⁴⁺ ²E state at various temperatures for Y₂Sn₂O₇:Mn⁴⁺ (1%) and Gd₂Sn₂O₇:Mn⁴⁺ (1%). For both phosphors the low-temperature PL decay is on the order of a millisecond, which is expected as the transition from the ²E state to the ⁴A₂ state is both parity- and spin-forbidden.

The multi-exponential character of the PL decay (even down to 4 K) indicates that not all Mn⁴⁺ centers have the same decay time, which is unexpected based on the fact that there

is a single crystallographic Sn^{4+} site for which Mn^{4+} substitutes. The non-exponential character may be due to differences in the local coordination of Mn^{4+} that affect the radiative and/or non-radiative decay rate. Because of the strongly forbidden character of the ${}^2\text{E}$ emission, a small variation in the local surroundings can result in a change of emission decay time explaining the non-exponential character. Because of thermally-activated non-radiative relaxation pathways, the PL decay becomes much faster with increasing temperature and as a result the luminescence is almost fully quenched at room temperature. This is clearly observed in Figure 4.5c, which displays the average PL decay time of $\text{Y}_2\text{Sn}_2\text{O}_7:\text{Mn}^{4+}$ and $\text{Gd}_2\text{Sn}_2\text{O}_7:\text{Mn}^{4+}$ as a function of temperature. The average PL decay time (τ_{avg}) of each decay curve was determined using $\tau_{\text{avg}} = \sum_i I_i t_i / \sum_i I_i$. The results in Figure 4.5c show that the PL decay time is relatively constant up to 100 K. The small initial decrease in decay time can be explained by the temperature dependence of the vibronic transition probabilities, which scale with the phonon occupation number n for anti-Stokes vibronics and $(1 + n)$ for Stokes vibronics. Above 100 K a rapid decrease in emission lifetime is observed until it reaches the μs range above 250 K, indicating strong thermal quenching of the emission. This is confirmed by intensity measurements which show a very weak Mn^{4+} luminescence at room temperature. Similar luminescence quenching behavior was observed for $\text{Lu}_2\text{Sn}_2\text{O}_7:\text{Mn}^{4+}$.

Strong thermal quenching of Mn^{4+} luminescence below room temperature has previously e.g. been observed for $\text{CaZrO}_3:\text{Mn}^{4+}$ and $\text{CaAl}_4\text{O}_7:\text{Mn}^{4+}$ [32,33]. For $\text{CaAl}_4\text{O}_7:\text{Mn}^{4+}$ the quenching was assigned to thermally activated crossover from the ${}^2\text{E}$ excited state to the ${}^4\text{A}_2$ ground state [33]. Since the parabola for the ${}^2\text{E}$ excited state and ${}^4\text{A}_2$ ground state are at the same equilibrium position (evidenced by sharp line emission) direct crossover is not possible. Only crossover via a third state with a large offset can explain thermal quenching. For $\text{CaZrO}_3:\text{Mn}^{4+}$, Blasse et al. assigned the absence of Mn^{4+} luminescence at room temperature to thermally activated crossover involving a low-lying $\text{O}^{2-} \rightarrow \text{Mn}^{4+}$ charge-transfer (CT) state (CT transition at $\sim 30000 \text{ cm}^{-1}$) [1,32]. The PL excitation and diffuse reflection spectra of $\text{RE}_2\text{Sn}_2\text{O}_7:\text{Mn}^{4+}$ in Figure 4.3b,c showed that the $\text{O}^{2-} \rightarrow \text{Mn}^{4+}$ CT transition of Mn^{4+} in $\text{RE}_2\text{Sn}_2\text{O}_7$ is relatively low in energy ($\sim 30000 \text{ cm}^{-1}$) and close to the ${}^4\text{T}_1$ crystal field state. Hence, we ascribe the thermal quenching observed for $\text{RE}_2\text{Sn}_2\text{O}_7:\text{Mn}^{4+}$ to a low-lying $\text{O}^{2-} \rightarrow \text{Mn}^{4+}$ CT state.

The configuration coordinate diagram in Figure 4.5d explains how the low-lying CT state causes quenching of the Mn^{4+} luminescence. Due to the low energy and large offset of the CT state (black parabola), thermal activation over a relatively low barrier already allows crossover from the ${}^4\text{T}_2$ and ${}^2\text{E}$ state to the CT state, which will be followed by non-radiative relaxation to the ground state via the crossing of the CT and ${}^4\text{A}_2$ parabola. As a consequence of this process (indicated by the arrows in Figure 4.5d), the Mn^{4+} luminescence is quenched by the increasing thermal energy available at higher temperatures. When the $\text{O}^{2-} \rightarrow \text{Mn}^{4+}$ CT state is higher in energy the quenching depicted in Figure 4.5d only occurs far above room temperature. For example, the commercial

Mn⁴⁺-activated magnesium fluorogermanate phosphor has a quenching temperature of 700 K in agreement with the higher energy position of the O²⁻ → Mn⁴⁺ CT transition, located at ~35000 cm⁻¹ [1,2].

4.4 Conclusions

Red-emitting Mn⁴⁺-doped crystalline materials have potential for application in light emitting devices (lamps, displays) and therefore it is important to understand how the spectroscopic properties of Mn⁴⁺ are influenced by the host lattice in which the Mn⁴⁺ ions are situated. Here we investigated the luminescence of three isostructural RE₂Sn₂O₇:Mn⁴⁺ (RE³⁺ = Y³⁺, Lu³⁺ or Gd³⁺) phosphors and compared the spectroscopic properties of Mn⁴⁺ in these three stannate pyrochlores. By measuring PL emission and excitation spectra of RE₂Sn₂O₇:Mn⁴⁺ at cryogenic temperatures, it was determined that the energies of the Mn⁴⁺ ⁴T₁ and ⁴T₂ states significantly increase with decreasing Mn⁴⁺–O²⁻ distance which is explained by an increase in crystal field splitting. The energy of the ²E state of Mn⁴⁺ shows a small shift to higher energies from Gd to Lu to Y. The observed shift is not in line with theoretical calculations reported previously. The vibronic structure of the Mn⁴⁺ luminescence revealed that asymmetrical vibronic modes couple to the ²E → ⁴A₂ transition. Surprisingly, the low-temperature spectra of Gd₂Sn₂O₇:Mn⁴⁺ showed relatively broad emission lines indicating more local disorder for Mn⁴⁺ in Gd₂Sn₂O₇ compared to the other two host lattices. Furthermore, we measured the PL decay of the Mn⁴⁺ ²E state as a function of temperature to investigate the thermal quenching behavior for Mn⁴⁺ in RE₂Sn₂O₇, which is an important parameter for applications. The PL decay measurements showed that the luminescence of RE₂Sn₂O₇:Mn⁴⁺ is strongly quenched below room temperature which is explained by relaxation via a low-lying O²⁻ → Mn⁴⁺ charge-transfer state.

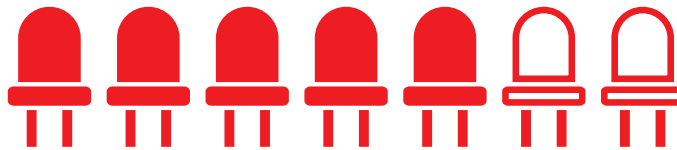
References

- [1] G. Blasse and B. C. Grabmaier, *Luminescent Materials*, Springer-Verlag, Heidelberg, 1994.
- [2] W. M. Yen, S. Shionoya and H. Yamamoto, *Phosphor Handbook*, 2nd ed., CRC Press, Boca Rotan, 2007.
- [3] C. C. Lin, A. Meijerink and R.-S. Liu, *J. Phys. Chem. Lett.* **7** (2016) 495–503.
- [4] E. V. Radkov, L. S. Grigorov, A. A. Setlur and A. M. Srivastava, United States Patent US 7,497,973 B2 (2009).
- [5] T. Murata, T. Tanoue, M. Iwasaki, K. Morinaga and T. Hase, *J. Lumin.* **114** (2005) 207–212.
- [6] M. A. Noginov and G. B. Loutts, *J. Opt. Soc. Am. B* **16** (1999) 3–11.
- [7] G. B. Loutts, M. Warren, L. Taylor, R. R. Rakhimov, H. R. Ries, G. Miller III, M. A. Noginov, M. Curley, N. Noginova, N. Kukhtarev, H. J. Caulfield and P. Venkateswarlu, *Phys. Rev. B* **57** (1998) 3706–3709.
- [8] Y. Zhydachevskii, A. Durygin, A. Suchocki, A. Matkovskii, D. Sugak, P. Bilski and S. Warchol, *Nucl. Instr. and Meth. in Phys. Res. B* **227** (2005) 545–550.
- [9] Y. Li, Y.-Y. Li, K. Sharafudeen, G.-P. Dong, S.-F. Zhou, Z.-J. Ma, M.-Y. Peng and J.-R. Qiu, *J. Mater. Chem. C* **2** (2014) 2019–2027.
- [10] M. G. Brik, S. J. Camardello and A. M. Srivastava, *ECS J. Solid State Sci. Technol.* **4** (2015) R39–R43.
- [11] R. Hoshino and S. Adachi, *Opt. Mater.* **48** (2015) 36–43.
- [12] M. G. Brik and A. M. Srivastava, *J. Lumin.* **133** (2013) 69–72.
- [13] A. M. Srivastava and M. G. Brik, *Opt. Mater.* **35** (2012) 196–200.

- [14] A. G. Paulusz, *J. Electrochem. Soc.* **120** (1973) 942–947.
- [15] A. M. Srivastava and M. G. Brik, *Opt. Mater.* **35** (2013) 1544–1548.
- [16] S. L. Chodos, A. M. Black and C. D. Flint, *J. Chem. Phys.* **65** (1976) 4816–4824.
- [17] H. F. Sijbom, J. J. Joos, L. I. D. J. Martin, K. van den Eeckhout, D. Poelman and P. F. Smet, *ECS J. Solid State Sci. Technol.* **5** (2016) R3040–R3048.
- [18] T. Takahashi and S. Adachi, *J. Electrochem. Soc.* **155** (2008) E183–E188.
- [19] Y. K. Xu and S. Adachi, *J. Appl. Phys.* **105** (2009) 013525.
- [20] R. D. Shannon, *Acta Cryst. A* **32** (1976) 751–767.
- [21] B. J. Kennedy, B. A. Hunter and C. J. Howard, *J. Solid State Chem.* **130** (1997) 58–65.
- [22] Y. Tanabe and S. Sugano, *J. Phys. Soc. Jpn.* **9** (1954) 776–779.
- [23] B. Henderson and G. F. Imbusch, *Optical Spectroscopy of Inorganic Solids*, Clarendon Press, Oxford, 1989.
- [24] M. G. Brik, A. M. Srivastava and N. M. Avram, *Opt. Mater.* **33** (2011) 1671–1676.
- [25] M. G. Brik and A. M. Srivastava, *Opt. Mater.* **35** (2013) 1251–1256.
- [26] D. F. Nelson and M. D. Sturge, *Phys. Rev.* **137** (1965) A1117–A1130.
- [27] M. H. Du, *J. Lumin.* **157** (2015) 69–73.
- [28] I. W. Forrest and A. P. Lane, *Inorg. Chem.* **15** (1976) 265–269.
- [29] A. J. H. Macke and G. Blasse, *J. Inorg. Nucl. Chem.* **38** (1976) 1409–1411.
- [30] M. T. Vandenborre and E. Husson, *J. Solid State Chem.* **50** (1983) 362–371.
- [31] J. F. McCaffrey, N. T. McDevitt and C. M. Phillippi, *J. Opt. Soc. Am.* **61** (1971) 209–212.
- [32] G. Blasse and P. H. M. de Korte, *J. Inorg. Nucl. Chem.* **43** (1981) 1505–1506.
- [33] P. Li, M. Peng, X. Yin, Z. Ma, G. Dong, Q. Zhang and J. Qiu, *Opt. Express* **21** (2013) 18943–18948.

5

Quenching of the red Mn^{4+} luminescence in Mn^{4+} -doped fluoride LED phosphors



Abstract

Red-emitting Mn^{4+} -doped fluorides are a promising class of materials to improve the color rendering and luminous efficacy of white light emitting diodes (w-LEDs). For w-LEDs the luminescence quenching temperature is very important but surprisingly no systematic research has been conducted to understand the mechanism for thermal quenching in Mn^{4+} -doped fluorides. Furthermore, concentration quenching of the Mn^{4+} luminescence can be an issue but detailed investigations are lacking. In this work we study thermal quenching and concentration quenching in Mn^{4+} -doped fluorides by measuring luminescence spectra and decay curves of $\text{K}_2\text{TiF}_6:\text{Mn}^{4+}$ between 4 and 600 K and for Mn^{4+} concentrations from 0.01 to 15.7%. Temperature-dependent measurements on $\text{K}_2\text{TiF}_6:\text{Mn}^{4+}$ and other Mn^{4+} -doped phosphors show that thermal quenching occurs through thermally activated crossover between the ${}^4\text{T}_2$ excited state and ${}^4\text{A}_2$ ground state. The quenching temperature can be optimized by designing host lattices in which Mn^{4+} has a high ${}^4\text{T}_2$ state energy. Concentration-dependent studies reveal that concentration quenching effects are limited in $\text{K}_2\text{TiF}_6:\text{Mn}^{4+}$ up to 5% Mn^{4+} . This is important as high Mn^{4+} concentrations are required for sufficient absorption of blue LED light in the parity-forbidden Mn^{4+} d-d transitions. At even higher Mn^{4+} concentrations (>10%) the quantum efficiency decreases, mostly due to energy transfer to quenching sites (defects, impurity ions). Optimization of the synthesis to reduce quenchers is crucial for developing more efficient highly absorbing Mn^{4+} phosphors. The present systematic study provides detailed insights in temperature and concentration quenching of Mn^{4+} emission and can be used to realize superior narrow band red Mn^{4+} phosphors for w-LEDs.

5.1 Introduction

White light emitting diodes (w-LEDs) are the next-generation light sources for display and illumination systems because of their small size, high luminous efficacy and long operation lifetime [1–5]. Conventional w-LEDs are composed of blue-emitting (In,Ga)N LEDs and yellow and red-emitting phosphors that convert part of the blue LED emission to yellow and red light [5–7]. Both yellow and red conversion phosphors are necessary to generate warm white light with high color rendering index (CRI > 85). The typical red phosphors in w-LEDs are Eu^{2+} -doped nitrides (e.g. $\text{CaAlSiN}_3:\text{Eu}^{2+}$) [4,8]. These phosphors exhibit high photoluminescence quantum efficiencies (QE > 90%), but their use has one serious drawback. The Eu^{2+} emission band of the Eu^{2+} -doped nitrides is broad and therefore extends into the deep red spectral region ($\lambda > 650$ nm) where the sensitivity of the human eye is low. This causes the luminous efficacy of the w-LED to decrease significantly (reduced lumen/W output). A worldwide search is therefore aimed at finding efficient narrow band red-emitting phosphors that can be excited by blue light. In this search, Mn^{4+} -doped fluoride phosphors like $\text{K}_2\text{SiF}_6:\text{Mn}^{4+}$ and $\text{K}_2\text{TiF}_6:\text{Mn}^{4+}$ have recently attracted considerable attention [9–13]. Under blue light excitation Mn^{4+} -doped fluorides show narrow red line emission ($\lambda_{\text{max}} \sim 630$ nm) with high luminescence quantum efficiencies [13–16]. Furthermore, they are prepared through low-cost simple wet-chemical synthesis at room temperature [11,17]. These aspects make Mn^{4+} -doped fluorides very promising red-emitting phosphors for developing energy-efficient high color-rendering w-LED systems [9].

The application of Mn^{4+} -doped fluoride phosphors in w-LEDs may however be hampered by thermal quenching of the Mn^{4+} luminescence. In high-power w-LEDs the temperature of the on-chip phosphor layer easily reaches 450 K. At these elevated temperatures thermal quenching has been observed for Mn^{4+} -doped fluorides. The luminescence quenching temperature $T_{1/2}$, the temperature at which the emission intensity is half of its maximum value, is typically between 400 and 500 K [15,18,19]. Although the temperature dependence of the emission intensity has been measured for many Mn^{4+} -doped fluorides, the understanding of the thermal quenching behavior is still limited. Most studies do not explain which non-radiative relaxation process quenches the Mn^{4+} luminescence [13,20–23]. Moreover, the few reports that do propose a quenching mechanism disagree. Paulusz [15] states that the luminescence of Mn^{4+} -doped fluorides is quenched due to thermally activated crossing of the $\text{Mn}^{4+} \ ^4\text{T}_2$ excited state and $\ ^4\text{A}_2$ ground state. In contrast, Dorenbos [24] finds a relation between the quenching temperature and the energy of the $\text{F}^- \rightarrow \text{Mn}^{4+}$ charge-transfer (CT) state and therefore suggests quenching involves crossover between the CT state and the $\ ^4\text{A}_2$ ground state. This CT state crossover mechanism was also used by Blasse and our group to explain thermal quenching in Mn^{4+} -doped oxides (see Chapter 4) [25–27]. Finally, other reports claim that the quenching temperature does not depend on the energy of a Mn^{4+} state but instead increases if the radius of the cation substituted by Mn^{4+} becomes

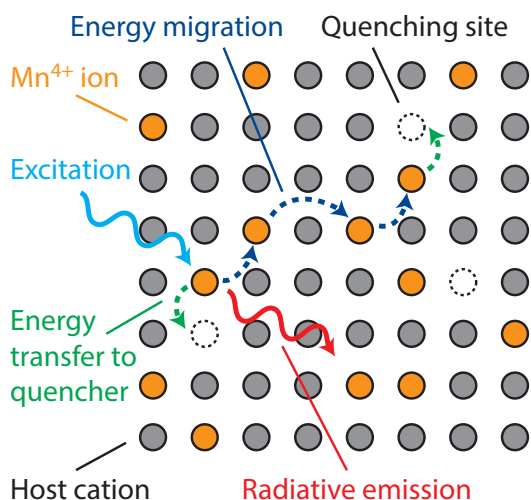


Figure 5.1 – Concentration quenching for Mn⁴⁺ in crystals. At high Mn⁴⁺ doping concentrations the Mn⁴⁺ ions (orange) are in close proximity in the crystal lattice. If the Mn⁴⁺ ions are close together, energy transfer between Mn⁴⁺ ions (dark blue) causes the excitation to migrate through the crystal. Eventually it may reach a quenching site such as a vacancy or impurity (dashed circle) where the excitation energy is lost as heat. This process competes with radiative emission (red) and reduces the luminescence efficiency.

smaller [11,18]. A better understanding of the thermal quenching behavior is essential for developing Mn⁴⁺-doped fluoride phosphors with superior quenching temperatures and thereby improving their potential for application in w-LEDs.

Besides thermal quenching, concentration quenching is an issue for the application of Mn⁴⁺-doped fluorides in w-LEDs. Since the Mn⁴⁺ d–d transitions are parity-forbidden, high Mn⁴⁺ doping concentrations (e.g. 5 mol%) are required for sufficient absorption of the blue LED light [12]. At these high dopant concentrations energy migration among the Mn⁴⁺ ions can result in concentration quenching [26,28], as is illustrated in Figure 5.1. If the distance between the Mn⁴⁺ ions is small, excitation energy may efficiently migrate from one Mn⁴⁺ ion to another until it reaches a quenching site (vacancy, impurity ion). At the quenching site the excitation energy is lost non-radiatively (heat), which causes the luminescence efficiency to decrease. Studies on concentration quenching in Mn⁴⁺-doped fluorides are limited. Several works have compared the luminescence properties of fluoride phosphors with varying Mn⁴⁺ concentrations but do not measure the actual Mn⁴⁺ concentration in the phosphors by elemental analysis [29–33]. Determining the Mn⁴⁺ concentration is necessary as in most cases only a fraction of Mn⁴⁺ ions is incorporated in the phosphor crystallites during the synthesis [19,34]. The actual Mn⁴⁺ concentration in the phosphor determines the absorption strength and needs to be known to understand concentration quenching. Reports that do perform elemental analysis study only a small range of Mn⁴⁺ doping concentrations and do not provide insight in the role of concentration quenching in Mn⁴⁺ doped fluorides [13,35,36]. An in depth investigation of concentration quenching in Mn⁴⁺-doped fluorides is thus lacking, despite it being very important for the application of Mn⁴⁺-doped fluorides in w-LEDs.

In this chapter we systematically investigate concentration quenching and thermal quenching in Mn⁴⁺-doped fluorides. The quenching is studied by measuring luminescence spectra and decay curves in the temperature range of 4 to 600 K for

$\text{K}_2\text{TiF}_6:\text{Mn}^{4+}$ phosphors with Mn^{4+} concentrations ranging from 0.01 to 15.7 mol% Mn^{4+} (actual Mn^{4+} concentration). The temperature-dependent luminescence measurements of $\text{K}_2\text{TiF}_6:\text{Mn}^{4+}$ and other Mn^{4+} -doped phosphors demonstrate that thermal quenching occurs because of thermally activated crossover from the ${}^4\text{T}_2$ excited state to the ${}^4\text{A}_2$ ground state. There is a strong correlation between the quenching temperature and the energy of the ${}^4\text{T}_2$ level. This insight in the quenching mechanism shows that the Mn^{4+} quenching temperature can be raised by finding fluoride hosts that have an increased Mn^{4+} ${}^4\text{T}_2$ level energy. Concentration studies show that the luminescence quantum efficiency of $\text{K}_2\text{TiF}_6:\text{Mn}^{4+}$ is high, around 80%, for doping concentrations up to 5 mol% Mn^{4+} . This shows that concentration quenching is limited for these relatively high Mn^{4+} dopant concentrations that are required for LED applications. At even higher doping concentrations of >10 mol% the quantum efficiency of $\text{K}_2\text{TiF}_6:\text{Mn}^{4+}$ however falls below 60%. Luminescence decay curves indicate that the drop in efficiency can be attributed to an increased probability for direct energy transfer to quenching sites (e.g. defects, impurity ions, Mn^{2+} and Mn^{3+}), the concentration of which seems to be higher for higher Mn^{4+} concentrations. Synthesis methods aimed at phosphor crystallites with a reduced number of quenching sites is the remedy for obtaining Mn^{4+} -doped phosphors with high luminescence efficiencies at high Mn^{4+} concentrations. The present results provide an improved understanding of thermal quenching and concentration quenching in Mn^{4+} -doped solids and can be used to develop superior Mn^{4+} -doped fluoride phosphors for w-LEDs.

5.2 Methods

5.2.1 Synthesis and characterization of $\text{K}_2\text{TiF}_6:\text{Mn}^{4+}$ phosphors

The $\text{K}_2\text{TiF}_6:\text{Mn}^{4+}$ ($x\%$) phosphors were synthesized according to the method of Zhu et al. [13]. For the synthesis of $\text{K}_2\text{TiF}_6:\text{Mn}^{4+}$ (0.8%), 0.0488 g of K_2MnF_6 (prepared following Refs. [37,38]) was dissolved in 2.5 mL of a 40 wt% HF solution (Fluka, 40 wt% HF in water). Next, the obtained yellow-brown solution was mixed with 4.5730 g of K_2TiF_6 (Sigma-Aldrich, p.a.) and then stirred for 1 hour at room temperature to form $\text{K}_2\text{TiF}_6:\text{Mn}^{4+}$ crystals. The $\text{K}_2\text{TiF}_6:\text{Mn}^{4+}$ phosphor was isolated by decanting the HF solution, washing twice with 15 mL of ethanol and then drying the phosphor for 7 hours at 75 °C. The other $\text{K}_2\text{TiF}_6:\text{Mn}^{4+}$ ($x\%$) phosphors were prepared following the same procedure but using other amounts of K_2MnF_6 and K_2TiF_6 as to obtain different Mn^{4+} doping concentrations.

Powder X-ray diffraction (Figure 5.2) confirms that the $\text{K}_2\text{TiF}_6:\text{Mn}^{4+}$ ($x\%$) phosphors exhibit the hexagonal crystal structure of K_2TiF_6 up to the highest doping concentration of 15.7% Mn^{4+} . Furthermore, no impurities of K_2MnF_6 or other crystal phases are observed in the diffraction patterns. Scanning electron microscopy (SEM) images show that most $\text{K}_2\text{TiF}_6:\text{Mn}^{4+}$ phosphor particles are irregularly-shaped and have sizes ranging from 1 to 200 μm (Figure 5.3a). Some particles have a hexagonal shape, in agreement

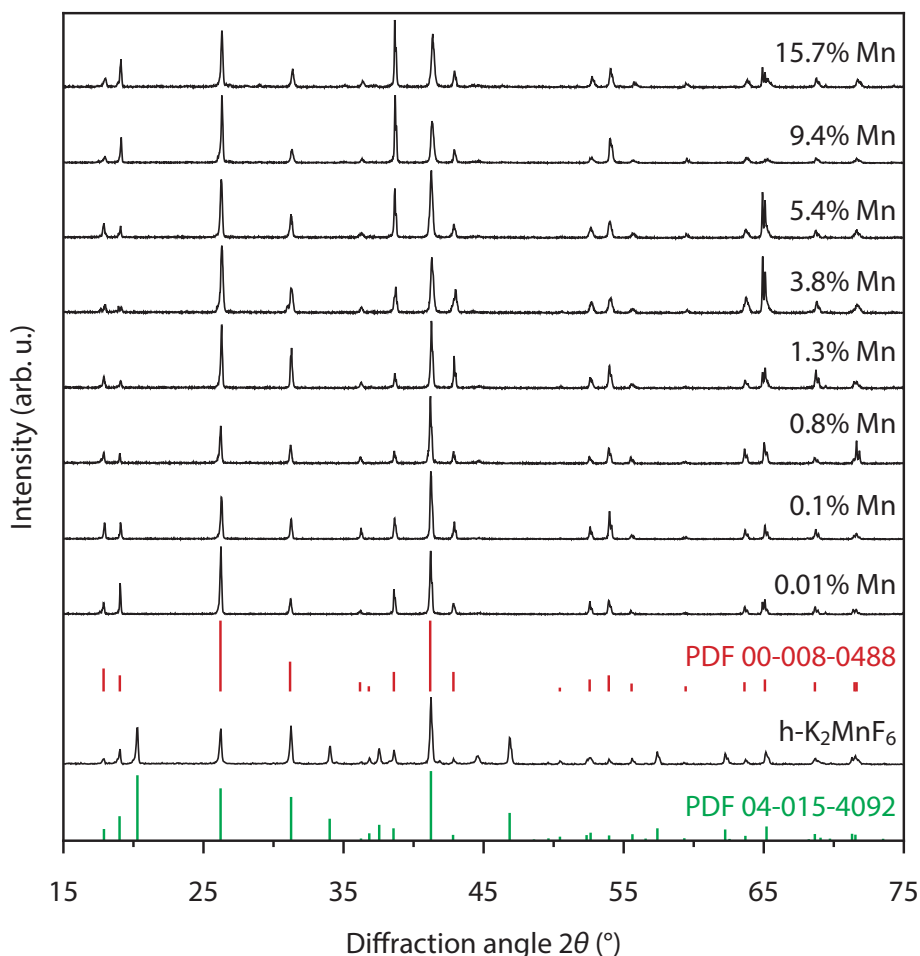


Figure 5.2 – Powder X-ray diffraction (XRD) patterns of K_2MnF_6 and the $\text{K}_2\text{TiF}_6:\text{Mn}^{4+}$ ($x\%$) phosphors. The diffraction patterns are in agreement with the literature references for hexagonal phase K_2MnF_6 (PDF 04-015-4092) and K_2TiF_6 (PDF 00-008-0488).

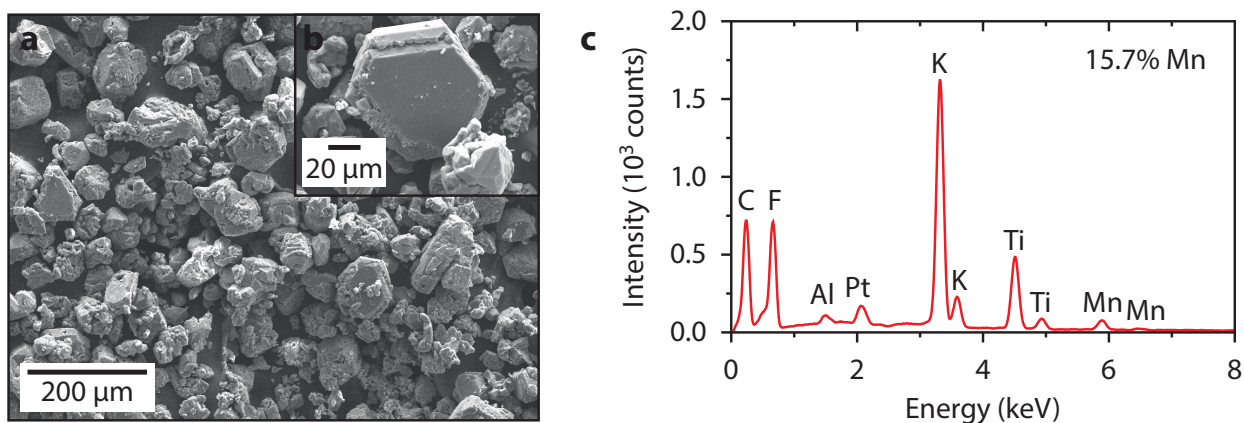


Figure 5.3 – (a) Representative scanning electron microscopy (SEM) image of $\text{K}_2\text{TiF}_6:\text{Mn}^{4+}$ (5.4%) phosphor. (b) SEM image of a single $\text{K}_2\text{TiF}_6:\text{Mn}^{4+}$ (5.4%) phosphor particle displaying the hexagonal crystal structure of K_2TiF_6 . (c) Energy dispersive X-ray (EDX) spectrum of $\text{K}_2\text{TiF}_6:\text{Mn}^{4+}$ (15.7%). The peaks in the spectrum are labeled with their corresponding elements. The aluminum (Al) and carbon (C) peaks originate from the aluminum holder and carbon tape beneath the sample. The platinum (Pt) peak is due to the platinum layer sputtered onto the phosphor particles for the SEM-EDX measurements.

with the hexagonal crystal structure of K_2TiF_6 (Figure 5.3b). Energy-dispersive X-ray (EDX) spectra (Figure 5.3c) confirm that the phosphor particles consist of potassium, titanium, fluorine and manganese ions. The manganese dopant concentrations in the $\text{K}_2\text{TiF}_6:\text{Mn}^{4+}$ phosphors were determined with inductively coupled plasma optical emission spectroscopy (ICP-OES). The ICP-OES measurements were performed on a Perkin-Elmer Optima 8300DV spectrometer ($\lambda_{\text{em}} = 257.61$ and 259.37 nm). For the ICP-OES analyses, the $\text{K}_2\text{TiF}_6:\text{Mn}^{4+}$ phosphors were dissolved in aqua regia.

5.2.2 Optical spectroscopy

Photoluminescence (PL) measurements were performed on an Edinburgh Instruments FLS920 fluorescence spectrometer, except for the PL decay measurements between 300 and 600 K (see below). For recording excitation and emission spectra, we used a 450 W Xe lamp as excitation source and a Hamamatsu R928 photomultiplier tube (PMT) with a grating blazed at 500 nm for detection of emission. For PL decay measurements excitation was done with a tunable optical parametric oscillator (OPO) Opotek Opolette HE 355II laser (pulse width 10 ns, repetition rate 10 Hz) and emission was detected with a Hamamatsu H74220-60 PMT. The PL decay curves between 300 and 600 K were recorded on a different setup, which had an Ekspla NT 342B OPO laser (pulse width 5 ns, repetition rate 10 Hz) as excitation source and a 0.55 m Triax 550 monochromator combined with a Hamamatsu H74220-60 PMT for detection of emission. All PL decay curves were obtained by multi-channel scaling (MCS) with a PicoQuant TimeHarp 260 computer card. The $\text{K}_2\text{TiF}_6:\text{Mn}^{4+}$ phosphors were cooled down to 4 K with an Oxford Instruments liquid helium flow cryostat. For PL measurements between 300 and 600 K samples were heated in a Linkam THMS600 temperature controlled stage. The PL quantum efficiencies of the phosphors were determined with a calibrated home-built setup which consisted of a 65 W Xe lamp, excitation monochromator, integrating sphere (Labsphere) and CCD camera (Avantes AvaSpec-2048).

5.3 Results and discussion

5.3.1 Luminescence of $\text{K}_2\text{TiF}_6:\text{Mn}^{4+}$

For our quenching studies we examine the luminescence of $\text{K}_2\text{TiF}_6:\text{Mn}^{4+}$ phosphors with a wide range of Mn^{4+} doping concentrations. A photographic image of the $\text{K}_2\text{TiF}_6:\text{Mn}^{4+}$ ($x\%$) phosphors is displayed in Figure 5.4a. The Mn^{4+} doping concentrations x (molar percentages with respect to Ti^{4+}) were determined by inductively coupled plasma optical emission spectroscopy (ICP-OES, see Methods). The body color of $\text{K}_2\text{TiF}_6:\text{Mn}^{4+}$ becomes more yellow with increasing Mn^{4+} concentration as a result of enhanced absorption in the blue. All investigated $\text{K}_2\text{TiF}_6:\text{Mn}^{4+}$ phosphors exhibit bright red Mn^{4+} luminescence under UV photoexcitation.

Figure 5.4b depicts the Tanabe–Sugano energy level diagram of Mn^{4+} ($3d^3$ electron configuration) in an octahedral crystal field [39,40]. The diagram gives the d^3 energy

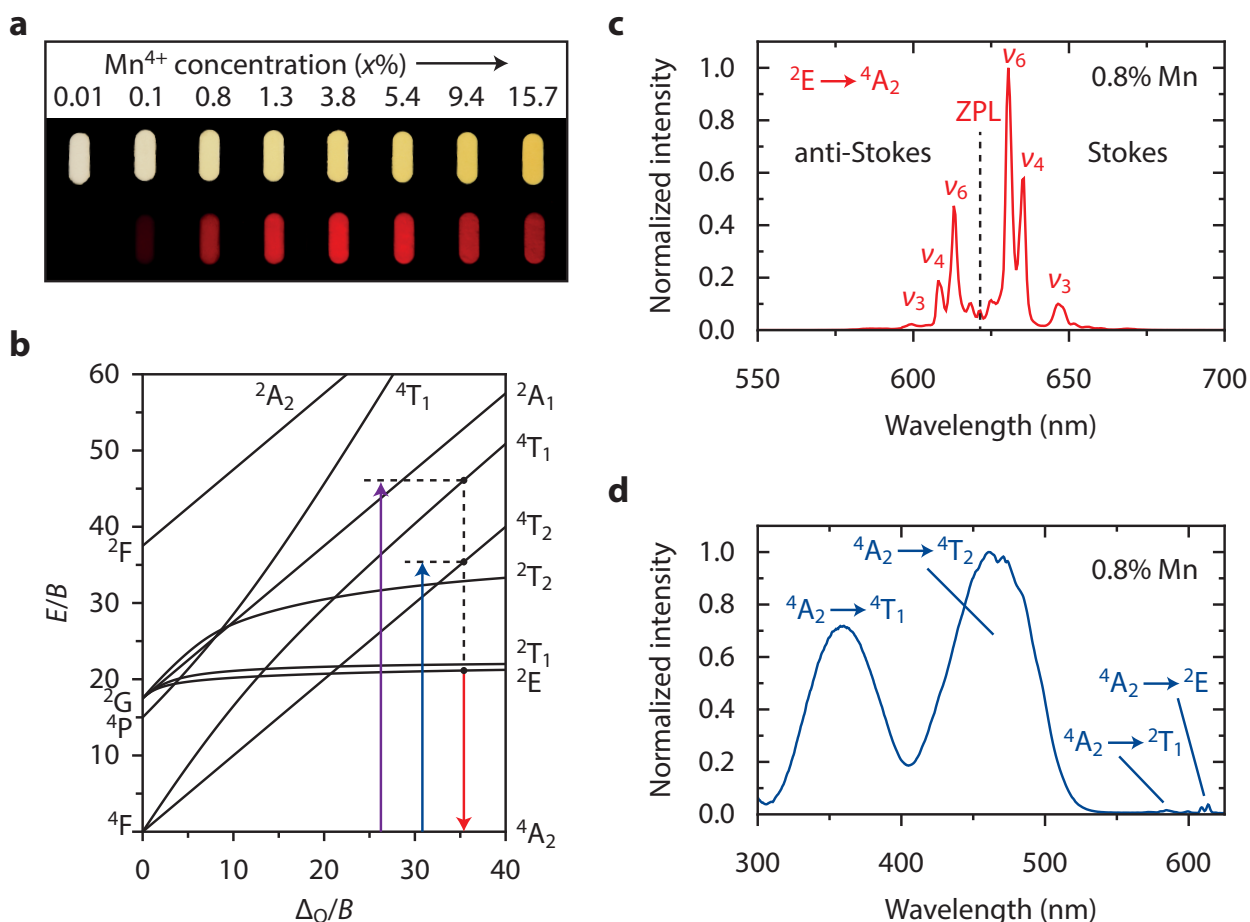


Figure 5.4 – Mn⁴⁺ luminescence of K₂TiF₆:Mn⁴⁺. (a) Photographic image of K₂TiF₆:Mn⁴⁺ (x%) phosphors with x = 0.01, 0.1, 0.8, 1.3, 3.8, 5.4, 9.4 and 15.7. The phosphors have a white to yellow body color under ambient light (top) and show red Mn⁴⁺ luminescence under 365 nm UV illumination (bottom). (b) Tanabe–Sugano energy level diagram of the d³ electron configuration in an octahedral crystal field. The ⁴A₂ → ⁴T₁, ⁴A₂ → ⁴T₂ and ²E → ⁴A₂ transitions of Mn⁴⁺ are indicated by the purple, blue and red arrows respectively. Note that the excitation transitions are displaced for clarity. For a specific coordination all transitions take place around the same crystal field Δ_O. (c) Emission spectrum of K₂TiF₆:Mn⁴⁺ (0.8%) upon excitation with blue light (λ_{exc} = 450 nm). (d) Excitation spectrum of the red Mn⁴⁺ luminescence (λ_{em} = 630 nm) from K₂TiF₆:Mn⁴⁺ (0.8%). Spectra are recorded at ambient temperature.

levels as a function of the crystal field splitting Δ_O. Due to its high positive charge, Mn⁴⁺ experiences a strong crystal field and therefore the ²E state is always the lowest energy excited state. Hence, the emission spectrum of K₂TiF₆:Mn⁴⁺ (0.8%) is dominated by narrow red emission lines due to spin- and parity-forbidden ²E → ⁴A₂ transitions, as can be seen in Figure 5.4c. The other K₂TiF₆:Mn⁴⁺ (x%) phosphors exhibit a similar emission spectrum. Since the potential energy curves of the ²E and ⁴A₂ state are at the same equilibrium position (no change in bonding between ground and excited state, Huang–Rhys parameter S ≈ 0), the ²E → ⁴A₂ emission is characterized by narrow zero-phonon and vibronic emission lines. The potential energy curves are at the same equilibrium position because the ²E and ⁴A₂ state originate from the same t_{2g}³ electron configuration.

The ${}^2E \rightarrow {}^4A_2$ emission spectrum consists of a weak zero-phonon line (ZPL) at ~ 622 nm and more intense anti-Stokes and Stokes vibronic emissions (labeled ν_3 , ν_4 and ν_6) on the high and low energy side of the ZPL, respectively [13,15]. The ZPL is very weak because Mn^{4+} is on a site with inversion symmetry in $K_2TiF_6:Mn^{4+}$. Due to the inversion symmetry, there are no odd-parity crystal field components to admix opposite parity states into the 4A_2 and 2E states and as a result the ${}^2E \rightarrow {}^4A_2$ transition is electric dipole forbidden. The ${}^2E \rightarrow {}^4A_2$ transition can however become partly electric dipole allowed by coupling with asymmetric vibrations of the MnF_6^{2-} group that induce odd-parity crystal field components. The most intense emission lines in Figure 5.4c are assigned to ${}^2E \rightarrow {}^4A_2$ transitions coupling with the asymmetric ν_3 , ν_4 and ν_6 vibrational modes (phonons) of the MnF_6^{2-} group. Thermal population of phonons at room temperature allows the transition to couple with ν_3 , ν_4 and ν_6 phonon modes in the 2E excited state (giving rise to the anti-Stokes lines) while transitions to these phonon modes in the 4A_2 ground state can occur at all temperatures (Stokes lines).

Figure 5.4d displays the excitation spectrum of the red Mn^{4+} luminescence from $K_2TiF_6:Mn^{4+}$. The excitation spectrum shows two broad excitation bands corresponding to the spin-allowed ${}^4A_2 \rightarrow {}^4T_1$ and ${}^4A_2 \rightarrow {}^4T_2$ transitions (violet and blue arrows in Tanabe-Sugano diagram in Figure 5.4b). Besides the ${}^4A_2 \rightarrow {}^4T_1$ and ${}^4A_2 \rightarrow {}^4T_2$ excitation bands, some weak excitation peaks are visible in the excitation spectrum around 600 nm. These peaks are assigned to the ${}^4A_2 \rightarrow {}^2E$ and ${}^4A_2 \rightarrow {}^2T_1$ transitions of Mn^{4+} . The ${}^4A_2 \rightarrow {}^2T_1, {}^2E$ transitions are spin-forbidden and therefore low in intensity compared to the spin-allowed ${}^4A_2 \rightarrow {}^4T_1, {}^4T_2$ transitions.

5.3.2 Temperature dependence of the Mn^{4+} luminescence

To study the thermal quenching of the Mn^{4+} emission, we measure the photoluminescence (PL) intensity and Mn^{4+} emission lifetime of $K_2TiF_6:Mn^{4+}$ (0.01%) as a function of temperature between 4 and 600 K. We use a very low Mn^{4+} doping concentration of 0.01% as we want to investigate the thermal quenching behavior of isolated Mn^{4+} ions. For higher Mn^{4+} concentrations reabsorption of emission and energy transfer between Mn^{4+} ions can occur. These processes will influence (the temperature dependence of) the Mn^{4+} luminescence spectra and decay curves [6]. As a result, with a high concentration of Mn^{4+} ions the observations may not reflect the intrinsic thermal quenching properties of Mn^{4+} .

Figure 5.5a shows emission spectra of $K_2TiF_6:Mn^{4+}$ (0.01%) at various temperatures between 4 and 600 K. At 4 K the Mn^{4+} ${}^2E \rightarrow {}^4A_2$ emission spectrum consists of zero-phonon and Stokes vibronic lines. There are no anti-Stokes emission lines at 4 K (no thermal occupation of the phonon modes in the 2E excited state). Once the temperature is increased, phonon modes are being thermally populated and anti-Stokes emission lines appear (indicated by solid arrow in Figure 5.5a). Due to the appearance of anti-Stokes lines, the relative intensity of the Stokes emission decreases between 4 and 300 K.

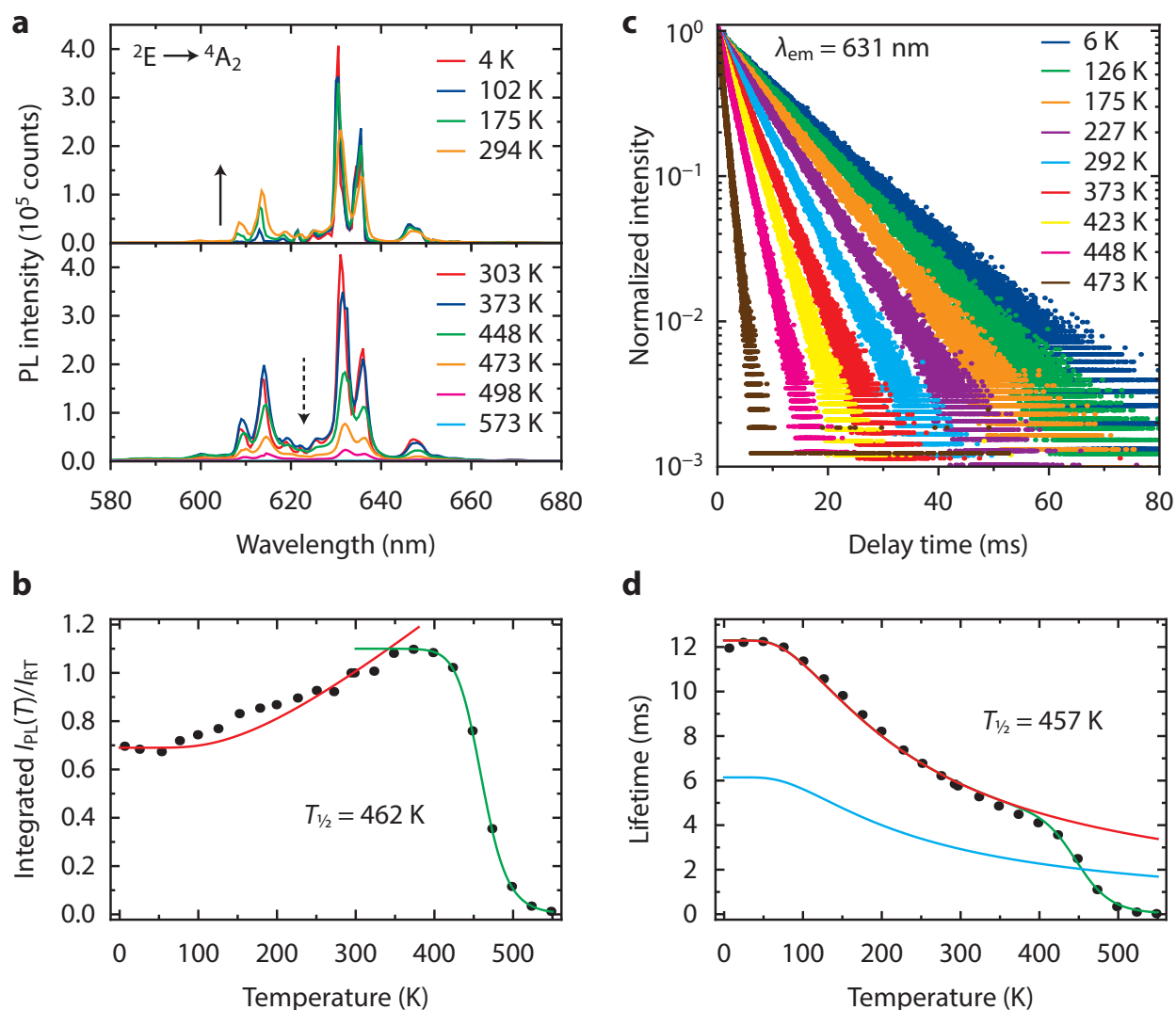


Figure 5.5 – Temperature dependence of the Mn⁴⁺ luminescence from K₂TiF₆:Mn⁴⁺ (0.01%). (a) Emission spectra ($\lambda_{exc} = 450$ nm) of K₂TiF₆:Mn⁴⁺ (0.01%) at various temperatures between 0 and 600 K. (b) Integrated PL intensity of K₂TiF₆:Mn⁴⁺ (0.01%) as a function of temperature. The integrated PL intensity I_{PL} is scaled to the integrated PL intensity at room temperature I_{RT} . The red and green lines represent fits to equations 5.6 and 5.7, respectively. (c) PL decay curves of the Mn⁴⁺ emission from K₂TiF₆:Mn⁴⁺ (0.01%) at various temperatures between 0 and 600 K ($\lambda_{exc} = 450$ nm and $\lambda_{em} = 631$ nm). (d) Temperature dependence of the Mn⁴⁺ emission lifetime for K₂TiF₆:Mn⁴⁺ (0.01%). The red and green lines represent fits to equations 5.4 and 5.8, respectively. The cyan line gives the fit for equation 5.4 (red line) divided by two.

Above a temperature of 400 K the intensities of both the anti-Stokes and Stokes emission lines start to decrease (marked by dashed arrow in Figure 5.5a), which indicates the onset of non-radiative transitions from the ²E excited state. The luminescence is fully quenched at 600 K. From the emission spectra recorded in the temperature range of 4 to 600 K we obtain the temperature dependence of the integrated PL intensity (I_{PL}), which is displayed in Figure 5.5b. The intensity is given relative to the integrated PL intensity at room temperature (I_{RT}). The PL intensity of K₂TiF₆:Mn⁴⁺ (0.01%) gradually increases

between 4 and 350 K, but then at higher temperatures rapidly drops due the onset of non-radiative transitions (luminescence quenching).

An alternative method to determine the luminescence quenching temperature is by measuring luminescence decay times. Here we examine the luminescence decay of $\text{K}_2\text{TiF}_6:\text{Mn}^{4+}$ (0.01%). Figure 5.5c shows a selection of the PL decay curves of $\text{K}_2\text{TiF}_6:\text{Mn}^{4+}$ (0.01%) we measured in the temperature range of 4 to 600 K. The decay of the Mn^{4+} emission is single exponential and becomes faster with increasing temperature. The PL decay is on the order of milliseconds, which is expected as the transition between the ${}^2\text{E}$ and ${}^4\text{A}_2$ state is both parity- and spin-forbidden. In Figure 5.5d the Mn^{4+} emission lifetime (determined by fitting the data to a single exponential decay function) is plotted as function of temperature. The Mn^{4+} emission lifetime shows a steady decrease, starting above 50 K. The decrease in lifetime begins to level off between 300 and 400 K but then shows a rapid decrease above 400 K.

The temperature dependences observed in Figure 5.5b,d are quite exceptional. For most luminescent materials such as lanthanide-doped inorganic phosphors the PL intensity and lifetime are usually relatively constant with temperature and start to decrease once thermal quenching sets in [6,41,42]. The PL intensity of $\text{K}_2\text{TiF}_6:\text{Mn}^{4+}$ however rises by 40% between 4 and 350 K and the lifetime decreases significantly before thermal quenching takes place. To understand the peculiar temperature dependences of the Mn^{4+} emission intensity and lifetime, we first discuss how the radiative decay rate of the ${}^2\text{E}$ state changes with temperature. The ${}^2\text{E} \rightarrow {}^4\text{A}_2$ emission of $\text{K}_2\text{TiF}_6:\text{Mn}^{4+}$ mainly consists of anti-Stokes and Stokes vibronic emissions, as was shown in Figure 5.4c. Since these vibronic emissions are due to coupling of the ${}^2\text{E} \rightarrow {}^4\text{A}_2$ transition with vibrational modes, their transition probabilities increase with phonon population. The population of phonon modes is given by the phonon occupation number n , which increases with temperature according to [43]:

$$n = \frac{1}{\exp(h\nu/k_{\text{B}}T) - 1} \quad (5.1)$$

In equation 5.1 k_{B} is the Boltzmann constant and $h\nu$ is the energy of the phonon coupling to the ${}^2\text{E} \rightarrow {}^4\text{A}_2$ transition. The transition probabilities P_{R} of the anti-Stokes and Stokes vibronics scale with n by,

$$\text{Anti-Stokes:} \quad P_{\text{R}}(T) = P_{\text{R}}(0) [n] \quad (5.2)$$

$$\text{Stokes:} \quad P_{\text{R}}(T) = P_{\text{R}}(0) [n + 1] \quad (5.3)$$

where $P_{\text{R}}(0)$ is the transition probability at $T = 0$ K. As the radiative lifetime τ_{R} is proportional to $1/[P_{\text{R}}(\text{anti-Stokes}) + P_{\text{R}}(\text{Stokes})]$, it follows from equations 5.1 to 5.3 that

$$\tau_R(T) = \frac{\tau_R(0)}{\coth(h\nu/2k_B T)} \quad (5.4)$$

Here $\tau_R(0)$ is the radiative lifetime at $T = 0$ K. In Figure 5.5d equation 5.4 (red line) is plotted for $\tau_R(0) = 12.3$ ms and $h\nu = 216$ cm⁻¹ (phonon energy of the intense ν_6 mode emission). It can be seen that equation 5.4 accurately describes the measured temperature dependence of the Mn⁴⁺ emission lifetime up to 375 K (102 °C), confirming that the decay of the ²E state is mainly radiative up to this temperature. The radiative lifetime of the Mn⁴⁺ emission shortens with temperature due to thermal population of asymmetric (odd-parity) vibrational modes at higher temperatures.

The present model assuming coupling with one dominant vibrational mode (ν_6) gives a good description of the experimentally observed decrease in lifetime between 4 and 375 K. The model could be refined by including all three asymmetric vibrational modes, weighed for the relative intensities of their emission lines. In addition, the energy difference between the ²E and ⁴T₂ state shows a small variation with temperature. This can also affect the lifetime due to partial lifting of the spin selection rule by enhanced admixture of the ⁴T₂ state through spin-orbit coupling when the ²E–⁴T₂ gap becomes smaller [44]. In first approximation these effects can however be neglected and it is clear that the decrease in lifetime up to 375 K is caused by an increase of the ²E radiative decay rate through enhanced Stokes and anti-Stokes emission rates for the ν_6 vibrational mode.

Next, we investigate the increase in PL intensity between 4 and 350 K. The PL intensity of a luminescent material is equal to the product of the PL quantum efficiency and number of absorbed photons. The PL quantum efficiency η of K₂TiF₆:Mn⁴⁺ can be expressed as,

$$\eta = \frac{\gamma_R}{\gamma_R + \gamma_{NR}} \quad (5.5)$$

where γ_R and γ_{NR} are the radiative and non-radiative decay rates of the ²E state. The results in Figure 5.5d show that the decay of the ²E state is mainly radiative up to 375 K, so we can assume that γ_{NR} is negligible between 0 and 350 K. The value for η is therefore approximated as a constant close to unity and will have no influence on the temperature dependence of the PL intensity between 0 and 350 K. On the other hand, the ⁴A₂ → ⁴T₂ absorption will change with temperature. Like the ²E → ⁴A₂ transition, the ⁴A₂ → ⁴T₂ transition is electric dipole (parity) forbidden but gains intensity by coupling with odd-parity vibrations of the MnF₆²⁻ group [15]. Similar to the vibronic emissions, the transition probabilities P_{AB} of the vibronic ⁴A₂ → ⁴T₂ absorptions scale with n for anti-Stokes vibronics and $n + 1$ for Stokes vibronics. As a result, the PL intensity I_{PL} scales with temperature as [43],

$$I_{PL}(T) = I(0) \coth\left(\frac{h\nu}{2k_B T}\right) \quad (5.6)$$

with $I(0)$ being the PL intensity at $T = 0$ K. The increase in PL intensity between 4 and 350 K agrees well with the temperature dependence given by equation 5.6 (see Figure 5.5b) and we conclude that the higher PL intensity at 350 K is due to a stronger absorption of excitation light by the $\text{K}_2\text{TiF}_6:\text{Mn}^{4+}$ (0.01%) phosphor. An increase in PL intensity between 4 and 350 K due to enhanced absorption is observed for all investigated Mn^{4+} doping concentrations (see Figure 5.6). At high Mn^{4+} doping concentrations (i.e. 5.4 and 15.7%) the intensity increase is however smaller because of saturation effects (strong absorption of light at high dopant concentrations causes a sub-linear increase of the fraction of absorbed light with the transition probability) [6]. The fit to equation 5.6 in Figure 5.5b was obtained with a phonon energy $h\nu$ of 350 cm^{-1} , which is higher than the ν_6 mode energy of 216 cm^{-1} . This indicates that besides the ν_6 mode also other higher energy vibrational modes are involved and need to be included for an accurate description of the temperature dependence of the PL intensity.

Above 400 K the PL intensity of $\text{K}_2\text{TiF}_6:\text{Mn}^{4+}$ (0.01%) starts to decrease, as is shown in Figure 5.5a,b. This indicates that non-radiative relaxation sets in above 400 K. The non-radiative decay probability quickly increases with temperature above 400 K and as a result the luminescence is quenched, with no emission intensity remaining at 600 K. The luminescence quenching temperature $T_{1/2}$, the temperature at which the PL intensity has decreased to half of its maximum value, is determined to be 462 K. The Mn^{4+} emission lifetime also rapidly decreases once thermal quenching sets in. The data in Figure 5.5d show that above 400 K the Mn^{4+} emission lifetime is shorter than the radiative lifetime τ_R predicted by equation 5.4 (red line). The lifetime shortens because of an additional thermally activated non-radiative contribution to the decay of the ${}^2\text{E}$ state. From the temperature dependence of the lifetime, the luminescence quenching temperature

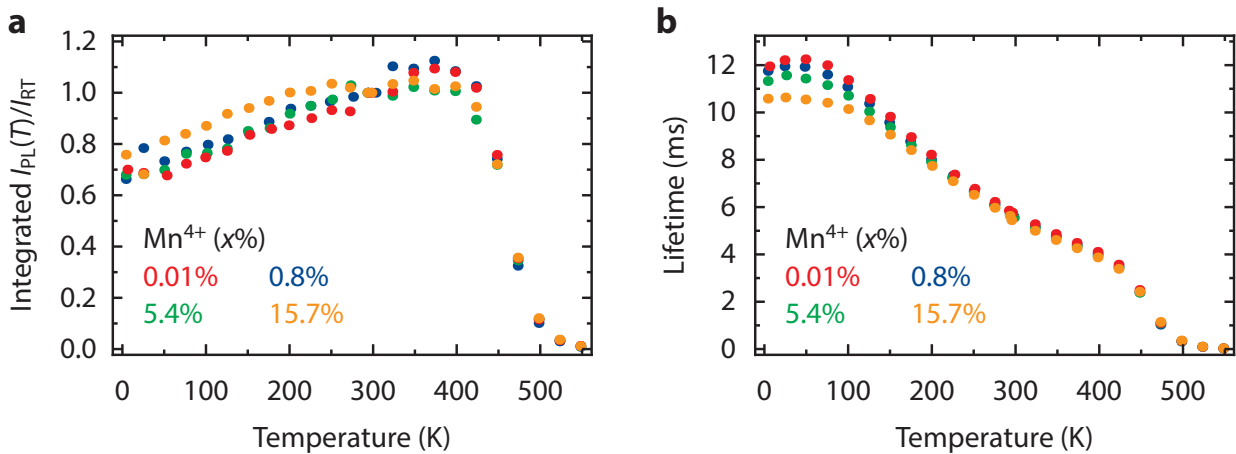


Figure 5.6 – (a) Integrated PL intensity of $\text{K}_2\text{TiF}_6:\text{Mn}^{4+}$ ($x\%$) as a function of temperature for $x = 0.01$ (red), 0.8 (blue), 5.4 (green) and 15.7% (orange). The integrated PL intensity I_{PL} is scaled to the integrated PL intensity at room temperature I_{RT} . (b) Temperature dependence of the Mn^{4+} emission lifetime for $\text{K}_2\text{TiF}_6:\text{Mn}^{4+}$ with 0.01% (red), 0.8% (blue), 5.4% (green) and 15.7% (orange) Mn^{4+} .

$T_{1/2}$ can be determined by locating the temperature at which the emission lifetime has decreased to half of its radiative lifetime value. To estimate $T_{1/2}$ we divide the value from the fit of equation 5.4 for the radiative lifetime τ_R by a factor of 2 (Figure 5.5d, cyan line). The cyan line crosses the data points at 457 K. This value for $T_{1/2}$ is very close to the $T_{1/2}$ of 462 K obtained from the PL intensity measurements.

Thermal quenching can be described by a thermally activated process with an activation energy ΔE . The activation energy is obtained by fitting a modified Arrhenius equation to the temperature dependence of the PL intensity I_{PL} between 350 and 600 K [42,45]:

$$I_{PL}(T) = \frac{I(0)}{1 + A \times \exp(-\Delta E/k_B T)} \quad (5.7)$$

In equation 5.7 $I(0)$ is the maximum PL intensity, k_B is the Boltzmann constant and A is a rate constant for the thermal quenching process. The best fit to equation 5.7 (green line in Figure 5.5b) gives an activation energy ΔE of 9143 cm⁻¹ and a rate constant A of 2.5×10^{12} . We can also determine ΔE by fitting the temperature dependence of the Mn⁴⁺ emission lifetime $\tau(T)$ to the following expression [46]:

$$\tau(T) = \frac{\tau_R(T)}{1 + \left(\frac{\tau_R(T)}{\tau_{NR}}\right) \exp(-\Delta E/k_B T)} \quad (5.8)$$

Here $1/\tau_{NR}$ is the non-radiative decay rate and $\tau_R(T)$ is the radiative lifetime as described by equation 5.4 with $\tau_R(0) = 12.3$ ms and $h\nu = 216$ cm⁻¹. We fit equation 5.8 to the Mn⁴⁺ emission lifetimes (green line in Figure 5.5d) and find an activation energy ΔE of 7100 cm⁻¹ and a prefactor $1/\tau_{NR}$ of 1.5×10^{12} s⁻¹. The ΔE is somewhat lower than the activation energy of 9143 cm⁻¹ determined from the PL intensity but based on the two values we conclude that the activation energy of the thermal quenching process is ~8000 cm⁻¹. The rate constants A and $1/\tau_{NR}$ should be approximately equal to the vibrational frequencies of the MnF₆²⁻ group. The ν_6 vibrational mode has a frequency of 6.5×10^{12} s⁻¹, which is close to the rate constants found by the fits with equations 5.7 and 5.8.

The variation in values for activation energy and prefactors can be explained by the fact that thermal quenching processes are more complex than a simple thermally activated process with a single activation energy. For example, for the thermally activated crossover from the excited state to the ground state, Struck and Fonger have shown that the temperature dependence of the non-radiative process is accurately described by considering vibrational wavefunction overlap [45,47]. For the present discussion this more complex analysis is not needed but it is important to realize that the Struck–Fonger model gives a more correct description of the actual quenching process (crossover to the ground state via overlap of resonant vibrational wavefunctions).

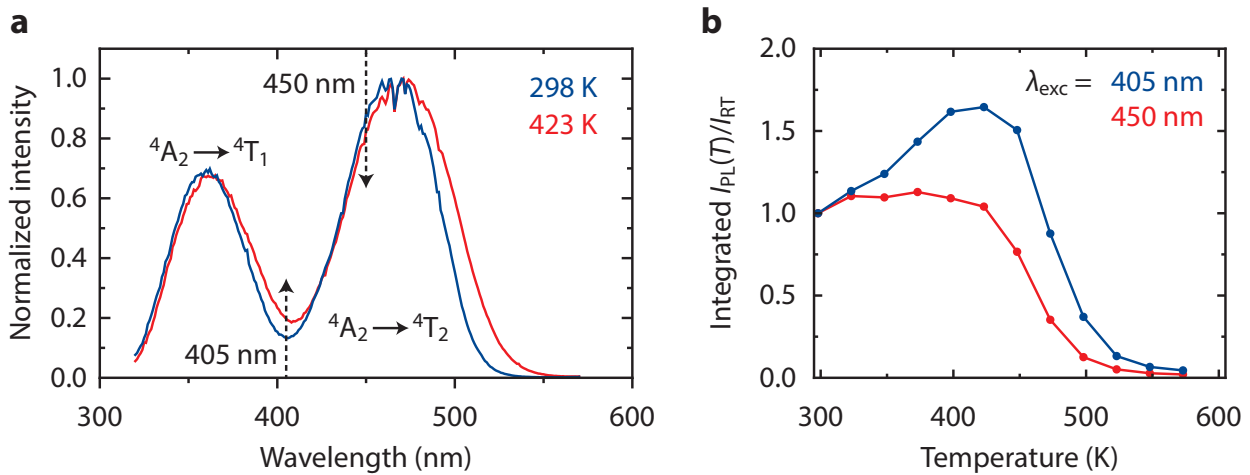


Figure 5.7 – (a) Excitation spectra ($\lambda_{em} = 631$ nm) of $K_2TiF_6:Mn^{4+}$ (0.8%) at $T = 298$ K (blue) and 423 K (red). (b) Temperature dependence of the integrated PL intensity from $K_2TiF_6:Mn^{4+}$ (0.8%) for $\lambda_{exc} = 405$ nm (blue) and 450 nm (red). The PL intensity I_{PL} is given relative to the PL intensity at room temperature I_{RT} .

Before we discuss the thermal quenching mechanism, we want to note that the excitation wavelength can have a large influence on the temperature dependence observed for I_{PL} . Because the Mn^{4+} excitation bands broaden and redshift with temperature (Figure 5.7a), exciting at the ${}^4A_2 \rightarrow {}^4T_2$ band maximum (450 nm) or ${}^4A_2 \rightarrow {}^4T_2$ band onset (405 nm) results in very different temperature dependences (Figure 5.7b). Consequently, different quenching temperatures and activation energies are obtained. As the true $T_{1/2}$ and ΔE are obtained when effects due to band broadening and shifting are minimized, the preferred excitation wavelength is at or close to the band maximum when measuring the temperature dependence for I_{PL} . However, even then a change in the emission intensity by variations in the absorption strength at the excitation wavelength can introduce an error in $T_{1/2}$. In general, temperature-dependent lifetime measurements provide a more reliable value for $T_{1/2}$ [6].

5.3.3 Thermal quenching in Mn^{4+} -doped fluorides

The activation energy and quenching temperature determined in the previous section can be used to study which non-radiative relaxation process is responsible for the quenching of the Mn^{4+} luminescence in Mn^{4+} -doped fluorides. We will discuss four possible quenching processes: (1) multi-phonon relaxation, (2) thermally activated photoionization, (3) thermally activated crossover via the $F^- \rightarrow Mn^{4+}$ charge-transfer (CT) state to the 4A_2 ground state and (4) thermally activated crossover via the $Mn^{4+} {}^4T_2$ excited state to the 4A_2 ground state.

In the configurational coordinate diagram the parabola of the $Mn^{4+} {}^2E$ and 4A_2 state are at the same equilibrium position and luminescence quenching due to direct crossover from the 2E excited state to the 4A_2 ground state is not possible (see configuration coordinate

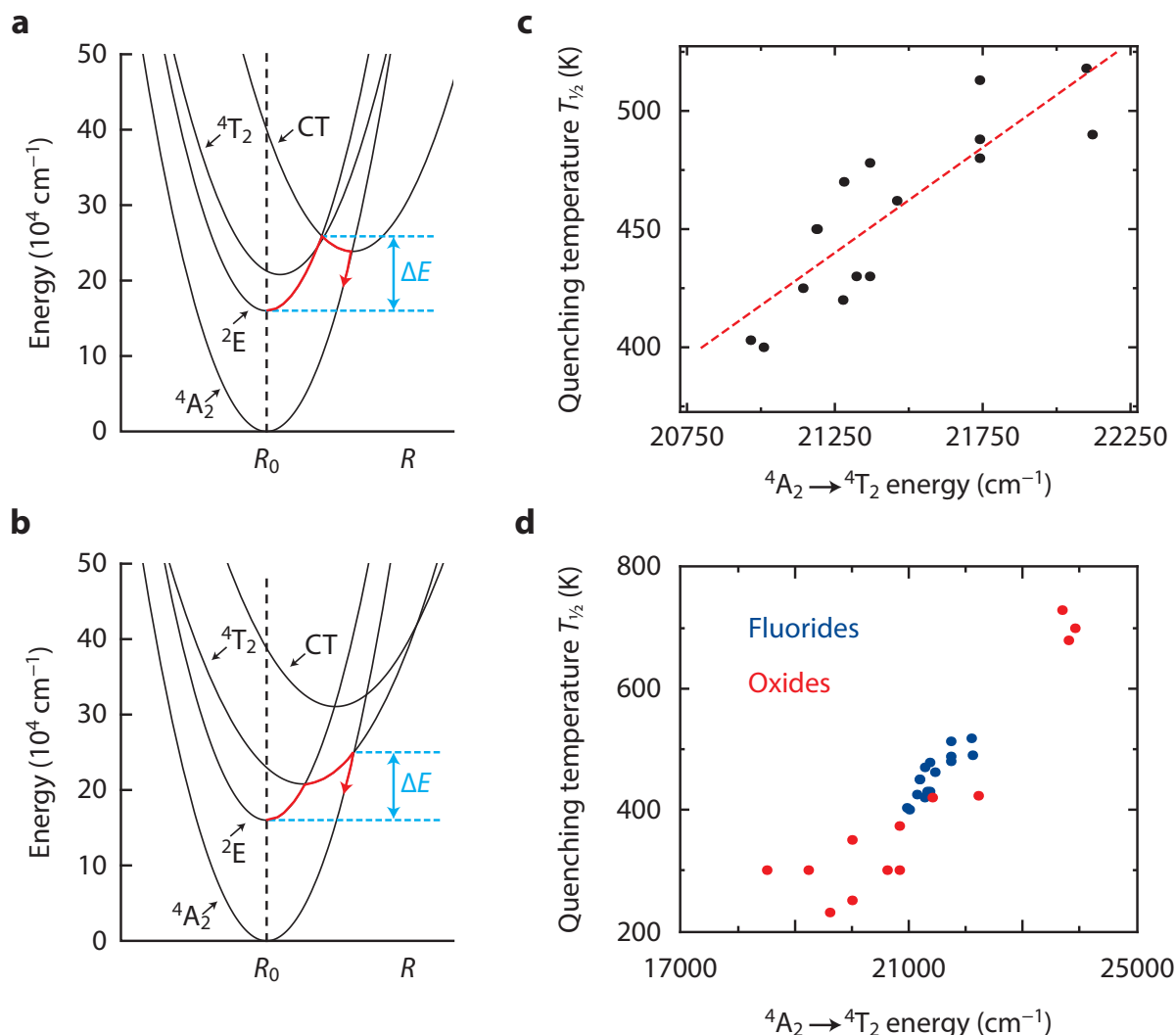


Figure 5.8 – Thermal quenching in Mn⁴⁺-doped fluorides. (a,b) Configuration coordinate diagrams showing luminescence quenching due to (a) thermally activated crossover via the F⁻ → Mn⁴⁺ charge-transfer (CT) state and (b) thermally activated crossover via the Mn⁴⁺ ⁴T₂ excited state. (c) Quenching temperature T_{1/2} of Mn⁴⁺-doped fluoride phosphors as a function of the ⁴A₂ → ⁴T₂ transition energy. The red dashed line is a linear fit to the data points (d) Quenching temperature T_{1/2} of Mn⁴⁺-doped fluorides (blue dots) and Mn⁴⁺-doped oxides (red dots) as a function of the ⁴A₂ → ⁴T₂ transition energy.

diagram in Figure 5.8a). The ⁴A₂ ground state may however be reached by multi-phonon relaxation. In some works on Mn⁴⁺-doped oxides, thermal quenching of the Mn⁴⁺ luminescence was attributed to multi-phonon relaxation [48–51]. The temperature dependence of the luminescence intensity and emission lifetime was explained with a multi-phonon relaxation process involving more than 40 phonons. Also in Mn⁴⁺-doped fluorides, a high number of phonons is necessary to reach the ⁴A₂ ground state via multi-phonon relaxation. In a fluoride, the maximum phonon energy ν_{\max} is ~ 500 cm⁻¹, so around 32 high energy vibrations are needed to bridge the ~ 16000 cm⁻¹ energy gap between the ²E and ⁴A₂ state [52]. For such high numbers of phonons ($p > 30$), it is unrealistic that non-radiative multi-phonon relaxation is responsible for thermal

quenching, as typically multi-phonon relaxation can only compete with radiative decay if the energy difference between the ground and excited state is equal to or less than 5 times the ν_{\max} of the surrounding lattice. Moreover, if quenching would occur through multi-phonon relaxation, it is expected that the $T_{1/2}$ is relatively similar for the different Mn^{4+} -doped fluoride phosphors since all hexafluorometallates will have around the same maximum phonon energy ν_{\max} [53]. There is however a large spread in the $T_{1/2}$ of Mn^{4+} -doped fluorides, varying from e.g. $T_{1/2} = 403$ K in $\text{Cs}_2\text{HfF}_6:\text{Mn}^{4+}$ to $T_{1/2} = 518$ K in $\text{K}_2\text{SiF}_6:\text{Mn}^{4+}$ (see Table 5.1 and Chapter 2) [54]. Finally, the non-radiative decay rate due to multi-phonon relaxation increases with temperature as the non-radiative decay rate at low temperatures multiplied by $(n + 1)^p$ [43]. This implies that also at low temperatures multi-phonon relaxation should be effective as phonon emission can always occur. The observation of quantum efficiencies close to 100% at ambient temperature is not consistent with multi-phonon relaxation. We conclude that thermal quenching of the Mn^{4+} luminescence cannot be due to multi-phonon relaxation from the ${}^2\text{E}$ state.

Alternatively, the thermal quenching can be due to thermally activated photoionization of an electron from the Mn^{4+} ${}^2\text{E}$ state to the fluoride host conduction band. Thermally activated photoionization typically quenches the emission from a luminescent center if the emitting state is close in energy to the host conduction band [26,55]. In DFT

Table 5.1 – Quenching temperature $T_{1/2}$ (K), ${}^4\text{A}_2 \rightarrow {}^4\text{T}_2$ energy (cm^{-1}) and M^{4+} -F distance (\AA) for Mn^{4+} -doped fluoride materials.

Host lattice	${}^4\text{A}_2 \rightarrow {}^4\text{T}_2$ energy (cm^{-1})	$T_{1/2}$ (K)	M^{4+} -F distance (\AA)	References
K_2TiF_6	21459	462	1.8605	This work
K_2SiF_6	22099	518	1.6827	This work
K_2SiF_6	22120	490	1.6827	[15]
K_2GeF_6	21280	470	1.7717	[15]
K_2TiF_6	21190	450	1.8605	[15]
K_2TiF_6	21368	478	1.8605	[13]
Na_2SiF_6	21739	488	1.6746	[21]
Rb_2SiF_6	21739	480	1.6904	[18]
Rb_2TiF_6	21186	450	unknown	[18]
Rb_2GeF_6	21739	513	1.7717	[60]
Cs_2GeF_6	21277	420	1.8042	[22]
Cs_2SiF_6	21368	430	1.8730	[22]
Cs_2HfF_6	20964	403	2.0288	[54]
BaSiF_6	21322	430	1.7065	[23]
BaSnF_6	21008	400	1.9485	[61]
BaTiF_6	21142	425	1.8487	[62]

calculations large bandgaps of around 8 eV have been found for fluoride hosts like K₂SiF₆ and K₂TiF₆ [44,56]. It is therefore unlikely that the Mn⁴⁺ ²E state is in close proximity of host conduction band levels. Furthermore, if quenching would occur by thermally activated photoionization, it is expected that the quenching temperature will be higher in Mn⁴⁺-doped fluorides than in Mn⁴⁺-doped oxides, as fluorides hosts have larger bandgaps than oxide hosts. Some Mn⁴⁺-doped oxides however have much higher quenching temperatures than Mn⁴⁺-doped fluorides (see Tables 5.1 and 5.2) [57–59]. We therefore conclude that thermal quenching in Mn⁴⁺-doped fluorides is not caused by thermally activated photoionization but instead occurs via another mechanism. It will however be interesting to perform photoconductivity measurements on Mn⁴⁺ phosphors at elevated temperatures to provide convincing evidence for a possible role of photoionization in thermal quenching processes of Mn⁴⁺ emission.

As mentioned in Section 5.1, it has been proposed that the thermal quenching in Mn⁴⁺-doped fluorides occurs by thermally activated crossover via the Mn⁴⁺ ⁴T₂ state or the F⁻ → Mn⁴⁺ charge-transfer (CT) state [15,24,26]. Both these states have a different electron configuration than the ⁴A₂ ground state and their potential curves are therefore displaced relative to the potential curve of the ⁴A₂ ground state (see configuration coordinate diagrams in Figure 5.8a,b). Hence, the parabolas of the ⁴T₂ and CT state cross the parabola of the ⁴A₂ ground state. The difference between the potential curve equilibrium positions of the ground state and excited states is given by the offset $\Delta R = R_0' - R_0$. By using the energies of the ⁴A₂ → ²E, ⁴A₂ → ⁴T₂ and ⁴A₂ → CT transitions in K₂TiF₆:Mn⁴⁺ (see Figure 5.4d and Ref. [13]) and assuming certain offsets ΔR for the ⁴T₂

Table 5.2 – Quenching temperature $T_{1/2}$ (K) and ⁴A₂ → ⁴T₂ energy (cm⁻¹) for Mn⁴⁺-doped oxide materials.

Host lattice	⁴ A ₂ → ⁴ T ₂ energy (cm ⁻¹)	$T_{1/2}$ (K)	References
Mg ₄ GeO ₆	23697	730	[57]
Mg ₂₈ Ge _{7.5} O ₃₈ F ₁₀	23923	700	[26,57,58]
K ₂ Ge ₄ O ₉	20833	373	[63]
La ₃ GaGe ₅ O ₁₆	21413	420	[64]
La ₂ ZnTiO ₆	19608	230	[65]
La ₂ MgTiO ₆	20000	250	[65]
CaZrO ₃	18500	300	[25,26]
Mg ₆ As ₂ O ₁₁	23810	680	[59]
Y ₃ Al ₅ O ₁₂	20619	300	[66]
Y ₃ Al ₅ O ₁₂	20833	300	[67]
Sr ₄ Al ₁₄ O ₂₅	22222	423	[68]
SrLaAlO ₄	19231	300	[69]
LiGa ₅ O ₈	20000	350	[49]

and CT states, we can construct the configuration coordinate diagrams in Figure 5.8a,b where non-radiative relaxation occurs either via (a) the crossing of the CT and 4A_2 state or (b) the crossing of the 4T_2 and 4A_2 state. The offset of the CT state is typically larger than the offset of the 4T_2 state because transfer of charge to a ligand ion has a larger effect on the chemical bonding than a transition to an excited state within the d^3 electron configuration. Note that the diagrams in Figure 5.8a,b are schematic configuration coordinate diagrams to illustrate the different quenching mechanisms. The diagrams should not be used as a quantitative measure for the offsets and curvatures of the Mn^{4+} energy states.

In the diagram shown in Figure 5.8a the CT state has a larger offset ΔR than the 4T_2 state, which causes the CT parabola to cross the 4A_2 parabola at lower energies than the 4T_2 parabola. Thermal activation over the energy barrier ΔE will allow crossover from the 2E state into the CT state, which is then followed by non-radiative relaxation to the ground state via the crossing of the CT and 4A_2 parabola. In this way the luminescence is quenched by thermally activated crossover via the CT state. Alternatively, thermal quenching of the Mn^{4+} luminescence may be due to the mechanism depicted in Figure 5.8b. Here the CT state has a smaller offset ΔR compared to Figure 5.8a and its potential curve is therefore at higher energies. In addition, the 4T_2 state has a slightly larger offset than in Figure 5.8a. As a result, the crossing of the 4T_2 and 4A_2 parabola is at lower energies than the crossing of the CT and 4A_2 parabola. In this case non-radiative relaxation to the ground state will take place via the crossing of the 4T_2 and 4A_2 parabola, which can be reached from the 2E state by thermal activation over the energy barrier ΔE in Figure 5.8b.

The activation energies ΔE in the configuration coordinate diagrams are $\sim 8000\text{ cm}^{-1}$, which is also the ΔE obtained from the temperature-dependent measurements. This indicates that both mechanisms in Figure 5.8a,b can explain the thermal quenching of the Mn^{4+} luminescence. To determine which of these two mechanisms is responsible for the luminescence quenching, we compare the quenching temperature $T_{1/2}$ of $K_2TiF_6:Mn^{4+}$ to the $T_{1/2}$ of other Mn^{4+} -doped materials. A relation between the quenching temperature and the energy of either the CT or 4T_2 state in a variety of hosts will give insight. If quenching occurs because of thermally activated crossover from the CT state to the 4A_2 state, $T_{1/2}$ will be higher for Mn^{4+} -doped solids with higher CT transition energies. In $K_2TiF_6:Mn^{4+}$ and other Mn^{4+} -doped fluorides the $F^- \rightarrow Mn^{4+}$ CT transition is at $\sim 40000\text{ cm}^{-1}$ [13,15]. Mn^{4+} -doped oxides have lower $O^{2-} \rightarrow Mn^{4+}$ CT transition energies of $30000\text{--}35000\text{ cm}^{-1}$ and are therefore expected to have lower $T_{1/2}$ than fluorides if quenching occurs by the mechanism in Figure 5.8a [26,27,69,70]. Some Mn^{4+} -doped oxides however have much higher quenching temperatures than Mn^{4+} -doped fluorides. For example, the compositions $Mg_4GeO_6:Mn^{4+}$, $Mg_{28}Ge_{7.5}O_{38}F_{10}:Mn^{4+}$ and $Mg_6As_2O_{11}:Mn^{4+}$ have a $T_{1/2}$ of $\sim 700\text{ K}$ [57–59], while $K_2TiF_6:Mn^{4+}$ and other Mn^{4+} -doped fluorides have a $T_{1/2}$ of $400\text{--}500\text{ K}$ (see Figure 5.5b and Tables 5.1 and 5.2). From this comparison we conclude

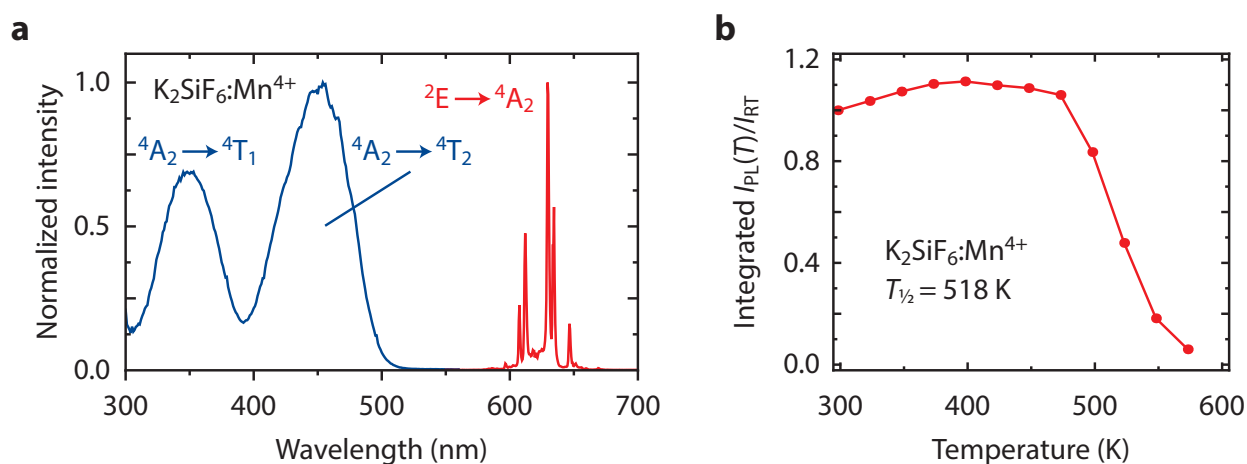


Figure 5.9 – (a) Room-temperature PL excitation (blue, $\lambda_{em} = 630$ nm) and emission (red, $\lambda_{exc} = 460$ nm) spectra of $K_2SiF_6:Mn^{4+}$. The emission and excitation bands/lines are assigned to corresponding transitions in the d^3 Tanabe–Sugano diagram. (b) Integrated PL intensity of $K_2SiF_6:Mn^{4+}$ ($\lambda_{exc} = 450$ nm) as a function of temperature between 300 and 600 K. The PL intensity I_{PL} is given relative to the PL intensity at room temperature I_{RT} . The luminescence quenching temperature $T_{1/2}$ is 518 K.

that thermal quenching in Mn⁴⁺-doped fluorides is not caused by thermally activated crossover from the $F^- \rightarrow Mn^{4+}$ CT state to the 4A_2 ground state.

Alternatively, thermal quenching of the Mn⁴⁺ luminescence can be caused by thermally activated crossover from the Mn⁴⁺ 4T_2 excited state to the 4A_2 ground state (Figure 5.8b). To investigate if for Mn⁴⁺ quenching occurs by this mechanism, we compare the $T_{1/2}$ and $^4A_2 \rightarrow ^4T_2$ transition energies for $K_2TiF_6:Mn^{4+}$ and a variety of other Mn⁴⁺-doped fluorides. From the literature and measurements on Mn⁴⁺ luminescence we have collected quenching temperatures and luminescence spectra, preferably for systems with low doping concentrations. The results in Figures 5.4d and 5.5b show that $K_2TiF_6:Mn^{4+}$ has a $^4A_2 \rightarrow ^4T_2$ energy of 21459 cm⁻¹ and a $T_{1/2}$ of 462 K (maximum of $^4A_2 \rightarrow ^4T_2$ excitation band taken as $^4A_2 \rightarrow ^4T_2$ energy). For $K_2SiF_6:Mn^{4+}$ we measured a $^4A_2 \rightarrow ^4T_2$ energy of 22099 cm⁻¹ and a $T_{1/2}$ of 518 K (Figure 5.9, $K_2SiF_6:Mn^{4+}$ BR301-C commercial phosphor from Mitsubishi Chemical, Japan). This indicates that the quenching temperature is higher for compositions with higher 4T_2 energies, which is expected when quenching occurs because of crossover from the 4T_2 state to the 4A_2 state. In Figure 5.8c we plot the quenching temperature $T_{1/2}$ against the $^4A_2 \rightarrow ^4T_2$ energy for $K_2TiF_6:Mn^{4+}$ and many other Mn⁴⁺-doped fluoride phosphors reported in literature (the data displayed in Figure 5.8c is also listed in Table 5.1). The data show that the $T_{1/2}$ increases linearly with the energy of the 4T_2 state. The clear relation shows that the thermal quenching in Mn⁴⁺-doped fluorides is due to thermally activated crossover from the 4T_2 excited state to the 4A_2 ground state.

Further confirmation for this quenching mechanism can be obtained from Mn⁴⁺

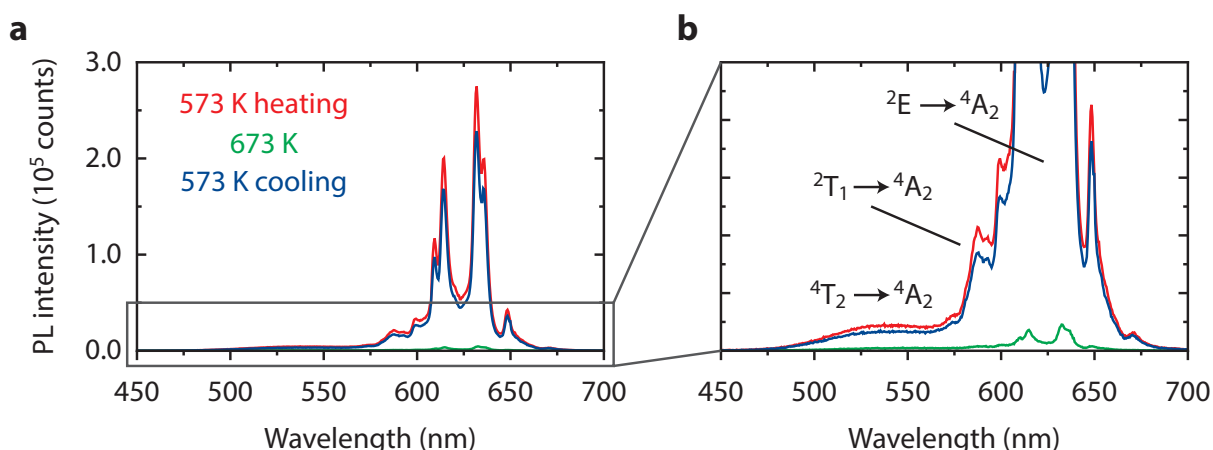


Figure 5.10 – High temperature ${}^4T_2 \rightarrow {}^4A_2$ and ${}^2T_1 \rightarrow {}^4A_2$ emission in $K_2SiF_6:Mn^{4+}$. (a) PL emission spectra of $K_2SiF_6:Mn^{4+}$ at $T = 573$ K (red), at $T = 673$ K (green) and at $T = 573$ K upon cooling from 673 K (blue). The excitation wavelength is 360 nm. (b) Zoom of the gray-lined area in (a). The intense emission peaks around 620 nm are assigned to the $Mn^{4+} {}^2E \rightarrow {}^4A_2$ transition, while the weaker emissions at wavelengths shorter than 600 nm are assigned to the $Mn^{4+} {}^4T_2 \rightarrow {}^4A_2$ and ${}^2T_1 \rightarrow {}^4A_2$ transitions.

luminescence spectra measured at elevated temperatures. Figure 5.10 shows emission spectra of $K_2SiF_6:Mn^{4+}$ (commercial phosphor) measured at $T = 573$ and 673 K. Besides the characteristic ${}^2E \rightarrow {}^4A_2$ emission lines, the luminescence spectra in Figure 5.10 exhibit some additional weak emission bands/lines at wavelengths shorter than 600 nm. These emissions are assigned to the $Mn^{4+} {}^4T_2 \rightarrow {}^4A_2$ and ${}^2T_1 \rightarrow {}^4A_2$ transitions. An excitation spectrum recorded for $\lambda_{em} = 530$ nm at $T = 473$ K (see Figure 5.11) confirms that the emission band centered at 530 nm is related to Mn^{4+} .

The observation of $Mn^{4+} {}^4T_2 \rightarrow {}^4A_2$ emission in $K_2SiF_6:Mn^{4+}$ at 573 K shows that the 4T_2 excited state is indeed thermally populated at elevated temperatures, and consequently can play a role in the thermal quenching process. Upon further heating to 673 K, the intensities of the ${}^4T_2 \rightarrow {}^4A_2$ and ${}^2E \rightarrow {}^4A_2$ emissions decrease (green spectrum in Figure 5.10), and after cooling to 573 K, most of the ${}^4T_2 \rightarrow {}^4A_2$ and ${}^2E \rightarrow {}^4A_2$ emission intensity is regained (blue spectrum in Figure 5.10). These measurements indicate that the emission intensity decrease between 573 and 673 K is due to thermal quenching of both the ${}^4T_2 \rightarrow {}^4A_2$ and ${}^2E \rightarrow {}^4A_2$ emission, and not due to chemical degradation of the phosphor (the small difference in intensity at 573 K before and after heating to 673 K is however attributed to phosphor degradation). The fact that both the ${}^4T_2 \rightarrow {}^4A_2$ and ${}^2E \rightarrow {}^4A_2$ emission are quenched upon raising the temperature from 573 to 673 K shows that the loss in ${}^2E \rightarrow {}^4A_2$ emission intensity is not accompanied an increase in the ${}^4T_2 \rightarrow {}^4A_2$ emission intensity, as is sometimes observed for Cr^{3+} (isoelectronic with Mn^{4+}) [47,71,72]. Instead, in $K_2SiF_6:Mn^{4+}$ the ${}^4T_2 \rightarrow {}^4A_2$ emission is quenched by non-radiative relaxation via the crossing of the 4T_2 state and 4A_2 ground state.

To investigate whether thermally activated crossing of the 4T_2 and 4A_2 state is also

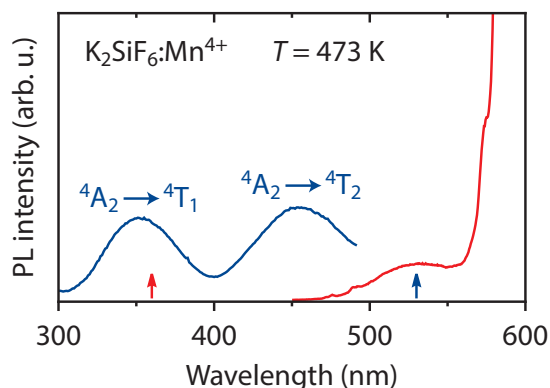


Figure 5.11 – PL excitation (blue, $\lambda_{em} = 530$ nm) and emission (red, $\lambda_{exc} = 360$ nm) spectra of $K_2SiF_6:Mn^{4+}$ at $T = 473$ K. The red and blue arrows indicate the excitation and emission wavelengths used for recording the spectra, respectively. The excitation spectrum (blue) of the weak emission band centered at 530 nm consists of two excitation bands that are assigned to the $^4A_2 \rightarrow ^4T_1$ and $^4A_2 \rightarrow ^4T_2$ transitions of Mn^{4+} .

responsible for temperature quenching of the Mn^{4+} -luminescence in Mn^{4+} -doped oxides, we extend the data set of Figure 5.8c with quenching temperatures reported for Mn^{4+} -doped oxides. Figure 5.8d shows the quenching temperature $T_{1/2}$ as a function of the $^4A_2 \rightarrow ^4T_2$ energy for the Mn^{4+} -doped fluorides and oxides listed in Tables 5.1 and 5.2. The results show that $T_{1/2}$ increases with the energy of the $^4A_2 \rightarrow ^4T_2$ transition. This indicates that the Mn^{4+} emissions of Mn^{4+} -doped fluorides and oxides are both quenched due to thermally activated crossover from the 4T_2 excited state to the 4A_2 ground state. This is in contrast with earlier findings that reported that the quenching temperature of Mn^{4+} in oxides is determined by the energy of the charge-transfer state [24–27].

The present results and analysis provide strong evidence that in many Mn^{4+} phosphors the thermal quenching mechanism involves thermally activated crossover via the 4T_2 excited state. A contribution from other mechanisms cannot be ruled out and further research, for example photoconductivity measurements and high pressure studies, can give additional information on the role of alternative quenching mechanisms.

Finally, in view of applications it is now interesting to see how we can control the 4T_2 level energy (and thereby $T_{1/2}$) through the choice of the host lattice. The energy of the Mn^{4+} 4T_2 state depends on the crystal field splitting Δ_O (see Figure 5.4b), where Δ_O is typically larger for shorter Mn–F distances [54,73]. As a result, the energy of the Mn^{4+} $^4A_2 \rightarrow ^4T_2$ transition increases if the distance between the M^{4+} host cation and F^- ligands becomes smaller (Figure 5.12a). This implies that the luminescence quenching temperature of Mn^{4+} -doped fluorides can be raised by choosing host lattices with short M^{4+} – F^- distances. Indeed, it has been suggested that the quenching temperature increases if the radius of the cation substituted by Mn^{4+} decreases [11,18]. In Figure 5.12b we plot the quenching temperature $T_{1/2}$ against the ionic radius of the M^{4+} host cation (ionic radii were obtained from Ref. [74]). The data show that in general the $T_{1/2}$ is lower for hosts with larger M^{4+} ions (Hf^{4+} , Sn^{4+} and Ti^{4+}). The huge spread in the data per M^{4+} ion however indicates that the M^{4+} ionic radius alone is not enough to predict the quenching temperature. The crystal field splitting, depending on the actual Mn^{4+} –ligand distance, will give a better indication of the quenching temperature.

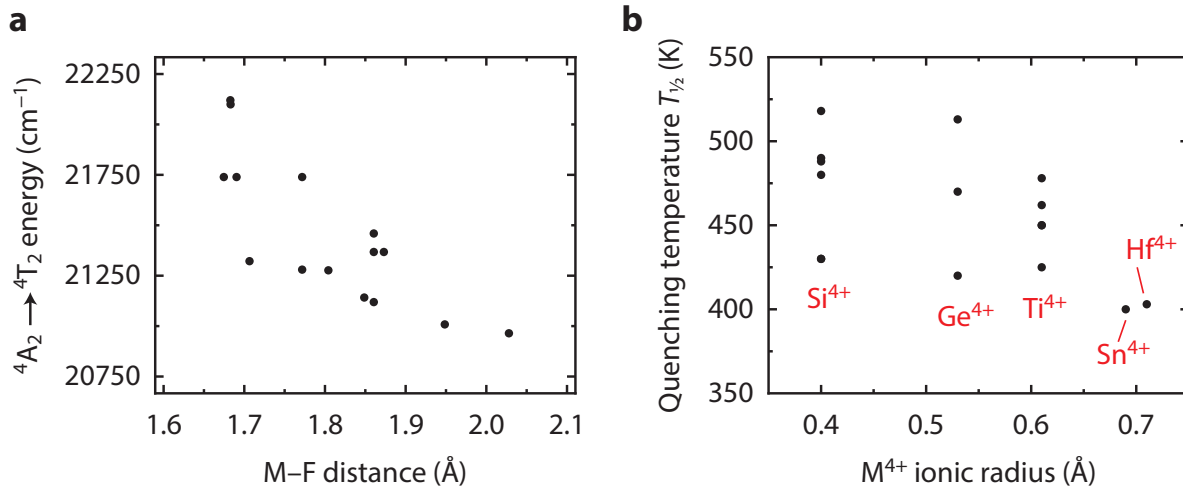


Figure 5.12 – (a) Energy of the $\text{Mn}^{4+} {}^4A_2 \rightarrow {}^4T_2$ transition against the $M^{4+}\text{-F}^-$ distance for Mn^{4+} -doped fluoride phosphors. (b) Dependence of the quenching temperature $T_{1/2}$ on the M^{4+} host cation ionic radius for Mn^{4+} -doped fluoride phosphors.

5.3.4 Concentration quenching

In addition to insight in the thermal quenching mechanism, concentration quenching in Mn^{4+} -doped fluorides is important for application of these phosphors in w-LEDs. The weak parity-forbidden ${}^4A_2 \rightarrow {}^4T_2$ absorption makes it necessary that commercial phosphors have high Mn^{4+} concentrations. If there is effective concentration quenching, the photoluminescence (PL) decay time and quantum efficiency (QE) will strongly decrease when the Mn^{4+} doping concentration is raised [26,28]. As an example we therefore investigate concentration quenching in $\text{K}_2\text{TiF}_6:\text{Mn}^{4+}$ by measuring the PL decay times and QE of $\text{K}_2\text{TiF}_6:\text{Mn}^{4+}$ phosphors with Mn^{4+} concentrations ranging from 0.01 to 15.7% Mn^{4+} .

Figure 5.13a presents room-temperature PL decay curves of the Mn^{4+} emission from $\text{K}_2\text{TiF}_6:\text{Mn}^{4+}$ with increasing Mn^{4+} doping concentration x . It can be seen that the PL decay becomes slightly faster as the Mn^{4+} concentration increases. We analyze the decay dynamics by fitting the PL decay curves to mono-exponential decay functions. The mono-exponential fit for $\text{K}_2\text{TiF}_6:\text{Mn}^{4+}$ (0.8%) is shown in Figure 5.13b. The fit residuals (bottom panel in Figure 5.13b) are random and the PL decay thus resembles a single exponential. This confirms that with 0.8% Mn^{4+} ions the decay of the 2E excited state is mainly radiative. Consequently, the $\text{K}_2\text{TiF}_6:\text{Mn}^{4+}$ (0.8%) phosphor has a very high QE of 90%. Figure 5.13c gives an overview of the fitted decay times (blue squares) and QE values (red dots) of $\text{K}_2\text{TiF}_6:\text{Mn}^{4+}$ with different Mn^{4+} concentrations. The emission lifetime barely shortens if the Mn^{4+} concentration is increased (5.7 ms for 0.01% Mn^{4+} to 5.4 ms for 15.7% Mn^{4+}). This suggests that in $\text{K}_2\text{TiF}_6:\text{Mn}^{4+}$ energy migration to quenching sites is inefficient. To verify this, we look at the QE values obtained for the $\text{K}_2\text{TiF}_6:\text{Mn}^{4+}$ ($x\%$) phosphors. The QE remains above 80% for Mn^{4+} doping concentrations of 5% or

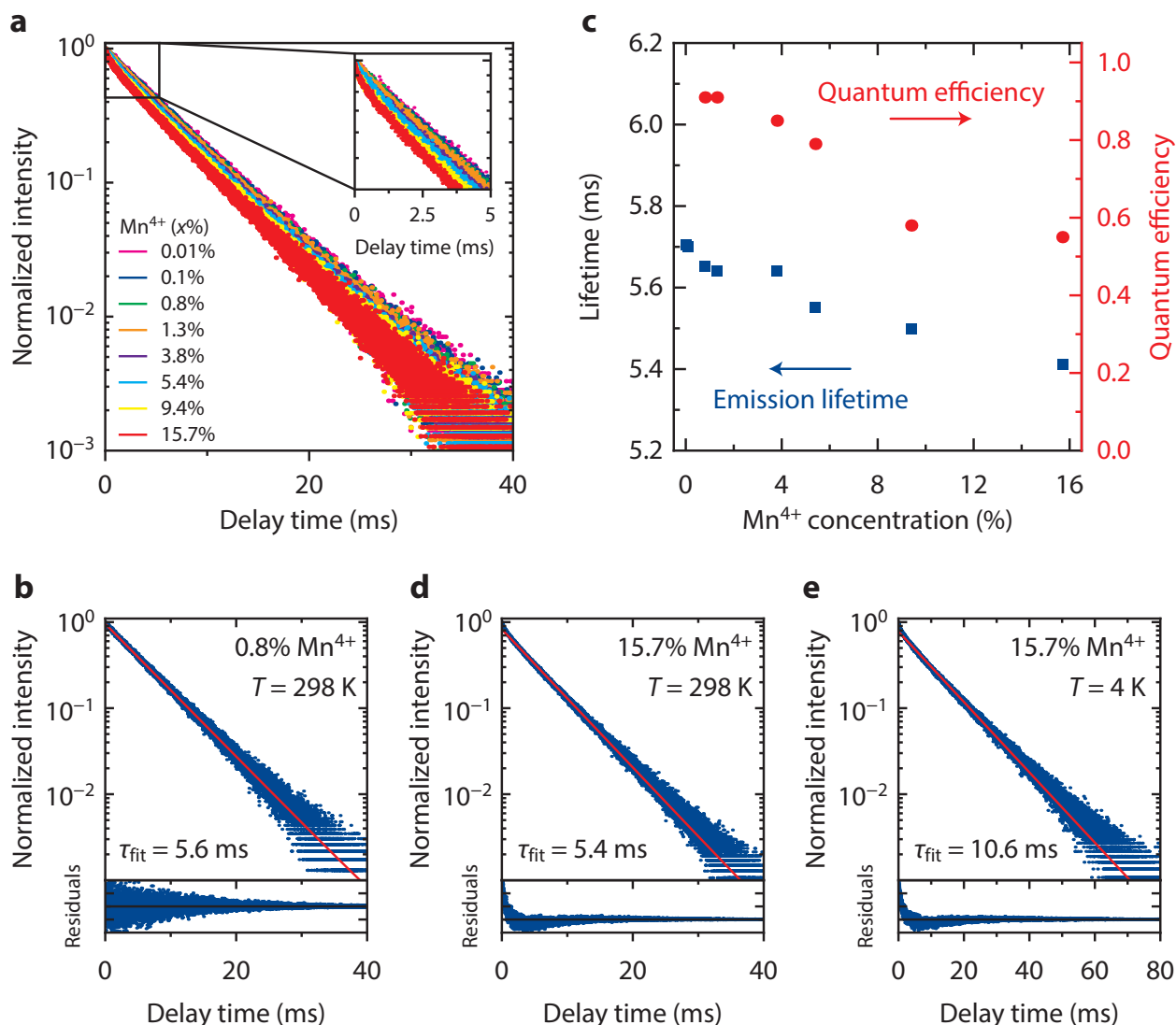


Figure 5.13 – Luminescence decay and quantum efficiency of $\text{K}_2\text{TiF}_6:\text{Mn}^{4+}$ as a function of the Mn^{4+} doping concentration. (a) Room-temperature PL decay curves of the Mn^{4+} emission from $\text{K}_2\text{TiF}_6:\text{Mn}^{4+}$ ($x\%$) for 0.01% (pink), 0.1% (blue), 0.8% (green), 1.3% (orange), 3.8% (purple), 5.4% (cyan), 9.4% (yellow) and 15.7% (red) Mn^{4+} ($\lambda_{\text{exc}} = 450\text{ nm}$ and $\lambda_{\text{em}} = 631\text{ nm}$). (b) PL decay curve of $\text{K}_2\text{TiF}_6:\text{Mn}^{4+}$ (0.8%) at $T = 298\text{ K}$. The decay time corresponding to the mono-exponential fit (red line) is 5.6 ms. The bottom panel shows the fit residuals. (c) Mn^{4+} emission lifetime (blue squares) and PL quantum efficiency (red dots) of $\text{K}_2\text{TiF}_6:\text{Mn}^{4+}$ with different Mn^{4+} doping concentrations. (d,e) PL decay curves of $\text{K}_2\text{TiF}_6:\text{Mn}^{4+}$ (15.7%) at (d) $T = 298\text{ K}$ and (e) $T = 4\text{ K}$. The decay times corresponding to the mono-exponential fits (red lines) are 5.4 and 10.6 ms, respectively. The bottom panels show the fit residuals.

less, which shows that concentration quenching is indeed limited up to a concentration of 5% Mn^{4+} ions. This result is important for applications in w-LEDs as these high Mn^{4+} doping concentrations (e.g. 5 mol%) are required for sufficient absorption of the blue LED light in the parity-forbidden d–d transitions [12].

For higher Mn^{4+} concentrations ($x > 10\%$) non-radiative decay from the ${}^2\text{E}$ excited state however becomes stronger and as a result the QE of $\text{K}_2\text{TiF}_6:\text{Mn}^{4+}$ falls below 60% (see

Figure 5.13c). The non-radiative decay is also visible in the PL decay curve of $\text{K}_2\text{TiF}_6:\text{Mn}^{4+}$ (15.7%), shown in Figure 5.13d. The decay dynamics are multi-exponential, which proves that with 15.7% Mn^{4+} the ${}^2\text{E}$ state decays both radiatively and non-radiatively. There is a deviation from exponential decay in the initial part of the decay curve. The faster initial decay indicates that there is enhanced quenching by single step energy transfer for Mn^{4+} ions close to a quencher. In case of energy migration, a faster decay is also expected for longer times after the excitation pulse. As this is not observed, the contribution of energy migration via many Mn^{4+} ions to quenching sites seems to be small.

To further investigate the role of energy migration in the concentration quenching of the Mn^{4+} emission, we measure a PL decay curve of $\text{K}_2\text{TiF}_6:\text{Mn}^{4+}$ (15.7%) at $T = 4$ K, which is displayed in Figure 5.13e. At $T = 4$ K energy migration among the Mn^{4+} ions (blue arrows in Figure 5.1) will be hampered as there is almost no spectral overlap between the Mn^{4+} ${}^2\text{E} \rightarrow {}^4\text{A}_2$ emission and ${}^4\text{A}_2 \rightarrow {}^2\text{E}$ excitation lines (Figure 5.14). Hence, at 4 K non-radiative decay because of energy migration to quenching sites will be suppressed. The Mn^{4+} decay dynamics in Figure 5.13e however show that the non-radiative decay is not suppressed at 4 K. The deviation from single exponential behavior is very similar to that observed at 300 K. There is an initial faster decay (explained by single step energy transfer to quenching sites) followed by a single exponential decay with a decay time very close to that measured for Mn^{4+} at low doping concentrations. This suggests that the decrease in QE at higher Mn^{4+} concentrations is not due to energy migration.

The absence of strong concentration quenching by energy migration is confirmed by the thermal quenching behavior measured for the different Mn^{4+} concentrations. In Figure 5.6 it can be seen that the luminescence quenching temperature is approximately the same for a doping concentration of 0.01% and 15.7% Mn^{4+} , which shows that effects due to thermally activated energy migration (i.e. concentration quenching) are weak. Hence, we conclude that the non-radiative decay at high Mn^{4+} concentrations is not caused by energy migration.

We instead assign the non-radiative decay to direct transfer of excitation energy from Mn^{4+} ions to quenchers (green arrow in Figure 5.1). This process can occur at all temperatures and becomes more efficient at higher Mn^{4+} dopant concentrations. With an increasing Mn^{4+} dopant concentration the stress on the K_2TiF_6 lattice grows and as a result more crystal defects (i.e. quenchers) may be formed. Additionally, more Mn^{2+} and Mn^{3+} quenchers may be incorporated in the phosphor particles at higher Mn^{4+} concentrations. Even if a very small fraction of Mn^{4+} has a different valence state than 4+, effective quenching can occur via metal-to-metal charge-transfer states. Consequently, the probability for energy transfer from Mn^{4+} ions to quenchers increases, with the result that the initial PL decay time and QE of $\text{K}_2\text{TiF}_6:\text{Mn}^{4+}$ decrease at high Mn^{4+} dopant concentrations. Synthesizing phosphor particles with few quenchers (defects, impurity ions) thus is crucial for obtaining highly luminescent Mn^{4+} -doped fluoride phosphors.

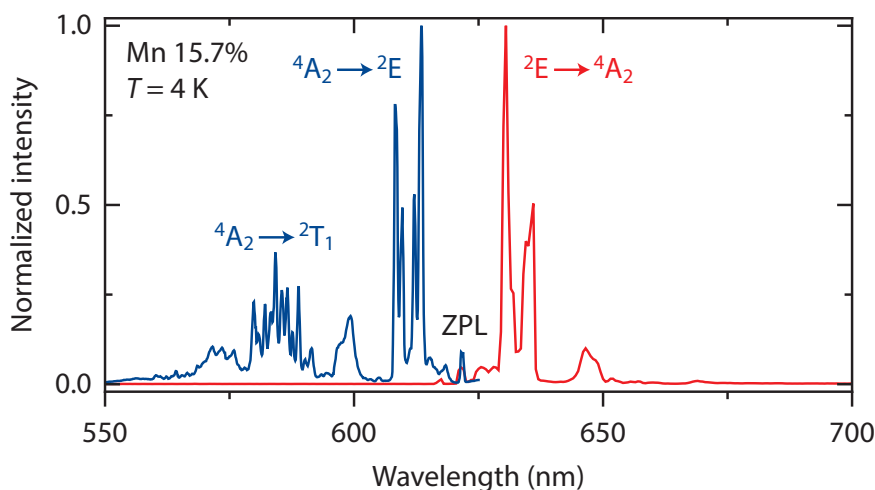


Figure 5.14 – PL excitation (blue, $\lambda_{\text{em}} = 636$ nm) and emission (red, $\lambda_{\text{exc}} = 450$ nm) spectra of $\text{K}_2\text{TiF}_6:\text{Mn}^{4+}$ (15.7%) at $T = 4$ K. For the excitation spectrum only the spectral region of the ${}^4\text{A}_2 \rightarrow {}^2\text{T}_1$ and ${}^4\text{A}_2 \rightarrow {}^2\text{E}$ transitions is shown.

The analysis presented above shows that concentration quenching via energy migration is weak in $\text{K}_2\text{TiF}_6:\text{Mn}^{4+}$. We attribute this to the fact that energy transfer between Mn^{4+} neighbors probably has to occur via exchange interaction [26,75]. The very small oscillator strength of the zero-phonon line prevents efficient resonant energy transfer via dipole-dipole interaction. Energy transfer via exchange interaction (wavefunction overlap) is possible but only active for very small (<5 Å) distances between the Mn^{4+} ions and is therefore limited to transfer between nearest neighbors (nearest neighbor distance is 4.7 Å in K_2TiF_6). With a Mn^{4+} doping concentration of e.g. 5%, most Mn^{4+} ions will not have Mn^{4+} neighbors within a distance of 5 Å [76]. Energy transfer between Mn^{4+} ions will therefore be very inefficient and as a consequence energy migration to quenching sites is limited in $\text{K}_2\text{TiF}_6:\text{Mn}^{4+}$. This situation will also apply to other Mn^{4+} -doped fluoride phosphors. We therefore expect concentration quenching by energy migration in general not to be an issue for the use of Mn^{4+} -doped fluorides in w-LEDs. The quenching that is observed for higher Mn^{4+} concentrations is explained by an increase in concentration of quenching centers with increasing manganese concentration.

5.4 Conclusions

Narrow band red-emitting Mn^{4+} phosphors form an important new class of materials for LED lighting and displays. For these applications it is important to understand and control the luminescence efficiency. We have therefore investigated quenching of the Mn^{4+} luminescence in Mn^{4+} -doped fluorides by measuring the PL intensity and luminescence lifetimes of $\text{K}_2\text{TiF}_6:\text{Mn}^{4+}$ between temperatures of 4 and 600 K and for Mn^{4+} dopant concentrations ranging from 0.01 to 15.7%. Temperature-dependent measurements of the Mn^{4+} emission intensity and lifetime for $\text{K}_2\text{TiF}_6:\text{Mn}^{4+}$ and other Mn^{4+} -doped phosphors show that thermal quenching is caused by thermally activated

crossover via the $\text{Mn}^{4+} \text{}^4\text{T}_2$ excited state. As a result, the quenching temperature is higher in Mn^{4+} -doped materials with higher $\text{}^4\text{T}_2$ state energies. These findings can be used to engineer Mn^{4+} -doped fluoride phosphors with higher quenching temperatures for application in high power w-LEDs.

Furthermore, quantum efficiency and luminescence decay measurements for a wide range of Mn^{4+} doping concentrations show that no concentration quenching occurs up to 5% Mn^{4+} in $\text{K}_2\text{TiF}_6:\text{Mn}^{4+}$. This is important for application of Mn^{4+} -doped materials in w-LEDs as high Mn^{4+} doping concentrations (e.g. 5 mol%) are required for sufficient absorption of the blue LED light in the parity-forbidden Mn^{4+} d–d transitions. At very high Mn^{4+} doping concentrations (>10 mol%) the quantum efficiency of $\text{K}_2\text{TiF}_6:\text{Mn}^{4+}$ decreases due to an increased probability for direct energy transfer from Mn^{4+} to quenching sites. Concentration quenching by Mn^{4+} – Mn^{4+} energy migration is limited. To optimize the efficiency in highly doped Mn^{4+} phosphors a synthesis procedure aimed at reducing quenching sites (defects, impurity ions, Mn^{2+} and Mn^{3+}) is crucial.

References

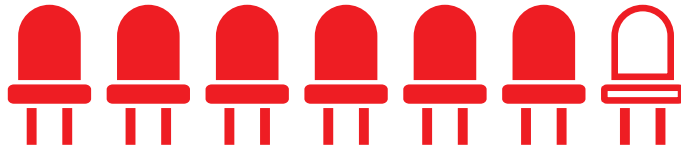
- [1] Charge of the LED brigade: A global switch to LEDs will change the lighting business, *The Economist* (2011).
- [2] M. R. Krames, O. B. Shchekin, R. Mueller-Mach, G. O. Mueller, L. Zhou, G. Harbers and M. G. Craford, *IEEE/OSA J. Disp. Technol.* **3** (2007) 160–175.
- [3] G. Harbers, S. J. Bierhuizen and M. R. Krames, *IEEE/OSA J. Disp. Technol.* **3** (2007) 98–109.
- [4] A. A. Setlur, *Electrochem. Soc. Interface.* **18** (2009) 32–36.
- [5] P. F. Smet, A. B. Parmentier and D. Poelman, *J. Electrochem. Soc.* **158** (2011) R37–R54.
- [6] V. Bachmann, C. Ronda and A. Meijerink, *Chem. Mater.* **21** (2009) 2077–2084.
- [7] S. Ye, F. Xiao, Y. X. Pan, Y. Y. Ma and Q. Y. Zhang, *Mater. Sci. Eng. R Reports.* **71** (2010) 1–34.
- [8] R. J. Xie and N. Hirosaki, *Sci. Technol. Adv. Mater.* **8** (2007) 588–600.
- [9] A. A. Setlur, E. V. Radkov, C. S. Henderson, J.-H. Her, A. M. Srivastava, N. Karkada, M. S. Kishore, N. P. Kumar, D. Aesram, A. Deshpande, B. Kolodin, L. S. Grigorov and U. Happek, *Chem. Mater.* **22** (2010) 4076–4082.
- [10] C. C. Lin, A. Meijerink and R.-S. Liu, *J. Phys. Chem. Lett.* **7** (2016) 495–503.
- [11] H.-D. Nguyen and R.-S. Liu, *J. Mater. Chem. C* **4** (2016) 10759–10775.
- [12] E. V. Radkov, L. S. Grigorov, A. A. Setlur and A. M. Srivastava, United States Patent No. US7,497,973 B2, 2009.
- [13] H. Zhu, C. C. Lin, W. Luo, S. Shu, Z. Liu, Y. Liu, J. Kong, E. Ma, Y. Cao, R.-S. Liu and X. Chen, *Nat. Commun.* **5** (2014) 4312.
- [14] J. McKittrick and L. E. Shea-Rohwer, *J. Am. Ceram. Soc.* **97** (2014) 1327–1352.
- [15] A. G. Paulusz, *J. Electrochem. Soc.* **120** (1973) 942–947.
- [16] T. Takahashi and S. Adachi, *J. Electrochem. Soc.* **155** (2008) E183–E188.
- [17] L.-L. Wei, C. C. Lin, M.-H. Fang, M. G. Brik, S.-F. Hu, H. Jiao and R.-S. Liu, *J. Mater. Chem. C* **3** (2015) 1655–1660.
- [18] S. Sakurai, T. Nakamura and S. Adachi, *ECS J. Solid State Sci. Technol.* **5** (2016) R206–R210.
- [19] H. F. Sijbom, J. J. Joos, L. I. D. J. Martin, K. Van den Eeckhout, D. Poelman and P. F. Smet, *ECS J. Solid State Sci. Technol.* **5** (2016) R3040–R3048.
- [20] R. Kasa and S. Adachi, *J. Electrochem. Soc.* **159** (2012) J89–J95.
- [21] H.-D. Nguyen, C. C. Lin, M.-H. Fang and R.-S. Liu, *J. Mater. Chem. C* **2** (2014) 10268–10272.
- [22] Y. Arai and S. Adachi, *J. Electrochem. Soc.* **158** (2011) J179–J183.

- [23] D. Sekiguchi, J. Nara and S. Adachi, *J. Appl. Phys.* **113** (2013) 183516.
- [24] P. Dorenbos, *Opt. Mater.* **69** (2017) 8–22.
- [25] G. Blasse and P. De Korte, *J. Inorg. Nucl. Chem.* **43** (1981) 1505–1506.
- [26] G. Blasse and B. C. Grabmaier, *Luminescent Materials*, Springer-Verlag, Berlin, 1994.
- [27] T. Senden, F. T. H. Broers and A. Meijerink, *Opt. Mater.* **60** (2016) 431–437.
- [28] D. L. Dexter and J. H. Schulman, *J. Chem. Phys.* **22** (1954) 1063–1070.
- [29] Q. Zhou, Y. Zhou, F. Lu, Y. Liu, Q. Wang, L. Luo and Z. Wang, *Mater. Chem. Phys.* **170** (2016) 32–37.
- [30] X. Jiang, Y. Pan, S. Huang, X. Chen, J. Wang and G. Liu, *J. Mater. Chem. C* **2** (2014) 2301–2306.
- [31] L. Lv, X. Jiang, S. Huang, X. Chen and Y. Pan, *J. Mater. Chem. C* **2** (2014) 3879–3884.
- [32] J. S. Zhong, D. Q. Chen, X. Wang, L. F. Chen, H. Yu, Z. G. Ji and W. D. Xiang, *J. Alloys Compd.* **662** (2016) 232–239.
- [33] L. Xi and Y. Pan, *Mater. Res. Bull.* **86** (2017) 57–62.
- [34] M. Kim, W. B. Park, C. H. Kim, K.-S. Sohn and B. K. Bang, *J. Mater. Chem. C* **3** (2015) 5484–5489.
- [35] J. Liao, L. Nie, L. Zhong, Q. Gu and Q. Wang, *Luminescence* **31** (2016) 802–807.
- [36] B. E. Yeo, Y. S. Cho and Y. D. Huh, *Opt. Mater.* **51** (2016) 50–55.
- [37] H. Bode, H. Jenssen and F. Bandte, *Angew. Chemie* **65** (1953) 304.
- [38] H. W. Roesky, *Efficient Preparations of Fluorine Compounds*, John Wiley & Sons Inc., Hoboken, 2012.
- [39] Y. Tanabe and S. Sugano, *J. Phys. Soc. Japan.* **9** (1954) 753–766.
- [40] Y. Tanabe and S. Sugano, *J. Phys. Soc. Japan.* **9** (1954) 766–779.
- [41] J. M. Ogiegło, A. Katelnikovas, A. Zych, T. Jüstel, A. Meijerink and C. R. Ronda, *J. Phys. Chem. A* **117** (2013) 2479–2484.
- [42] V. Bachmann, T. Jüstel, A. Meijerink, C. R. Ronda and P. J. Schmidt, *J. Lumin.* **121** (2006) 441–449.
- [43] B. Henderson and G. F. Imbusch, *Optical Spectroscopy of Inorganic Solids*, Oxford University Press, Oxford, 1989.
- [44] Y. Jin, M.-H. Fang, M. Grinberg, S. Mahlik, T. Lesniewski, M. G. Brik, G.-Y. Luo, J. G. Lin and R.-S. Liu, *ACS Appl. Mater. Interfaces* **8** (2016) 11194–11203.
- [45] C. W. Struck and W. H. Fonger, *J. Lumin.* **10** (1975) 1–30.
- [46] A. M. Srivastava, H. A. Comanzo, S. Camardello, S. B. Chaney, M. Aycibin and U. Happek, *J. Lumin.* **129** (2009) 919–925.
- [47] W. Fonger and C. W. Struck, *Phys. Rev. B* **11** (1975) 3251–3260.
- [48] J. F. Donegan, T. J. Glynn, G. F. Imbusch and J. P. Remeika, *J. Lumin.* **36** (1986) 93–100.
- [49] R. J. M. Da Fonseca and T. Abritta, *Phys. B Condens. Matter.* **190** (1993) 327–332.
- [50] A. Brenier, A. Suchocki, C. Pedrini, G. Boulon and C. Madej, *Phys. Rev. B* **46** (1992) 3219–3227.
- [51] A. Suchocki, J. D. Allen, R. C. Powell and G. M. Loiacono, *Phys. Rev. B* **36** (1987) 6729–6734.
- [52] M. de Jong, L. Seijo, A. Meijerink and F. T. Rabouw, *Phys. Chem. Chem. Phys.* **17** (2015) 16959–16969.
- [53] I. W. Forrest and A. P. Lane, *Inorg. Chem.* **15** (1976) 265–269.
- [54] T. Senden, E. J. van Harten and A. Meijerink, *J. Lumin.* **194** (2018) 131–138.
- [55] P. Dorenbos, *J. Phys. Condens. Matter.* **15** (2003) 2645–2665.
- [56] M. G. Brik and A. M. Srivastava, *J. Electrochem. Soc.* **159** (2012) J212–J216.
- [57] L. Thorington, *J. Opt. Soc. Am.* **40** (1950) 579–583.
- [58] G. Kemeny and C. H. Haake, *J. Chem. Phys.* **33** (1960) 783–789.
- [59] M. Travníček, F. A. Kröger, T. P. J. Botden and P. Zalm, *Physica* **18** (1952) 33–42.
- [60] W.-L. Wu, M.-H. Fang, W. Zhou, T. Lesniewski, S. Mahlik, M. Grinberg, M. G. Brik, H.-S. Sheu, B.-M. Cheng, J. Wang and R.-S. Liu, *Chem. Mater.* **29** (2017) 935–939.
- [61] R. Hoshino, T. Nakamura and S. Adachi, *ECS J. Solid State Sci. Technol.* **5** (2016) R37–R43.
- [62] G. Mo, W. Wang, K. Wang, G. Wen, M. Zhu and J. Wang, *J. Mater. Sci. Mater. Electron.* **28** (2017) 8155–8159.
- [63] P. Li, L. Wondraczek, M. Peng and Q. Zhang, *J. Am. Ceram. Soc.* **99** (2016) 3376–3381.
- [64] S. Zhang, Y. Hu, H. Duan, L. Chen, Y. Fu, G. Ju, T. Wang and M. He, *RSC Adv.* **5** (2015) 90499–90507.
- [65] Y. Takeda, H. Kato, M. Kobayashi, H. Kobayashi and M. Kakihana, *Chem. Lett.* **44** (2015) 1541–1543.
- [66] D. Chen, Y. Zhou and J. Zhong, *RSC Adv.* **6** (2016) 86285–86296.

- [67] L. A. Riseberg and M.J. Weber, *Solid State Commun.* **9** (1971) 791–794.
- [68] M. Peng, X. Yin, P. A. Tanner, M. G. Brik and P. Li, *Chem. Mater.* **27** (2015) 2938–2945.
- [69] Y. Zhydachevskii, A. Suchocki, A. Pajęczkowska, A. Kłos, A. Szysiak and A. Reszka, *Opt. Mater.* **35** (2013) 1664–1668.
- [70] S. Geschwind, P. Kisliuk, M. P. Klein, J. P. Remeika and D.L. Wood, *Phys. Rev.* **126** (1962) 1684–1686.
- [71] B. Malysa, A. Meijerink and T. Jüstel, *J. Lumin.* **171** (2016) 246–253.
- [72] Y. R. Shen and K. L. Bray, *Phys. Rev. B* **56** (1997) 882–891.
- [73] A. M. Srivastava and M. G. Brik, *Opt. Mater.* **35** (2012) 196–200.
- [74] R. D. Shannon, *Acta Crystallogr. Sect. A.* **32** (1976) 751–767.
- [75] R. J. Birgeneau, *J. Chem. Phys.* **50** (1969) 4282–4287.
- [76] O. Göbel, *Acta Crystallogr. Sect. C* **56** (2000) 521–522.

6

The d–f luminescence of Eu^{2+} , Ce^{3+} and Yb^{2+} ions in $\text{Cs}_2\text{MP}_2\text{O}_7$ ($\text{M} = \text{Ca}^{2+}, \text{Sr}^{2+}$)



Abstract

The efficient narrow band emission of Eu^{2+} in $\text{Cs}_2\text{MP}_2\text{O}_7$ ($\text{M} = \text{Ca}^{2+}, \text{Sr}^{2+}$) is characterized by a large Stokes shift and a high quenching temperature which makes the material promising for application in warm white LEDs. The unusual Eu^{2+} luminescence properties were reported recently but an explanation for the peculiar behavior is lacking. In this paper we aim at providing new insights in the luminescence of the Eu^{2+} emission in $\text{Cs}_2\text{MP}_2\text{O}_7$ through measurements at cryogenic temperatures (down to 4 K) and by comparison with the d–f luminescence of Ce^{3+} and Yb^{2+} in the same host. The results reveal a sharp onset of the Eu^{2+} emission and excitation bands at 4 K. Usually the sharp onset for narrow excitation and emission bands coincide at an energy corresponding to the zero-phonon (purely electronic) transition, but for Eu^{2+} in $\text{Cs}_2\text{MP}_2\text{O}_7$ there is a large shift of 3500 cm^{-1} between the onsets, consistent with the large Stokes shift observed. The onset shift can be explained by emission from a lower energy distorted excited $4f^65d^1$ state. For Ce^{3+} , the f–d absorption bands are at energies expected based on the relation between the absorption energies for Eu^{2+} and Ce^{3+} reported by Dorenbos. Contrary to Eu^{2+} , the emission for Ce^{3+} shows a normal Stokes shift and therefore the emission bands are at much higher energies than predicted from the energy of the Eu^{2+} emission and the Dorenbos relations. Based on the present results the unusually large Stokes shift for the Eu^{2+} emission in $\text{Cs}_2\text{MP}_2\text{O}_7$ is assigned to a Jahn–Teller like deformation in the excited $4f^65d^1$ state of Eu^{2+} that is not present in the $5d$ state of Ce^{3+} .

6.1 Introduction

The optical properties of the Eu^{2+} ion ($4f^7$) have been thoroughly investigated [1–5] and the efficient luminescence of Eu^{2+} is widely applied, e.g. in fluorescent tubes, white light LEDs (wLEDs), displays, scintillators and anti-counterfeiting labels [6–10]. The emission and absorption spectra of Eu^{2+} are characterized by broad absorption and emission bands corresponding to transitions between the $4f^7$ ground state and the $4f^65d^1$ excited states. The energy level structure in the $4f^65d^1$ excited state is strongly influenced by covalency and crystal field splitting [8]. As a result, the d–f emission of Eu^{2+} can vary from the ultraviolet to the red spectral region, depending on the host lattice.

In phosphates Eu^{2+} ions typically show a violet or blue emission and emission wavelengths between 375 nm (for $\text{Ba}(\text{PO}_3)_2:\text{Eu}^{2+}$) and 505 nm (for $\text{NaCaPO}_4:\text{Eu}^{2+}$) have been reported [1]. However, recently an unusual red Eu^{2+} emission was reported for a Eu^{2+} -doped phosphate. In $\text{Cs}_2\text{CaP}_2\text{O}_7$ the d–f emission of Eu^{2+} is around 600 nm, while the absorption is in the usual blue–ultraviolet spectral region [11]. As a result, the Stokes shift of the emission is very large ($\Delta S > 6000 \text{ cm}^{-1}$). The emission is further characterized by a high quantum efficiency and a high quenching temperature ($T_{1/2} \sim 600 \text{ K}$), which is unexpected in combination with a large Stokes shift [8]. These special optical properties make $\text{Cs}_2\text{CaP}_2\text{O}_7:\text{Eu}^{2+}$ promising as a red-emitting phosphor in warm white LEDs, where a narrow band red emission is required to reduce efficiency loss that is inherent to the use of broad band red emitters. Broad band red emitters that are used to shift the color temperature of white LEDs into the desired warm white spectral region have a significant part of their emission between 630 and 700 nm where the eye sensitivity is low. This reduces the lumen/W efficiency [9].

The large Stokes shift and narrow band emission reported for Eu^{2+} in $\text{Cs}_2\text{MP}_2\text{O}_7$ ($M = \text{Ca}^{2+}, \text{Sr}^{2+}$) were discussed by Srivastava et al. [11]. Based on the narrow band emission ($\Gamma^{\text{em}} \sim 2000 \text{ cm}^{-1}$ at 80 K), normal emission lifetime ($\tau \sim 1 \mu\text{s}$) and high quenching temperature ($T_{1/2} \sim 600 \text{ K}$) it was concluded that the large Stokes shift cannot be explained by anomalous emission from a Eu-trapped exciton state. In the past large Stokes shifts for Eu^{2+} emission have been explained by a trapped exciton emission, but in addition to a large Stokes shift, this emission is characterized by a large spectral width, longer lifetime and low quenching temperature [2]. Clearly, these characteristics are not observed for the Eu^{2+} emission in $\text{Cs}_2\text{MP}_2\text{O}_7$. An alternative explanation that was suggested in Refs. [11,12] involves distortions in the $4f^65d^1$ excited state. In $\text{Cs}_2\text{MP}_2\text{O}_7$ the Eu^{2+} ion is in an octahedral coordination. In Figure 6.1 the crystal field splitting in O_h symmetry is illustrated. In the excited 5d state a, for example, tetragonal deformation can lower the energy of the lowest $4f^65d^1$ state as illustrated in Figure 6.1. Emission from the lowest $4f^65d^1$ state will be shifted to a lower energy and can explain the large Stokes shift.

Substantial lattice deformations in the 5d excited state have previously been shown to give rise to large Stokes shifts ($\Delta S > 5000 \text{ cm}^{-1}$) for d–f emission of Ce^{3+} in halides

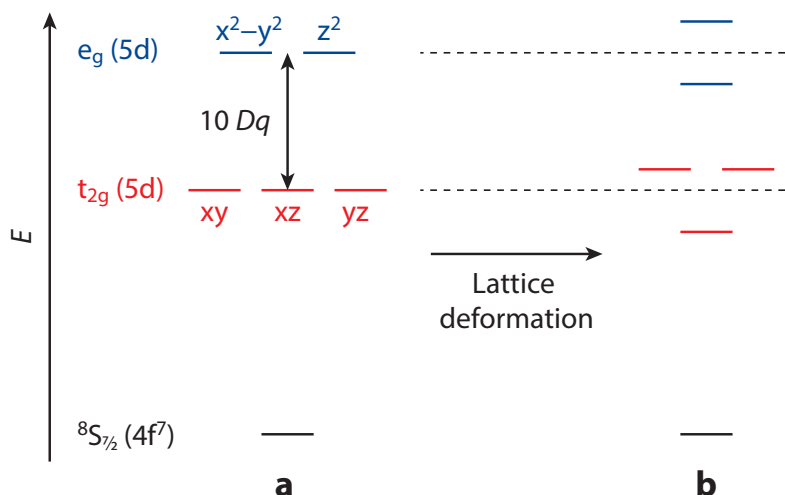


Figure 6.1 – Schematic representation of the Eu^{2+} energy level scheme in (a) octahedral and (b) strongly deformed configuration.

[13–16]. As an example, for $\text{LaCl}_3:\text{Ce}^{3+}$ ($\Delta S = 5800 \text{ cm}^{-1}$) it was found with ab initio calculations that in the excited $5d^1$ configuration there is an off-center movement of the Ce^{3+} ion, which is accompanied by a strong deformation of the ligand prism around the Ce^{3+} ion [14]. Due to this deformation the crystal field splitting almost doubles, resulting in a very large Stokes shift. The results also explained why the concentrated system CeCl_3 , despite having the same crystal structure as LaCl_3 , had a very small Stokes shift of only 900 cm^{-1} . It was found that in CeCl_3 the more stable off-center Ce^{3+} position is already occupied in the ground state $4f^1$ configuration, resulting in a small Stokes shift. It was determined that the off-center movement of the Ce^{3+} ion is due to a reorientation of the occupied $5d$ orbital by a (pseudo) Jahn–Teller mixing between the two lowest $5d$ states, as these are very close in energy [16]. A similar Jahn–Teller type deformation may play a role in explaining the large Stokes shift for $\text{Cs}_2\text{MP}_2\text{O}_7:\text{Eu}^{2+}$.

To investigate the origin of the large Stokes shift for the Eu^{2+} emission in $\text{Cs}_2\text{MP}_2\text{O}_7$, here we report luminescence spectra recorded at cryogenic temperatures. At low temperatures often zero-phonon lines and sharp onsets of excitation and emission spectra are observed which give information on the energy of the electronic origin of excited states involved. A shift of the zero-phonon line or sharp onset between emission and excitation spectra can provide evidence for electronic relaxation in the excited state. In addition, the d–f luminescence for other lanthanide ions, Ce^{3+} and Yb^{2+} , is investigated and compared with the luminescence properties of Eu^{2+} .

The results reveal a large shift between the sharp onset in the Eu^{2+} excitation and emission spectra. Contrary to the unusually large Stokes shift and red-shifted emission observed for Eu^{2+} in $\text{Cs}_2\text{MP}_2\text{O}_7$, the luminescence of Ce^{3+} is normal in $\text{Cs}_2\text{MP}_2\text{O}_7$ indicating that the unusual luminescence properties are specific for the d–f emission of Eu^{2+} .

6.2 Methods

Microcrystalline samples of $\text{Cs}_2\text{MP}_2\text{O}_7$ ($M = \text{Ca}^{2+}, \text{Sr}^{2+}$) doped with 0.1 or 1% of Eu^{2+} , Ce^{3+} or Yb^{2+} ions were synthesized using solid-state reaction techniques. The starting materials Cs_2CO_3 (10 mole% excess, Aldrich, 99.9%), $(\text{NH}_4)_2\text{HPO}_4$ (10 mole% excess, Merck, p.a.), CaO (Sigma-Aldrich, reagent grade), SrCO_3 (Aldrich, 99.9%) and Eu_2O_3 (Highways International, 99.99%), Yb_2O_3 (Highways International, 99.99%) or CeO_2 (Merck, p.a.) were thoroughly mixed and ground with a pestle in an agate mortar. The powder mixtures were dried at 300 °C for 1 h in air and, subsequently, fired twice at 750 °C ($\text{Cs}_2\text{CaP}_2\text{O}_7$) or 800 °C ($\text{Cs}_2\text{SrP}_2\text{O}_7$) for 5 h in a reducing atmosphere (10% H_2 /90% N_2). The samples were thoroughly ground between each heating step. X-ray diffraction measurements confirmed that the $\text{Cs}_2\text{CaP}_2\text{O}_7$ and $\text{Cs}_2\text{SrP}_2\text{O}_7$ powders were single phase (see Figure 6.2).

Photoluminescence (PL) spectra and decay curves of the samples were measured using an Edinburgh Instruments FLS920 fluorescence spectrometer, equipped with a 450 W xenon lamp as excitation source, a double excitation monochromator (0.22 m) and a

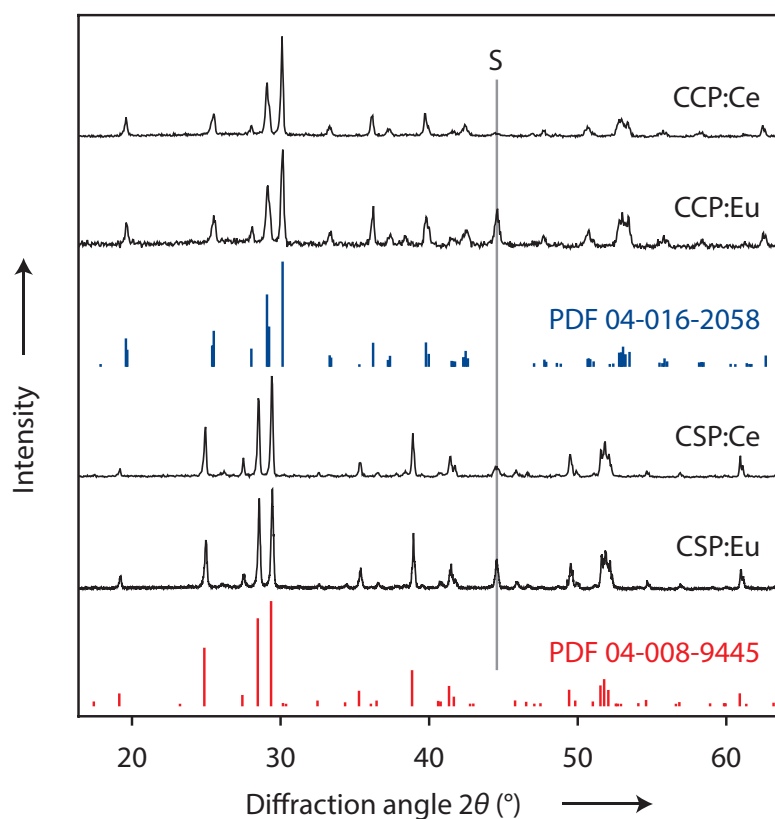


Figure 6.2 – X-ray diffraction patterns of $\text{Cs}_2\text{CaP}_2\text{O}_7$ samples doped with 1% Eu^{2+} (CCP:Eu) and 1% Ce^{3+} (CCP:Ce), and $\text{Cs}_2\text{SrP}_2\text{O}_7$ samples doped with 0.1% Eu^{2+} (CSP:Eu) and 1% Ce^{3+} (CSP:Ce). The peak at 45° is caused by the aluminum sample holder, indicated by the gray line (S) in the figure. The XRD patterns of the samples are in excellent agreement with reference patterns for $\text{Cs}_2\text{CaP}_2\text{O}_7$ (PDF-04-016-2058, blue) and $\text{Cs}_2\text{SrP}_2\text{O}_7$ (PDF-04-008-9445, red).

single emission monochromator (0.22 m). For measurements down to 4 K, the samples were cooled in an Oxford Instruments liquid helium flow cryostat. Emission was detected with a Hamamatsu R928 photomultiplier tube (PMT). For lifetime measurements, Ce^{3+} ions were excited with a PicoQuant pulsed diode (PDL 800-B combined with PLS 270, $\lambda_{\text{exc}} = 270$ nm, pulse width 650 ps) and Eu^{2+} was excited with an Edinburgh EPL375 pulsed diode laser ($\lambda_{\text{exc}} = 376.8$ nm, pulse width 65 ps). The decay curves were recorded with a Hamamatsu H74422-40 PMT.

Excitation spectra in the deep UV and vacuum ultraviolet (VUV) region (between 150 and 300 nm) were recorded at the BL3B beamline of the UVSOR facility (Okazaki, Japan). This beamline consists of a 2.5 m off-plane Eagle type normal incidence monochromator, which covers the VUV, UV and visible (VIS) regions. In the present experiments a spherical grating with a groove density of 600 lines/mm optimized at a photon energy of ~ 16 eV was used. For the photoluminescence measurements in the UV-VIS region, a 0.22 m Acton monochromator with a Princeton Instruments CCD detector was used. Excitation spectra were recorded using a Hamamatsu R4220 PMT connected to the same monochromator.

6.3 Results and discussion

6.3.1 Eu^{2+} luminescence

To investigate the origin of the large Stokes shift luminescence spectra were recorded at cryogenic temperatures. At 4 K only the lowest vibrational level in the ground and excited states are thermally populated resulting in narrow bands in emission and excitation. Also, in case of weak electron–phonon coupling (small Huang–Rhys parameter S) zero-phonon lines may be observed in excitation and emission. For a specific electronic transition the zero-phonon line in excitation and emission are expected at the same energy, as has been observed for e.g. Eu^{2+} and Ce^{3+} [17–20]. Figures 6.3 and 6.4 show the emission (red lines) and excitation spectra (blue lines) at $T = 4$ K of $\text{Cs}_2\text{CaP}_2\text{O}_7:\text{Eu}^{2+}$ (1%) and $\text{Cs}_2\text{SrP}_2\text{O}_7:\text{Eu}^{2+}$ (0.1%), respectively. The blue solid lines are the excitation spectra that were measured using the Edinburgh Instruments FLS920 fluorescence spectrometer and the blue dotted lines are the excitation spectra that were recorded at beamline BL3B of the UVSOR facility.

In the excitation spectra a broad band is observed between 22500 and 35000 cm^{-1} , which is assigned to the $\text{Eu}^{2+} 4f^7 \rightarrow 4f^65d^1(t_{2g})$ transition. At higher energy, around 45000 cm^{-1} , another absorption band is observed that is assigned to the $\text{Eu}^{2+} 4f^7 \rightarrow 4f^65d^1(e_g)$ transition. The lower energy band shows the characteristic staircase structure of a $\text{Eu}^{2+} 4f^7 \rightarrow 4f^6[{}^7F_J]5d^1$ absorption band, which is caused by transitions to the seven 7F_J ($J = 0–6$) multiplets of the $4f^6$ configuration in the $4f^65d^1$ excited state.

In order to calculate the crystal field splitting $10 Dq$, we determine the energy difference

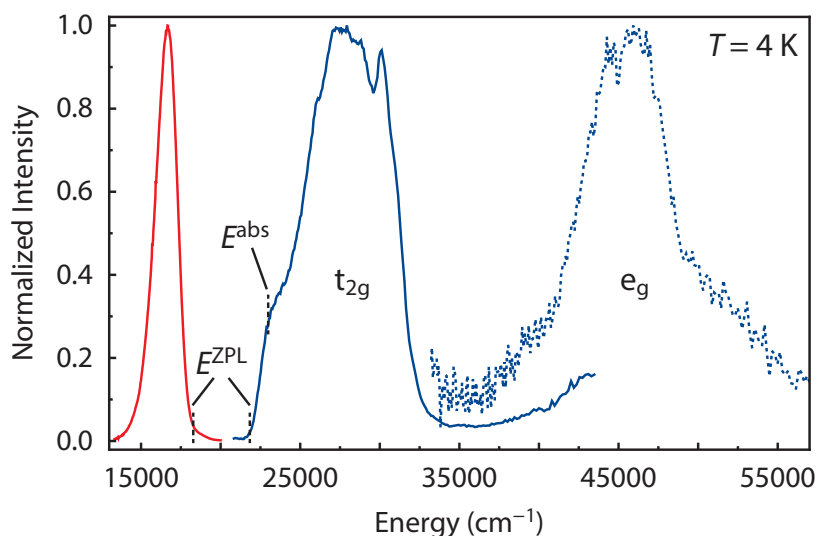


Figure 6.3 – The emission (red line; $\lambda_{\text{exc}} = 340$ nm) and (V)UV excitation spectra (blue solid line; $\lambda_{\text{em}} = 630$ nm and blue dashed line; $\lambda_{\text{em}} = 640$ nm) of $\text{Cs}_2\text{CaP}_2\text{O}_7:\text{Eu}^{2+}$ (1%) at $T = 4$ K. The spectra recorded with the Edinburgh Instruments FLS920 fluorescence spectrometer are the solid lines and the excitation spectrum measured at the UVSOR facility is the dotted line.

between the onsets of the t_{2g} and e_g absorption bands. We find a crystal field splitting of 18982 cm^{-1} for $\text{Cs}_2\text{CaP}_2\text{O}_7$ and 17281 cm^{-1} for $\text{Cs}_2\text{SrP}_2\text{O}_7$. Alternatively, we can estimate the crystal field splitting by taking the energy difference between the maximums of t_{2g} and e_g absorption bands. Using this method, a crystal field splitting of 17677 cm^{-1} and 16422 cm^{-1} was found for $\text{Cs}_2\text{CaP}_2\text{O}_7$ and $\text{Cs}_2\text{SrP}_2\text{O}_7$, respectively. The results show that the crystal field splitting is larger in $\text{Cs}_2\text{CaP}_2\text{O}_7$ than in $\text{Cs}_2\text{SrP}_2\text{O}_7$, in agreement with Ref. [11]. The stronger crystal field splitting for Eu^{2+} in $\text{Cs}_2\text{CaP}_2\text{O}_7$ is consistent with the shorter $\text{Eu}^{2+}-\text{O}^{2-}$ distance in $\text{Cs}_2\text{CaP}_2\text{O}_7$.

The emission spectrum of Eu^{2+} activated $\text{Cs}_2\text{CaP}_2\text{O}_7$ and $\text{Cs}_2\text{SrP}_2\text{O}_7$ at $T = 4$ K is a narrow asymmetrical band centered around a peak energy E^{em} of 16694 cm^{-1} (599 nm) and 17857 cm^{-1} (560 nm) with a full width at half maximum intensity Γ^{em} of 1618 and 1506 cm^{-1} , respectively (see Figures 6.3 and 6.4 and Table 6.1). At room temperature the emission bands are more symmetrical and broader (see Figure 6.5), with a Γ^{em} that has increased to 3045 cm^{-1} for $M = \text{Ca}^{2+}$ and to 3138 cm^{-1} for $M = \text{Sr}^{2+}$. The increase in emission bandwidth is due to thermal broadening. Previously it was reported that Γ^{em} is 2191 and 2147 cm^{-1} at $T = 80$ K for $M = \text{Ca}^{2+}$ and Sr^{2+} , respectively [11]. These values fit nicely between the Γ^{em} values that we have obtained at $T = 4$ K and room temperature. Besides an increase in bandwidth, the E^{em} has slightly shifted to higher energy (a blue shift of approximately 10 nm) when the temperature is increased to 298 K (see Figure 6.5). The shift in E^{em} is attributed to emission from thermally occupied higher vibrational levels in the excited state and/or a small decrease in the crystal field strength when the temperature increases (longer $\text{Eu}^{2+}-\text{O}^{2-}$ distance). The luminescence properties in Figures 6.3 and 6.4 are in agreement with the results previously reported

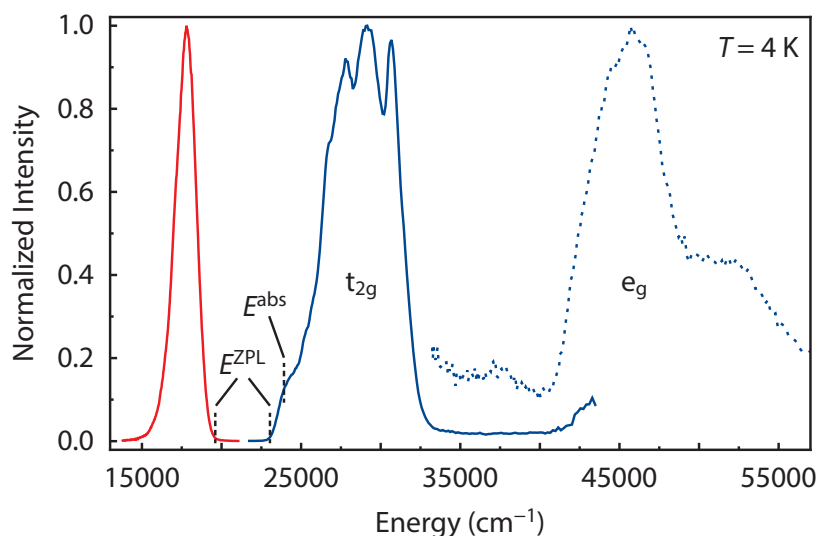


Figure 6.4 – The emission (red line; $\lambda_{\text{exc}} = 340$ nm) and (V)UV excitation spectra (blue solid line; $\lambda_{\text{em}} = 570$ nm and blue dashed line; $\lambda_{\text{em}} = 560$ nm) of $\text{Cs}_2\text{SrP}_2\text{O}_7:\text{Eu}^{2+}$ (0.1%) at $T = 4$ K. The spectra recorded with the Edinburgh Instruments FLS920 fluorescence spectrometer are the solid lines and the excitation spectrum measured at the UVSOR facility is the dotted line.

for $\text{Cs}_2\text{MP}_2\text{O}_7:\text{Eu}^{2+}$ at 80 K in Ref. [11]. However, the spectra shown in this chapter were recorded at 4 K instead of 80 K. At 4 K (the onsets of) the emission and excitation bands are better resolved, which is important for e.g. correctly determining the Stokes shift of the Eu^{2+} emission.

The Eu^{2+} emission is in the red ($\text{Cs}_2\text{CaP}_2\text{O}_7:\text{Eu}^{2+}$) or yellow ($\text{Cs}_2\text{SrP}_2\text{O}_7:\text{Eu}^{2+}$) spectral region, which is highly unusual for Eu^{2+} in a phosphate host lattice. The low energy luminescence originates from the very large Eu^{2+} Stokes shift (ΔS). ΔS of the Eu^{2+} emission is defined as the difference between the energy of the $4f^7 \rightarrow 4f^6[{}^7F_0]5d^1$ transition E^{abs} and the peak energy of the emission band E^{em} . The transition from the $4f^7 {}^8S_{7/2}$ ground state to the $4f^6[{}^7F_0]5d^1$ excited state corresponds to the first “step” in the characteristic staircase structure of the f–d absorption band. However, if the first step is not resolved in the spectra, E^{abs} can be determined by taking the energy at which, on the low-energy side, the excitation band has risen to 15–20% of the maximum of the “staircase” [1].

The values for E^{abs} and E^{em} are most accurately determined at cryogenic temperatures, as at 4 K there is least thermal broadening of the emission and excitation bands. Hence, the first step in the staircase is clearly resolved in our excitation spectra measured at 4 K (see Figures 6.3 and 6.4). By locating the first step in the staircase structure, it is estimated that $E^{\text{abs}} = 22989$ cm^{-1} for $\text{Cs}_2\text{CaP}_2\text{O}_7$ and 23923 cm^{-1} for $\text{Cs}_2\text{SrP}_2\text{O}_7$ (see also Table 6.1). The E^{abs} is lower for $\text{Cs}_2\text{CaP}_2\text{O}_7$ compared to $\text{Cs}_2\text{SrP}_2\text{O}_7$ as the stronger crystal field splitting in $\text{Cs}_2\text{CaP}_2\text{O}_7$ shifts the lowest $4f^65d^1$ state to lower energies.

The values we find for E^{abs} are approximately 2000 cm^{-1} lower in energy compared

Table 6.1 – Optical properties of Eu^{2+} ions in $\text{Cs}_2\text{CaP}_2\text{O}_7$ and $\text{Cs}_2\text{SrP}_2\text{O}_7$. Peak energy of the emission band E^{em} , full width at half maximum intensity of the emission band Γ^{em} , estimated energy of the $4f^7 \rightarrow 4f^6[{}^7F_0]5d^1$ transition E^{abs} and the Stokes shift $\Delta S = E^{\text{abs}} - E^{\text{em}}$. All values are in cm^{-1} and at $T = 4$ K.

Host	E^{em}	Γ^{em}	E^{abs}	ΔS
$\text{Cs}_2\text{CaP}_2\text{O}_7$	16694	1618	22989	6294
$\text{Cs}_2\text{SrP}_2\text{O}_7$	17857	1506	23923	6066

to those reported in Ref. [11]. However, in Ref. [11] a different method was used to estimate E^{abs} . Instead of using the common method to locate E^{abs} at the first step in the staircase, E^{abs} was determined by first fixing the 7F_6 level on the highest energy peak in the excitation spectra and then use a 5080 cm^{-1} multiplet splitting of the $\text{Eu}^{3+} {}^7F_j$ term to locate the position of the $4f^6[{}^7F_0]5d^1$ level. However, the splitting of the 7F_j multiplets in the $4f^65d^1$ state is often larger than the $\sim 5080 \text{ cm}^{-1}$ observed for Eu^{3+} [1,21], explaining the difference in E^{abs} between Ref. [11] and the present work.

Using the values determined for E^{abs} and E^{em} , we calculate the Stokes shift $\Delta S = E^{\text{abs}} - E^{\text{em}}$. It is found that $\Delta S = 6294$ and 6066 cm^{-1} for $M = \text{Ca}^{2+}$ and Sr^{2+} , respectively (see Table 6.1). The estimated ΔS are approximately 2000 cm^{-1} smaller compared to what is reported in Ref. [11], consistent with the lower values determined for E^{abs} . The ΔS values are significantly larger than the typical Stokes shift of $\Delta S = 1000\text{-}2000 \text{ cm}^{-1}$ observed for Eu^{2+} d–f luminescence [1]. Moreover, the Stokes shift of Eu^{2+} in $\text{Cs}_2\text{MP}_2\text{O}_7$ is larger than the largest Stokes shift value ever reported for Eu^{2+} d–f luminescence ($\Delta S \sim 5300 \text{ cm}^{-1}$ for Eu^{2+} in Sr_2SiO_4) [22].

At cryogenic temperatures the Stokes shift and emission bandwidth are expected to be of similar energy [19,21]. However, this is not the case for Eu^{2+} in $\text{Cs}_2\text{MP}_2\text{O}_7$ (see Table 6.1). In a first approximation ΔS (equation 6.1) and Γ^{em} (equation 6.2) can both be interpreted in terms of the Huang–Rhys parameter S and the lattice phonon energies. In the configurational coordinate model, assuming harmonic oscillators [23,24]:

$$\Delta S = (2S - 1)\hbar\omega \quad (6.1)$$

$$\Gamma(T) \cong 2.36\hbar\omega\sqrt{S}\sqrt{\coth\frac{\hbar\omega}{2kT}} \quad (6.2)$$

Using equations 6.1 and 6.2, we can estimate the expected Stokes shift from the emission bandwidth at 4 K, assuming that $\hbar\omega = 400 \text{ cm}^{-1}$ for a $\text{Eu}^{2+}\text{-O}^{2-}$ vibration [24]. It is calculated that ΔS should be around 1950 and 1650 cm^{-1} for $\text{Cs}_2\text{CaP}_2\text{O}_7$ and $\text{Cs}_2\text{SrP}_2\text{O}_7$, respectively. These values are significantly smaller than what is observed for Eu^{2+} in

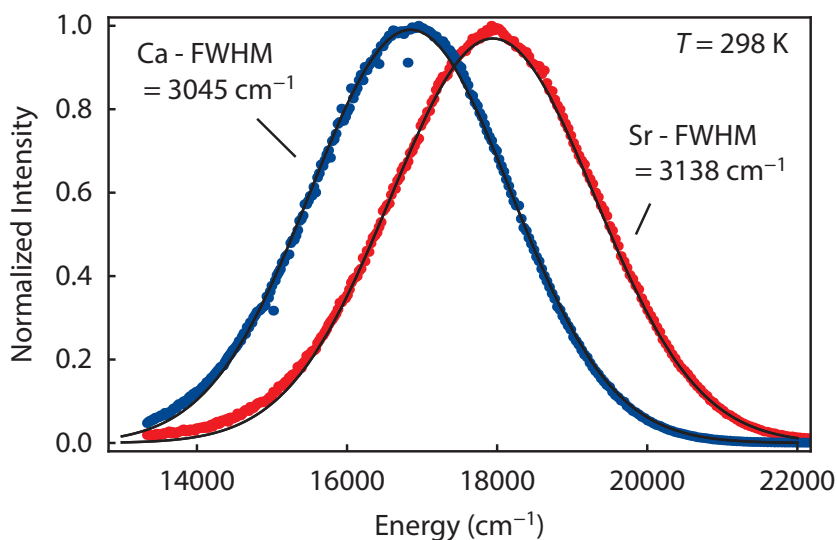


Figure 6.5 – Room-temperature emission spectra of $\text{Cs}_2\text{CaP}_2\text{O}_7:\text{Eu}^{2+}$ (blue, $\lambda_{\text{exc}} = 350$ nm) and $\text{Cs}_2\text{SrP}_2\text{O}_7:\text{Eu}^{2+}$ (red, $\lambda_{\text{exc}} = 355$ nm). Gaussian fits to the spectra (solid black lines) show that the emission bands are nearly symmetrical.

$\text{Cs}_2\text{MP}_2\text{O}_7$ (see also Table 6.1). The low-temperature spectra shown in Figures 6.3 and 6.4 provide information on the origin of the unusually large Stokes shift that is observed for Eu^{2+} in $\text{Cs}_2\text{MP}_2\text{O}_7$. At cryogenic temperatures often zero-phonon lines and/or sharp onsets of the excitation and emission spectra are observed, coinciding on the energy of the electronic origin of excited states involved. Consequently, the low-temperature spectra can show whether the emission and excitation bands used for determining the Stokes shift belong to the same electronic transition [24].

The spectra in Figures 6.3 and 6.4 do not show any zero-phonon lines, but do reveal sharp onsets for the emission and excitation bands. Using the sharp onsets, we can estimate the energy of the zero-phonon (purely electronic) transition (E^{ZPL}) for the emission and excitation bands. For a specific electronic transition the sharp onsets of narrow excitation and emission bands coincide at an energy corresponding to the zero-phonon transition [17–20]. However, this is not the case for Eu^{2+} in $\text{Cs}_2\text{MP}_2\text{O}_7$, as there is a large energy difference between the sharp onsets (and estimated E^{ZPL}) of the emission and excitation bands. It is estimated that the shift between the onsets of the Eu^{2+} emission and excitation bands is around 3500 cm^{-1} , both for $\text{Cs}_2\text{CaP}_2\text{O}_7$ and $\text{Cs}_2\text{SrP}_2\text{O}_7$. This large “onset shift” is consistent with the large Stokes shift observed.

The large shift between the onsets of the Eu^{2+} emission and excitation bands shows that different excited states are involved in the emission and absorption process. This indicates that there is a substantial electronic relaxation in the $4f^65d^1$ excited state, which can be due to a Jahn–Teller like deformation. As a consequence of this deformation in the excited state, the emission occurs from a lower energy excited $4f^65d^1$ state, resulting

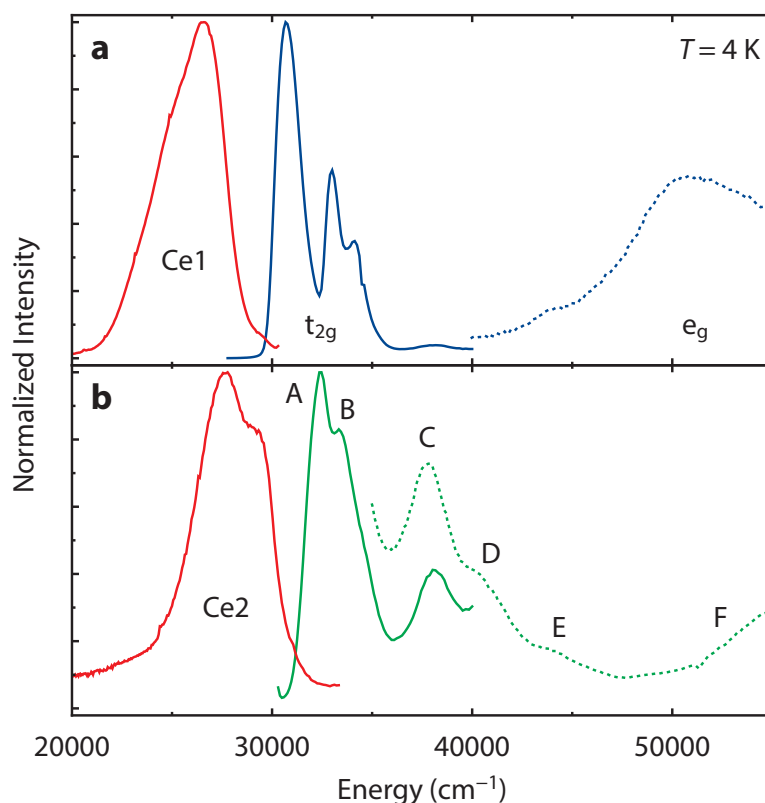


Figure 6.6 – Excitation and emission spectra of $\text{Cs}_2\text{CaP}_2\text{O}_7:\text{Ce}^{3+}$ (1%) at $T = 4$ K. (a) Excitation (blue) and emission spectra (red) measured for $\lambda_{\text{em}} = 420$ nm and $\lambda_{\text{exc}} = 320$ nm. (b) Excitation (green) and emission spectra (red) measured for $\lambda_{\text{em}} = 340$ nm and $\lambda_{\text{exc}} = 262$ nm. The spectra recorded with the Edinburgh FLS920 fluorescence spectrometer are the solid lines and the excitation spectra measured at the UVSOR facility are the dotted lines.

in a very large Stokes shift. Jahn–Teller distortions in the $\text{Eu}^{2+} 4f^65d^1$ state have e.g. previously been observed for Eu^{2+} in CaF_2 and SrF_2 [25,26]. The Jahn–Teller splittings reported in Refs. [25,26] are smaller than 1000 cm^{-1} and cannot explain the large Stokes shift observed for Eu^{2+} in $\text{Cs}_2\text{MP}_2\text{O}_7$. However, for Ce^{3+} there are several reports that substantial Jahn–Teller like deformations in the 5d excited state give rise to unusually large Stokes shifts [13–16]. For example, it was found that the large Stokes shift of Ce^{3+} in LaCl_3 ($\Delta S = 5800 \text{ cm}^{-1}$) is due to an off-center movement of the Ce^{3+} ion accompanied by a strong deformation of the ligand prism. It was determined in Ref. [16] that the off-center movement of the Ce^{3+} ion is due to a reorientation of the occupied 5d orbital by a (pseudo) Jahn–Teller mixing between the two lowest 5d states. Similar Jahn–Teller deformations can occur in the $4f^65d^1$ excited state of Eu^{2+} in $\text{Cs}_2\text{MP}_2\text{O}_7$. Therefore, based on the results presented here we assign the unusually large Stokes shift for the Eu^{2+} emission in $\text{Cs}_2\text{MP}_2\text{O}_7$ to a Jahn–Teller like deformation in the excited $4f^65d^1$ state of Eu^{2+} .

6.3.2 Ce^{3+} luminescence

In this section we will present the luminescence properties of $\text{Cs}_2\text{MP}_2\text{O}_7:\text{Ce}^{3+}$. Usually

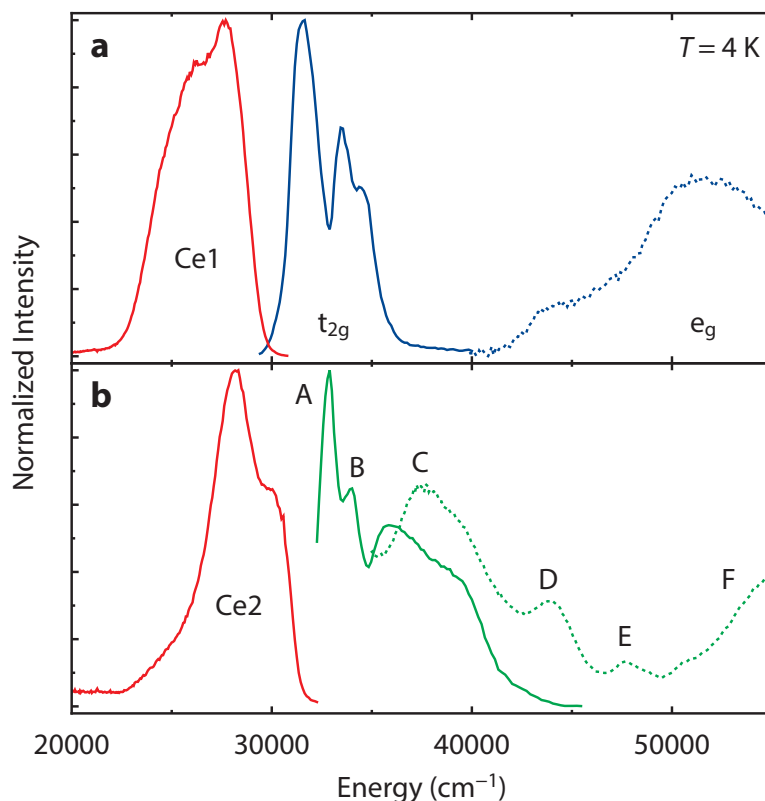


Figure 6.7 – Excitation and emission spectra of $\text{Cs}_2\text{SrP}_2\text{O}_7:\text{Ce}^{3+}$ (1%) at $T = 4$ K. (a) Excitation (blue) and emission spectra (red) measured for $\lambda_{\text{em}} = 410$ nm and $\lambda_{\text{exc}} = 316$ nm. (b) Excitation (green) and emission spectra (red) measured for $\lambda_{\text{em}} = 330$ nm and $\lambda_{\text{exc}} = 260$ nm. The spectra recorded with the Edinburgh FLS920 fluorescence spectrometer are the solid lines and the excitation spectra measured at the UVSOR facility are the dotted lines.

the d–f emission properties of Eu^{2+} and Ce^{3+} are related [27]. Hence, we investigate if Ce^{3+} also has an unusually large Stokes shift of emission in $\text{Cs}_2\text{MP}_2\text{O}_7$.

Figures 6.6 and 6.7 show emission and excitation spectra at 4 K of $\text{Cs}_2\text{CaP}_2\text{O}_7:\text{Ce}^{3+}$ (1%) and $\text{Cs}_2\text{SrP}_2\text{O}_7:\text{Ce}^{3+}$ (1%), respectively. We have measured the luminescence of the samples for $\lambda_{\text{exc}} \sim 320$ nm (Figures 6.6a and 6.7a) and $\lambda_{\text{exc}} \sim 260$ nm (Figures 6.6b and 6.7b). For both excitation wavelengths the samples show a strong blue/UV emission, which is attributed to the parity-allowed $5d^1 \rightarrow 4f^1$ transition of Ce^{3+} . The lifetime of the emission is 28 ns, which is characteristic for the spin- and parity-allowed d–f transition of Ce^{3+} .

The emission spectra displayed in Figures 6.6a and 6.7a ($\lambda_{\text{exc}} = 320$ nm (Ca) or 316 (Sr) nm) show the typical doublet emission band observed for Ce^{3+} ions on a single lattice site (Ce1). The two emission bands are due to transitions from the lowest crystal field component of the $5d^1$ configuration to the ${}^2F_{5/2}$ and ${}^2F_{7/2}$ levels of the $4f^1$ ground state, which is split by spin–orbit coupling. The band of the lower-energy $5d^1 \rightarrow {}^2F_{7/2}$ transition is weaker and therefore less apparent, especially for $\text{Cs}_2\text{CaP}_2\text{O}_7:\text{Ce}^{3+}$ where

only a weak shoulder is observed around 25000 cm^{-1} . The two peaks of the band are separated by $\sim 2000\text{ cm}^{-1}$, which corresponds to the spin-orbit splitting of the 2F ground state term of Ce^{3+} [8].

Figures 6.6b and 6.7b show that the shape of the Ce^{3+} emission spectra is different when excitation is at $\sim 260\text{ nm}$ instead of $\sim 320\text{ nm}$. This indicates that two different Ce^{3+} emission sites are present in $\text{Cs}_2\text{MP}_2\text{O}_7$. The presence of two distinct Ce^{3+} sites is confirmed by the excitation spectra shown in Figures 6.6 and 6.7. The excitation spectra of the Ce1 and Ce2 emission both consist of several overlapping bands, which are attributed to $4f^1 \rightarrow 5d^1$ transitions of Ce^{3+} . However, it is observed that the structure, i.e. peak positions and splitting of the excitation spectra of the Ce1 emission band (see Figures 6.6a and 6.7a) is significantly different from the excitation spectra recorded for the Ce2 emission (see Figures 6.6b and 6.7b). This confirms that the local environment of the two Ce^{3+} centers is different.

The splitting of the $5d^1$ state in the excitation spectra provides information on the local environment of the two Ce^{3+} sites. Ce^{3+} is in octahedral coordination in $\text{Cs}_2\text{MP}_2\text{O}_7$ and therefore a splitting of the $5d^1$ state into a $5d^1(t_{2g})$ and $5d^1(e_g)$ state is expected, the t_{2g} state being lower in energy. For the lower energy Ce1 site (Figures 6.6a and 6.7a), the excitation band between 30000 and 40000 cm^{-1} is assigned to the $4f^1 \rightarrow 5d^1(t_{2g})$ transition. The t_{2g} excitation band is split into three bands, which is explained by either a large spin-orbit coupling [19,28] or a slightly lower site symmetry for the Ce^{3+} ion (distorted octahedron). The excitation band between 40000 and 55000 cm^{-1} is assigned to the $4f^1 \rightarrow 5d^1(e_g)$ transition. In the excitation spectra of the higher energy Ce2 site (Figures 6.6b and 6.7b) we identify six $4f^1 \rightarrow 5d^1$ excitation bands (A-F), which means that the $5d^1$ configuration is split into at least six different states. This indicates that the symmetry of the Ce2 site is much lower than (slightly distorted) octahedral.

The formation of two geometrically different Ce^{3+} sites for $\text{Cs}_2\text{MP}_2\text{O}_7:\text{Ce}^{3+}$ is probably due to the charge compensation required for the $\text{Ce}_{\text{M}^{2+}}^{\bullet}$ site. The charge compensating defect can be local or distant, i.e. in the first shell of cations around the Ce^{3+} ion or further away in the lattice. A distant defect will not influence the local geometry around the Ce^{3+} ions, whereas a local defect can cause a deformation of the oxygen octahedron around the Ce^{3+} ion. Hence, we expect that the (octahedral) Ce1 site is the distantly charge compensated site, whereas the lower symmetry Ce2 site has local charge compensation in $\text{Cs}_2\text{MP}_2\text{O}_7$. Alternatively, the extra Ce^{3+} emission center can be in a second crystal phase doped with Ce^{3+} ions. This however seems unlikely, as the XRD patterns in Figure 6.2 show that no impurity crystal phases are present in our samples.

The crystal field splitting of the $5d$ configuration (ϵ_{cfs}) for Ce^{3+} in $\text{Cs}_2\text{MP}_2\text{O}_7$ can be estimated from the excitation spectra of the (slightly distorted) octahedral Ce1 site. The ϵ_{cfs} is calculated by taking the energy difference between the maxima of the t_{2g} and e_g

Table 6.2 – Optical properties of Ce^{3+} ions in $\text{Cs}_2\text{CaP}_2\text{O}_7$ and $\text{Cs}_2\text{SrP}_2\text{O}_7$. Estimated energy of the lowest $4f^1 \rightarrow 5d^1$ absorption band E^{abs} , peak energy of the $5d^1 \rightarrow {}^2F_{5/2}$ emission band E^{em} , and the Stokes shift $\Delta S = E^{\text{abs}} - E^{\text{em}}$. All values are in cm^{-1} and at $T = 4$ K.

Host	E^{abs}	E^{em}	ΔS
$\text{Cs}_2\text{CaP}_2\text{O}_7:\text{Ce1}$	30675	26738	3937
$\text{Cs}_2\text{SrP}_2\text{O}_7:\text{Ce1}$	31546	27624	3922
$\text{Cs}_2\text{CaP}_2\text{O}_7:\text{Ce2}$	32468	29499	2969
$\text{Cs}_2\text{SrP}_2\text{O}_7:\text{Ce2}$	32895	30211	2684

excitation bands. We find a ϵ_{cfs} of 20346 and 19736 cm^{-1} for $\text{Cs}_2\text{CaP}_2\text{O}_7$ and $\text{Cs}_2\text{SrP}_2\text{O}_7$, respectively. The ϵ_{cfs} of the Ce^{3+} 5d configuration is stronger in $\text{Cs}_2\text{CaP}_2\text{O}_7$, in agreement with the results for Eu^{2+} . There are several compounds for which the ϵ_{cfs} of the 5d configuration for both Ce^{3+} and Eu^{2+} is known. Using the data of these compounds, it was determined that the ϵ_{cfs} in Eu^{2+} on average is 0.77 times the ϵ_{cfs} in Ce^{3+} [27]. If we compare the ϵ_{cfs} of Eu^{2+} and Ce^{3+} in $\text{Cs}_2\text{MP}_2\text{O}_7$, we find an $\epsilon_{\text{cfs}}(\text{Eu}^{2+})/\epsilon_{\text{cfs}}(\text{Ce}^{3+})$ ratio of 0.87 and 0.83 for $\text{Cs}_2\text{CaP}_2\text{O}_7$ and $\text{Cs}_2\text{SrP}_2\text{O}_7$, respectively (ϵ_{cfs} values determined by taking the energy difference between the maxima of the t_{2g} and e_g band). These values are close to the 0.77 ratio determined in Ref. [27].

From the excitation and emission spectra in Figures 6.6 and 6.7 we can determine the Stokes shift of the Ce^{3+} emission of $\text{Cs}_2\text{MP}_2\text{O}_7:\text{Ce}^{3+}$. If the Stokes shift of the Ce^{3+} emission is anomalously large like the Stokes shift of the Eu^{2+} d–f emission, this would indicate that also substantial electronic relaxation occurs in the 5d excited state of Ce^{3+} . The Stokes shift (ΔS) of the Ce^{3+} emission is defined as the difference between the energy E^{abs} of the transition from the $4f^1 {}^2F_{5/2}$ ground state to the lowest $5d^1$ excited state and the peak energy E^{em} of the emission band belonging to the reverse $5d^1 \rightarrow {}^2F_{5/2}$ transition. E^{abs} is the peak energy of the lowest-energy excitation band in the excitation spectra. The E^{abs} , E^{em} and ΔS values determined for the Ce1 and Ce2 emission centers in $\text{Cs}_2\text{CaP}_2\text{O}_7$ and $\text{Cs}_2\text{SrP}_2\text{O}_7$ are listed in Table 6.2.

Before we discuss the ΔS , let us consider the absorption energy E^{abs} and emission energy E^{em} . For both emission centers, the energy E^{abs} of the Ce^{3+} $4f^1 \rightarrow 5d^1$ transition is lower for $\text{Cs}_2\text{CaP}_2\text{O}_7$ compared to $\text{Cs}_2\text{SrP}_2\text{O}_7$. This is attributed to the stronger crystal field splitting for Ce^{3+} in $\text{Cs}_2\text{CaP}_2\text{O}_7$. The E^{em} is lower for $\text{Cs}_2\text{CaP}_2\text{O}_7:\text{Ce}^{3+}$ (both Ce1 and Ce2), which is in agreement with the results obtained for Eu^{2+} . The values for E^{abs} and E^{em} of $\text{Cs}_2\text{MP}_2\text{O}_7:\text{Ce}^{3+}$ are also in agreement with what is typically found for Ce^{3+} in phosphate host lattices [29,30].

In Table 6.2 it can be seen that for $\text{Cs}_2\text{CaP}_2\text{O}_7:\text{Ce}^{3+}$ the Stokes shift of the Ce1 emission center ($\Delta S = 3937 \text{ cm}^{-1}$) is larger than the Stokes shift of the Ce2 emission center ($\Delta S =$

2969 cm^{-1}). A similar result is observed for $\text{Cs}_2\text{SrP}_2\text{O}_7:\text{Ce}^{3+}$. The Stokes shift values of both emission centers are in the range of $\Delta S = 1000\text{--}5000 \text{ cm}^{-1}$ that is typically observed for Ce^{3+} in (phosphate) compounds [15,29]. This is in contrast with the Stokes shift obtained for the Eu^{2+} d–f emission in $\text{Cs}_2\text{MP}_2\text{O}_7$, which is unusually large.

The E^{abs} and ΔS values of Ce^{3+} and Eu^{2+} in $\text{Cs}_2\text{MP}_2\text{O}_7$ can be compared quantitatively using relations that have been determined by Dorenbos [27]. In Ref. [27] it was shown that the redshift of absorption, the Stokes shift of emission, the centroid shift of the 5d configuration and the total crystal field splitting of the 5d levels of Eu^{2+} and Ce^{3+} all appear to be linearly related to one another. The relations for E^{abs} and ΔS are [27]:

$$E^{\text{abs}}(\text{Eu}^{2+}) = (0.64 \pm 0.02)E^{\text{abs}}(\text{Ce}^{3+}) + (0.53 \mp 0.06) \text{ eV} \quad (6.3)$$

$$\Delta S(\text{Eu}^{2+}) = (0.61 \pm 0.03)\Delta S(\text{Ce}^{3+}) \text{ eV} \quad (6.4)$$

We use the results of $\text{Cs}_2\text{MP}_2\text{O}_7:\text{Eu}^{2+}$ and equations 6.3 and 6.4 to predict the E^{abs} and ΔS of Ce^{3+} in $\text{Cs}_2\text{CaP}_2\text{O}_7$ and $\text{Cs}_2\text{SrP}_2\text{O}_7$. The calculated Ce^{3+} (calc) values for E^{abs} and ΔS are listed in Table 6.3, together with the experimental values of Eu^{2+} and the Ce1 and Ce2 emission centers. The data in Table 6.3 show a good agreement between the experimental E^{abs} values of the Ce1 emission and E^{abs} values calculated for Ce^{3+} . However, the experimental E^{abs} values of the Ce2 sites are just outside the range predicted for E^{abs} . This discrepancy can be due to a weaker crystal field splitting for the locally charge compensated Ce2 site.

In contrast to E^{abs} , we observe large differences between the calculated and experimental values for the Ce^{3+} Stokes shift in Table 6.3. The Stokes shift predicted for the Ce^{3+} emission is more than 1.2 eV, which is larger than Stokes shifts experimentally observed for Eu^{2+} (~ 0.75 eV). The Stokes shifts obtained for Ce^{3+} from the spectra in Figures 6.6 and 6.7 are however significantly smaller, with values of 0.3–0.5 eV for the Ce1 and Ce2 emission centers. It is clear that the Stokes shift of Eu^{2+} and Ce^{3+} in $\text{Cs}_2\text{MP}_2\text{O}_7$ do not show any relation. The observation of a normal Stokes shift for Ce^{3+} indicates that

Table 6.3 – 4f → 5d absorption energy E^{abs} and Stokes shift ΔS of Eu^{2+} and Ce^{3+} in $\text{Cs}_2\text{CaP}_2\text{O}_7$ and $\text{Cs}_2\text{SrP}_2\text{O}_7$. The values displayed for Ce^{3+} (calc) were determined using equations 6.3 and 6.4. Ce1 and Ce2 represent the two different Ce^{3+} emission centers observed for $\text{Cs}_2\text{MP}_2\text{O}_7:\text{Ce}^{3+}$. All values are in eV.

Property	Eu^{2+}	Ce^{3+} (calc)	Ce1	Ce2
E^{abs} (Ca)	2.85	3.63 ± 0.21	3.80	4.03
ΔS (Ca)	0.78	1.28 ± 0.06	0.49	0.37
E^{abs} (Sr)	2.97	3.81 ± 0.21	3.91	4.08
ΔS (Sr)	0.75	1.23 ± 0.06	0.49	0.33

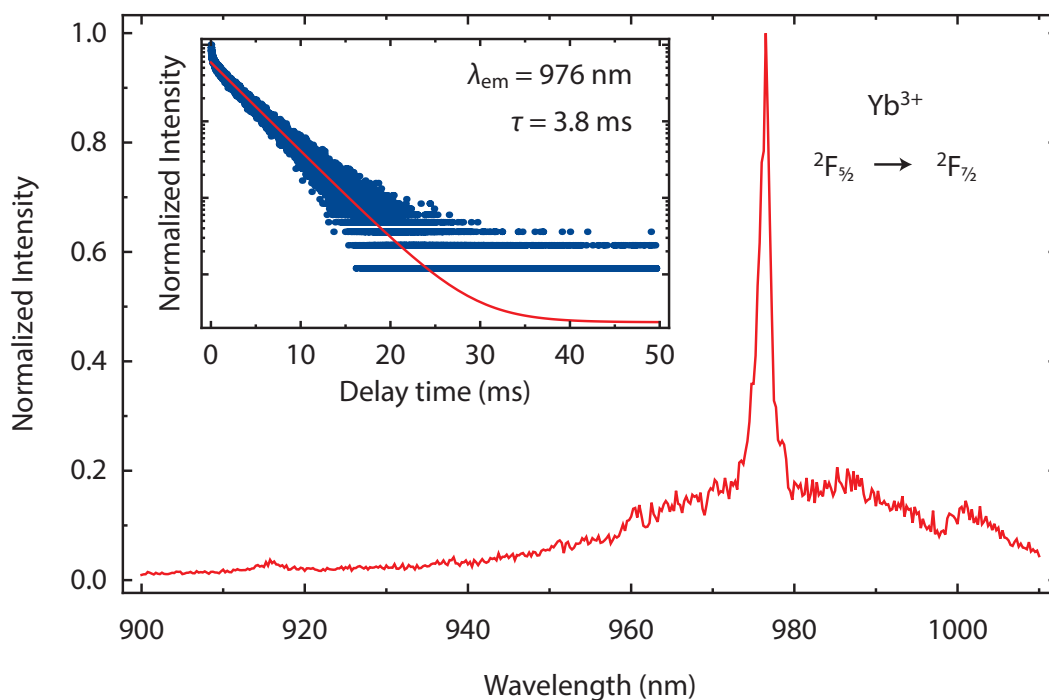


Figure 6.8 – Room temperature emission spectrum (red) of $\text{Cs}_2\text{SrP}_2\text{O}_7:\text{Yb}$ (1%) for $\lambda_{\text{exc}} = 212$ nm. The inset shows the typical millisecond decay of the parity-forbidden $\text{Yb}^{3+} \ ^2\text{F}_{5/2} \rightarrow \ ^2\text{F}_{7/2}$ emission at $\lambda_{\text{em}} = 976$ nm.

only weak electronic relaxation takes place in the 5d excited state, and consequently there is no evidence for a substantial excited state deformation as suggested for Eu^{2+} in $\text{Cs}_2\text{MP}_2\text{O}_7$.

6.3.3 Ytterbium luminescence

We have synthesized ytterbium doped $\text{Cs}_2\text{CaP}_2\text{O}_7$ and $\text{Cs}_2\text{SrP}_2\text{O}_7$ to investigate the d–f luminescence of Yb^{2+} ions in $\text{Cs}_2\text{MP}_2\text{O}_7$. The d–f luminescence of Yb^{2+} and Eu^{2+} are expected to be related [31] and therefore the Stokes shift of the Yb^{2+} emission may also be unusually large. In contrast to Ce^{3+} ions, Yb^{2+} ions require no charge compensation when substituted into $\text{Cs}_2\text{MP}_2\text{O}_7$. As a consequence, Yb^{2+} -doped $\text{Cs}_2\text{MP}_2\text{O}_7$ will better resemble $\text{Cs}_2\text{MP}_2\text{O}_7:\text{Eu}^{2+}$.

The syntheses of Yb-doped $\text{Cs}_2\text{CaP}_2\text{O}_7$ and $\text{Cs}_2\text{SrP}_2\text{O}_7$ were carried out under a reducing atmosphere (10% $\text{H}_2/90\%$ N_2) to reduce the Yb^{3+} ions of the Yb-precursor (Yb_2O_3) to Yb^{2+} ions. However, no Yb^{2+} d–f luminescence was observed for $\text{Cs}_2\text{MP}_2\text{O}_7:\text{Yb}$, even down to 4 K. Furthermore, no Yb^{2+} f–d absorption band was visible in the diffuse reflection spectra between 300 and 400 nm. We instead did observe $\text{Yb}^{3+} \ ^2\text{F}_{5/2} \rightarrow \ ^2\text{F}_{7/2}$ f–f luminescence for Yb-doped $\text{Cs}_2\text{MP}_2\text{O}_7$ (see Figure 6.8). These observations indicate that Yb is not stable in the divalent state in $\text{Cs}_2\text{MP}_2\text{O}_7$. Of all the lanthanides, Eu is most easily reduced to the divalent state, but also in the Eu-doped $\text{Cs}_2\text{MP}_2\text{O}_7$ luminescence of Eu^{3+} ions was observed. Based on this, it is not surprising that Yb^{2+} cannot be stabilized

in $\text{Cs}_2\text{MP}_2\text{O}_7$. Since no Yb^{2+} luminescence is measured, no comparison can be made between the luminescence properties of Eu^{2+} and Yb^{2+} ions in $\text{Cs}_2\text{CaP}_2\text{O}_7$ and $\text{Cs}_2\text{SrP}_2\text{O}_7$.

6.4 Conclusions

Previous reports have shown that the d–f luminescence of Eu^{2+} ions in $\text{Cs}_2\text{MP}_2\text{O}_7$ ($M = \text{Ca}^{2+}, \text{Sr}^{2+}$) is characterized by an unusually large Stokes shift $\Delta S > 6000 \text{ cm}^{-1}$. To gain insight in the origin of this large Stokes shift, we investigated the d–f luminescence of Eu^{2+} ions in $\text{Cs}_2\text{MP}_2\text{O}_7$ at cryogenic temperatures (down to 4 K). Furthermore, we compared the Eu^{2+} luminescence to the d–f luminescence of Ce^{3+} and Yb^{2+} ions in $\text{Cs}_2\text{MP}_2\text{O}_7$. At cryogenic temperatures, a large energy shift of around 3500 cm^{-1} between the sharp onsets of the Eu^{2+} emission and excitation bands was observed. This is surprising as the emission and excitation onsets of a specific electronic transition usually coincide. The onset shift indicates that there is a substantial electronic relaxation in the $4f^65d^1$ excited state, which can be due to a Jahn–Teller like deformation in the excited state. As a consequence of this deformation, the emission occurs from a lower energy excited $4f^65d^1$ state, resulting in a very large Stokes shift.

$\text{Cs}_2\text{MP}_2\text{O}_7:\text{Ce}^{3+}$ showed UV/blue Ce^{3+} d–f luminescence from two different Ce^{3+} sites. The formation of two distinct Ce^{3+} sites can be understood from the need for charge compensation for Ce^{3+} ions on the M^{2+} site. Contrary to Eu^{2+} , the emission for Ce^{3+} showed a normal Stokes shift of $2500\text{--}4000 \text{ cm}^{-1}$ and therefore the emission bands are at much higher energies than would be predicted from the energy of the Eu^{2+} emission and the Dorenbos relations. The normal Ce^{3+} Stokes shift indicates that, in contrast to Eu^{2+} , no Jahn–Teller like deformation takes place in the $5d$ state of Ce^{3+} . Unfortunately no Yb^{2+} d–f luminescence was observed for $\text{Cs}_2\text{MP}_2\text{O}_7:\text{Yb}$.

The results in this chapter indicate that the large Stokes shift for the Eu^{2+} emission of $\text{Cs}_2\text{MP}_2\text{O}_7:\text{Eu}^{2+}$ can be explained by a Jahn–Teller like deformation in the excited state. To confirm that a substantial deformation in the excited state occurs, it is interesting to try to measure the changes in the local geometry around the Eu^{2+} ion in the excited state, i.e. differences in the $\text{Eu}^{2+}\text{--O}^{2-}$ distances. An excellent technique to measure the local geometry around an impurity ion is X-ray absorption spectroscopy, more particularly, Extended X-ray Absorption Fine Structure (EXAFS) and X-ray absorption Near Edge Structure (XANES) [32]. Recently, time-resolved X-ray absorption spectroscopy (TR-XAS) experiments have been used to measure local geometric changes in the excited state of various organometallic complexes and metal ions in solids [33,34]. Hence, future experiments with EXAFS and XANES are interesting for investigating the geometric structure in the $\text{Eu}^{2+} 4f^65d^1$ excited state.

Acknowledgments

We thank Prof. M. Kitaura, Prof. J. Ueda and K. Asami for their help and skillful assistance

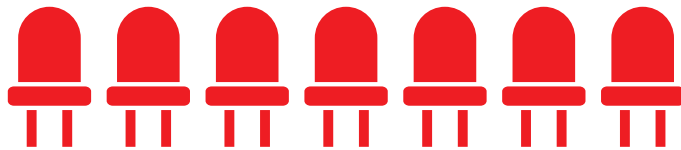
in the VUV experiments at the UVSOR facility (UVSOR project number 27-515). The support of the UVSOR (Okazaki, Japan) is gratefully acknowledged.

References

- [1] P. Dorenbos, *J. Lumin.* **104** (2003) 239–260.
- [2] P. Dorenbos, *J. Phys. Condens. Matter* **15** (2003) 2645–2665.
- [3] S. H. M. Poort, H. M. Reijnhoudt, H. O. T. van der Kuip and G. Blasse, *J. Alloys Compd.* **241** (1996) 75–81.
- [4] S. H. M. Poort, A. Meijerink and G. Blasse, *J. Phys. Chem. Solids* **58** (1997) 1451–1456.
- [5] K. van den Eeckhout, P. F. Smet and D. Poelman, *Materials* **3** (2010) 2536–2566.
- [6] B. M. J. Smets, *Mater. Chem. Phys.* **16** (1987) 283–299.
- [7] C. Feldmann, T. Jüstel, C. R. Ronda and P. J. Schmidt, *Adv. Funct. Mater.* **13** (2003) 511–516.
- [8] G. Blasse and B. C. Grabmaier, *Luminescent Materials*, Springer-Verlag, Heidelberg, 1994.
- [9] P. F. Smet, A. B. Parmentier and D. Poelman, *J. Electrochem. Soc.* **158** (2011) R37–R54.
- [10] F. Suyver and A. Meijerink, *Chemisch2Weekblad* **98** (2002) 12–13.
- [11] A. M. Srivastava, H. A. Comanzo, S. Camardello, S. B. Chaney, M. Aycibin and U. Happek, *J. Lumin.* **129** (2009) 919–925.
- [12] A. M. Srivastava, H. A. Comanzo, S. Camardello, M. Aycibin and U. Happek, *ECS Trans.* **25** (2009) 201–204.
- [13] M. Marsman, J. Andriessen and C. W. E. van Eijk, *Phys. Rev. B* **61** (2000) 16477–16490.
- [14] J. Andriessen, O. T. Antonyak, P. Dorenbos, P. A. Rodnyi, G. B. Stryganyuk, C. W. E. van Eijk and A. S. Voloshinovskii, *Opt. Commun.* **178** (2000) 355–363.
- [15] P. Dorenbos, J. Andriessen, M. Marsman and C. W. E. van Eijk, *Radiat. Eff. Defects Solids* **154** (2001) 237–241.
- [16] J. Andriessen, E. van der Kolk and P. Dorenbos, *Phys. Rev. B* **76** (2007) 075124.
- [17] S. Lizzo, A. H. Velders, A. Meijerink, G. J. Dirksen and G. Blasse, *J. Lumin.* **65** (1995) 303–311.
- [18] Z. Pan, L. Ning, B.-M. Cheng and P. A. Tanner, *Chem. Phys. Lett.* **428** (2006) 78–82.
- [19] L. van Pieterse, M. F. Reid, R. T. Wegh, S. Soverna and A. Meijerink, *Phys. Rev. B* **65** (2002) 045113.
- [20] V. Bachmann, C. R. Ronda and A. Meijerink, *Chem. Mater.* **21** (2009) 2077–2084.
- [21] A. Meijerink and G. Blasse, *J. Lumin.* **43** (1989) 283–289.
- [22] S. H. M. Poort, W. Janssen and G. Blasse, *J. Alloys Compd.* **260** (1997) 93–97.
- [23] B. Henderson and G. F. Imbusch, *Optical Spectroscopy of Inorganic Solids*, Clarendon Press, Oxford, 1989.
- [24] M. de Jong, L. Seijo, A. Meijerink and F. T. Rabouw, *Phys. Chem. Chem. Phys.* **17** (2015) 16959–16969.
- [25] L. L. Chase, *Phys. Rev. Lett.* **23** (1969) 275–277.
- [26] L. L. Chase, *Phys. Rev. B* **2** (1970) 2308–2318.
- [27] P. Dorenbos, *J. Phys. Condens. Matter* **15** (2003) 4797–4807.
- [28] R. W. Schwartz and P. N. Schatz, *Phys. Rev. B* **8** (1973) 3229–3236.
- [29] P. Dorenbos, *J. Lumin.* **91** (2000) 155–176.
- [30] P. Dorenbos, *Phys. Rev. B* **64** (2001) 125117.
- [31] P. Dorenbos, *J. Phys. Condens. Matter* **15** (2003) 575–594.
- [32] D. C. Koningsberger and R. Prins, *X-Ray Absorption: Principles, Applications, Techniques of EXAFS, SEXAFS and XANES*, Wiley-Interscience, Hoboken, 1987.
- [33] E. Vorobeva, S. L. Johnson, P. Beaud, C. J. Milne, M. Benfatto and G. Ingold, *Phys. Rev. B* **80** (2009) 134301.
- [34] R. M. van der Veen, C. J. Milne, A. El Nahhas, F. A. Lima, V.-T. Pham, J. Best, J. A. Weinstein, C. N. Borca, R. Abela, C. Bressler and M. Chergui, *Angew. Chem. Int. Ed.* **48** (2009) 2711–2714.

7

Summary and outlook



Abstract

The results presented in this thesis provide new insights in the synthesis and luminescence of two types of narrow band red-emitting phosphors: Mn^{4+} -doped phosphors and Eu^{2+} -activated $\text{Cs}_2\text{MP}_2\text{O}_7$ ($\text{M} = \text{Ca}^{2+}, \text{Sr}^{2+}$) phosphates. We describe the synthesis and optical properties of new Mn^{4+} -doped phosphors and investigate how the Mn^{4+} emission and energy levels are influenced by the host lattice the Mn^{4+} ions are situated in. Furthermore, we investigate which processes are responsible for thermal quenching and concentration quenching of the Mn^{4+} luminescence in Mn^{4+} -doped phosphors, as both these effects are crucial for the performance of w-LEDs containing Mn^{4+} phosphors. Finally, we study the unusual narrow yellow/red Eu^{2+} luminescence and large Stokes shift of $\text{Cs}_2\text{MP}_2\text{O}_7:\text{Eu}^{2+}$ through extensive low-temperature spectroscopic measurements. In this chapter we summarize the main results and discuss potential directions for future research.

7.1 Introduction

White light emitting diodes (w-LEDs) are revolutionizing the display and lighting industries due to their small size, high luminous efficacy and long operation lifetime. In order to realize a full color spectrum with high color rendering, in conventional w-LEDs Eu^{2+} -doped nitrides are used as red-emitting phosphors in addition to green or yellow emitting phosphors. These nitride phosphors exhibit a high quantum efficiency (QE), but a major drawback is that the Eu^{2+} emission band of these phosphors is broad and extends into the deep-red spectral region ($\lambda > 60 \text{ nm}$) where the eye sensitivity is low. This causes a reduction in the luminous efficacy of the w-LED. A worldwide search is therefore aimed at finding efficient narrow band red-emitting materials. In this thesis we have investigated two new types of narrow band red phosphors: Mn^{4+} -doped phosphors and Eu^{2+} -activated $\text{Cs}_2\text{MP}_2\text{O}_7$ ($\text{M} = \text{Ca}^{2+}, \text{Sr}^{2+}$) phosphates.

7.2 Mn^{4+} -doped phosphors

Upon blue photoexcitation, Mn^{4+} -doped fluorides show narrow red line emission in the 600–640 nm spectral region. These characteristics make Mn^{4+} -doped fluorides interesting narrow band red phosphors for w-LEDs. In Chapters 2 to 5 we report on the synthesis and luminescence properties of Mn^{4+} -doped phosphors. We focus on synthesizing (new) Mn^{4+} phosphors, understanding how the positions of the Mn^{4+} energy levels can be controlled by the host lattice, and determining which processes are responsible for quenching of the Mn^{4+} luminescence.

In **Chapter 2** we present the synthesis and optical properties of a new Mn^{4+} -activated fluoride host: a Mn^{4+} -doped fluorohafnate. The phosphor $\text{Cs}_2\text{HfF}_6:\text{Mn}^{4+}$ is synthesized by initially preparing the Mn^{4+} -precursor K_2MnF_6 and then in a second step precipitating $\text{Cs}_2\text{HfF}_6:\text{Mn}^{4+}$ from an aqueous HF solution containing Cs^+ , Hf^{4+} and Mn^{4+} ions. ICP-OES measurements confirm that the Mn^{4+} ions are effectively incorporated into the Cs_2HfF_6 host. The $\text{Cs}_2\text{HfF}_6:\text{Mn}^{4+}$ phosphor shows bright red Mn^{4+} luminescence with a QE higher than 80%, which makes it an interesting red-emitting material for w-LEDs and other lighting applications. As the Mn^{4+} emission from $\text{Cs}_2\text{HfF}_6:\text{Mn}^{4+}$ shows quenching above 100 °C, the use of this phosphor will be limited to low-power LED lighting.

Chapter 3 reports the synthesis of different $\text{M}_3\text{AlF}_6:\text{Mn}^{4+}$ ($\text{M} = \text{Na}, \text{K}$) phosphors via a simple two-step co-precipitation method. Our synthesis method provides good control over Mn^{4+} doping and yields highly monodisperse $\sim 20 \text{ }\mu\text{m}$ smoothed octahedron shaped crystallites for $\text{K}_2\text{NaAlF}_6:\text{Mn}^{4+}$, while irregularly shaped particles with a broad size distribution are obtained for $\text{K}_3\text{AlF}_6:\text{Mn}^{4+}$ and $\text{Na}_3\text{AlF}_6:\text{Mn}^{4+}$. Luminescence spectra recorded at cryogenic temperatures reveal that multiple Mn^{4+} sites exist in $\text{M}_3\text{AlF}_6:\text{Mn}^{4+}$, which is explained by the charge compensation that is required for Mn^{4+} on Al^{3+} sites. The luminescence measurements show that charge compensating defects have a large influence on the optical properties (e.g. spectra, QE, luminescence lifetime)

of Mn^{4+} -doped fluorides. Thermal annealing results in a change in the optical spectra which is explained by a change in the Mn^{4+} site distribution after heating.

In **Chapter 4** we study how the optical properties of Mn^{4+} are influenced by the host lattice the Mn^{4+} ions are situated in. We investigate the effect of the host cations in the second coordination sphere on the Mn^{4+} luminescence by comparing the luminescence spectra of Mn^{4+} ions doped into three isostructural $\text{RE}_2\text{Sn}_2\text{O}_7$ pyrochlores ($\text{RE}^{3+} = \text{Y}^{3+}$, Lu^{3+} or Gd^{3+}). It is found that the energies of the Mn^{4+} ${}^4\text{T}_1$ and ${}^4\text{T}_2$ states increase with decreasing $\text{Mn}^{4+}\text{-O}^{2-}$ distance, whereas the energy of the ${}^2\text{E}$ level shows a small shift to higher energies from $\text{RE}^{3+} = \text{Gd}^{3+}$ to Lu^{3+} to Y^{3+} . The observed trend for the ${}^2\text{E}$ level energy is not related to the size of the RE^{3+} ion. Low-temperature emission spectra of the $\text{RE}_2\text{Sn}_2\text{O}_7:\text{Mn}^{4+}$ phosphors reveal that there is significant and unexpected local disorder for Mn^{4+} in $\text{Gd}_2\text{Sn}_2\text{O}_7$ that is not observed for Mn^{4+} in the other hosts.

Chapter 5 presents an extensive study aimed at unravelling the mechanisms behind thermal quenching and concentration quenching of the Mn^{4+} luminescence in Mn^{4+} -doped fluorides. For practical application both processes are highly relevant but until now the mechanisms were not well understood. To obtain insight in the quenching, we measured luminescence spectra and decay curves for $\text{K}_2\text{TiF}_6:\text{Mn}^{4+}$ between 4 and 600 K and for Mn^{4+} concentrations from 0.01 to 15.7%. Analysis of the results and data in the literature reveal that thermal quenching occurs through thermally activated crossover between the ${}^4\text{T}_2$ excited state and ${}^4\text{A}_2$ ground state. The quenching temperature can therefore be optimized by designing host lattices in which Mn^{4+} has a high ${}^4\text{T}_2$ state energy. Furthermore, concentration-dependent studies show that concentration quenching effects are limited in $\text{K}_2\text{TiF}_6:\text{Mn}^{4+}$ up to 5% Mn^{4+} . This is important as high Mn^{4+} concentrations are required for sufficient absorption of blue LED light in the parity-forbidden Mn^{4+} d-d transitions. At even higher Mn^{4+} concentrations (>10%) the QE decreases, mostly due to direct energy transfer to quenching sites (defects, impurity ions, Mn^{2+} and Mn^{3+}). Optimized synthesis procedures to avoid quenching sites are crucial in raising the Mn concentration in commercially applied phosphors to levels of 10% or more to enhance the absorption of blue LED light.

Several different directions can be explored in future research on Mn^{4+} -doped phosphors. Based on the results presented in Chapters 2 to 5, there are a number of interesting and relevant follow-up experiments. First of all, w-LED prototypes containing $\text{Cs}_2\text{HfF}_6:\text{Mn}^{4+}$ as red phosphor should be constructed to evaluate the performance of $\text{Cs}_2\text{HfF}_6:\text{Mn}^{4+}$ in w-LEDs. Analysis of the device performance will then indicate whether $\text{Cs}_2\text{HfF}_6:\text{Mn}^{4+}$ has potential for application in w-LEDs. Secondly, the synthesis of $\text{Cs}_2\text{HfF}_6:\text{Mn}^{4+}$ and $\text{M}_3\text{AlF}_6:\text{Mn}^{4+}$ ($\text{M} = \text{Na}, \text{K}$) can be optimized to try to increase the QE of these phosphors. In the case of $\text{M}_3\text{AlF}_6:\text{Mn}^{4+}$, charge compensating ions can be added during the synthesis to try to decrease the defect concentration in these phosphors. For example, part of the Al^{3+} ions could be replaced by Mg^{2+} ions to compensate for the additional charges of

Mn⁴⁺ ions on Al³⁺ sites [1].

More extensive studies on the synthesis of Mn⁴⁺-doped fluorides are interesting to optimize synthesis procedures for realizing high QEs at high Mn⁴⁺ doping concentrations. The results in Chapter 5 demonstrate that the QE of K₂TiF₆:Mn⁴⁺ decreases at high Mn⁴⁺ concentrations due to direct energy transfer to quenching sites, i.e. defects, impurity ions, Mn²⁺ and Mn³⁺. The occurrence of Mn in many different oxidation states (more than other 3d transition metal ions) makes it particularly challenging to synthesize a material in which all Mn is tetravalent. Optimization of the synthesis is required to reduce quenching sites and is thus crucial for developing more efficient highly absorbing Mn⁴⁺ phosphors. Hence, it is interesting to systematically investigate which synthesis method results in Mn⁴⁺-doped phosphor particles with the lowest number of crystal defects and Mn ions in other valence states [2,3]. In addition, a systematic investigation of the synthesis can show which method gives the best control over the Mn⁴⁺ dopant concentration. A better understanding of the synthesis may also increase the control over the Mn⁴⁺ phosphor particle morphology. This will aid the reproducible preparation of Mn⁴⁺-doped crystallites with narrow size and shape distributions, like observed (but not fully understood) in Chapter 3 for K₂NaAlF₆:Mn⁴⁺.

In lighting the large scale application of Mn⁴⁺-doped fluorides is still limited, partly due to issues related to thermal and chemical stability of the Mn⁴⁺ phosphors at high LED pump powers. An important future challenge is thus to improve the thermal and chemical stability of Mn⁴⁺-doped phosphors. The results in Chapter 5 show that the Mn⁴⁺ luminescence quenching temperature can be raised by designing host lattices in which Mn⁴⁺ has an increased ⁴T₂ level energy. Future research should therefore be directed towards developing Mn⁴⁺-doped fluorides with high ⁴T₂ state energies. For this purpose, ab-initio calculations of the Mn⁴⁺ energy levels in a large variety of fluoride hosts can help to predict which lattices are most interesting [4]. Furthermore, several possible ways to improve the chemical stability of Mn⁴⁺-doped fluorides can be investigated. Coating of the phosphor particles with metal oxide shells (e.g. SiO₂ or TiO₂) or alkyl phosphate layers may enhance the chemical stability and moisture resistance [5–7]. In addition, the synthesis of Mn⁴⁺-doped fluoride particles with a core/shell structure is interesting. K₂SiF₆:Mn⁴⁺/K₂SiF₆ core/shell particles have been prepared by stirring K₂SiF₆:Mn⁴⁺ particles in HF or H₂SiF₆ solutions, which causes leaching of surface layer Mn⁴⁺ ions [8]. This removes Mn⁴⁺ ions from the surface and creates an undoped protective K₂SiF₆ surface layer, thereby improving the long term stability of the phosphor particles. Alternative methods to grow a protective undoped shell may result in even higher (photo)chemical stability.

Other interesting future experiments regarding the optical properties of Mn⁴⁺-doped fluorides involve reduction of the radiative lifetime and tuning the spectral output. The parity- and spin-forbidden ²E → ⁴A₂ emission of Mn⁴⁺ has a long luminescence lifetime,

around 3 to 8 milliseconds in fluorides. Due to the long luminescence lifetime, saturation can occur at high LED excitation powers. Understanding of the role of saturation effects in (high power) w-LEDs is presently lacking, despite it being very important for the application of Mn^{4+} -doped fluorides in w-LEDs [9]. Systematic research is needed to provide insight in the saturation behavior. For example, it would be interesting to study if there are significant differences in saturation behavior between Mn^{4+} phosphors with a lifetime of 8 milliseconds (e.g. $\text{K}_2\text{SiF}_6:\text{Mn}^{4+}$) and Mn^{4+} phosphors with a slightly shorter lifetime of around 4 milliseconds (e.g. $\text{Cs}_2\text{HfF}_6:\text{Mn}^{4+}$, see Chapter 2).

Furthermore, it would be interesting to compare the color rendering and luminous efficacy of w-LEDs with different Mn^{4+} -doped fluorides. So far, $\text{K}_2\text{SiF}_6:\text{Mn}^{4+}$ is the only Mn^{4+} -doped fluoride phosphor being used in commercial w-LEDs. $\text{K}_2\text{SiF}_6:\text{Mn}^{4+}$ has a very weak zero-phonon line at 620 nm because of the highly symmetric octahedral coordination for Mn^{4+} . Also $\text{Cs}_2\text{HfF}_6:\text{Mn}^{4+}$ (Chapter 2) and $\text{K}_2\text{TiF}_6:\text{Mn}^{4+}$ (Chapter 5) show a very low emission intensity at this wavelength. There are however several Mn^{4+} -doped fluorides which exhibit a strong zero-phonon line at ~ 620 nm, for example $\text{Na}_2\text{SiF}_6:\text{Mn}^{4+}$ and $\text{Na}_2\text{GeF}_6:\text{Mn}^{4+}$ [10]. These phosphors therefore can be an interesting alternative for $\text{K}_2\text{SiF}_6:\text{Mn}^{4+}$. LEDs containing these phosphors may exhibit a better color quality and luminous efficacy than LEDs containing $\text{K}_2\text{SiF}_6:\text{Mn}^{4+}$. Further research is necessary to investigate this.

7.3 Eu^{2+} -doped $\text{Cs}_2\text{MP}_2\text{O}_7$ ($\text{M} = \text{Ca}^{2+}, \text{Sr}^{2+}$) phosphates

The luminescence of $\text{Cs}_2\text{MP}_2\text{O}_7:\text{Eu}^{2+}$ ($\text{M} = \text{Ca}^{2+}, \text{Sr}^{2+}$) is characterized by a narrow yellow/red Eu^{2+} d–f emission band and a high luminescence quenching temperature. These optical properties make $\text{Cs}_2\text{MP}_2\text{O}_7:\text{Eu}^{2+}$ a promising red-emitting phosphor for w-LEDs. The $\text{Cs}_2\text{MP}_2\text{O}_7:\text{Eu}^{2+}$ phosphates exhibit yellow to red Eu^{2+} emission because of an unusually large Stokes shift. In **Chapter 6** we investigated the origin of the large Stokes shift in $\text{Cs}_2\text{MP}_2\text{O}_7:\text{Eu}^{2+}$ through measurements at cryogenic temperatures, and by comparison with the d–f luminescence of Ce^{3+} and Yb^{2+} in the same host lattice. In the spectra measured at 4 K a large energy difference between the onsets of the Eu^{2+} emission and excitation bands is observed. This is unusual and indicates that there is a substantial electronic relaxation in the $\text{Eu}^{2+} 4f^65d^1$ excited state. This can be due to a Jahn–Teller like deformation in the excited state. As a consequence of this deformation, the emission occurs from a lower energy $4f^65d^1$ excited state, resulting in a very large Stokes shift. Contrary to the unusually large Stokes shift observed for Eu^{2+} , the luminescence of Ce^{3+} is normal in $\text{Cs}_2\text{MP}_2\text{O}_7$, indicating that the special luminescence properties are specific for the d–f emission of Eu^{2+} .

To confirm that a substantial deformation occurs in the $\text{Eu}^{2+} 4f^65d^1$ excited state of $\text{Cs}_2\text{MP}_2\text{O}_7:\text{Eu}^{2+}$ ($\text{M} = \text{Ca}^{2+}, \text{Sr}^{2+}$), it would be interesting to measure the changes in the local geometry around the Eu^{2+} ion in the excited state, i.e. differences in the $\text{Eu}^{2+}-\text{O}^{2-}$

distances. An excellent technique to measure the local geometry around an impurity ion is X-ray absorption spectroscopy, particularly Extended X-ray Absorption Fine Structure (EXAFS) spectroscopy [11]. Recently, time-resolved X-ray absorption spectroscopy (TR-XAS) experiments have been used to measure local geometric changes in the excited states of various organometallic complexes and metal ions in solids [12–14]. In these experiments, the luminescent center is excited by a laser pulse and then shortly after the laser pulse probed with an X-ray beam to measure EXAFS spectra of its excited state. For future research, similar TR-XAS experiments are interesting for $\text{Cs}_2\text{MP}_2\text{O}_7:\text{Eu}^{2+}$ as to investigate the suggested excited state deformation.

The compounds $\text{Cs}_2\text{CaP}_2\text{O}_7$ and $\text{Cs}_2\text{SrP}_2\text{O}_7$ are hygroscopic [15]. The use of $\text{Cs}_2\text{MP}_2\text{O}_7:\text{Eu}^{2+}$ phosphates in w-LEDs is therefore challenging and will require strong protection of the phosphors from moisture. Hence, in future experiments it should be investigated whether other Eu^{2+} phosphors can be developed that exhibit the special optical properties observed in $\text{Cs}_2\text{MP}_2\text{O}_7:\text{Eu}^{2+}$ (large Stokes shift, narrow Eu^{2+} emission band). As Jahn–Teller like deformations are observed for luminescent centers with a high (octahedral) symmetry, we propose to incorporate Eu^{2+} in octahedral sites in Ca and Sr compounds, including borates, phosphates, silicates and sulfates where the anion network provides a strong backbone for octahedral cages in which the Eu^{2+} ion can be incorporated.

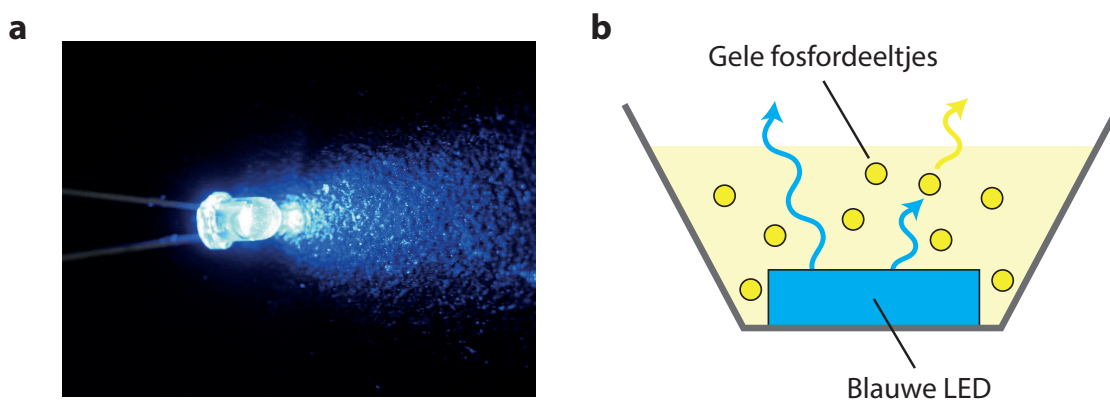
References

- [1] J. F. Donegan, T. J. Glynn, G. F. Imbusch and J. P. Remeika, *J. Lumin.* **36** (1986) 93–100.
- [2] H.-D. Nguyen and R.-S. Liu, *J. Mater. Chem. C* **4** (2016) 10759–10775.
- [3] H. F. Sijbom, R. Verstraete, J. J. Joos, D. Poelman and P.F. Smet, *Opt. Mater. Express* **7** (2017) 3332–3365.
- [4] L. Seijo, Z. Barandiarán and D. S. McClure, *Int. J. Quantum Chem.* **80** (2000) 623–635.
- [5] R. G. Geitenbeek, P. T. Prins, W. Albrecht, A. van Blaaderen, B. M. Weckhuysen and A. Meijerink, *J. Phys. Chem. C* **121** (2017) 3503–3510.
- [6] W. Su, M. Zheng, L. Li, K. Wang, R. Qiao, Y. Zhong, Y. Hu and Z. Li, *J. Mater. Chem. A* **2** (2014) 13486–13491.
- [7] H.-D. Nguyen, C. C. Lin and R.-S. Liu, *Angew. Chemie Int. Ed.* **54** (2015) 10862–10866.
- [8] A. A. Setlur, O. P. Siclovan, R. J. Lyons, and L. S. Grigorov, U.S. Patent No. 8,057,706 B1, 2011.
- [9] H. F. Sijbom, J. J. Joos, L. I. D. J. Martin, K. Van den Eeckhout, D. Poelman and P. F. Smet, *ECS J. Solid State Sci. Technol.* **5** (2016) R3040–R3048.
- [10] Y. K. Xu and S. Adachi, *J. Appl. Phys.* **105** (2009) 013525.
- [11] D. C. Koningsberger and R. Prins, X-Ray Absorption: Principles, Applications, Techniques of EXAFS, SEXAFS and XANES, Wiley-Interscience, Hoboken, 1987.
- [12] E. Vorobeva, S. L. Johnson, P. Beaud, C. J. Milne, M. Benfatto and G. Ingold, *Phys. Rev. B* **80** (2009) 134301.
- [13] R. M. van der Veen, C. J. Milne, A. El Nahhas, F. A. Lima, V.-T. Pham, J. Best, J. A. Weinstein, C. N. Borca, R. Abela, C. Bressler and M. Chergui, *Angew. Chem. Int. Ed.* **48** (2009) 2711–2714.
- [14] A. El Nahhas, R. M. van der Veen, T. J. Penfold, V. T. Pham, F. A. Lima, R. Abela, A. M. Blanco-Rodriguez, S. Zálíš, A. Vlček, I. Tavernelli, U. Rothlisberger, C. J. Milne and M. Chergui, *J. Phys. Chem. A* **117** (2013) 361–369.
- [15] A. M. Srivastava, H. A. Comanzo, S. Camardello, S. B. Chaney, M. Aycibin and U. Happek, *J. Lumin.* **129** (2009) 919–925.

Samenvatting in het Nederlands

In ons dagelijks leven zijn we sterk afhankelijk van artificiële lichtbronnen. Zowel overdag als na zonsondergang gebruiken we wereldwijd miljarden gloeilampen, TL-buizen, spaarlampen en LED-lampen om onze omgeving te verlichten. Witte LED-lampen (Figuur 1a) hebben een hogere efficiëntie en langere levensduur dan gloeilampen, TL-buizen en spaarlampen en worden daarom gezien als de lichtbronnen van de toekomst. De verwachting is dat witte LED-lampen de traditionele lichtbronnen grotendeels zullen vervangen in de komende tien jaar. Het gebruik van LED-lampen in plaats van gloeilampen en spaarlampen vermindert ons elektriciteitsverbruik en draagt daarmee bij aan een duurzame oplossing voor de huidige klimaat- en energieproblemen.

De meeste LED-lampen maken wit licht met behulp van een blauwe indiumgalliumnitride LED en een luminescerend materiaal (een fosfor) die een deel van het blauwe licht absorbeert en omzet in geel licht, zoals weergegeven in Figuur 1b. Blauw en geel licht samen nemen wij waar als wit licht. Deze combinatie van blauw en geel licht is deficiënt in het rode spectrale gebied en wordt daarom ervaren als onaangenaam koud wit licht. Toevoeging van een fosfor die blauw licht omzet in rood licht zorgt voor warmer wit licht met een betere kleurweergave. De toevoeging van een rode fosfor gaat helaas samen met een drastische verlaging van de efficiëntie van de LED-lamp. De efficiëntie is lager doordat de huidige rode fosforen (europium-gedoteerde nitrides) een breedbandig emissiespectrum hebben en daarbij een deel van het rode licht uitzenden in een golflengtegebied waar de gevoeligheid van onze ogen erg laag is (langgolfiger dan 640 nm). Er is daarom een wereldwijde zoektocht naar materialen die blauw licht kunnen absorberen en efficiënt omzetten in smalbandig rood licht met een golflengte van ongeveer 620 nm. Materialen met deze optische eigenschappen maken het mogelijk



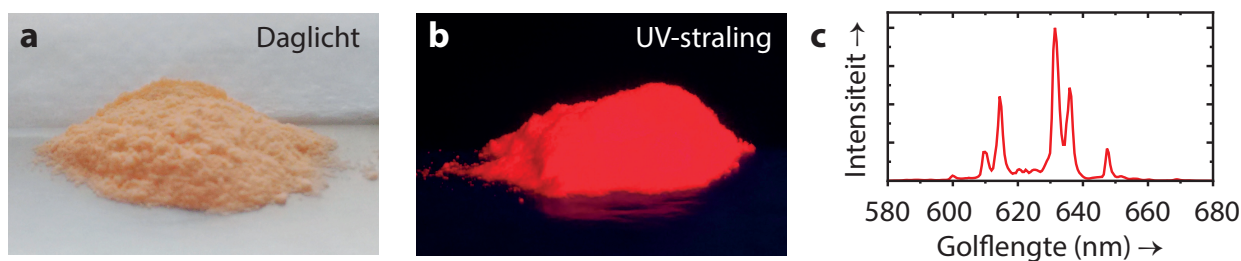
Figuur 1 – De witte LED-lamp. (a) Foto van een LED-lamp. Bron: Wikimedia Commons. (b) Schematische weergave van een witte LED-lamp. De LED-lamp maakt wit licht met behulp van een blauwe LED en een gele fosfor die een deel van het blauwe licht omzet in geel licht. De combinatie van blauw en geel licht wordt waargenomen als wit licht.

om LED-lampen te ontwikkelen met warm wit licht zonder veel te hoeven inleveren op de efficiëntie.

In dit proefschrift worden twee nieuwe soorten smalbandig rode fosforen onderzocht. Het doel van het onderzoek is het vinden van nieuwe smalbandig rode fosforen en het verkrijgen van een beter inzicht in de luminescentie-eigenschappen die belangrijk zijn voor toepassing van smalbandig rode fosforen in witte LED-lampen. Naast een smalbandig rode emissie rond 620 nm zijn ook aspecten als de temperatuurstabiliteit van de luminescentie-efficiëntie, concentratiedoving en de luminescentielevensduur van belang. Inzicht in deze eigenschappen zal bijdragen aan de ontwikkeling van nieuwe fosforen voor betere witte LED-lampen.

De eerste soort smalbandig rode fosforen die onderzocht worden in dit proefschrift zijn fosforen gedoteerd met vierwaardig mangaan (Mn^{4+}). De Mn^{4+} -ionen in deze fosforen zenden rood licht uit na absorptie van blauw licht of UV-straling (zie Figuur 2). Omdat Mn^{4+} alleen het blauwe licht uit het zichtbare spectrum sterk absorbeert, hebben Mn^{4+} -gedoteerde fosforen een oranje-gele kleur in daglicht (zie Figuur 2a). Het licht dat uitgezonden wordt door de fosfor wordt 'luminescentie' genoemd. In Figuur 2c is een spectrum van de rode Mn^{4+} -luminescentie te zien. In het spectrum wordt de intensiteit van het licht dat de fosfor uitzendt weergegeven als functie van de golflengte van de uitgezonden fotonen (lichtdeeltjes). Het spectrum toont dat de rode luminescentie bestaat uit enkele smalle emissiepieken rond een golflengte van 620 nm. Deze optische eigenschappen maken Mn^{4+} -gedoteerde fosforen zeer interessante materialen voor toepassing in witte LED-lampen.

De hoofdstukken 2 tot en met 5 van dit proefschrift beschrijven onderzoek aan Mn^{4+} -gedoteerde fosforen. Het onderzoek richt zich vooral op het synthetiseren van (nieuwe) Mn^{4+} -gedoteerde fosforen en het bestuderen van de luminescentie van deze materialen.



Figuur 2 – De rode luminescentie van een Mn^{4+} -gedoteerde fosfor. (a) Een foto van Mn^{4+} -gedoteerd cesiumfluorohafnaat (Cs_2HfF_6) onder daglicht. Het materiaal heeft een oranje-gele kleur omdat de Mn^{4+} -ionen het blauwe licht uit het lichtspectrum absorberen. (b) Als hetzelfde materiaal wordt beschonen met blauw licht of UV-straling vertoont het rode luminescentie. (c) Spectrum van de rode luminescentie in Mn^{4+} -gedoteerd cesiumfluorohafnaat. Het spectrum toont de intensiteit van het licht dat de fosfor uitzendt als functie van de golflengte van de uitgezonden fotonen (lichtdeeltjes).

In **Hoofdstuk 2** beschrijven we de synthese en optische eigenschappen van een nieuwe Mn⁴⁺-gedoteerde fosfor: cesiumfluorohafnaat (Cs₂HfF₆) gedoteerd met Mn⁴⁺. We laten zien dat deze fosfor gesynthetiseerd kan worden via een simpele co-precipitatiemethode bij kamertemperatuur. De fosfor vertoont efficiënte rode luminescentie onder excitatie met blauw licht of UV-straling (zie Figuur 2b). Dit maakt Mn⁴⁺-gedoteerd Cs₂HfF₆ een interessant materiaal voor gebruik in LED-lampen en andere verlichting.

Hoofdstuk 3 behandelt de synthese en luminescentie van diverse Mn⁴⁺-gedoteerde fluoroaluminaten. We beschrijven een nieuwe syntheseroute voor het maken van deze fosforen via co-precipitatie. Onze synthesesmethode geeft goede controle over de Mn⁴⁺-doteringsconcentratie en resulteert in fraaie uniforme kristallen voor Mn⁴⁺-gedoteerd kaliumnatriumfluoroaluminaat (K₂NaAlF₆). De rode luminescentie van de Mn⁴⁺-gedoteerde fluoroaluminaten wordt uitgebreid bestudeerd. Uit de luminescentiemetingen blijkt dat de MnF₆-groepen in deze fosforen niet allemaal dezelfde structuur hebben. Dit wordt veroorzaakt door ladingsdefecten in de kristallen die ontstaan doordat de Al³⁺-ionen in de kristallen deels vervangen worden door Mn⁴⁺-ionen. De ladingsdefecten veroorzaken niet alleen een variatie in de structuur van de MnF₆-groepen maar hebben ook een nadelig effect op de efficiëntie van de rode luminescentie in Mn⁴⁺-gedoteerde fluoroaluminaten.

In **Hoofdstuk 4** bestuderen we hoe de optische eigenschappen van Mn⁴⁺ beïnvloed worden door het kristalrooster rond de Mn⁴⁺-ionen. Dit doen we door de luminescentie van Mn⁴⁺ in drie verschillende stannaten te vergelijken, namelijk yttriumstannaat (Y₂Sn₂O₇), lutetiumstannaat (Lu₂Sn₂O₇) en gadoliniumstannaat (Gd₂Sn₂O₇). De luminescentiespectra van Mn⁴⁺ in deze stannaten laten zien dat de blauwe absorptieband van Mn⁴⁺ opschuift naar een hogere energie als de afstand tussen Mn⁴⁺ en de omringende oxide-ionen (O²⁻) korter wordt. Daarentegen is de energie (golflengte) van de rode luminescentie bijna gelijk voor de verschillende Mn⁴⁺-gedoteerde stannaten. Naast het vergelijken van de energie van de absorptie- en emissiebanden, analyseren we de structuur van de luminescentiespectra en onderzoeken we hoe de Mn⁴⁺-luminescentie verandert als functie van de temperatuur.

In **Hoofdstuk 5** onderzoeken we thermische doving en concentratiedoving van Mn⁴⁺-luminescentie. Thermische doving en concentratiedoving zijn respectievelijk het afnemen (doven) van de luminescentie-intensiteit bij hoge temperaturen en bij hoge doteringsconcentraties. Beide processen zijn belangrijk om te bestuderen voor toepassing van Mn⁴⁺-fosforen in LED-lampen. De temperatuur van de fosfor kan oplopen tot 150 °C of zelfs 200 °C in hoog-vermogen LED-lampen. Een hoge luminescentiedooftemperatuur is daarom essentieel voor LED-fosforen, en het is dus belangrijk om te begrijpen wanneer en waarom er thermische doving optreedt. Concentratiedoving is relevant omdat een hoge Mn⁴⁺-doteringsconcentratie nodig is voor sterke absorptie van het blauwe licht in LED-lampen. Om inzicht te krijgen in de

doving van Mn^{4+} -luminescentie, bestuderen we in Hoofdstuk 5 de luminescentie van Mn^{4+} -gedoteerd kaliumfluorotitanaat (K_2TiF_6) voor een breed temperatuurgebied (4 tot 600 K) en voor een grote variatie aan Mn^{4+} -doteringsconcentraties (0.01 tot 15.7 mol%). Op basis van de resultaten en een uitgebreide studie van literatuurgegevens over temperaturovergang van Mn^{4+} -luminescentie in andere fluorides en oxides verkrijgen we inzicht in het mechanisme voor thermische doving. De doving van de rode luminescentie verloopt via thermische bezetting van een hogere aangeslagen toestand van waaruit het Mn^{4+} -ion na absorptie van blauw licht direct kan relaxeren naar de begintoestand, zonder rood licht uit te zenden. In plaats hiervan wordt de energie omgezet in warmte (trillingen van het kristalrooster). De kennis over het mechanisme kan gebruikt worden om de dooftemperatuur van de Mn^{4+} -luminescentie te verhogen. Onze experimenten tonen verder aan dat er nauwelijks concentratiedoving plaatsvindt in Mn^{4+} -gedoteerd K_2TiF_6 tot een Mn^{4+} -doteringsconcentratie van 5 mol%. Dit vergroot de kansen voor het toepassen van Mn^{4+} -gedoteerde fosforen in LED-lampen.

De tweede soort smalbandig rode fosforen die we onderzoeken in dit proefschrift zijn kristallen van cesiumcalciumfosfaat ($\text{Cs}_2\text{CaP}_2\text{O}_7$) en cesiumstrontiumfosfaat ($\text{Cs}_2\text{SrP}_2\text{O}_7$) gedoteerd met tweewaardig europium (Eu^{2+}). De smalbandig geel/rode luminescentie van deze fosforen is interessant voor lichttoepassingen, maar ook zeer bijzonder omdat Eu^{2+} -gedoteerde fosfaten normaal violet of blauw licht uitzenden. In **Hoofdstuk 6** van dit proefschrift onderzoeken we wat de reden is voor de ongebruikelijke geel/rode luminescentie in Eu^{2+} -gedoteerd $\text{Cs}_2(\text{Ca},\text{Sr})\text{P}_2\text{O}_7$. De luminescentie is geel tot rood omdat de Stokes-verschuiving onverwacht groot is in deze fosforen. De Stokes-verschuiving is het energieverschil tussen het maximum van de absorptieband en het maximum van de emissieband van een optische overgang. Uit de luminescentiespectra blijkt dat de grote Stokes-verschuiving veroorzaakt kan worden door een vervorming in de aangeslagen toestand van Eu^{2+} . De aangeslagen toestand is de toestand waarin Eu^{2+} een overschot aan energie heeft door absorptie van licht. Een substantiële vervorming van de EuO_6 -octaëder in deze toestand zou de grote Stokes-verschuiving kunnen verklaren. Metingen aan een vergelijkbare optische overgang voor driewaardig cerium (Ce^{3+}) laten zien dat de Stokes-verschuiving voor de Ce^{3+} -luminescentie normaal is en dat er in de aangeslagen toestand van Ce^{3+} geen vervorming lijkt op te treden.

List of publications

This thesis is based on the following publications:

- T. Senden, E. J. van Harten and A. Meijerink, Synthesis and narrow red luminescence of $\text{Cs}_2\text{HfF}_6:\text{Mn}^{4+}$, a new phosphor for warm white LEDs, *Journal of Luminescence* **194**, 131–138 (2018). (Chapter 2)
- T. Senden, R. G. Geitenbeek and A. Meijerink, Co-precipitation synthesis and optical properties of Mn^{4+} -doped hexafluoroaluminate w-LED phosphors, *Materials* **10**, 1322 (2017). (Chapter 3)
- T. Senden, F. T. H. Broers and A. Meijerink, Comparative study of the $\text{Mn}^{4+} \ ^2\text{E} \rightarrow \ ^4\text{A}_2$ luminescence in isostructural $\text{RE}_2\text{Sn}_2\text{O}_7:\text{Mn}^{4+}$ pyrochlores ($\text{RE}^{3+} = \text{Y}^{3+}, \text{Lu}^{3+}$ or Gd^{3+}), *Optical Materials* **60**, 431–437 (2016). (Chapter 4)
- T. Senden, R. J. A. van Dijk-Moes and A. Meijerink, Quenching of the red Mn^{4+} luminescence in Mn^{4+} -doped fluoride LED phosphors, *submitted*. (Chapter 5)
- T. Senden and A. Meijerink, The d–f luminescence of Eu^{2+} , Ce^{3+} and Yb^{2+} ions in $\text{Cs}_2\text{MP}_2\text{O}_7$ ($\text{M} = \text{Ca}^{2+}, \text{Sr}^{2+}$), *Journal of Luminescence* **177**, 254–260 (2016). (Chapter 6)

Other publications by the author:

- Z. Wang, T. Senden and A. Meijerink, Photonic effects for magnetic dipole transitions, *The Journal of Physical Chemistry Letters* **8**, 5689–5694 (2017).
- M. Suta, T. Senden, J. Olchowka, M. Adlung, A. Meijerink and C. Wickleder, Decay times of the spin-forbidden and spin-enabled transitions of Yb^{2+} doped in CsCaX_3 and CsSrX_3 ($\text{X} = \text{Cl}, \text{Br}, \text{I}$), *Physical Chemistry Chemical Physics* **19**, 7188–7194 (2017).
- L. Mattera, S. Bhuckory, K. D. Wegner, X. Qiu, F. Agnese, C. Lincheneau, T. Senden, D. Djurado, L. J. Charbonnière, N. Hildebrandt and P. Reiss, Compact quantum dot–antibody conjugates for FRET immunoassays with subnanomolar detection limits, *Nanoscale* **8**, 11275–11283 (2016).
- T. Senden, F. T. Rabouw and A. Meijerink, Photonic effects on the radiative decay rate and luminescence quantum yield of doped nanocrystals, *ACS Nano* **9**, 1801–1808 (2015).
- F. T. Rabouw, S. A. den Hartog, T. Senden and A. Meijerink, Photonic effects on the Förster resonance energy transfer efficiency, *Nature Communications* **5**, 3610 (2014).

List of conference contributions

Thermal quenching of red Mn⁴⁺ luminescence in Mn⁴⁺-doped fluoride wLED phosphors (oral presentation).

International Conference on Luminescence, João Pessoa, Brazil, August 2017. Awarded with prize for best oral presentation.

Synthesis and optical properties of Cs₂HfF₆:Mn⁴⁺, a new phosphor for warm white LEDs (poster).

International Conference on Luminescence, João Pessoa, Brazil, August 2017.

Concentration quenching of red Mn⁴⁺ luminescence in K₂TiF₆:Mn⁴⁺ w-LED phosphors (oral presentation).

European Materials Research Society Spring Meeting, Strasbourg, May 2017.

Concentration quenching of red Mn⁴⁺ luminescence in K₂TiF₆:Mn⁴⁺ w-LED phosphors (oral presentation).

Phosphor Safari - International Symposium on Luminescence, Spectroscopy and Applications, Hong Kong, November 2016.

Photonic effects on the radiative decay rate and quantum efficiency of doped nanocrystals (poster).

CHAINS conference, Veldhoven, The Netherlands, December 2015.

The d-f luminescence of Eu²⁺ and Ce³⁺ ions in Cs₂M²⁺P₂O₇ (M = Ca, Sr) (oral presentation).

International Conference on the Physics of Optical Materials and Devices, Budva, Montenegro, September 2015.

The d-f luminescence of Eu²⁺ and Ce³⁺ ions in Cs₂(Ca,Sr)P₂O₇ (oral presentation).

17th International Krutyn Summer School, Krutyn, Poland, June 2015.

Local-field effects on the radiative decay rate of lanthanide-doped LaPO₄ nanocrystals (poster).

International Conference on Luminescence, Wrocław, Poland, July 2014.

Dankwoord

Het is klaar. Na vier jaar lang maken, meten en schrijven is mijn proefschrift af. Dit was niet gelukt zonder de hulp en steun van veel mensen. De afgelopen vier jaar waren erg speciaal. Ik wil hier graag iedereen bedanken die op een of andere manier heeft bijgedragen aan mijn onderzoek en de leuke tijd die ik heb gehad.

Als eerste wil ik Andries, mijn promotor, bedanken. Ik ben blij dat jij mij de kans hebt gegeven dit onderzoek te doen, bedankt voor het vertrouwen. Ik vond het prettig om met je samen te werken en ik heb veel van je geleerd. Je deur stond altijd open voor vragen of als ik hulp nodig had bij de spectroscopische metingen. Dat je graag helpt bij het onderzoek blijkt ook uit dat je voor mij metingen verrichtte bij de UVSOR in Japan, en dat je meedeed aan de experimenten bij de Advanced Photon Source in Chicago. Ik heb genoten van onze trip naar Chicago. Je hebt me daar een mooie introductie in de Amerikaanse cultuur gegeven. Ook op de reizen naar conferenties heb ik veel plezier met je gehad.

Every six months I presented my results to the STW user committee of my project. A lot of people have been part of this committee: Cees Ronda, Dick de Boer, Réne Wegh, Pieter Dorenbos, Marie Anne van de Haar, Mike Krames and Gerry Sorce. I want to thank you all for the interest in my work and the nice suggestions you came up with during the STW meetings. Dick en Réne hebben ook geregeld dat ik quantum efficiency metingen kon doen bij Philips Lighting. Deze metingen waren erg nuttig voor mijn onderzoek. Ik wil hierbij ook graag Mart Peeters bedanken die alle quantum efficiency metingen voor me heeft uitgevoerd.

Een promotieonderzoek is niet mogelijk zonder de hulp van goede technici. Hans en Peter, bedankt voor de technische assistentie bij mijn experimenten en metingen. Jullie hebben allerlei monsterhoudertjes voor me gemaakt en ook veel belangrijke apparatuur gerepareerd, waaronder een hele reeks aan cryostaten. Stephan, jij hebt mooie SEM-foto's en EDX-spectra voor me gemeten. Relinde, jij hebt me bijgestaan bij het opzetten en doen van de syntheses met HF. Tevens wil ik graag de secretaresses Thea en Linda bedanken voor hun hulp met allerlei (administratief) papierwerk en het verzenden van pakketjes voor experimenten.

De afgelopen vier jaar heb ik zeven bachelorstudenten mogen begeleiden bij hun thesisonderzoek. Daniël, Dennis, Harriët, Frédérique, Maarten-Harm, Oscar en Saydi, ik wil jullie allemaal bedanken voor jullie inzet en ideeën. De resultaten van jullie werk waren belangrijk voor mijn promotieonderzoek. Ik vond het daarnaast leuk en leerzaam om jullie te begeleiden.

Tijdens mijn PhD heb ik samengewerkt met veel leuke collega's. De eerste twee jaar van mijn PhD zat ik op kamer OL110 met Elleke, Carlo en Jaco. Elleke, tijdens ons werk en het fietsen naar Overvecht hebben we veel gepraat over experimenten en onderzoeksproblemen, maar ook over sport. We houden allebei van schaatsen en zijn een keer samen naar Thialf geweest. Ik vond het erg gezellig met je op de E-MRS in Straatsburg. Daar hebben we in een Irish pub ook de finale van de Europa League gekeken. Jammer genoeg viel de uitslag van deze finale voor jou een beetje tegen. Carlo, ik kan altijd erg genieten van je mooie verhalen over wetenschap en alledaagse dingen. Ik bewonder je nuchtere kijk op het onderzoek. Daarnaast inspireerde je mij om andere dingen te blijven doen naast mijn onderzoek. Jij bent de volgende van CMI die promoveert. Ik wens je veel succes met je verdediging. Jaco, je was een prettige kamergenoot. Halverwege mijn tijd in OL110 vertrok je helaas naar het ESRF in Grenoble om daar voor een jaar experimenten te doen. Hierdoor kon je me wel een interessante rondleiding bij het ESRF geven toen ik op vakantie was in de Franse Alpen. Je kennis over synchrotrons kwam goed van pas toen ik proposals voor synchrotronexperimenten wilde schrijven.

Halverwege mijn PhD verhuisde ik naar kamer OL168 (mede door een herriemakende ventilator in OL110). Kamer OL168 deelde ik met Robin en Jacobine. Robin, jij was mijn sportmaatje tijdens mijn PhD. We hebben samen intensief getraind voor de halve marathon van Utrecht en mooie tochtjes op de racefiets gemaakt. Daarnaast heb ik genoten van de avondjes met spelletjes en speciaalbier. Ik ben blij dat je mijn paranimf wil zijn. Jacobine, of voor mij meestal Joca, we hebben beiden hard gewerkt om ons proefschrift af te krijgen. Gelukkig hebben we het nu af. Ik ga je (Brabantse) gezelligheid tijdens het werk missen, inclusief alle toepasselijke GIF'jes. Robin en Jacobine, jullie hebben me vaak geholpen met experimenten en we hebben veel over 'brand new information' gepraat. Ook heb ik veel plezier met jullie gehad op conferenties (ik hoop dat ons magnetenbord nog lang blijft hangen). Succes nu met het afronden van jullie promoties.

Naast mijn kamergenoten waren er meer fantastische collega's. Freddy, ik heb veel van je geleerd tijdens mijn PhD, zowel over luminescentie als over de Japanse taal. Je hebt een enorme wetenschappelijke kennis en was altijd bereid om te helpen met metingen of bij het analyseren van data. We hebben ook heel wat uurtjes geklaverjast in de lunchpauzes, al werd dit wat minder toen je naar Zürich ging om daar een postdoc te doen. Gelukkig ben je teruggekomen naar Utrecht en werk je hier nu 'braaf' als een 'echte' professor. Ward, bij de meeste potjes klaverjassen was jij ook van de partij. Daarnaast hebben we vaak als "De Beunhazen" aan een pubquiz meegedaan. Ik vond het ook leuk om met je over voetbal en beker finales te praten. Annelies, op spelletjesavonden hebben we aardig wat dobbelstenen gegooid en fiches geruild. Voor mij waren deze spelletjesavonden een goede afleiding van mijn werk. Mathijs, je bent een zeer kundige onderzoeker. Ik was daarom blij dat je mee wilde naar het synchrotron in Chicago toen ik daar experimenten

ging doen. We zijn ook samen naar Tenerife geweest. De zonsopkomst die we daar op de vulkaan El Teide hebben gezien was onvergetelijk.

On Tenerife I also met Pedro. He was first a PhD researcher at the University of Bern, but later joined the CMI group as a postdoc. Pedro, you are a great guy and it is always nice to drink beer or eat tortilla with you. Maryam, poke, you are such a kind and funny person. It is always great to talk and laugh with you. I also very much enjoy your excellent Persian cooking skills. Good luck with finishing your PhD thesis, I am sure you will be fine. Chenghui, you introduced me to the Chinese culture when I was in Hong Kong. Thanks a lot for your hospitality. Furthermore, I would like to thank all my other CMI colleagues for the great time: Joep, Federico, Tim, Kelly, Serena, Christa, Anne, Annalisa, Christiaan, Sophia, Saoirse, Peter, Marlou, Zijun, Joost, Nadine, Wenjin, Ting, Joren, Mark, Chun Che, Vasya, Kunyuan, Jumpei, Per-Anders, Daniël, Celso, Ingmar and everyone I forgot to mention. You all have contributed to the success of my PhD.

Er zijn meer mensen die ik graag wil bedanken. Jan, Willem-Bart (Wiba), Mischa, Paul, Ingrid en Nienke, ik ken jullie vanaf 2007 toen we samen Aardwetenschappen gingen studeren. Ik vind het fijn dat we nog steeds vrienden zijn, ondanks dat ik in 2008 overstapte naar Scheikunde. Ik wil jullie en alle andere mensen van "jaartje 007" bedanken voor de gezelligheid tijdens de koffiepauzes, (botatu)lunches, weekendjes weg, fietstochten, feestjes, (Franse) filmavonden en vele andere activiteiten.

Stephan, ik ben jaloers op jouw kookkunsten. Het is altijd prettig om met jou te koken en te eten. Ik ben blij dat je mijn paranimf wil zijn en ik hoop dat je nog een mooie tijd in Brussel gaat hebben. Jasper, de tripjes naar jou in Lund waren voor mij een plezierige afleiding tussen al het onderzoek. Vooral het weekend in nationaal park Söderåsen was erg speciaal. Jij ook veel succes met het afronden van je PhD-project. Marit, Marjolein en Matthijs, jullie waren geweldige huisgenootjes. Ik heb altijd veel lol met jullie. Ik hoop dat we nog vaak samen zullen eten, feesten en op stap gaan.

Annie, Dick, Luuk, Ida en Stef, ik ben blij dat ik zo'n lieve en leuke schoonfamilie heb. Bedankt voor de interesse en steun in de afgelopen jaren. Ik wil ook al mijn ooms, tantes, neefjes en nichtjes van de families Senden en Keus bedanken. Ik vind het altijd gezellig met jullie en ik heb veel plezier op de familiedagen. Bedankt allemaal voor de interesse in mijn werk en voor het geduld wanneer ik probeerde uit te leggen wat ik nou precies onderzocht. Lieske en Wieger, ik kom graag langs bij jullie in Delft. Gesprekken met jullie geven me vaak goede ideeën. Lieske, bedankt voor alle steun van jongs af aan. In januari zijn we allebei klaar met onze thesis, dat gaan we een keer goed vieren. Mama, Papa, ik ben dankbaar voor alle steun die jullie me al mijn hele leven geven. Jullie geven me veel vertrouwen en hebben vaak goede raad. Bedankt voor de interesse in mijn werk en alle hulp de afgelopen vier jaar.

Lieve Suzanne, het laatste stukje van dit dankwoord is voor jou. Ik wil je bedanken voor al je hulp en liefde. Je kennis en scherpe blik hebben me veel geholpen bij mijn onderzoek. Daarnaast was je er ook altijd voor mij als het even allemaal wat moeilijker ging. Ik kijk uit naar een mooie toekomst met jou. Bedankt voor alles, ik hou van je!

- Tim, December 2017 -



About the author

Tim Senden was born in Rotterdam on the 3rd of September in 1989. In 2007 he graduated from the Wolfert van Borselen Scholengroep and started studying Earth Sciences at Utrecht University. After completing the first year of the bachelor Earth Sciences, he started studying Chemistry at Utrecht University in 2008. He obtained his bachelor's degree *cum laude* in 2011 after finishing his thesis on supported cobalt catalysts at the Inorganic Chemistry and Catalysis group. He then followed the Master programme Nanomaterials: Chemistry and Physics and obtained his master's degree *cum laude* in 2013. His thesis research entitled "Energy transfer and radiative decay properties of lanthanide doped LaPO₄ nanocrystals" was performed in the Condensed Matter and Interfaces group under the supervision of Freddy Rabouw and Andries Meijerink. Furthermore, he did a six-month internship at the CEA in Grenoble, France, where he worked on the synthesis of InP-based nanocrystals for LED applications. During his studies, Tim was a student representative in several department and faculty councils. Also he was a board member of Stichting PAC, which organizes the annual national PAC symposium for chemistry students.

In October 2013 Tim started as PhD researcher in the Condensed Matter and Interfaces group under the supervision of Andries Meijerink. The main results of his work are described in this thesis, have been published in peer-reviewed scientific journals, and presented at (inter)national conferences. Tim was awarded the prize for best oral presentation at the 18th International Conference on Luminescence in João Pessoa, Brazil. During his PhD project, Tim supervised seven students and was a teaching assistant for several chemistry courses.

In his spare time Tim likes to run and cycle. Furthermore, he enjoys going to concerts, meeting with friends, browsing maps and reading books about history.

